NASA TECHNICAL NOTE

NASA TN D-7670

NASA TN D-7670

LONGITUDINAL AERODYNAMIC CHARACTERISTICS OF AN EXTERNALLY BLOWN FLAP POWERED-LIFT MODEL WITH SEVERAL PROPULSIVE SYSTEM SIMULATORS

by Danny R. Hoad

Langley Directorate

U.S. Army Air Mobility R&D Laboratory

Hampton, Va. 23665

NATIONAL AERONAUTICS AND SPACE ADMINISTRATION • WASHINGTON, D. C. • SEPTEMBER 1974

1. Report No.	2. Government Accession No.	3. Recipient's Catalog No.
NASA TN D-7670		

4. Title and Subtitle	5. Report Date
LONGITUDINAL AERODYNAMIC CHARACTERISTICS OF AN EXTERNALLY BLOWN FLAP POWERED-LIFT MODEL WITH SEVERAL PROPULSIVE SYSTEM SIMULATORS	September 1974
	6. Performing Organization Code

7. Author(s)	8. Performing Organization Report No.
Danny R. Hoad, Langley Directorate, U.S. Army Air Mobility R&D Laboratory	L-9538
	10. Work Unit No.
	760-61-02-03

9. Performing Organization Name and Address	11. Contract or Grant No.
NASA Langley Research Center Hampton, Va. 23665	
	13. Type of Report and Period Covered
	Technical Note

12. Sponsoring Agency Name and Address	14. Sponsoring Agency Code
National Aeronautics and Space Administration Washington, D.C. 20546	

15. Supplementary Notes

16. Abstract

An investigation of a four-engine externally blown flap (EBF) powered-lift transport was conducted in the Langley V/STOL tunnel to determine the effect of different engine configurations on the longitudinal aerodynamic characteristics. The different engine configurations were simulated by five different sets of propulsion simulators on a single aircraft model. Longitudinal aerodynamic data were obtained for each simulator on each flap deflection corresponding to cruise, take-off, and landing at a range of angles of attack and various thrust coefficients.

The bypass ratio (BPR) 6.2 engine simulator provided the best lift and drag characteristics of the five simulators tested in the take-off and landing configurations. The poor performance of the BPR 10.0 and 3.2 engine simulators can be attributed to a mismatch of engine-model sizes or poor engine location and orientation. Isolated engine wake surveys indicated that a reasonable assessment of the aerodynamic characteristics of an engine—wing-flap configuration could be made if qualitative information were available which defined the engine wake characteristics. All configurations could be trimmed easily with relatively small horizontal-tail incidence angles; however, the take-off and landing configurations required a high-lift tail.

17. Key Words (Suggested by Author(s))	18. Distribution Statement
Externally blown flap Powered lift model Daisy nozzle engine Triple-slotted flap Engine comparison	Unclassified — Unlimited STAR Category 01

19. Security Classif. (of this report)	20. Security Classif. (of this page)	21. No. of Pages	22. Price*
Unclassified	Unclassified	141	$4.75

*For sale by the National Technical Information Service, Springfield, Virginia 22151

LONGITUDINAL AERODYNAMIC CHARACTERISTICS OF AN EXTERNALLY BLOWN FLAP POWERED-LIFT MODEL WITH SEVERAL PROPULSIVE SYSTEM SIMULATORS

By Danny R. Hoad
Langley Directorate, U.S. Army Air Mobility R&D Laboratory

SUMMARY

An investigation of a four-engine externally blown flap (EBF) powered-lift transport was conducted in the Langley V/STOL tunnel to determine the effect of different engine configurations on the longitudinal aerodynamic characteristics. The different engine configurations were simulated by five different sets of propulsion simulators on a single aircraft model. Longitudinal aerodynamic data were obtained for each simulator on each flap deflection corresponding to cruise, take-off, and landing at a range of angles of attack and various thrust coefficients.

The bypass ratio (BPR) 6.2 engine simulator provided the best lift and drag characteristics of the five simulators tested in the take-off and landing configurations. The poor performance of the BPR 10.0 and 3.2 engine simulators can be attributed to a mismatch of engine-model sizes or poor engine location and orientation. Isolated engine wake surveys indicated that a reasonable assessment of the aerodynamic characteristics of an engine—wing-flap configuration could be made if qualitative information were available which defined the engine wake characteristics. All configurations could be trimmed easily with relatively small horizontal-tail incidence angles; however, the take-off and landing configurations required a high-lift tail.

INTRODUCTION

The externally blown flap (EBF) concept considered for use on a jet-powered STOL transport has been investigated on various engine and model configurations. (See refs. 1 to 7.) Very few investigations to date have considered the effect of engine type, size, and fan-exit location on the aerodynamic characteristics of the configuration. This wind-tunnel investigation was conducted to determine these effects with five available engine simulators. Three sets of engine simulators were designed to represent bypass ratio 3.2, bypass ratio 6.2, and bypass ratio 10.0 engines. The bypass ratio (BPR) as designated is correct; however, the physical size and locations are not necessarily optimum for this

research model. The BPR of these engine simulators does not describe in any way the size, horizontal position, or vertical position of the simulator. The data presented for the BPR 3.2 engine configuration were obtained from reference 8. One of these simulators was designed to represent the exhaust characteristics of a daisy-nozzle exhaust shape. This shape was representative of a design such as the ones in references 9, 10, and 11 which reduce exhaust velocity near the flaps and therefore reduce jet-impingement noise. This multilobe nozzle, which will be referred to as the daisy-nozzle engine, was sized so that the inlet and exit areas would match the BPR 6.2 engine. One parameter which was not held constant was the relative chordwise position of the engine exhaust with respect to the flap system. In an attempt to determine whether there was an effect of the relative chordwise position of the engine exhaust, an extension was added to the BPR 6.2 fan cowl so that its exit would be positioned at the same relative chordwise location as the daisy-nozzle fan exit.

The investigation was conducted in the Langley V/STOL tunnel. The longitudinal data are presented at several thrust coefficients with flap deflections which represent a cruise configuration, a take-off configuration, and a landing configuration. The thrust-removed longitudinal data and isolated engine exhaust pressure decay characteristics are also presented.

SYMBOLS

The longitudinal aerodynamic data in this report are referred to the stability axes. (See fig. 1.) The origin of the axes was located on the fuselage center line longitudinally at 0.40 mean aerodynamic chord and vertically at the average center line of each engine configuration.

The units for the physical quantities defined in this paper are given in both the International System of Units (SI) and the U.S. Customary Units. Equivalent dimensions were determined by using the conversion factors given in reference 12.

c local wing chord, meters (ft)

$\bar{c}$ mean aerodynamic chord, meters (ft)

c_s local chord, horizontal stabilizer, meters (ft)

C_D drag coefficient, $\frac{\text{Drag}}{q_\infty S}$

C_L lift coefficient, $\frac{\text{Lift}}{q_\infty S}$

C_m pitching-moment coefficient, $\frac{\text{Pitching moment}}{q_\infty S\bar{c}}$

C_μ thrust coefficient, $\frac{\text{Thrust}}{q_\infty S}$

i_t horizontal-tail incidence angle (positive direction, trailing edge down), degrees

q_j effective jet-exhaust dynamic pressure, newtons/meter^2 (lb/ft^2)

q_∞ free-stream dynamic pressure, newtons/meter^2 (lb/ft^2)

r radius, meters (ft)

S wing area, meters^2 (ft^2)

t/c airfoil thickness ratio

T static thrust, newtons (lb)

x longitudinal distance from leading edge of wing (positive when measured aft of leading edge of wing), meters (ft)

X,Z body reference axes (see fig. 1)

α angle of attack, degrees

δ_e elevator deflection (positive when deflected down), degrees

δ_f wing trailing-edge flap deflection (positive when deflected down), degrees

δ_j jet-exhaust deflection (measured from body reference axis X, positive when deflected down), $\tan^{-1}\left(\frac{\text{Normal force}}{\text{Axial force}}\right)$, degrees

δ_{sh} horizontal stabilizer leading-edge slat deflection (positive when deflected down), degrees

δ_{sw} wing leading-edge slat deflection (positive when deflected down), degrees

η static thrust recovery efficiency, $\frac{\sqrt{(\text{Normal force})^2 + (\text{Axial force})^2}}{T}$

MODEL AND APPARATUS

A three-view drawing of the model with dimensional characteristics is presented in figure 2. This model was identical to the model in reference 8. (See ref. 8 for all airfoil ordinates.) Photographs of the model showing the daisy-nozzle engine simulator installed and the triple-slotted flap system are presented in figure 3.

The outboard leading-edge slat element had an airfoil section that was a 25-percent-chord St. Cyr 178 modified to $t = 0.0065c$ at the trailing edge. This slat element extended from the outboard engine pylon to the wing tip. Two inboard slat elements had an airfoil section that was a 15-percent-chord St. Cyr 178 modified to $t = 0.0065c$ at the trailing edge. The innermost slat element extended from the fuselage to the inboard engine pylon, and the third slat element extended between the inboard and outboard engine pylons. In the deployed position, the slat gap was 0.015c.

The wing flaps were triple-slotted, full-span flaps with 15-, 20-, and 22.5-percent local wing chord for the first, second, and third elements, respectively. The first and second flap elements had a St. Cyr 178 airfoil section modified slightly to provide a finite trailing-edge thickness and to fit the upper surface contours of the wing in the retracted position. The third flap element had a NACA 4412 airfoil section modified to $t = 0.0045c$ at the trailing edge. All flap-slat gaps were 0.015c. The geometric characteristics of the wing leading-edge slats and flaps are presented in figure 4.

The geometric characteristics of the horizontal tail are shown in figure 5. The horizontal tail was pivoted about 0.555 root chord with an incidence range of $\pm 15^{\circ}$ in 5° increments. It had a 15-percent local-chord leading-edge slat set at -40°. The 35-percent local-chord elevator had three deflections relative to the tail chord: 0°, -25°, and -50°.

Four air ejector engine simulators were used to represent each fan-jet propulsion system. Each engine simulator was a two-part ejector with individual air-supply lines and control valves designed to provide the efflux of the fan- and gas-generator stages. A typical ejector assembly is presented in figure 6. Each engine simulator was fitted with five separate cowl assemblies intended to represent the five different engine configurations. (See fig. 7.)

The bypass ratio (BPR) is defined as the ratio of total fan-exit mass flow to total gas-generator-exit mass flow. The five separate cowl assemblies fitted to these ejector simulators were designed to represent a BPR 6.2 daisy-nozzle engine, a BPR 6.2 engine, a modified BPR 6.2 engine, a BPR 10.0 engine, and a BPR 3.2 engine. The daisy-nozzle

engine simulator was designed to represent an engine whose exit and inlet area are identical to those of the BPR 6.2 engine. This type of nozzle exit is designed to increase the velocity decay characteristics of the engine and thereby reduce the velocity at the flaps, which, in turn, reduces flap-impingement noise. Although the inlet and exit areas of the BPR 6.2 and daisy-nozzle engines were identical, the longitudinal positions of their fan exits relative to the flap system were not. The BPR 6.2 engine simulator was modified during the investigation. An extension was added which relocated the fan exit at the same relative location as that of the daisy-nozzle engine simulator. This engine simulator will be referred to as the modified BPR 6.2 engine simulator. (See fig. 7.)

The model was mounted in the Langley V/STOL tunnel on a sting-supported six-component strain-gage balance for measurements of the total forces and moments.

TEST AND CORRECTIONS

This investigation was conducted in the Langley V/STOL tunnel. The free-stream dynamic pressure for the entire investigation was 814 N/m^2 (17 lb/ft^2). The Reynolds number (based on wing $\bar{c}$ and free-stream velocity) was approximately 0.697×10^6. The data presented in this report are not corrected for wind-tunnel wall effects. Since the corrections calculated by the method of reference 13 were found to be small and this report is a comparison of the engine-model configurations of the test, it is felt that the data are valid.

Calibrations were made to determine the thrust, inlet mass-flow rate, and primary mass-flow rate of the fan- and gas-generator stage of each engine simulator assembly separately as a function of their respective plenum pressures. These data were run at zero airspeed and reflect the static thrust only. The values of thrust coefficient are based on this static-thrust calibration and are presented as the conventional thrust coefficient, that is, static thrust nondimensionalized by the product of free-stream dynamic pressure and wing area $\left(C_\mu = \frac{T}{q_\infty S}\right)$.

The static inlet and primary mass flow rates were used to set the desired pressure in the plenum of each separate stage of each engine to provide the correct ratio of total fan exit mass flow rate to total gas generator exit mass flow rate (BPR).

Isolated engine-exhaust-wake surveys were conducted. Dynamic-pressure measurements were made with a pressure rake positioned so that the probes were alined with the flow and parallel to the engine geometric center line. The probes were alined along a radial line from the geometric center line. Four radial positions were chosen for the

daisy nozzle and two radial positions were chosen for the other four engine simulators. These profiles were repeated at various downstream locations to obtain dynamic-pressure decay characteristics.

Jet-deflection angles δ_j and static-thrust recovery efficiency η were determined from measurements of the normal and axial forces made in the static thrust condition with flaps deflected and leading-edge slat deployed.

Each of the five engine configurations was tested in the cruise configuration, the take-off configuration, and the landing configuration at an angle-of-attack range from -4° to 24°. Each configuration was tested at a thrust coefficient range from 0 to 4 and at various horizontal-tail incidences.

The cruise configuration was defined as the model with 0° flaps, no wing leading-edge slats, no horizontal-tail leading-edge slats, and elevator set at 0°. The take-off configuration was defined as the model with the elements of the three-element flap system set at 0°, 20°, and 40°; wing leading-edge slat deployed at 50°; horizontal-tail leading-edge slat deployed at -40°; and elevator set at -25°. The landing configuration was defined as the model with the flap system elements set at 15°, 35°, and 55°; wing leading-edge slats deployed at 50°; horizontal-tail leading-edge slats deployed at -40°; and elevator set at -25°. The wing cross sections for these configurations are presented in figure 4.

PRESENTATION OF RESULTS

Results of the present investigation are presented in the following figures:

DISCUSSION OF RESULTS

The reader should be reminded that each engine simulator used in this investigation is not necessarily indicative of the geometric size of the respective full-scale engine whose bypass ratio might be the same. The engine position and size relationship to the model are not necessarily that which would be used on the full-scale airplane.

Static Thrust Characteristics

The flap static turning effectiveness parameters δ_j and η are presented in figures 8 and 9. Figure 8 presents these parameters in a polar coordinate form. These parameters for the five distinct engine simulator assemblies installed on the model in the take-off configuration $\left(\delta_f = 0^o/20^o/40^o\right)$ and in the landing configuration $\left(\delta_f = 15^o/35^o/55^o\right)$ are presented at a thrust which would correspond to a thrust coefficient of 3 with a forward-speed dynamic pressure of 814 N/m^2 (17 lb/ft^2).

A perpendicular distance from a data point in figure 8 to the horizontal axis would represent the lift component due to thrust at an angle of attack of 0^o, and a perpendicular distance from the data point to the vertical axis would represent the negative drag component due to thrust at an angle of attack of 0^o. If it were assumed that with zero power all engine simulator configurations had identical characteristics and that the only additions to the aerodynamic characteristics at an angle of attack of 0^o are those components in figure 8, an assessment could be made as to the relative merit of the five configurations. In the landing configuration at a thrust coefficient of 3, the relative lift-producing capabilities at an angle of attack of 0^o of each of the five engine configurations would be expected to be (from best to worst): (1) the daisy nozzle, (2) the bypass ratio 6.2 and the modified bypass ratio 6.2, and (3) the bypass ratio 10.0 and the bypass ratio 3.2. In the take-off configuration, it would be expected that the relative lift-producing capabilities at an angle of attack of 0^o would be (from best to worst): (1) the modified bypass ratio 6.2, the daisy nozzle, and the bypass ratio 6.2; and (2) the bypass ratio 10.0 and the bypass ratio 3.2.

As discussed in reference 4, this assessment of the aerodynamic characteristics of an engine-model configuration is not necessarily true. A more pertinent comparison, with data to substantiate it, is presented later in this report.

Figure 9 presents the same flap static turning effectiveness parameters as a function of thrust for the take-off and landing configurations. This figure indicates that δ_j and η vary only slightly with thrust above 400 newtons (90 lb) (which is a thrust corresponding to a $C_\mu \approx 1.0$ at the forward-velocity test condition for this investigation).

Longitudinal Aerodynamic Characteristics

Wind-tunnel wall corrections were applied to sample cases of the data by using reference 13 to determine their effect on the basic longitudinal aerodynamic data. These data are presented in figure 10. These corrections resulted in a slight change in angle of attack and free-stream dynamic pressure. Since this report is intended to be a comparison of the engine simulator configurations and these corrections are so small, the data are presented in the uncorrected form.

The basic longitudinal aerodynamic data for all configurations are presented in figures 11 to 25 at various flap settings and tail incidences. The data are presented with lift coefficient as a function of angle of attack, drag coefficient, and pitching-moment coefficient. Pitching-moment coefficient is also presented as a function of angle of attack. All the data are presented at various thrust coefficients. Generally, addition of power to any one of these configurations causes an increase in maximum lift coefficient, in angle of attack for maximum lift coefficient, and in lift-curve slope. The data for the cruise configurations indicate that the various lift curves at different thrust coefficients rotate about a specific angle of attack. With power, the lift coefficient increases at angles of attack above this point and decreases below it. These effects can be attributed to power effects and possibly to interference effects related to inlet characteristics at cruise speeds. This point of rotation is configuration oriented and is not affected by tail incidence.

Longitudinal Stability and Control Characteristics

The pitching-moment coefficient for all configurations is presented in figures 26 to 30 as a function of angle of attack and lift coefficient. The data are presented at various thrust coefficients and at various i_t values to determine the effect of thrust coefficient on trim capability and longitudinal stability.

The pitching-moment coefficients are referenced to the fuselage center line longitudinally at $0.40\bar{c}$ and vertically at the average center line of the engines. Also presented in figures 26 to 30 are the pitching-moment coefficients for the tail-off configurations for the various engine-wing combinations. Tail-off data for the daisy-nozzle cruise configuration were not obtained and were therefore not presented. Examination of the tail-on cruise configurations data indicates that the pitching-moment characteristics for the daisy nozzle, bypass ratio 6.2, and modified bypass ratio 6.2 are very similar; therefore, the faired curve in figure 26(a) is a tracing of the bypass ratio 6.2 and modified bypass ratio 6.2 tail-off cruise pitching-moment coefficients. In general, all the configurations displayed decreasing stability due to increasing power. All the tail-on take-off and landing configurations data were longitudinally stable to maximum lift coefficient. The tail-on cruise configurations data, however, were stable up to the angle

of attack at which stall occurred. The ranges of i_t required to trim the configurations (at any angle of attack) throughout the range of thrust coefficients of the test are summarized in the following table:

	Cruise, $\delta_f = 0^o$	Take-off, $\delta_f = 0^o/20^o/40^o$	Landing, $\delta_f = 15^o/35^o/55^o$
Daisy nozzle	-5^o to 0^o	0^o to 7^o	0^o to 7^o
BPR 6.2	-5^o to 1^o	-3^o to 7^o	-5^o to 10^o
Modified BRP 6.2	-5^o to 1^o	-2^o to 7^o	-5^o to 7^o
BPR 10.0	-5^o to 1^o	0^o to 10^o	0^o to 10^o
BPR 3.2	-5^o to 1^o	0^o to 7^o	0^o to 7^o

The cruise configuration required only a symmetrical airfoil, whereas the take-off and landing configurations required a high-lift horizontal tail.

Effect of Engine Type on Longitudinal Aerodynamic Characteristics

In figures 31 to 35, the longitudinal aerodynamic characteristics of the five configurations are compared as presented at various flap deflections and thrust coefficients. Where data are presented as dashed lines, they were interpolated to levels of thrust coefficients comparable with the data for the other configurations presented. For the cruise configuration, data are presented for the tail-off case in figure 31 and for the tail-on case with an i_t of 0^o in figure 32. The longer bypass ratio 3.2 engine simulators increased power-off maximum lift coefficient. The data presented at a thrust coefficient of 1.8 indicate that the larger bypass ratio 3.2 and bypass ratio 10.0 engine simulators are producing more lift. Contrary to expected results for increased lift coefficient, these configurations produced more nose-up pitching moment. This result indicates that the thrust center line was below the engine geometric center and/or these engine simulators shifted the center of lift toward the leading edge of the wing. The static-engine calibration confirmed that the thrust center line was below the geometric center line.

The data for the take-off configurations are presented in figure 33. The daisy-nozzle and the modified bypass ratio 6.2 engine simulator configurations delayed stall to $\alpha = 15^o$ in the power-off case. At a thrust coefficient of 3.0, there was a definite difference among the engine simulator configurations. The daisy nozzle, bypass ratio 6.2, and modified bypass ratio 6.2 engines produced larger lift coefficients than the bypass ratio 10.0 and bypass ratio 3.2. The modified bypass ratio 6.2 engine had an early stall and lower maximum lift coefficient than the bypass ratio 6.2 and daisy nozzle engine.

With relatively lower lift coefficient, the bypass ratio 10.0 and bypass ratio 3.2 also generated less nose-down pitching-moment coefficient; however, the bypass ratio 3.2 engine produced less than the bypass ratio 10.0 engine at about the same levels of lift coefficient and indicated that the center of lift had been shifted toward the leading edge of the wing.

The data for the landing configuration are presented in figure 34. Similar to the take-off power-off data, the daisy nozzle and the modified bypass ratio 6.2 engine simulator delayed stall. The aerodynamic characteristics of each engine simulator configuration differed and were easily discernible at a thrust coefficient of 4.0. The bypass ratio 6.2 engine provided the largest lift coefficient; the modified bypass ratio 6.2 engine provided the next largest lift coefficient at low angles of attack. At large angles of attack, this configuration experienced stall problems. The daisy nozzle, bypass ratio 10.0, and bypass ratio 3.2 provided decreasing levels of lift coefficient in that order. Higher levels of lift coefficient corresponded to higher levels of nose-down pitching-moment coefficient and indicated that the differences in lift produced can be attributed to differences in loads generated by the flap system. The reader should be reminded that the physical sizes and locations of the engine simulators are not necessarily optimum for this research model. The poor performance of the bypass ratio 10.0 and bypass ratio 3.2 engine configurations could possibly be improved by properly matching engine size to model size or by positioning the engines in an advantageous location or attitude.

Effect of Engine Type on Lift Coefficient

Figure 35 presents the lift coefficient of each engine simulator configuration at an angle of attack of 0° as a function of the thrust coefficient for the take-off and landing configurations. In the take-off configuration, the bypass ratio 6.2, modified bypass ratio 6.2, and the daisy-nozzle engine simulators produced essentially the same lift coefficient. The bypass ratio 10.0 and bypass ratio 3.2 engine simulator configurations produced much less lift coefficient at comparable thrust coefficients. In the landing configuration, the bypass ratio 6.2 and modified bypass ratio 6.2 simulators produce the most lift coefficient. The daisy nozzle, bypass ratio 10.0, and bypass ratio 3.2, in that order, provided decreasing amounts of lift at comparable thrust coefficients. Again the reader should be reminded that the size of the bypass ratio 10.0 and bypass ratio 3.2 engine models could be mismatched. Improvements to this mismatch could improve the performance of these configurations.

Thrust-Removed Lift-Drag Polars

Figures 36 to 41 present the thrust-removed lift coefficient as a function of the thrust-removed drag coefficient at various thrust coefficients. These data are presented

for all engine simulators in the cruise, take-off, and landing configurations. The thrust-removed lift coefficient was obtained by subtracting the component of lift due to thrust from the gross lift. This component $\left(C_\mu \sin(\alpha + \delta_j)\eta\right)$ uses the thrust coefficient and flap-effectiveness parameters presented in figure 9. The thrust-removed drag coefficient was obtained in a similar manner by adding the component of thrust to the gross drag. This component $\left(C_\mu \cos(\alpha + \delta_j)\eta\right)$ also used the flap effectiveness parameters from figure 9.

The thrust-removed data for each configuration at all thrust coefficients tested combine into a set of curves with an envelope similar to that for the power-off data, and indicate that the data generally follow the same polar curve for a given engine and flap configuration. These polar curves are presented in figure 41 as tracings of the corresponding data at thrust coefficients ranging from 0 to 4; fairings are also presented in applicable parts of figures 30 to 40. In figure 41 symbols are used to distinguish between curves and are not data points. These data present a relative comparison of the circulation lift among the configurations. For the take-off configuration, the bypass ratio 6.2 and the modified bypass ratio 6.2 engine simulator configurations provided the largest circulation lift. The daisy nozzle provided a little less, and the bypass ratio 10.0 and bypass ratio 3.2 provided the least. For the landing configuration, the data were similar except that (1) the modified bypass ratio 6.2 configuration again shows early stall, and (2) the daisy-nozzle circulation lift is now better than that of the bypass ratio 10.0, and, at low thrust coefficients, no better than that of the bypass ratio 3.2.

The results from this comparison and the comparison of the flap static turning effectiveness parameters are different. The pertinent comparison is at forward speed at some angle of attack. This comparison has been made at an angle of attack of 0° in figure 35.

Isolated Engine Dynamic Pressure Decay

In an attempt to understand the reasons for the different lift performance of the various engine simulator configurations, isolated engine-wake surveys were conducted. At various positions downstream of the engine exit, dynamic-pressure measurements were made at four radial positions for the daisy nozzle and at two radial positions for the other four simulators. Then these measurements were integrated over the entire exhaust areas at that position to arrive at an average dynamic pressure. These data are presented in figure 42. The average dynamic pressure is nondimensionalized by static thrust over the wing area and presented as a function of downstream distance, nondimensionalized by the wing mean aerodynamic chord. The relative positions of the wing leading edge, engine exit positions, and inboard and outboard third element flap leading-edge positions are superimposed in the figure to present a comparison at significant positions. For clarity,

the daisy nozzle, bypass ratio 6.2, and modified bypass ratio 6.2 engine simulators are presented in figure 42(a); the daisy nozzle, bypass ratio 10.0, and bypass ratio 3.2 engine simulators are presented in figure 42(b). The daisy nozzle is presented in both parts for relative comparisons.

Comparing these data at the position of the flaps with the previous data in figure 35 provides a possible explanation for the differences in performance; a trend does exist. The engine simulators with the largest average dynamic pressure at the flaps (bypass ratio 6.2 and modified bypass ratio 6.2) did produce the most lift. Those with the smallest average dynamic pressure at the flaps (bypass ratio 10.0 and bypass ratio 3.2) did produce the least lift. These data indicate only a trend, in that, to assess qualitatively the relative merit of several engine configurations on a wing-flap combination, some engine exhaust information must be known. Quantitatively, these data are not conclusive enough to form the basis which could permit a prediction of the aerodynamics of an engine-wing-flap system. However, they do indicate that with a more comprehensive examination of each engine wake, a method of superimposing this known engine wake onto the known aerodynamic characteristics of a wing-flap combination could possibly lead to a reasonable prediction of the overall aerodynamic characteristics of the engine-wing-flap arrangement.

CONCLUDING REMARKS

An investigation of a four-engine externally blown flap STOL transport was conducted to determine the effects of different engine configurations on the longitudinal aerodynamic characteristics. The different engine configurations were simulated by five different sets of propulsion simulators on a single aircraft model. The results of this investigation are as follows:

1. In the take-off configuration, the bypass ratio 6.2, modified bypass ratio 6.2, and the daisy-nozzle simulators all produced nearly the same levels of lift coefficient whereas the bypass ratio 10.0 and bypass ratio 3.2 both produced nearly the same lower level of lift coefficient.

2. In the landing configuration, each engine simulator configuration produced different lift coefficient capabilities at low angles of attack. They are (from best to worst): (1) bypass ratio 6.2, (2) modified bypass ratio 6.2, (3) daisy nozzle, (4) bypass ratio 10.0, and (5) bypass ratio 3.2.

3. The poor performance of the bypass ratio 10.0 and bypass ratio 3.2 can be attributed to the mismatch of engine size to model, or engine location and orientation.

4. Isolated engine dynamic-pressure surveys indicated that the engine simulators producing the better lift coefficients also had the higher average dynamic pressures at a point where they would intersect the flaps. These data indicate only a trend. Quantitatively, these data are not conclusive enough to form a basis which would permit the prediction of the aerodynamics of an engine wing flap system.

5. Addition of thrust to all the configurations reduced the level of longitudinal stability. All the tail-on take-off and landing configurations were longitudinally stable to maximum lift coefficient. All the tail-on cruise configurations were longitudinally stable only to the angle of attack for stall.

6. All configurations, even at the highest thrust coefficients, could be trimmed with relatively low tail incidence. The cruise configuration only required the simple symmetrical airfoil, whereas the take-off and landing configuration required a high-lift horizontal tail.

7. The engine type and size does affect the lift-curve slope and maximum lift coefficient for the cruise configuration.

Langley Research Center,
National Aeronautics and Space Administration,
Hampton, Va., April 9, 1974.

REFERENCES

1. Parlett, Lysle P.; Freeman, Delma C., Jr.; and Smith, Charles C., Jr.: Wind-Tunnel Investigation of a Jet Transport Airplane Configuration With High Thrust-Weight Ratio and an External-Flow Jet Flap. NASA TN D-6058, 1970.

2. Freeman, Delma C., Jr.; Parlett, Lysle P.; and Henderson, Robert L.: Wind-Tunnel Investigation of a Jet Transport Airplane Configuration With an External-Flow Jet Flap and Inboard Pod-Mounted Engines. NASA TN D-7004, 1970.

3. Vogler, Raymond D.: Wind-Tunnel Investigation of a Four-Engine Externally Blowing Jet-Flap STOL Airplane Model. NASA TN D-7034, 1970.

4. Anon.: STOL Technology. NASA SP-320, 1972.

5. Smith, Charles C., Jr.: Effect of Wing Aspect Ratio and Flap Span on Aerodynamic Characteristics of an Externally Blown Jet-Flap STOL Model. NASA TN D-7205, 1973.

6. Parlett, Lysle P.; Smith, Charles C., Jr.; and Megrail, James L.: Wind-Tunnel Investigation of Effects of Variations in Reynolds Number and Leading-Edge Treatment on the Aerodynamic Characteristics of an Externally Blown Jet-Flap Configuration. NASA TN D-7194, 1973.

7. Aoyagi, Kiyoshi; Falarski, Michael D.; and Koenig, David G.: Wind-Tunnel Investigation of a Large-Scale 25° Swept-Wing Jet Transport Model With an External Blowing Triple-Slotted Flap. NASA TM X-62197, 1973.

8. Gentry, Garl L., Jr.: Wind-Tunnel Investigation of an Externally Blown Flap STOL Transport Model Including an Investigation of Wall Effects. NASA TM X-3009, 1974.

9. Von Glahn, U. H.; Groesbeck, D. E.; and Huff, R. G.: Peak Axial-Velocity Decay With Single- and Multi-Element Nozzles. NASA TM X-67979, 1972.

10. Maiden, Donald L.: Performance Comparison of a Lobed-Daisy Mixer Nozzle With a Convergent Nozzle at Subsonic Speeds. NASA TM X-2806, 1973.

11. Goodykoontz, Jack H.; Dorsch, Robert G.; and Groesbeck, Donald E.: Noise Tests of a Mixer Nozzle—Externally Blown Flap System. NASA TN D-7236, 1973.

12. Mechtly, E. A.: The International System of Units – Physical Constants and Conversion Factors (Second Revision). NASA SP-7012, 1973.

13. Heyson, Harry H.: Use of Superposition in Digital Computers To Obtain Wind-Tunnel Interference Factors for Arbitrary Configurations, With Particular Reference to V/STOL Models. NASA TR R-302, 1969.

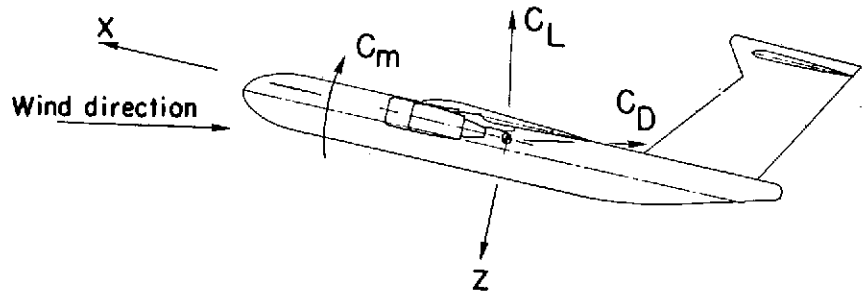

Figure 1.- Axis system used in presentation of data. Arrows indicate positive direction of forces and moments.

Wing:	
Airfoil section-root	NACA 63_2A214
Airfoil section-tip	NACA 63_2A211
Area, sq m (sq ft)	.499 (5.374)
Mean aerodynamic chord, m (ft)	.278 (.913)
Span, m (ft)	1.905 (6.250)
Aspect ratio	7.269
Horizontal tail:	
Airfoil section	NACA 64-012
Area, sq m (sq ft)	.180 (1.940)
Mean aerodynamic chord, m (ft)	.221 (.724)
Span, m (ft)	.849 (2.784)
Aspect ratio	3.995
Vertical tail:	
Airfoil section	NACA 0012
Area, sq m (sq ft)	.183 (1.968)
Mean aerodynamic chord, m (ft)	.374 (1.228)
Span, m (ft)	.493 (1.617)
Aspect ratio	1.328

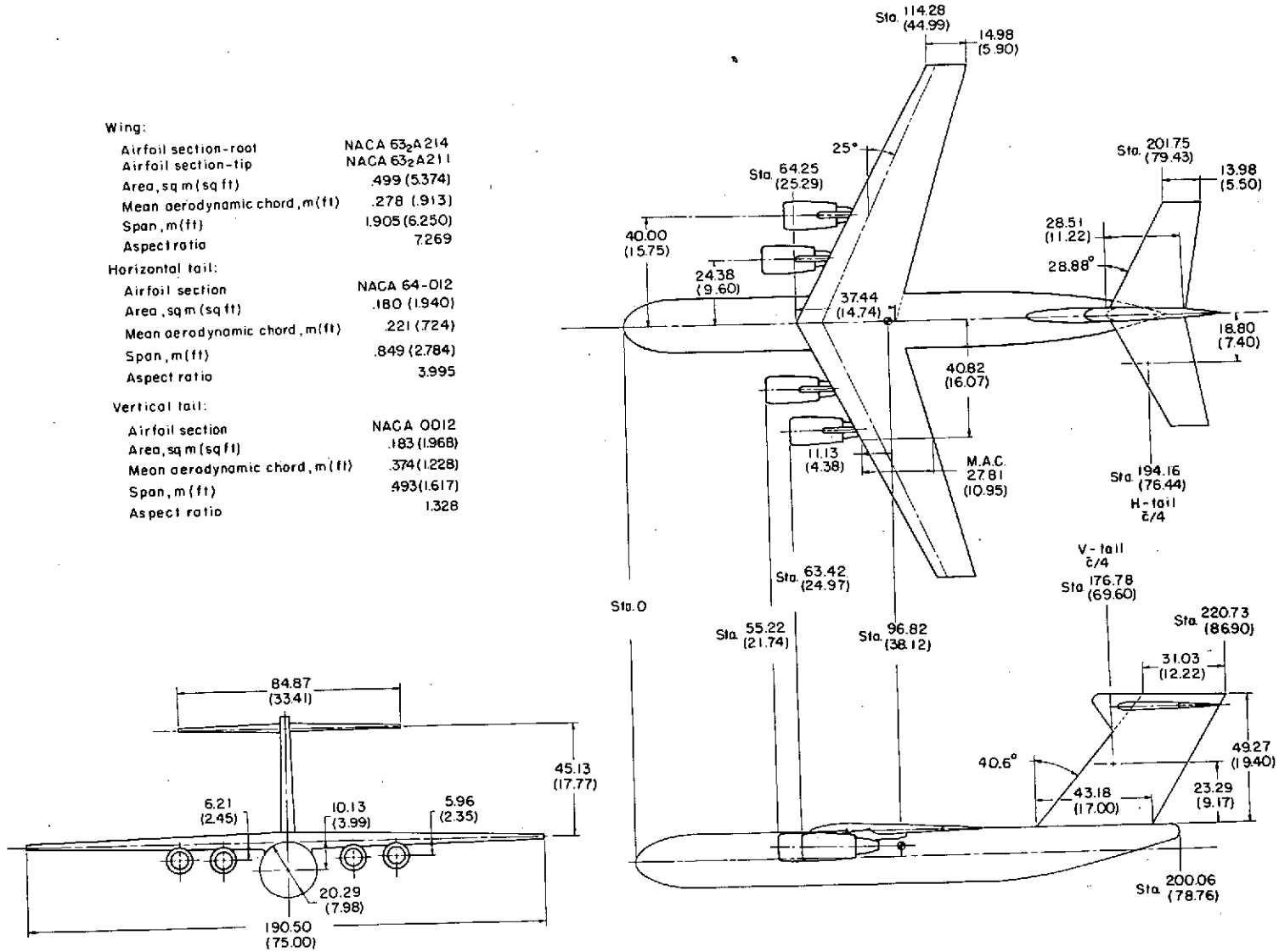

Figure 2.- Dimensions and characteristics of the model. Dimensions are in centimeters (in.) unless otherwise noted.

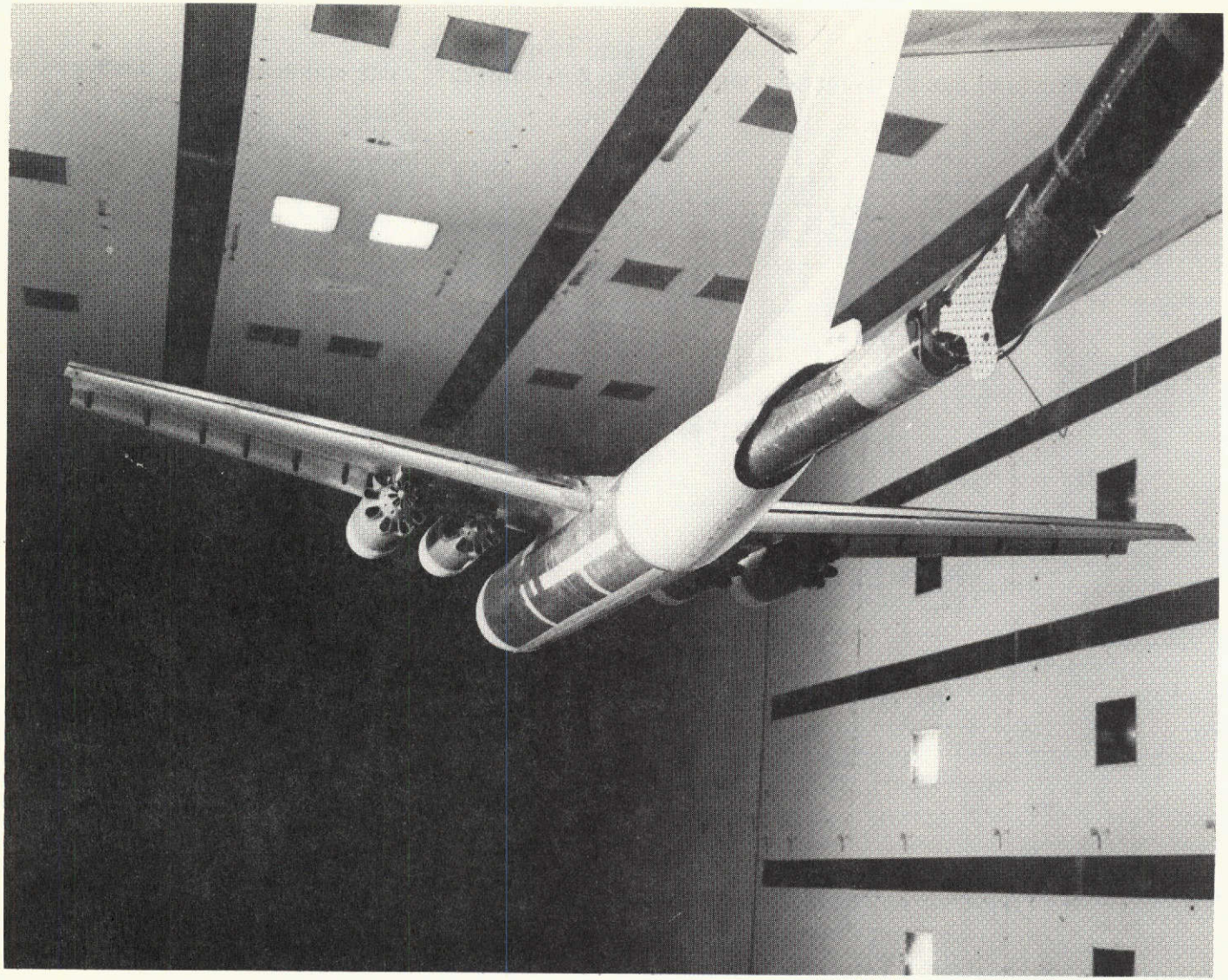

L-72-3354

(a) Rear view of model with daisy-nozzle engine simulators installed.

Figure 3.- Model installed in Langley V/STOL tunnel.

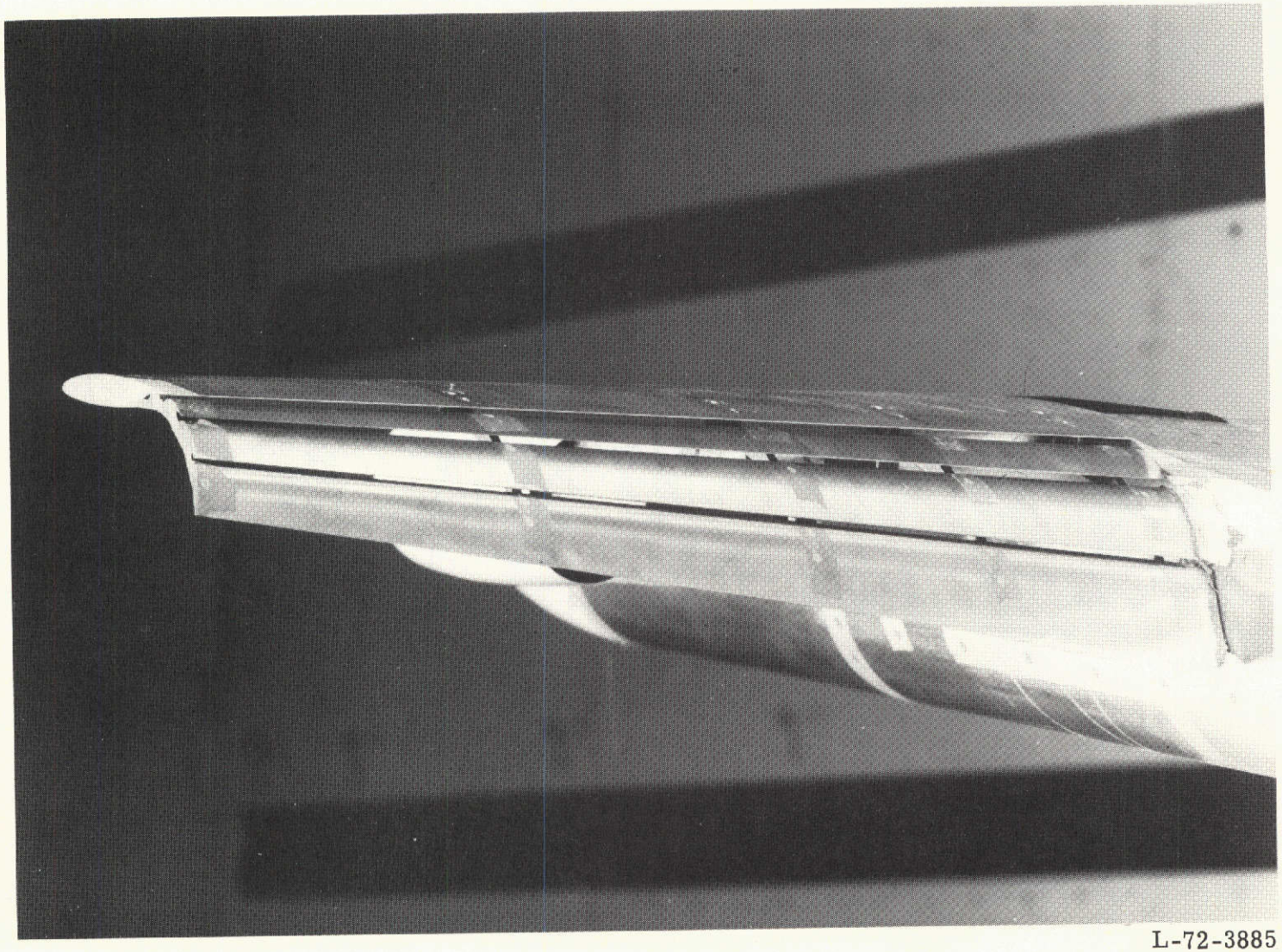

L-72-3885

(b) Rear view of model showing the details of the triple-slotted flap system.

Figure 3.- Concluded.

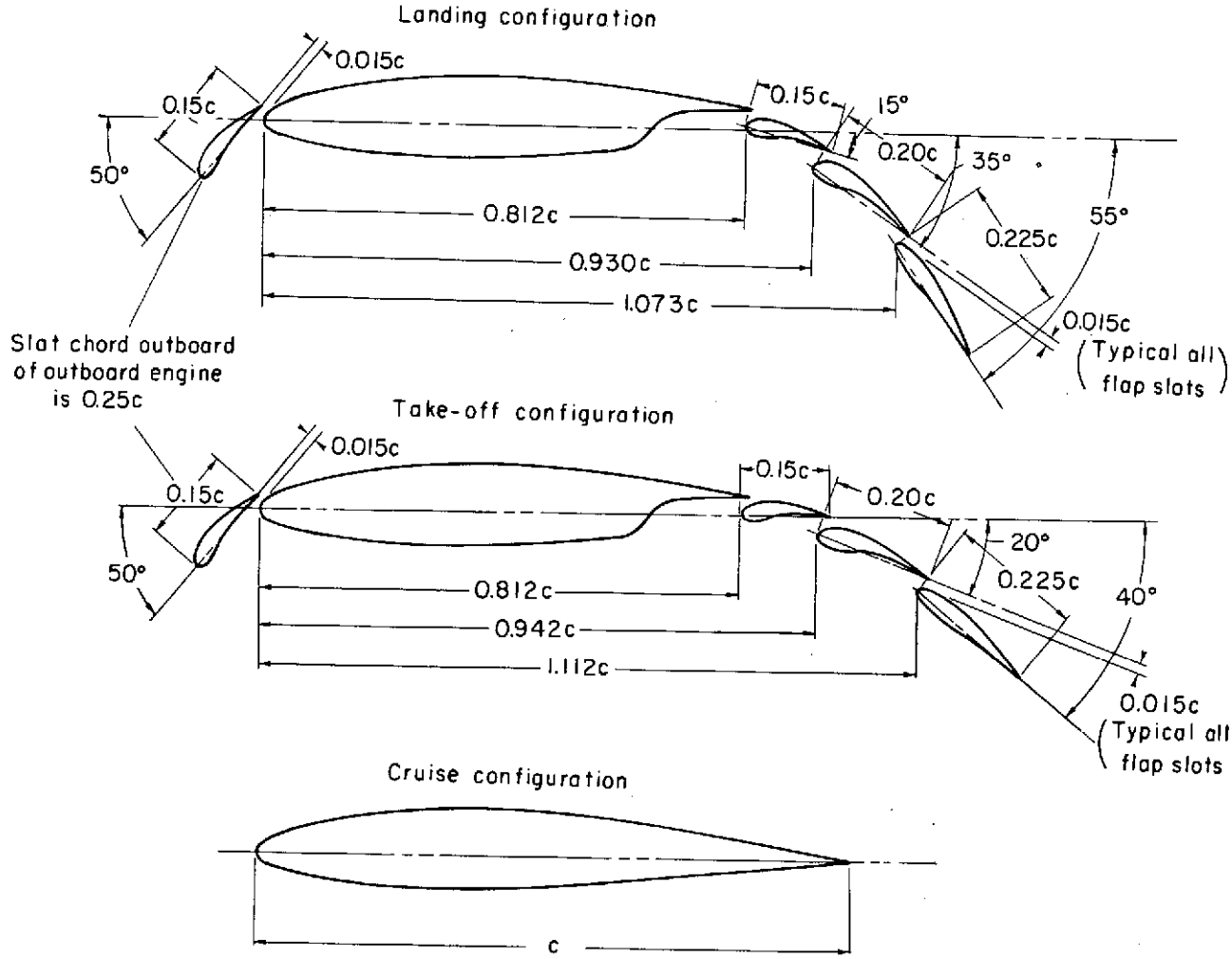

Figure 4.- Wing details in the cruise, take-off, and landing configurations. Dimensions are given in fraction of local chord.

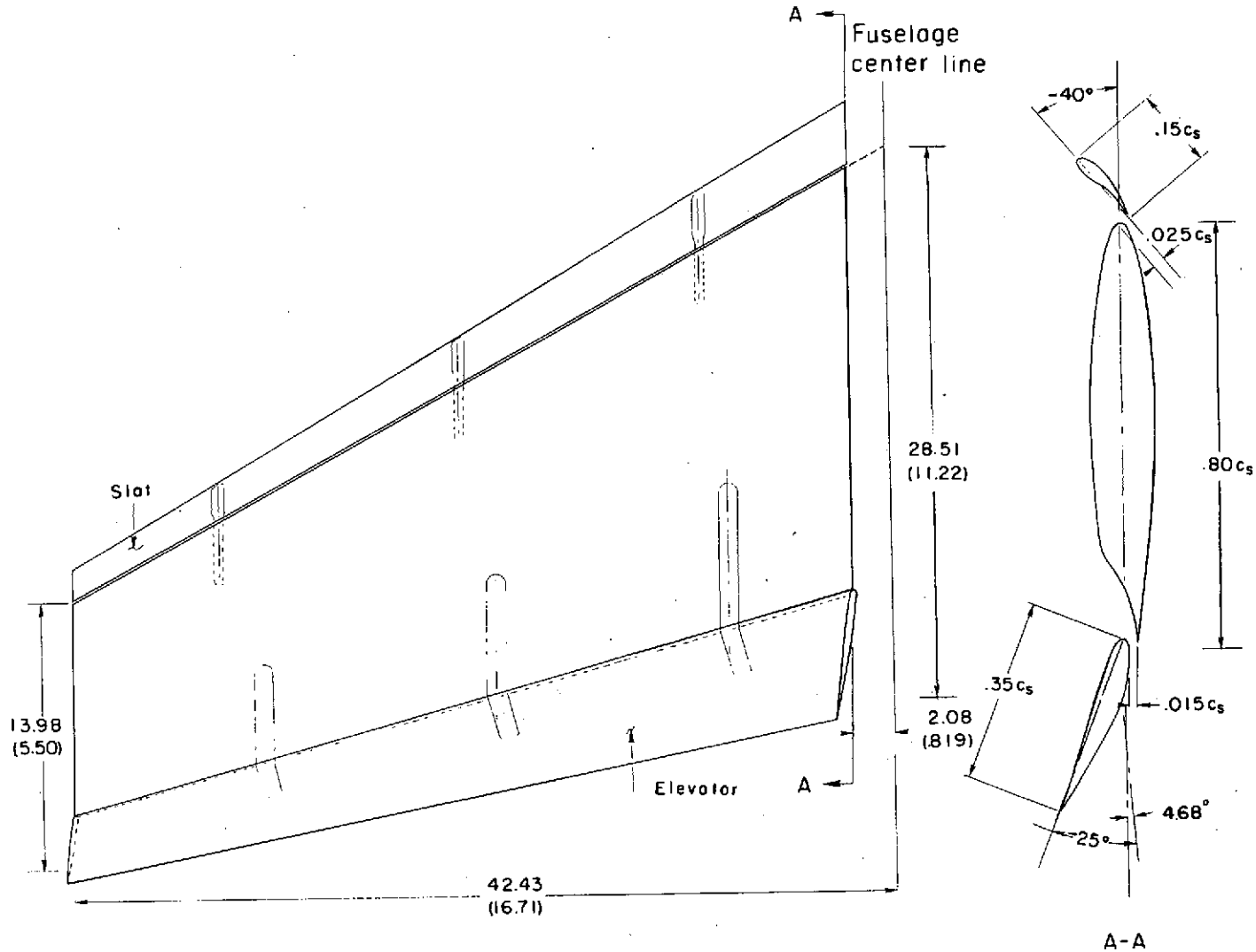

Figure 5.- Details of the horizontal tail used in the wind-tunnel investigation. Dimensions are in centimeters (in.) or fraction of local wing chord in section A-A.

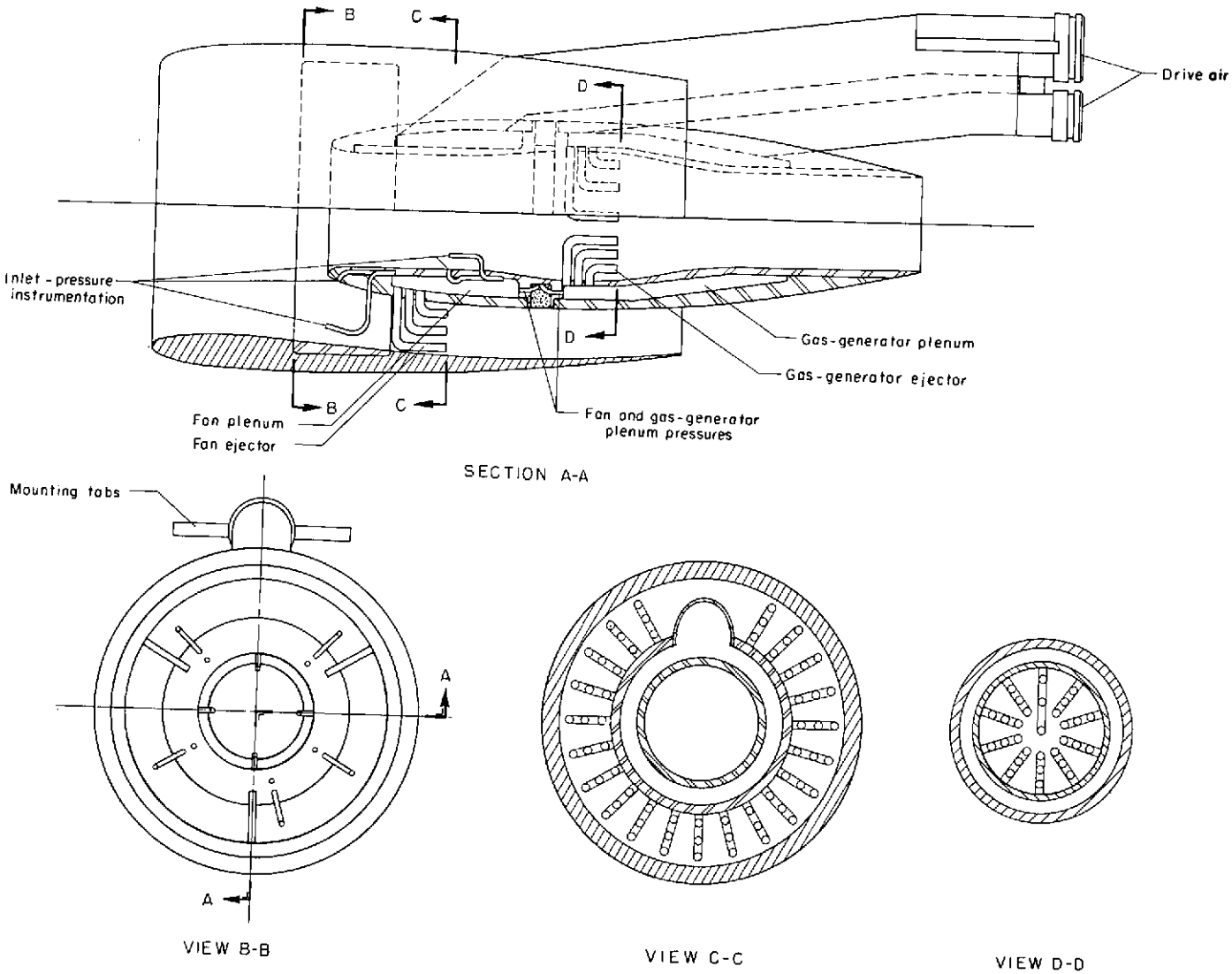

Figure 6.- Details of basic ejector used on all engine simulators.

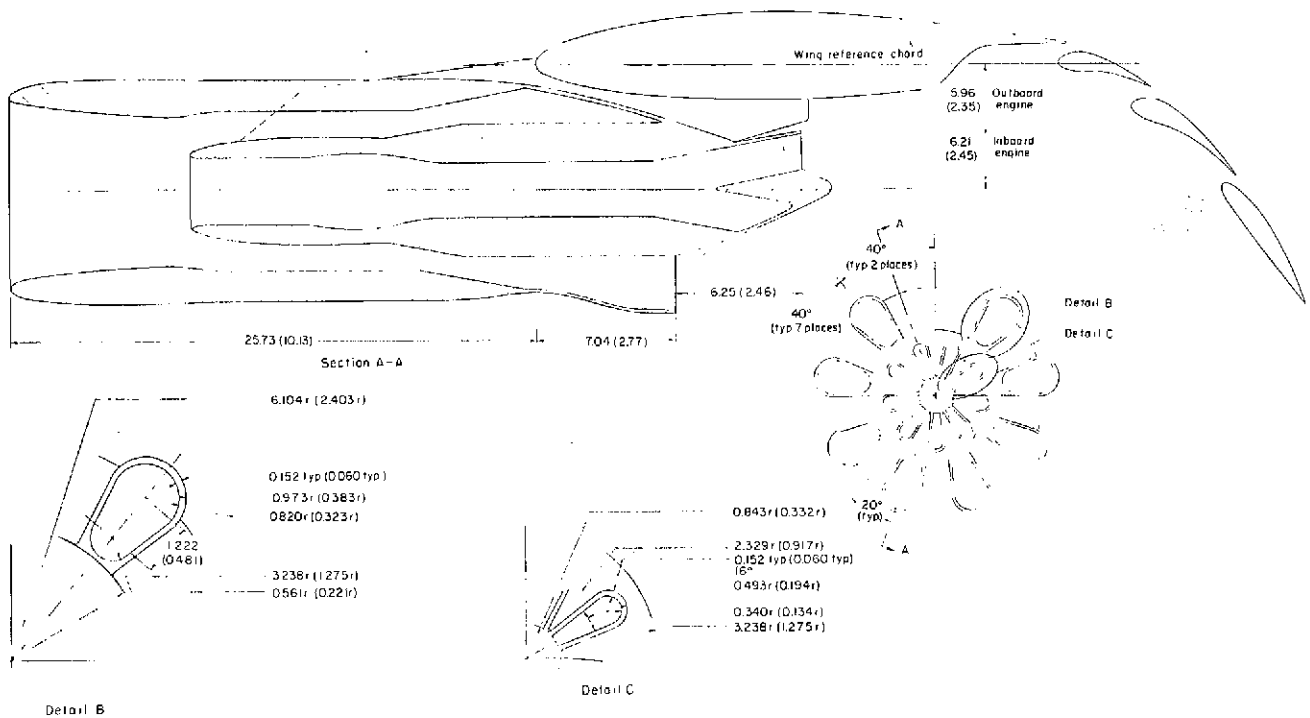

(a) Daisy nozzle.

Figure 7.- Details of each engine simulator installed in the outboard position on the model. Dimensions are in centimeters (in.).

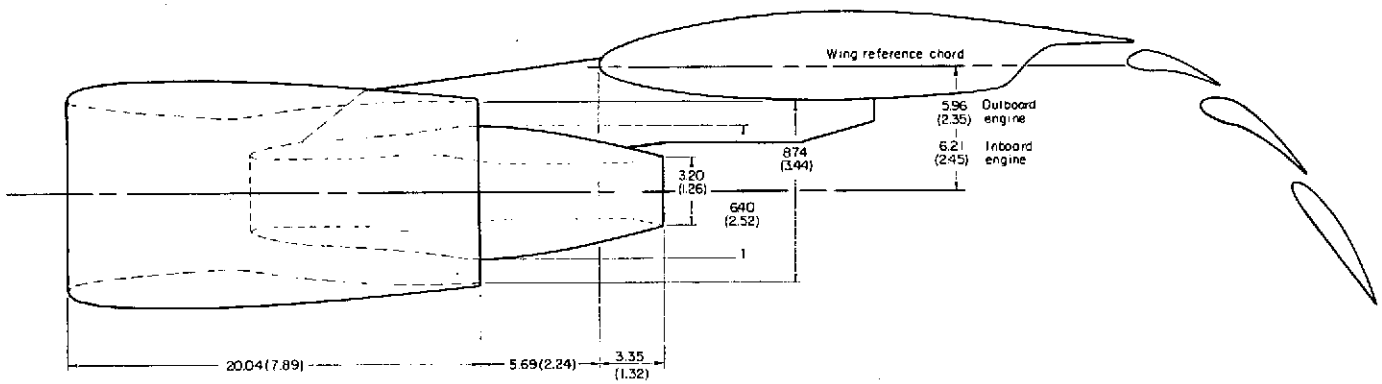

(b) Bypass ratio 6.2.

Figure 7.- Continued.

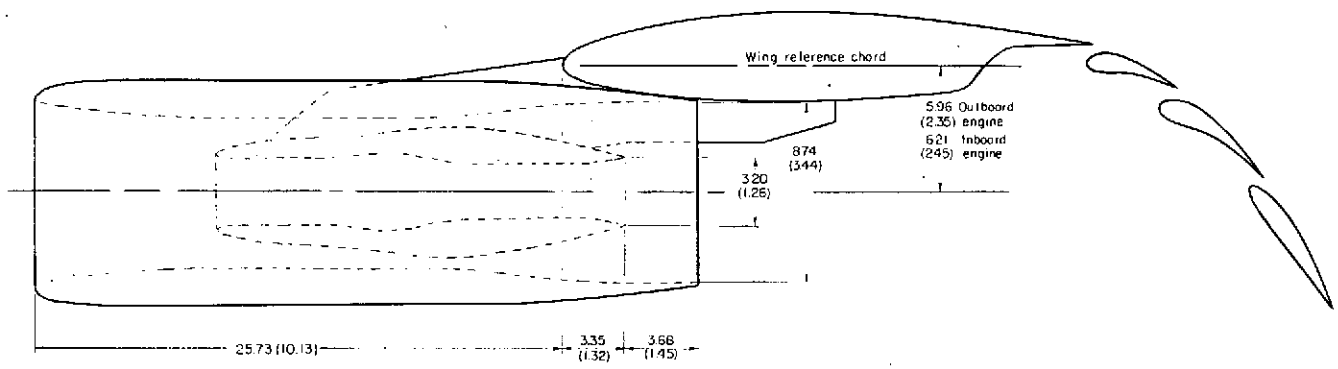

(c) Modified bypass ratio 6.2.

Figure 7.- Continued.

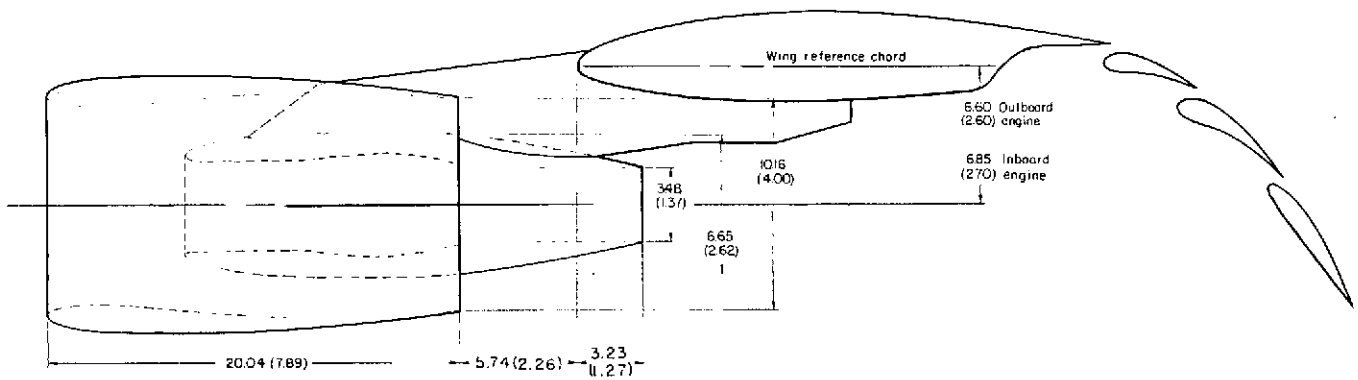

(d) Bypass ratio 10.0.

Figure 7.- Continued.

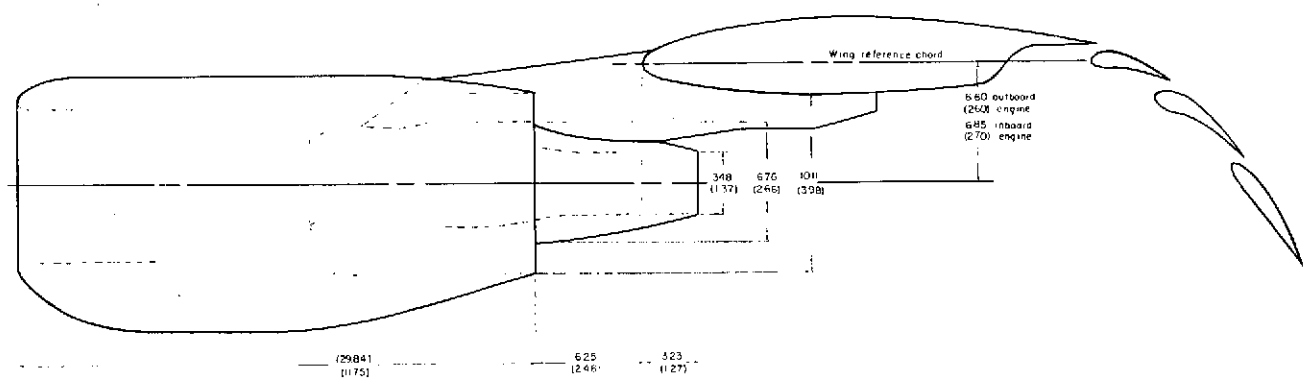

(e) Bypass ratio 3.2.

Figure 7.- Concluded.

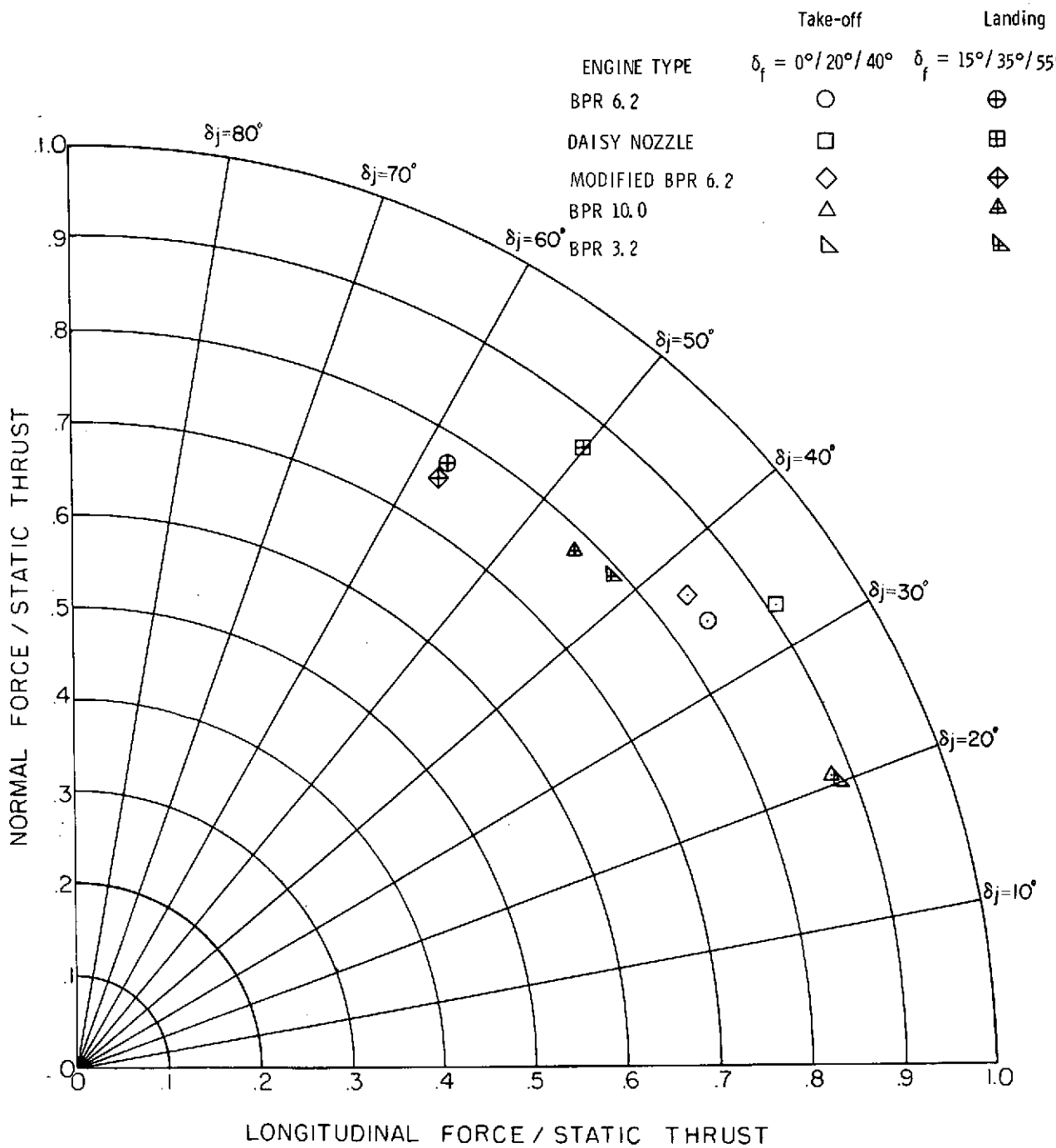

Figure 8.- Flap static turning effectiveness. $\delta_{sw} = 50^{o}$; tail off; $q_{\infty} = 0$; T = 1219 N (274 lb).

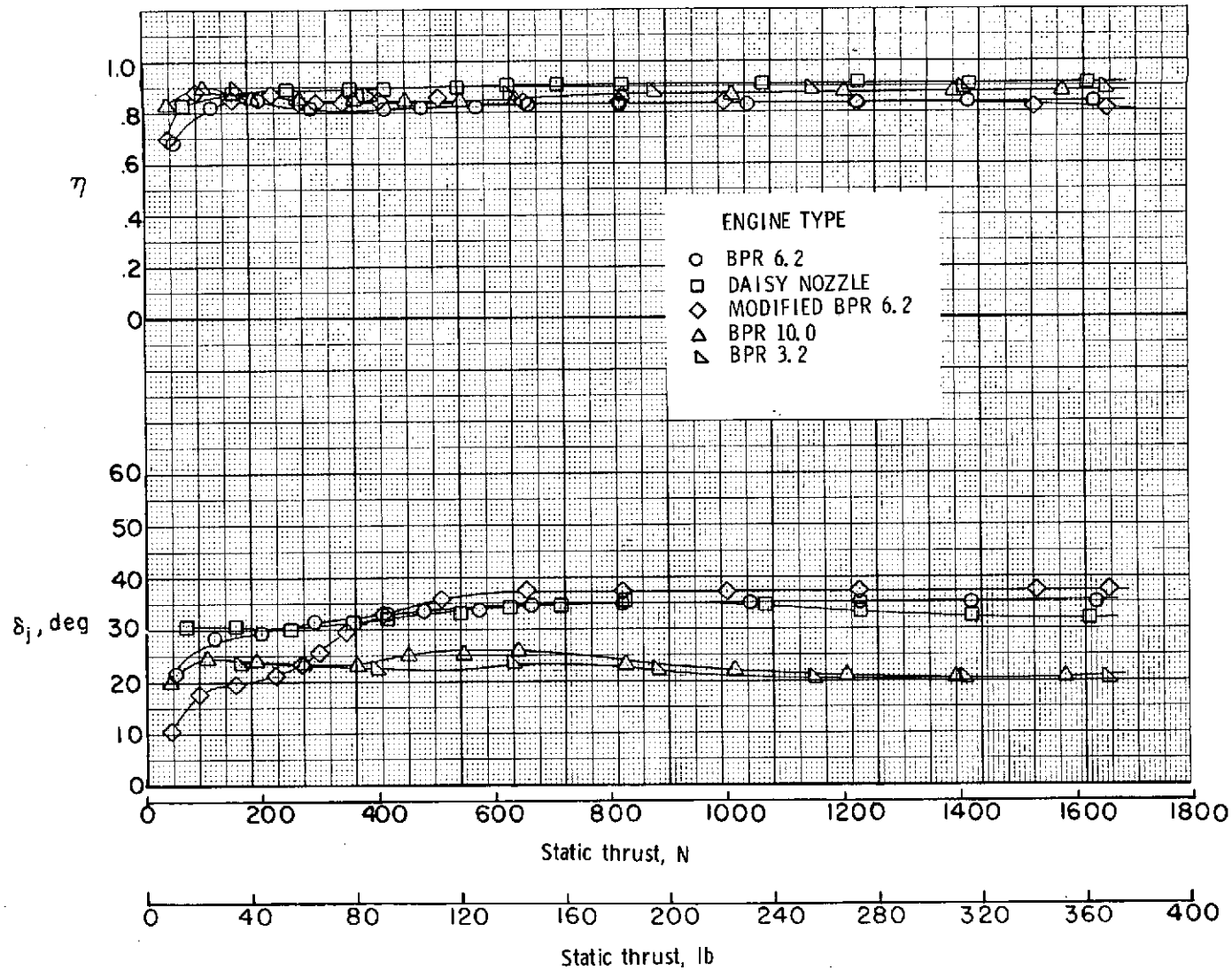

(a) $\delta_f = 0^o/20^o/40^o$ (take-off).

Figure 9.- Effect of engine type on variation of static turning effectiveness parameters with thrust. $\delta_{sw} = 50^o$; tail off; $q_\infty = 0$.

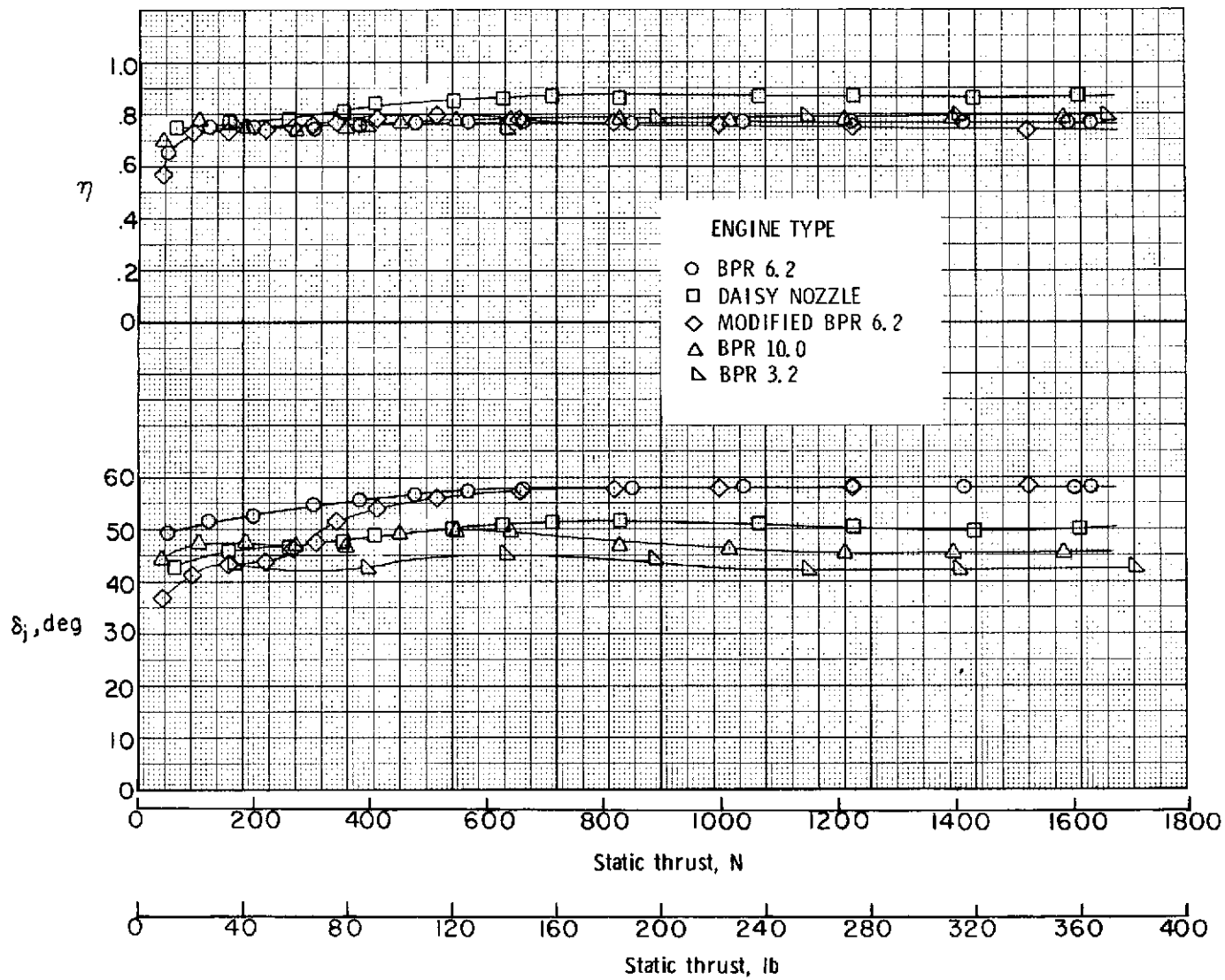

(b) $\delta_f = 15^o/35^o/55^o$ (landing).

Figure 9.- Concluded.

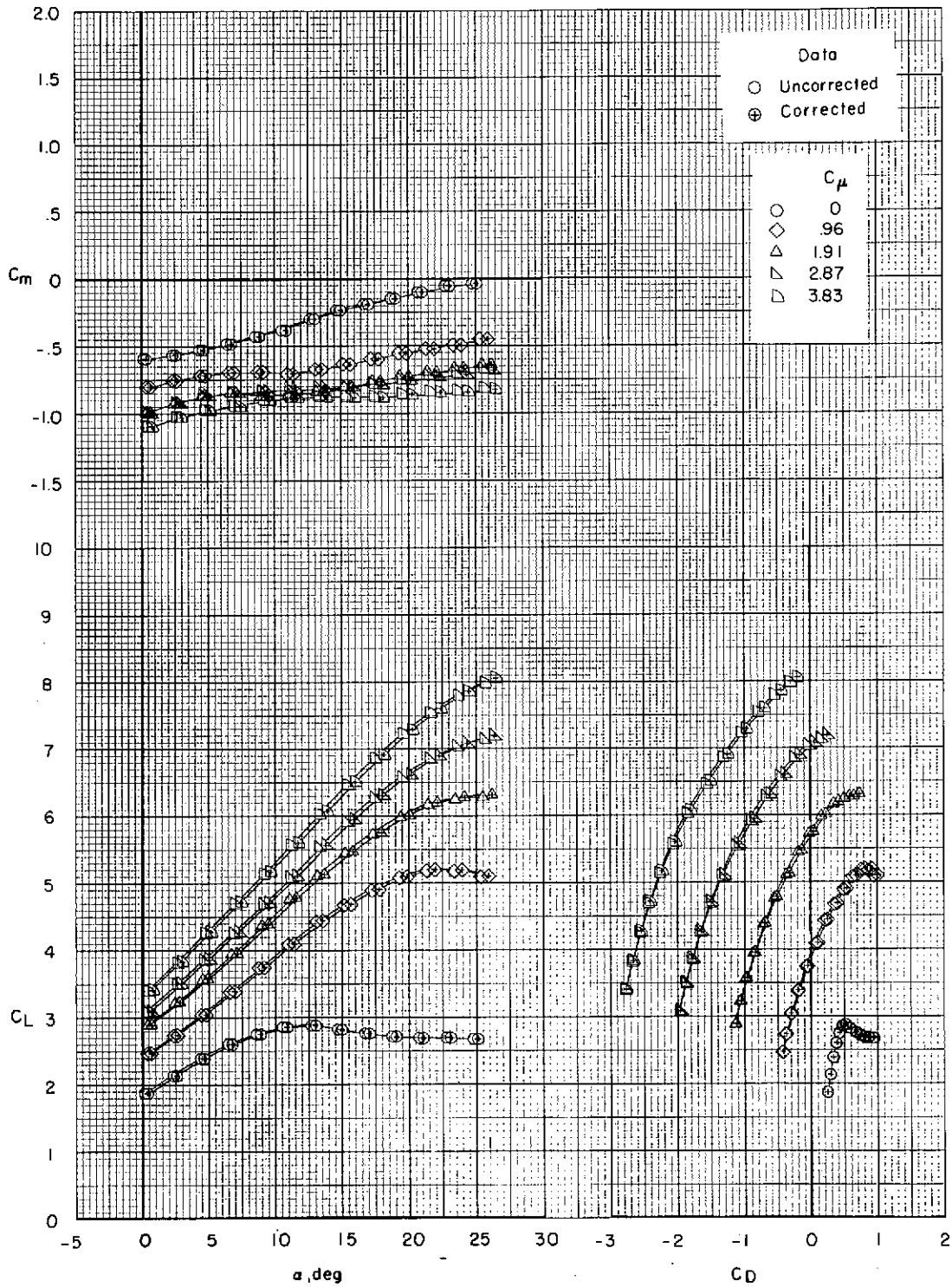

(a) $\delta_f = 0^o/20^o/40^o$ (take-off); $\delta_{sw} = 50^o$.

Figure 10.- Effect of wind-tunnel wall corrections. Bypass ratio 3.2; tail off.

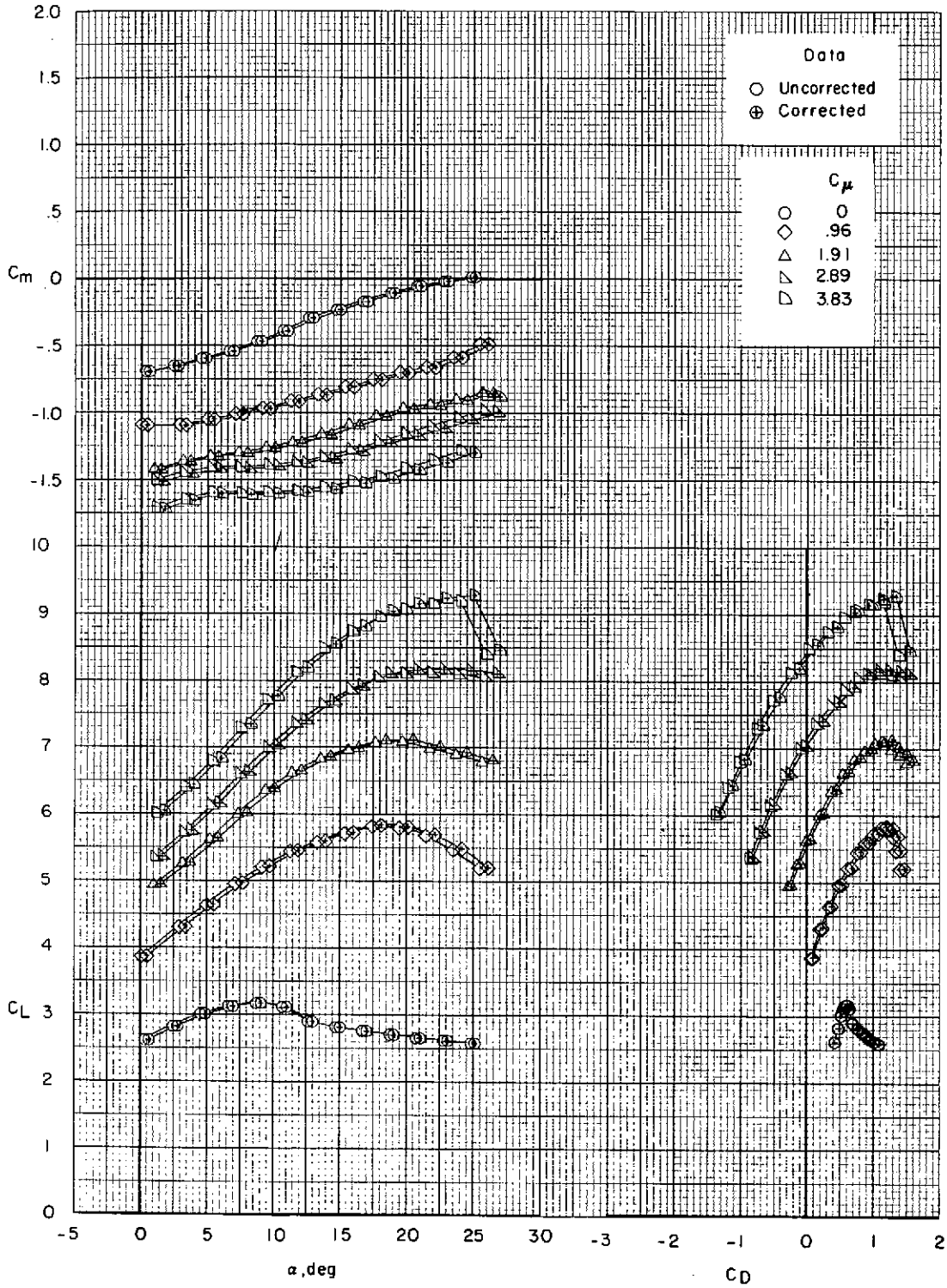

(b) $\delta_f = 15^o/35^o/55^o$; $\delta_{sw} = 50^o$.

Figure 10.- Concluded.

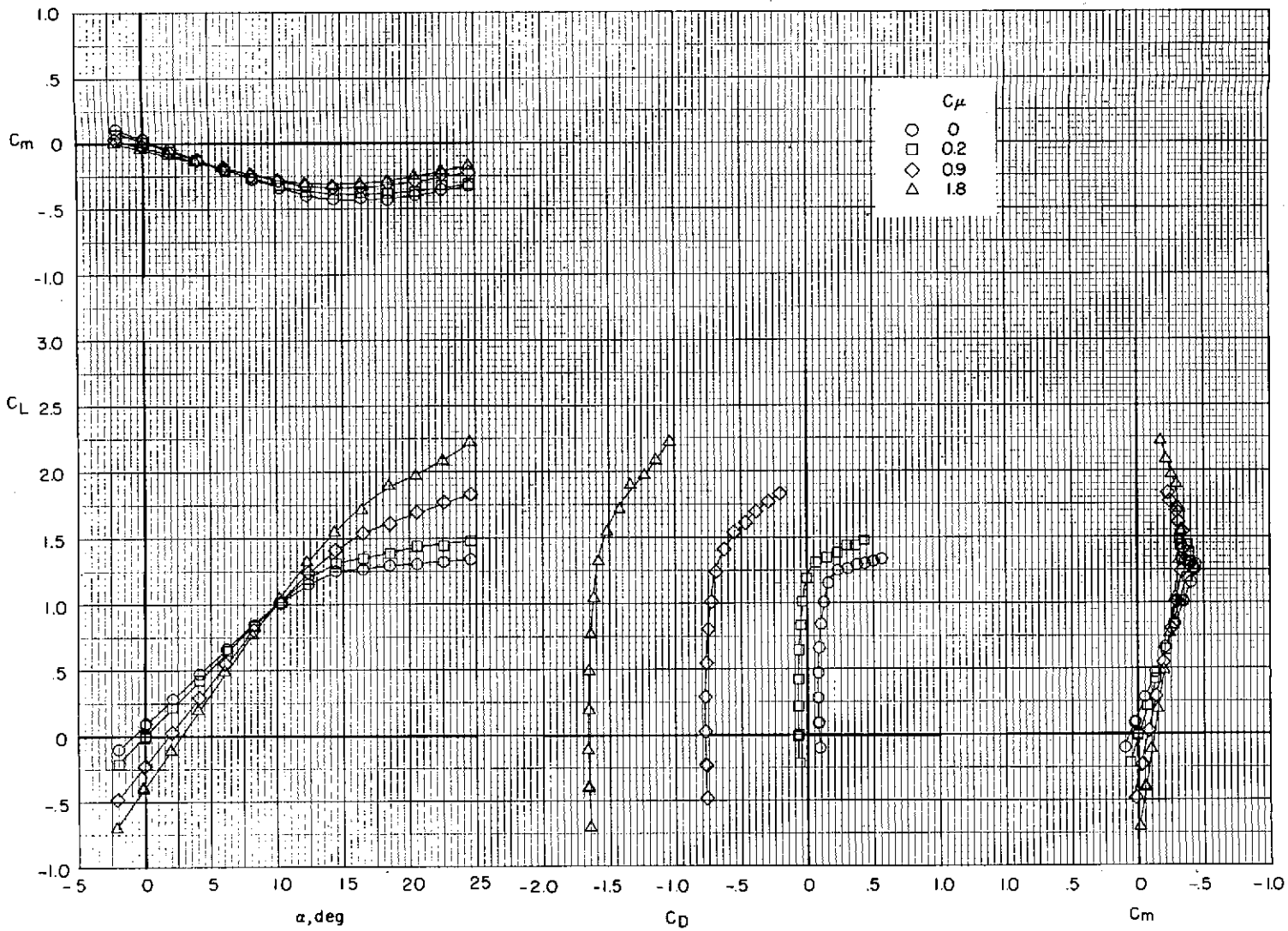

(a) $i_t = 0^o$; $\delta_e = 0^o$; δ_{sh} = off.

Figure 11.- Effect of thrust coefficient on longitudinal aerodynamic characteristics. Daisy nozzle; $\delta_f = 0^o$ (cruise); δ_{sw} = off.

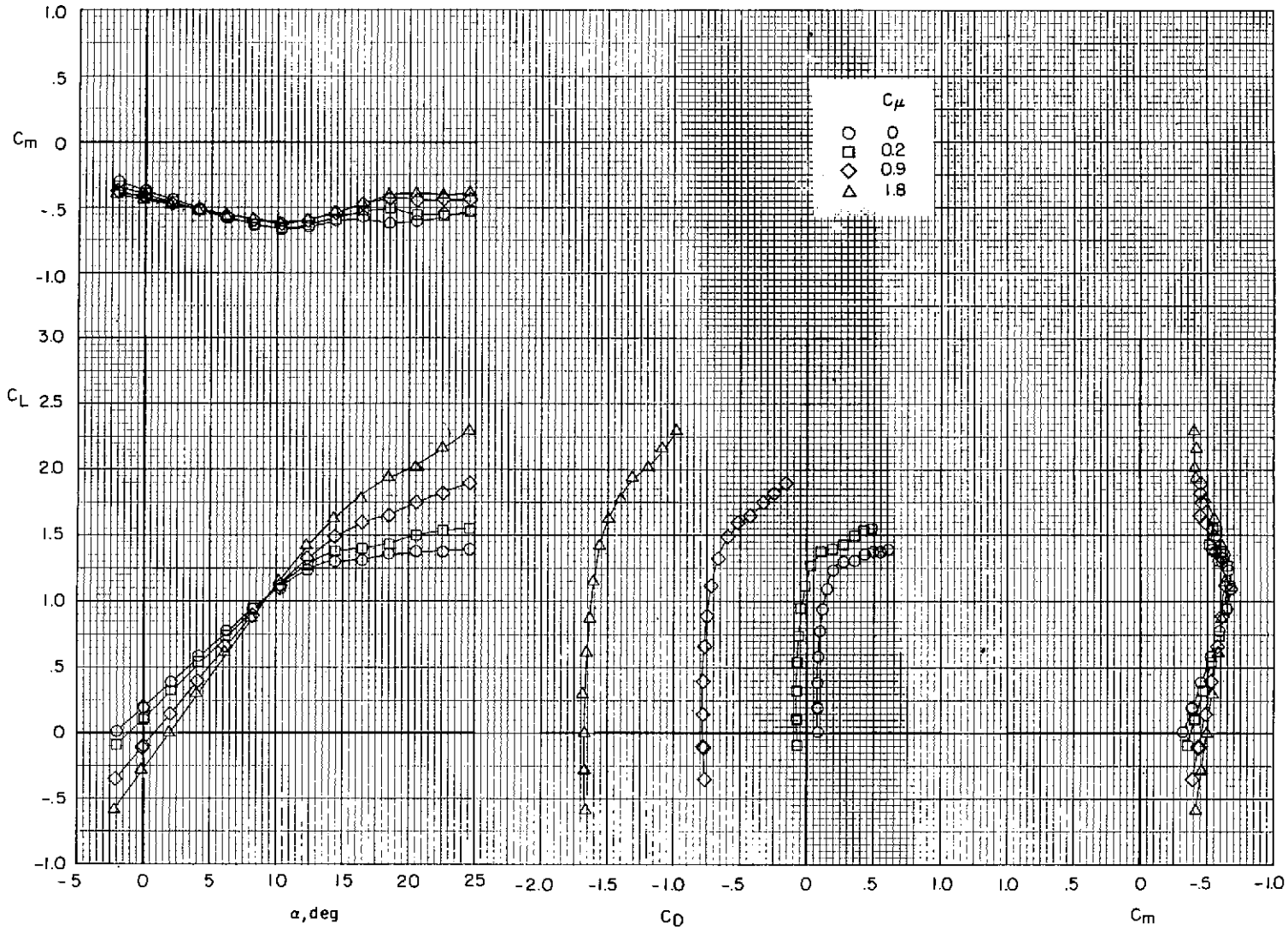

(b) $i_t = 5^o$; $\delta_e = 0^o$; δ_{sh} = off.

Figure 11.- Concluded.

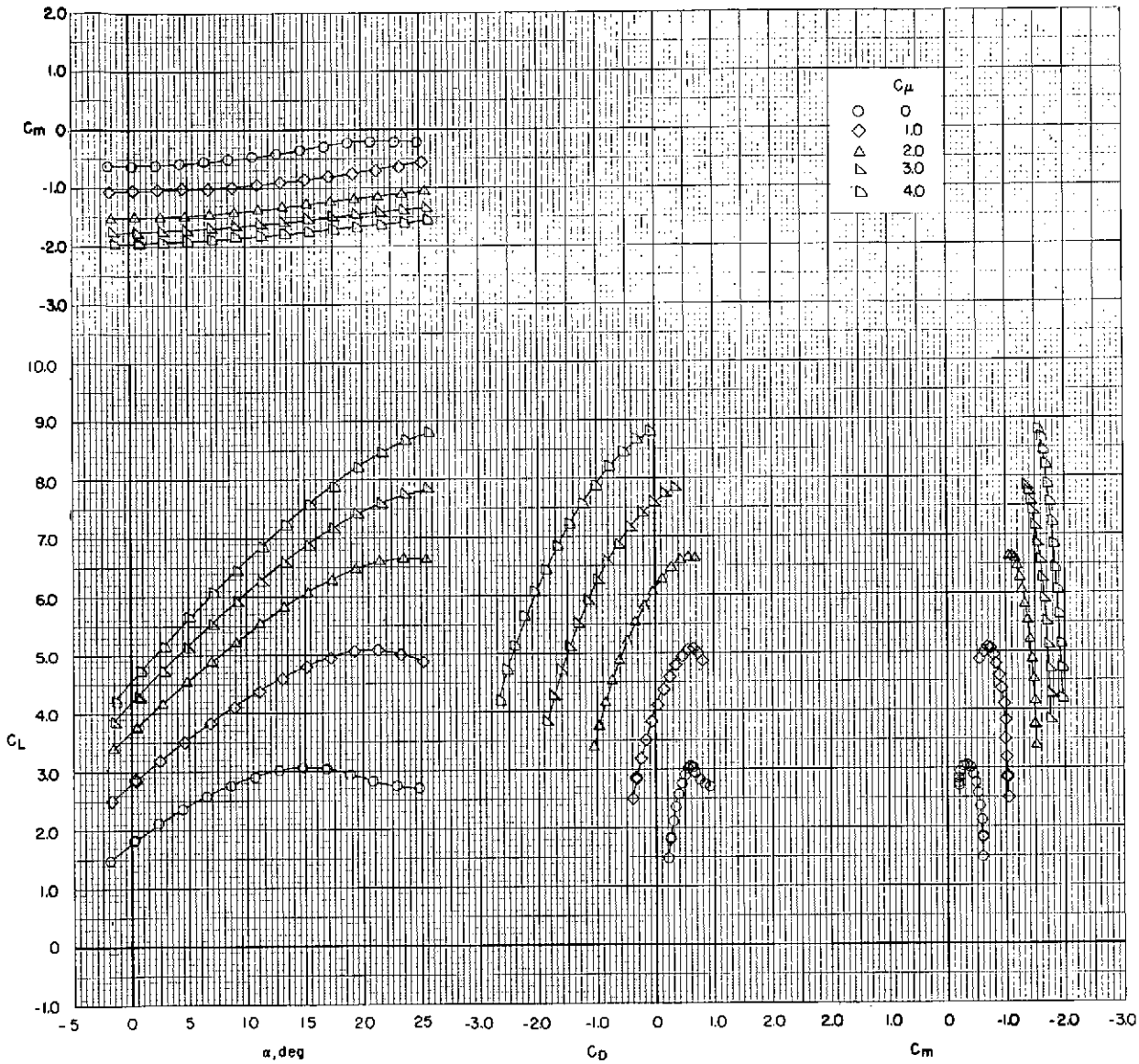

(a) Tail off.

Figure 12.- Effect of thrust coefficient on longitudinal aerodynamic characteristics. Daisy nozzle; $\delta_f = 0^o/20^o/40^o$ (take-off); $\delta_{sw} = 50^o$.

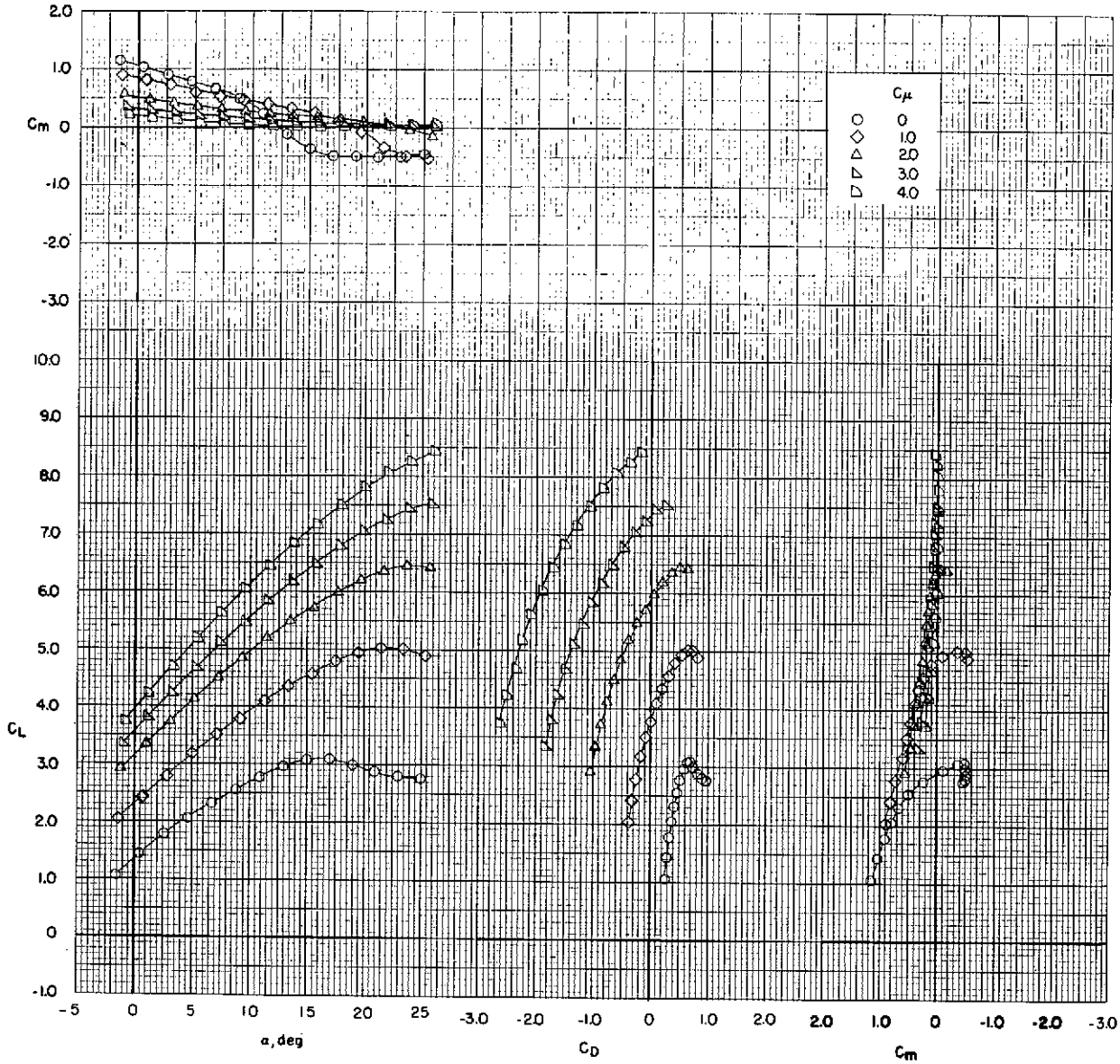

(b) $i_t = 0^o$; $\delta_e = -25^o$; $\delta_{sh} = -40^o$.

Figure 12.- Continued.

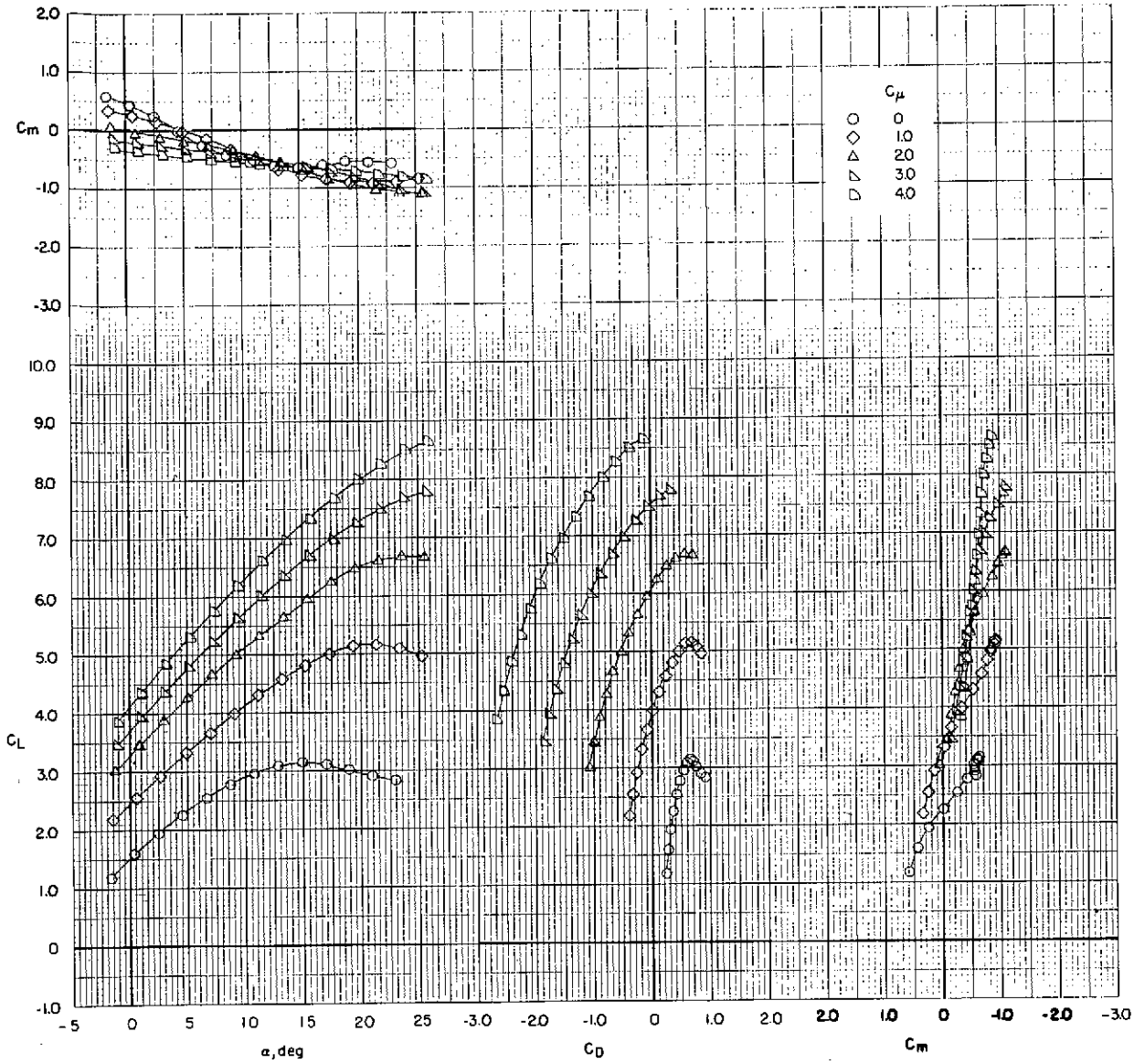

(c) $i_t = 5^o$; $\delta_e = -25^o$; $\delta_{sh} = -40^o$.

Figure 12.- Concluded.

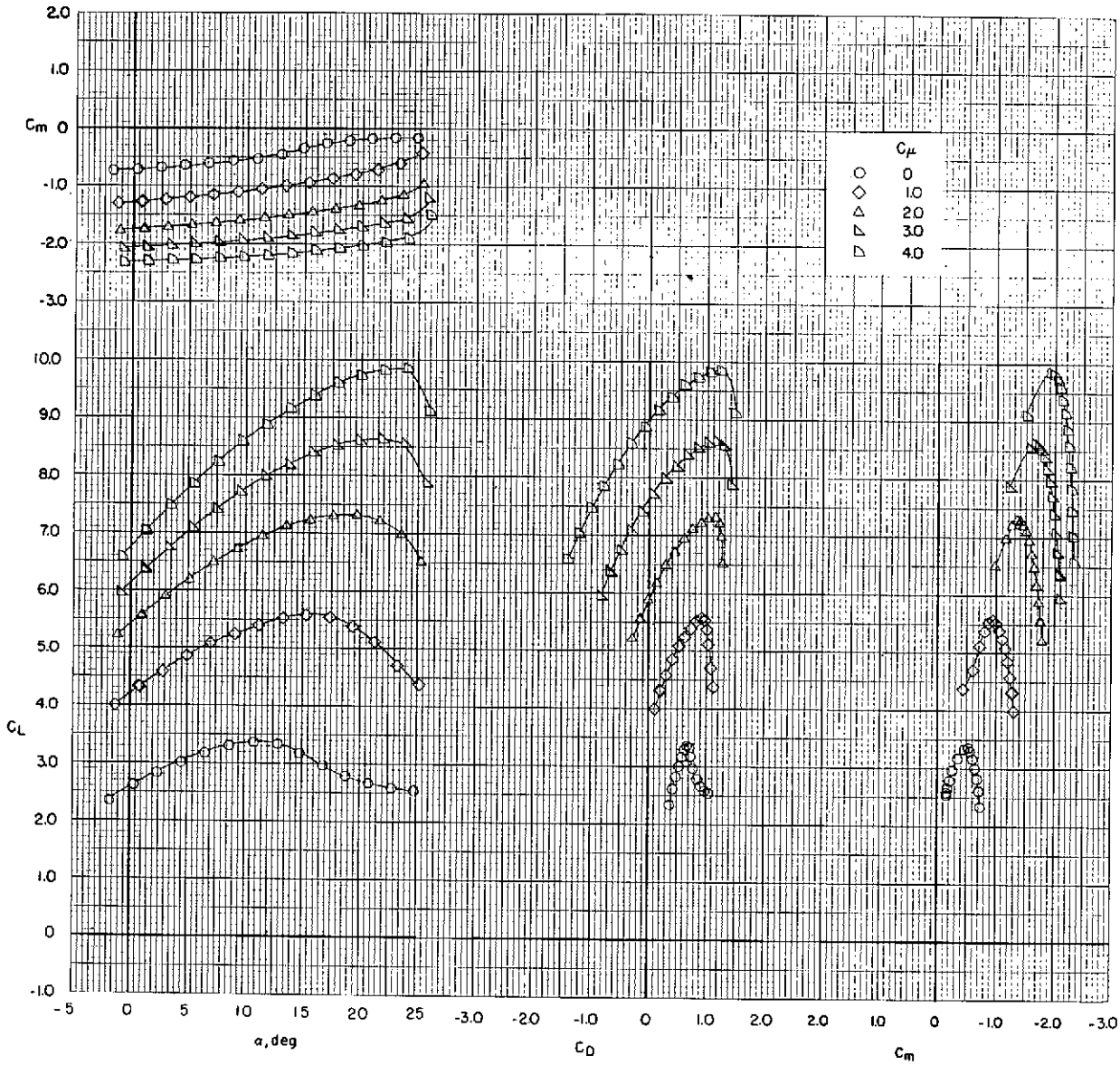

(a) Tail off.

Figure 13.- Effect of thrust coefficient on longitudinal aerodynamic characteristics. Daisy nozzle; $\delta_f = 15^o/35^o/55^o$ (landing); $\delta_{sw} = 50^o$.

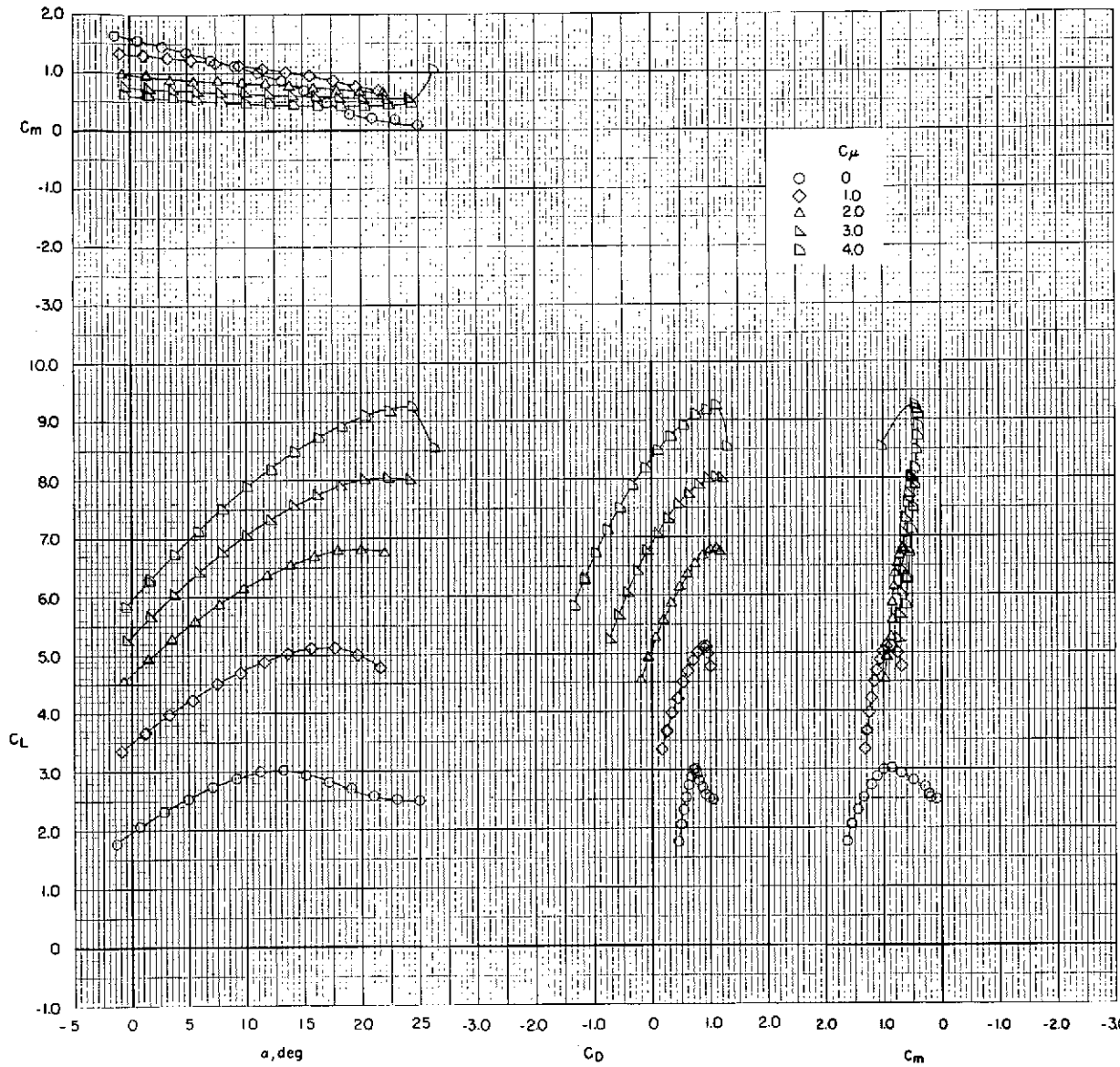

(b) $i_t = -5^o$; $\delta_e = -25^o$; $\delta_{sh} = -40^o$.

Figure 13.- Continued.

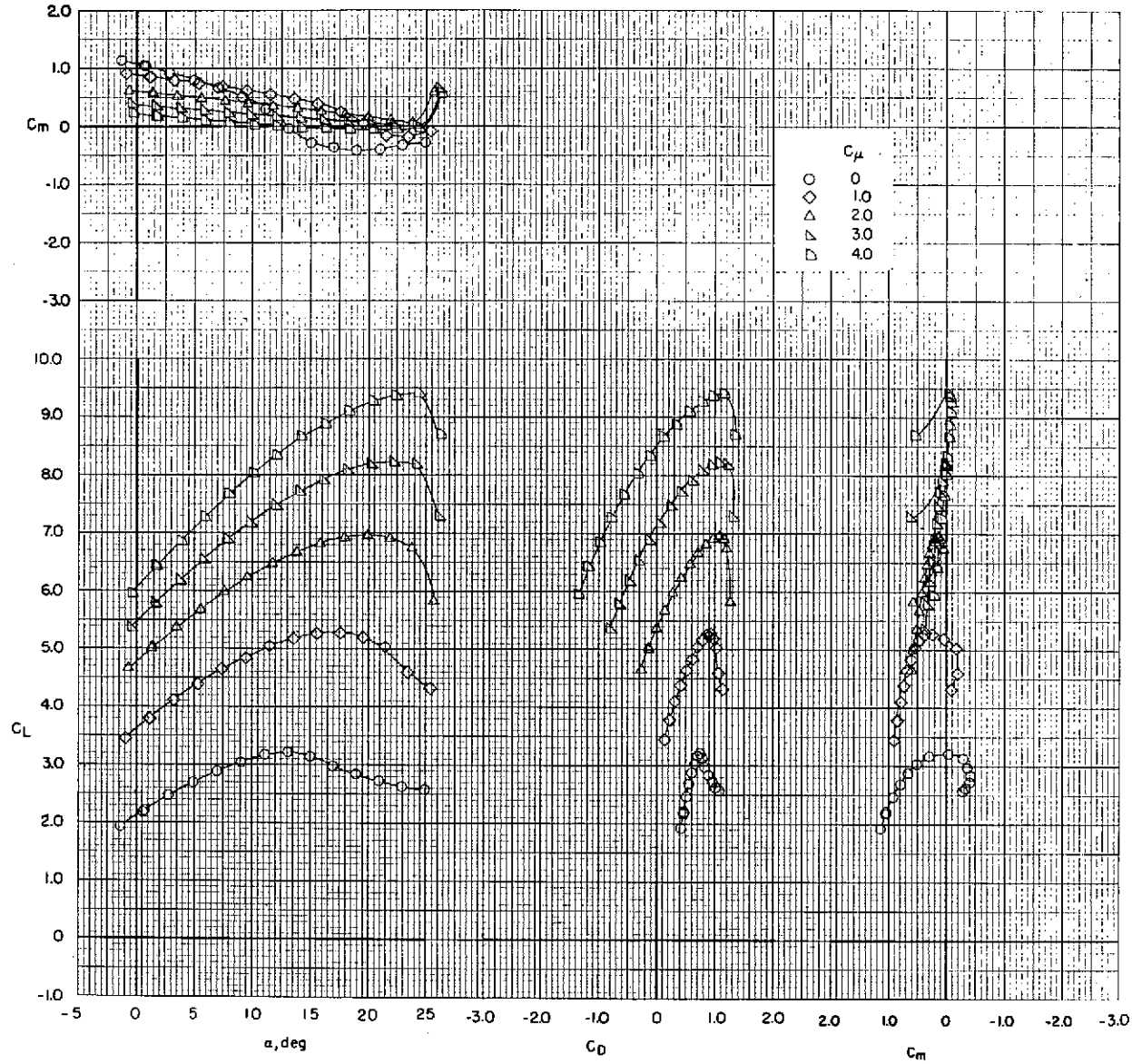

(c) $i_t = 0^o$; $\delta_e = -25^o$; $\delta_{sh} = -40^o$.

Figure 13.- Continued.

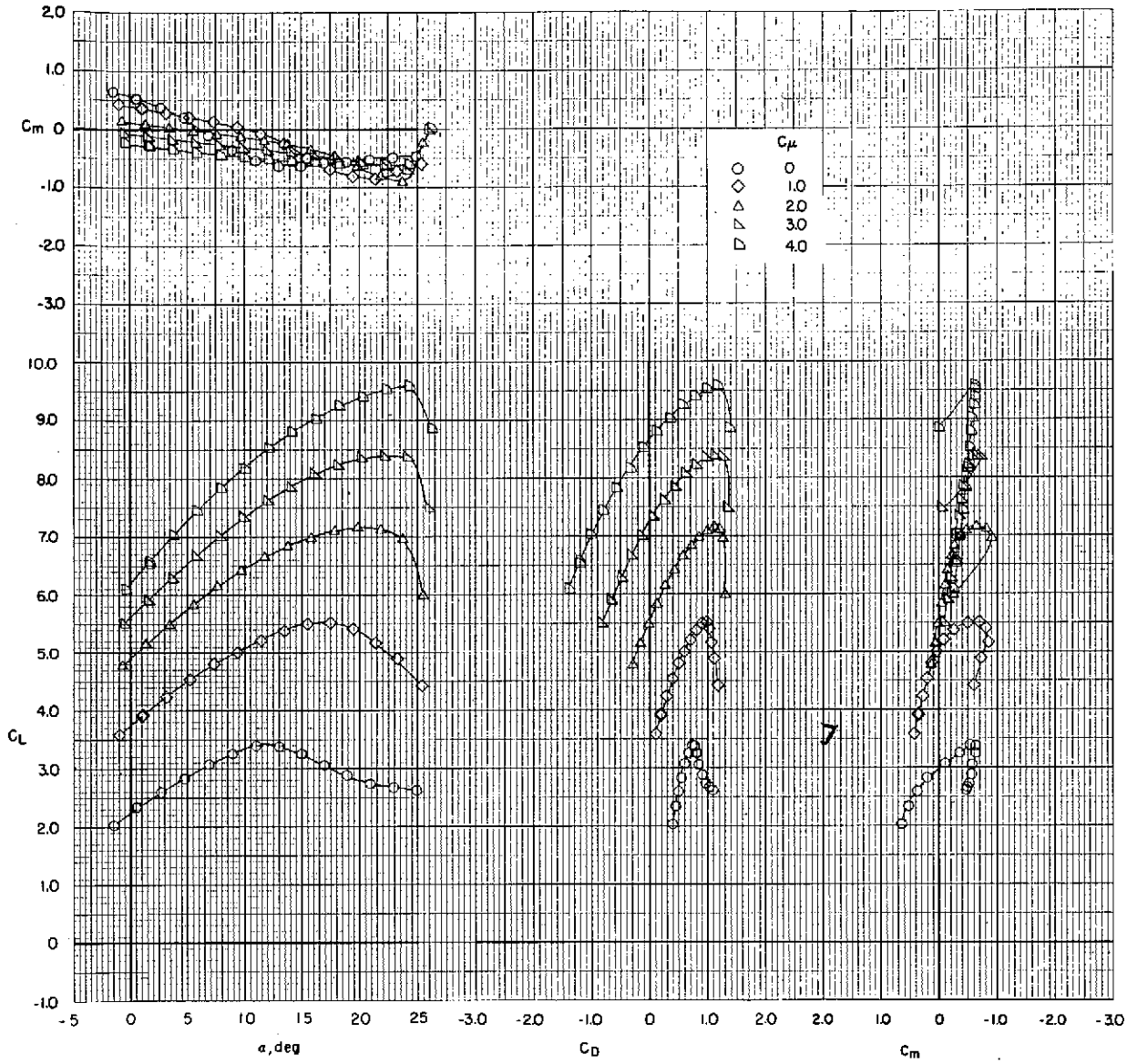

(d) $i_t = 5^o$; $\delta_e = -25^o$; $\delta_{sh} = -40^o$.

Figure 13.- Concluded.

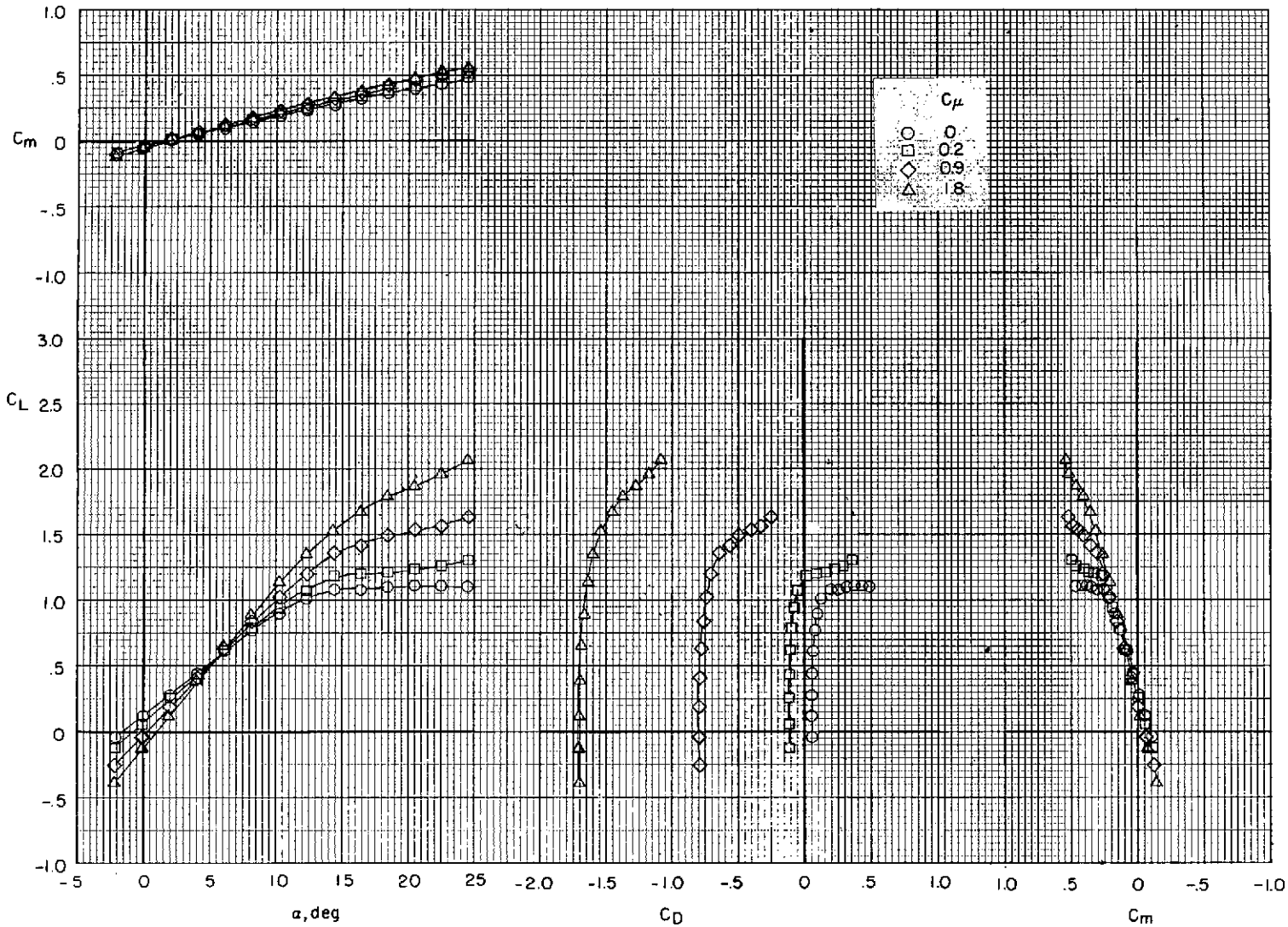

(a) Tail off.

Figure 14.- Effect of thrust coefficient on longitudinal aerodynamic characteristics. Bypass ratio 6.2; $\delta_f = 0^o$ (cruise); δ_{sw} = off.

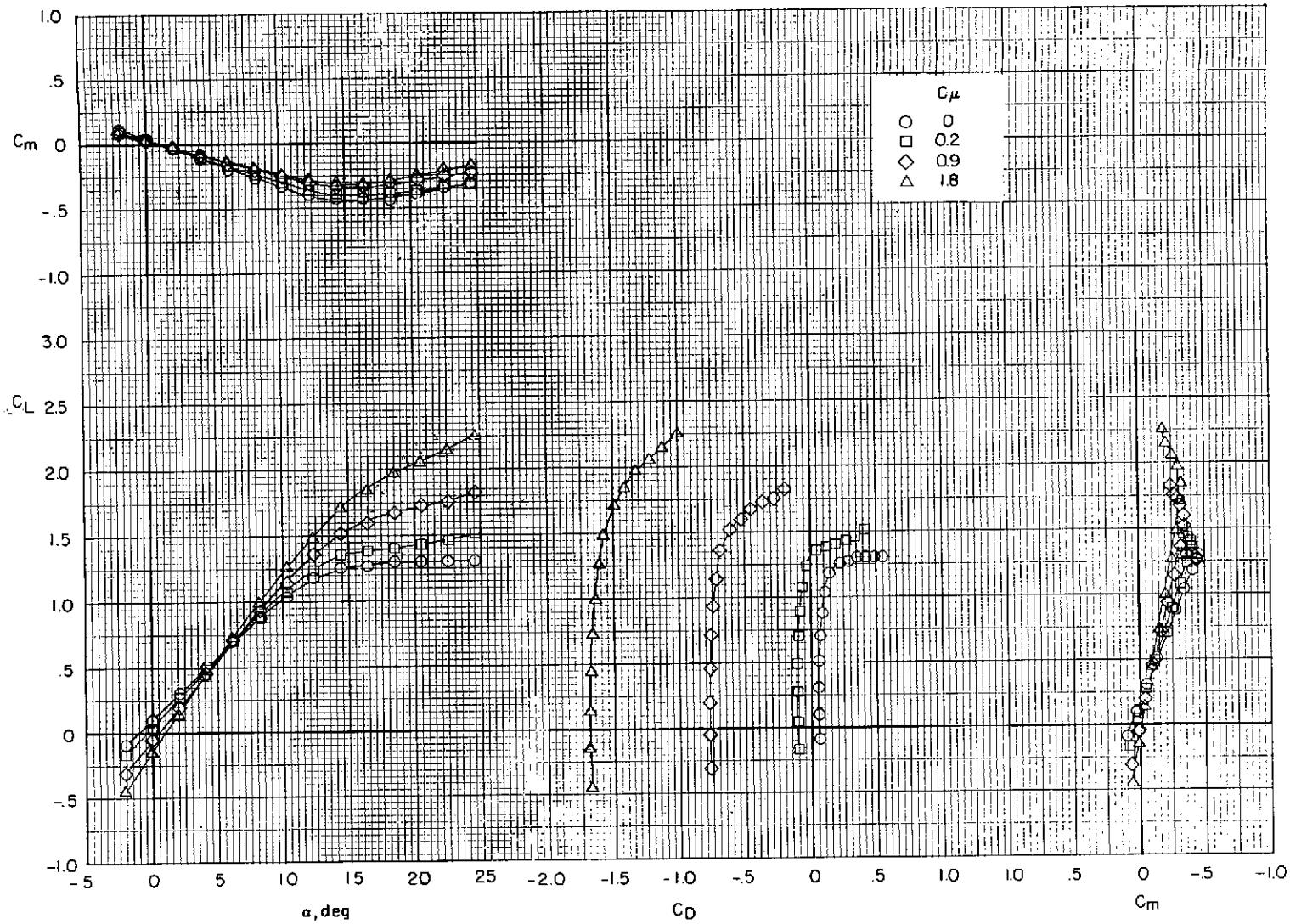

(b) $i_t = 0^o$; $\delta_e = 0^o$; δ_{sh} = off.

Figure 14.- Continued.

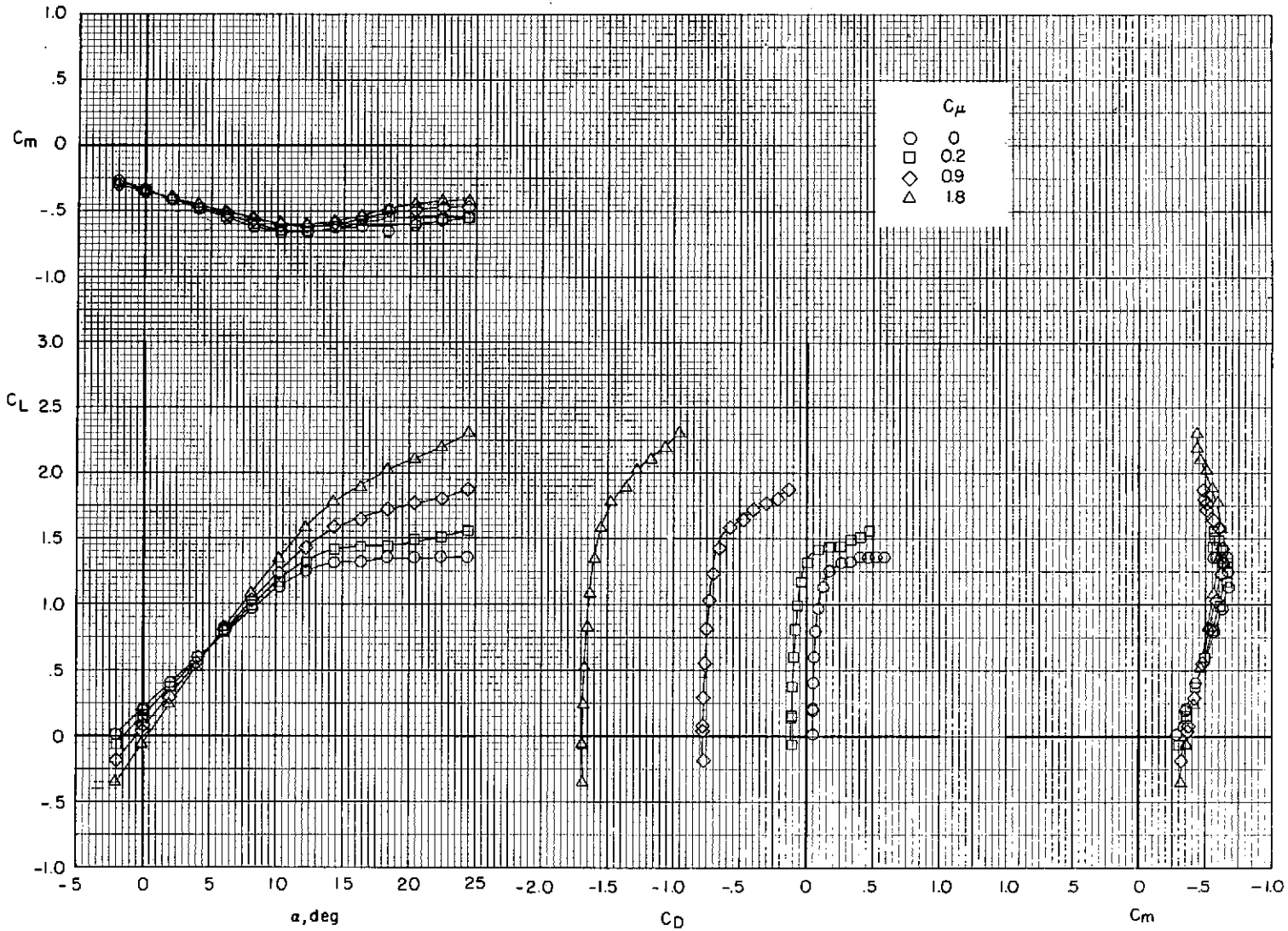

(c) $i_t = 5^o$; $\delta_e = 0^o$; δ_{sh} = off.

Figure 14.- Concluded.

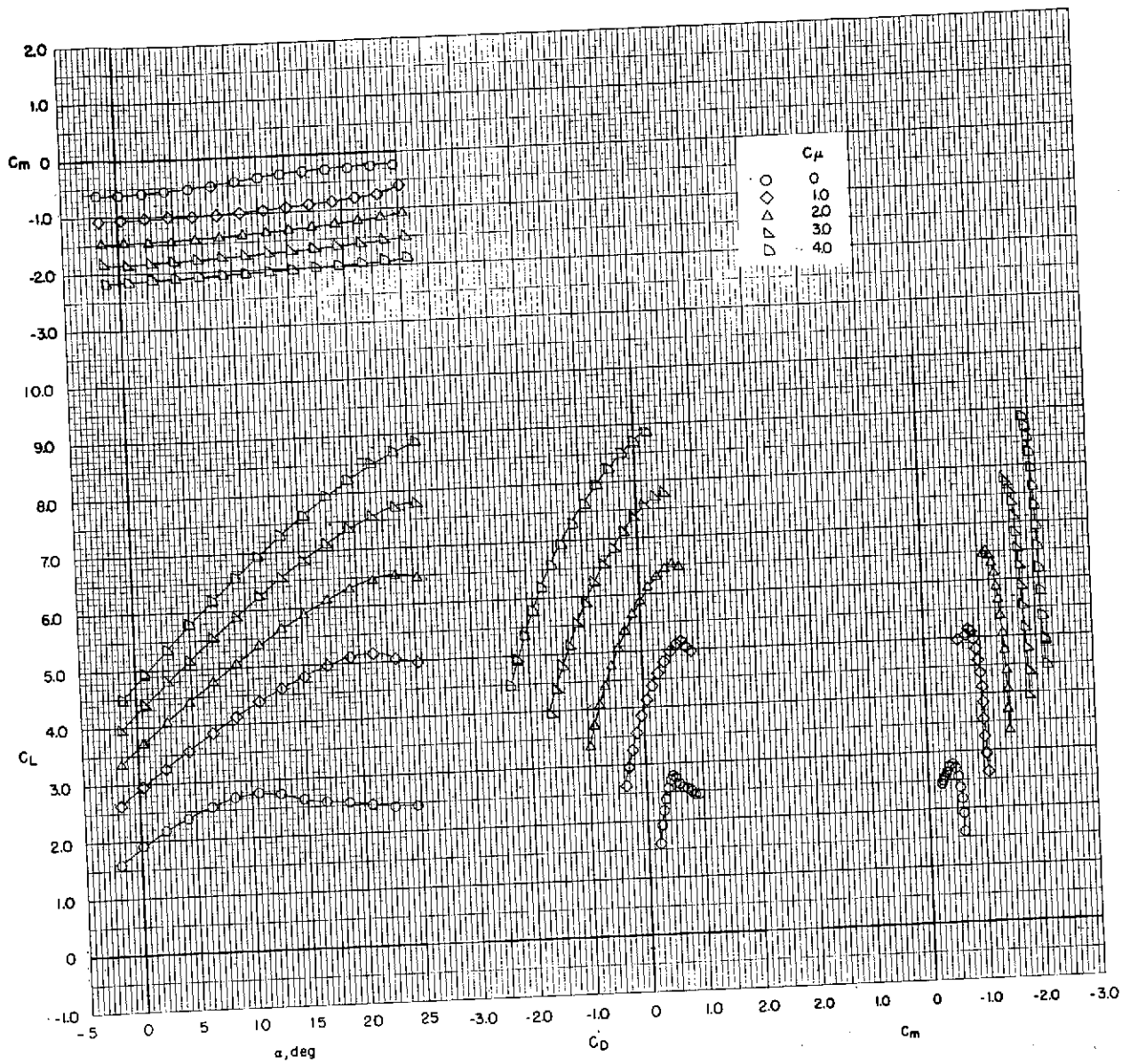

(a) Tail off.

Figure 15.- Effect of thrust coefficient on longitudinal aerodynamic characteristics. Bypass ratio 6.2; $\delta_f = 0^o/20^o/40^o$ (take-off); $\delta_{sw} = 50^o$.

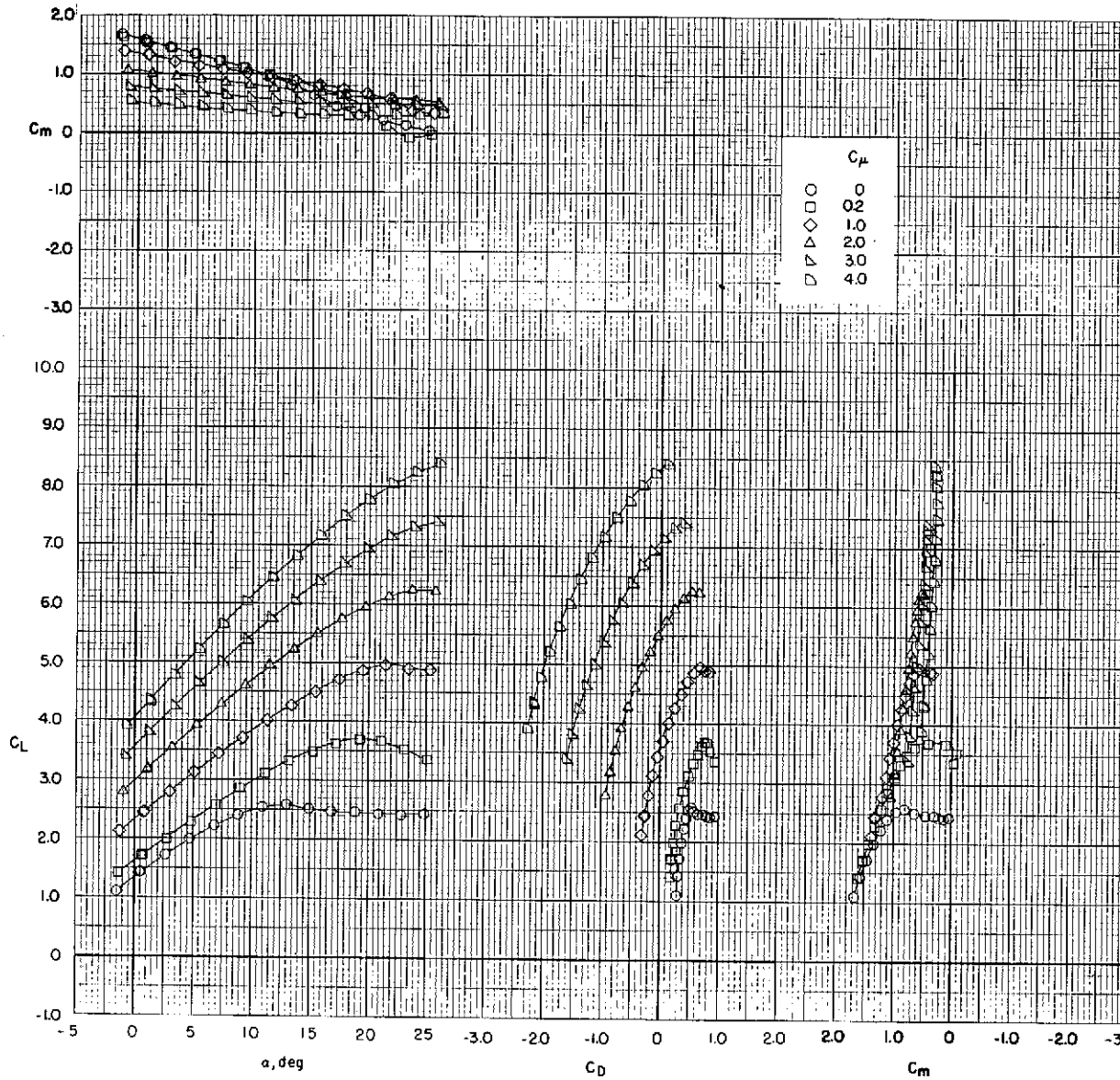

(b) $i_t = -5^o$; $\delta_e = -25^o$; $\delta_{sh} = -40^o$.

Figure 15.- Continued.

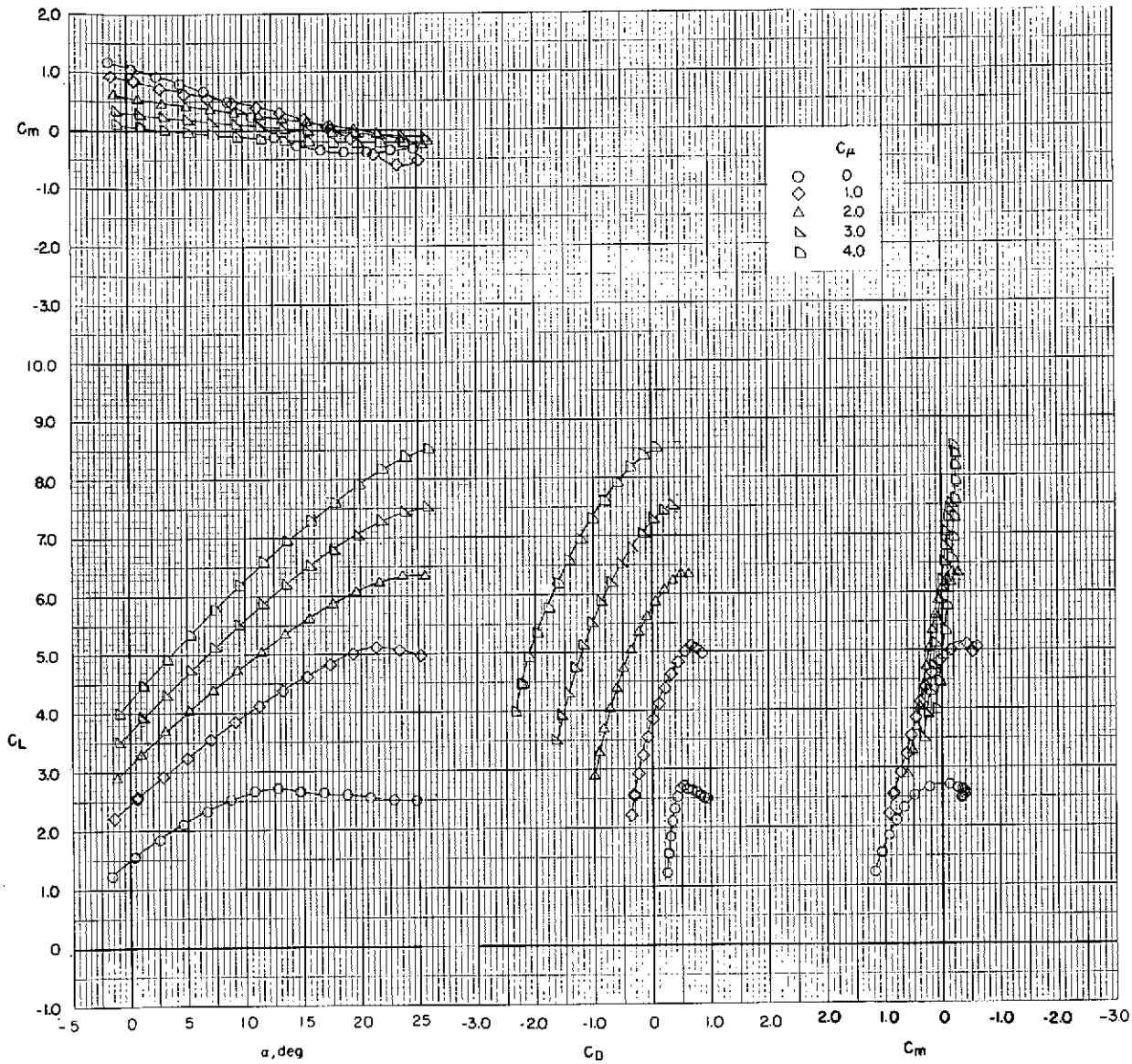

(c) $i_t = 0^o$; $\delta_e = -25^o$; $\delta_{sh} = -40^o$.

Figure 15.- Continued.

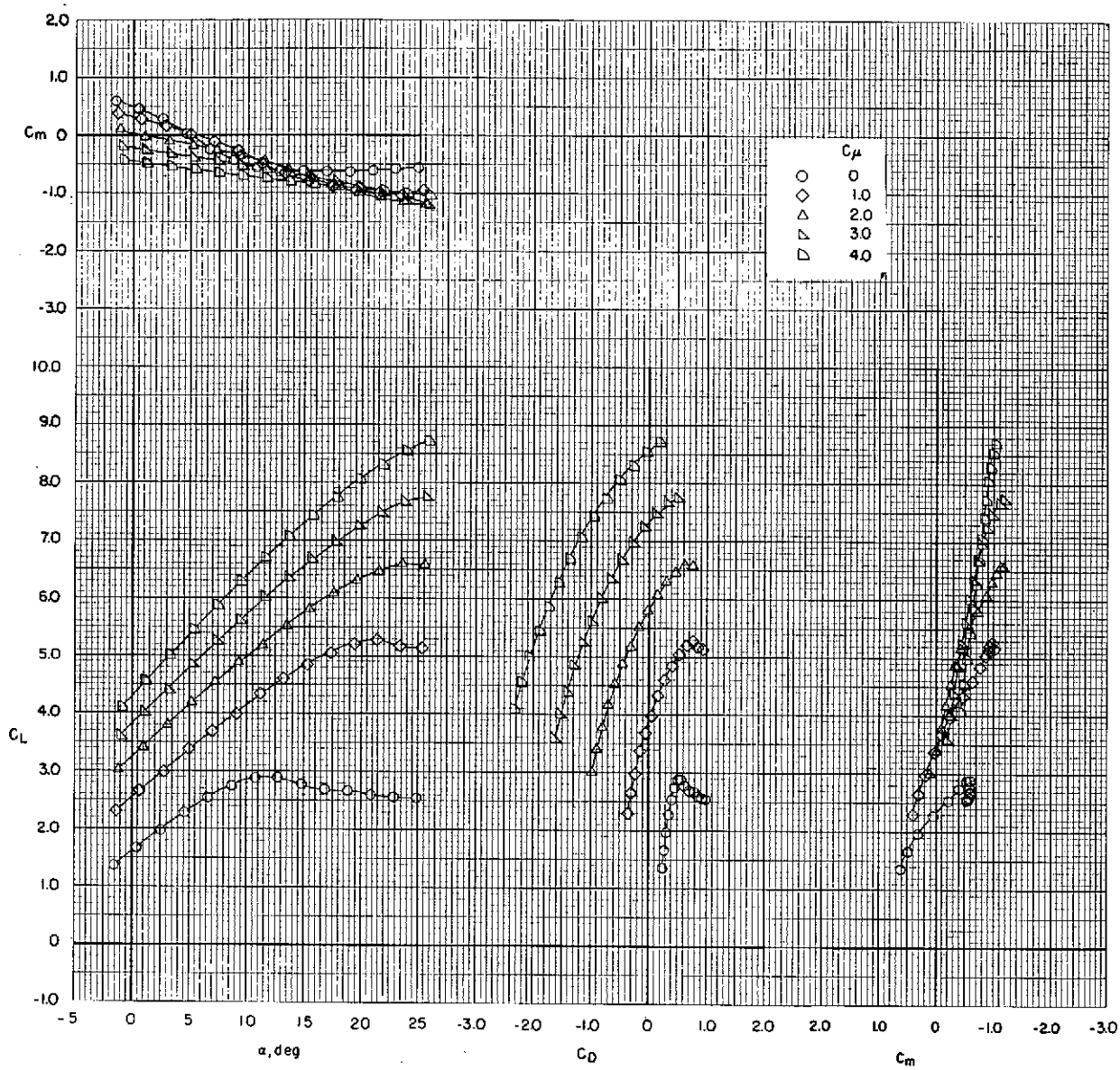

(d) $i_t = 5^o$; $\delta_e = -25^o$; $\delta_{sh} = -40^o$.

Figure 15.- Concluded.

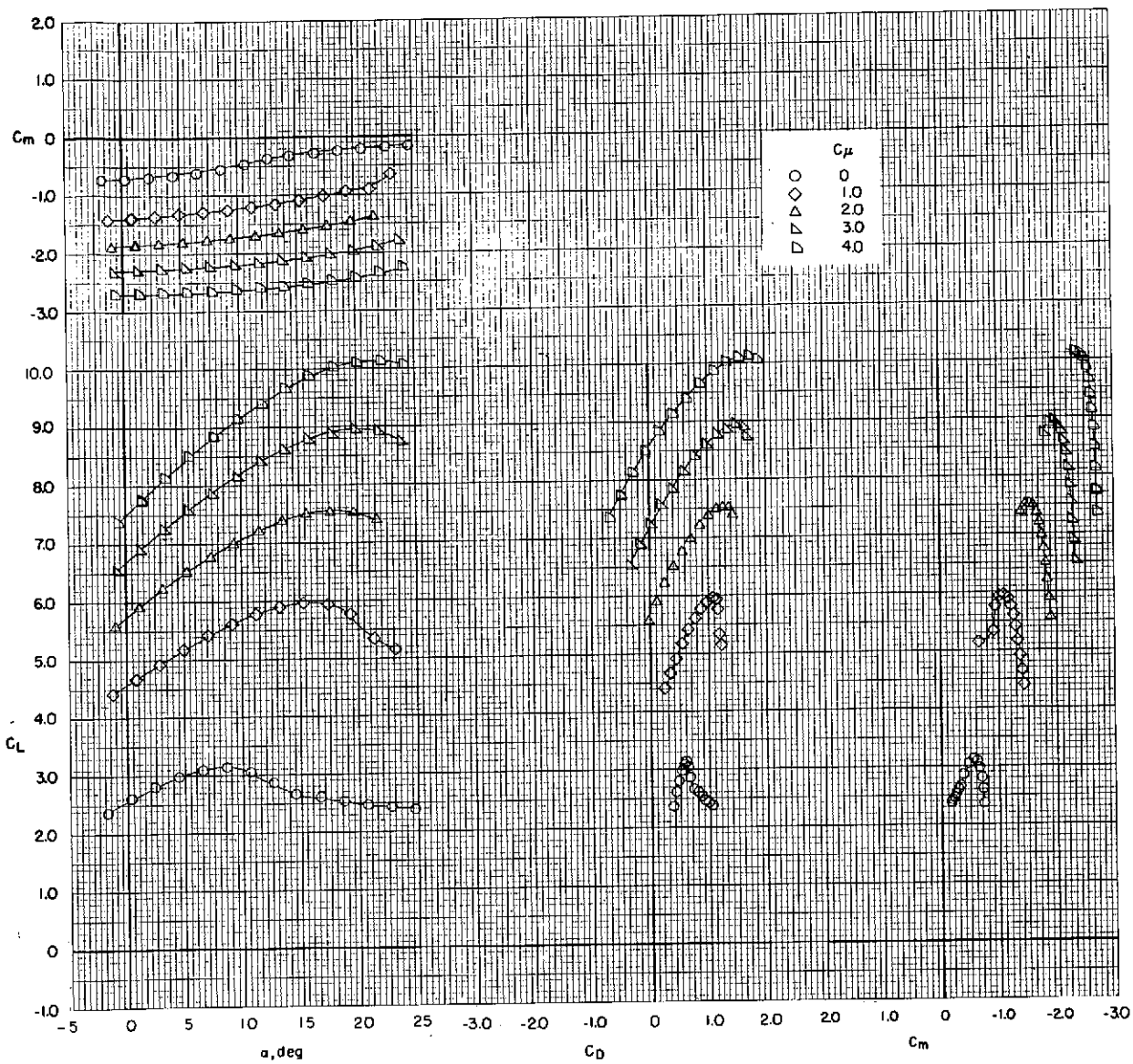

(a) Tail off.

Figure 16.- Effect of thrust coefficient on longitudinal aerodynamic characteristics. Bypass ratio 6.2; $\delta_f = 15^o/35^o/55^o$ (landing); $\delta_{sw} = 50^o$.

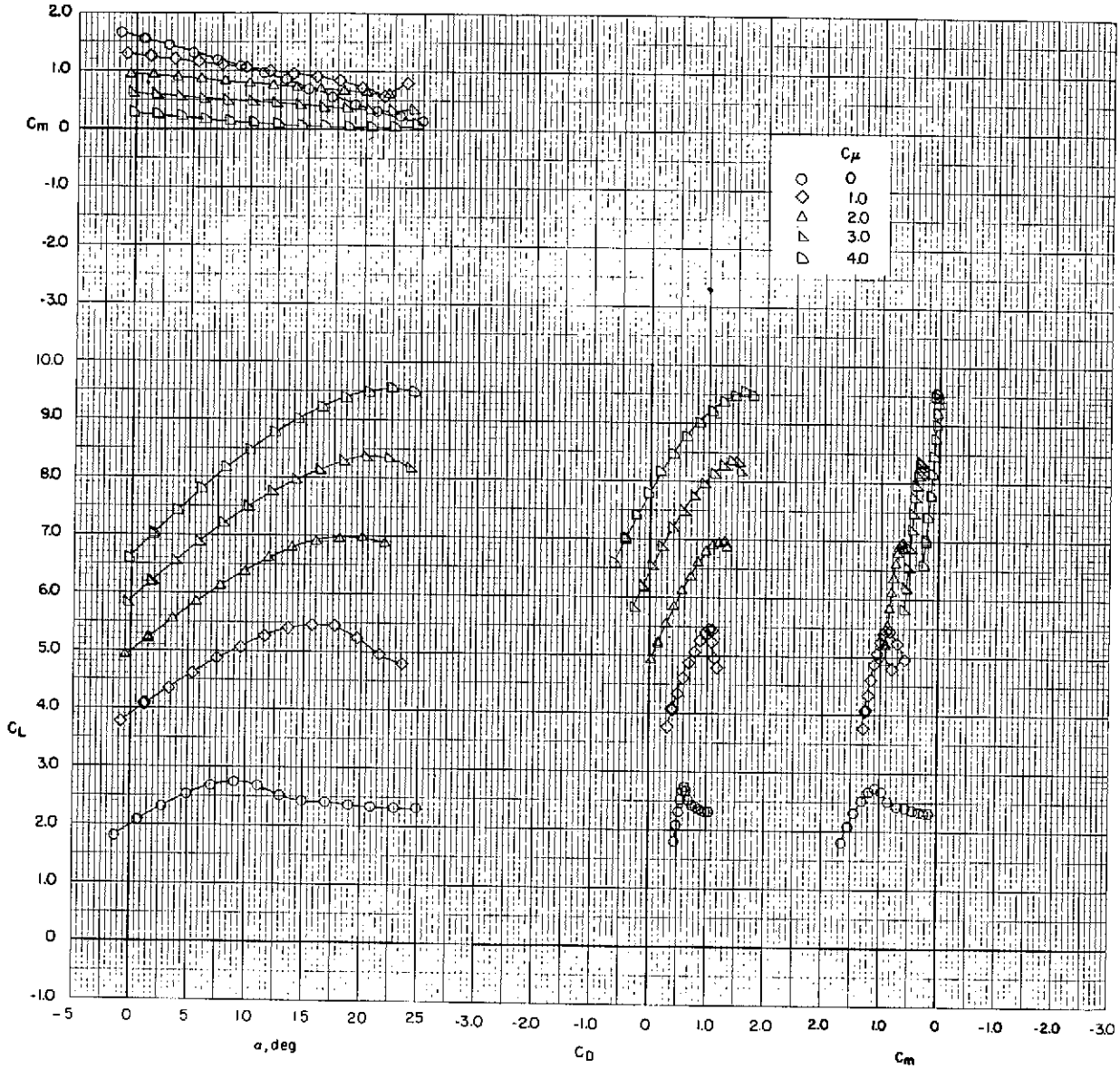

(b) $i_t = -5^o$; $\delta_e = -25^o$; $\delta_{sh} = -40^o$.

Figure 16.- Continued.

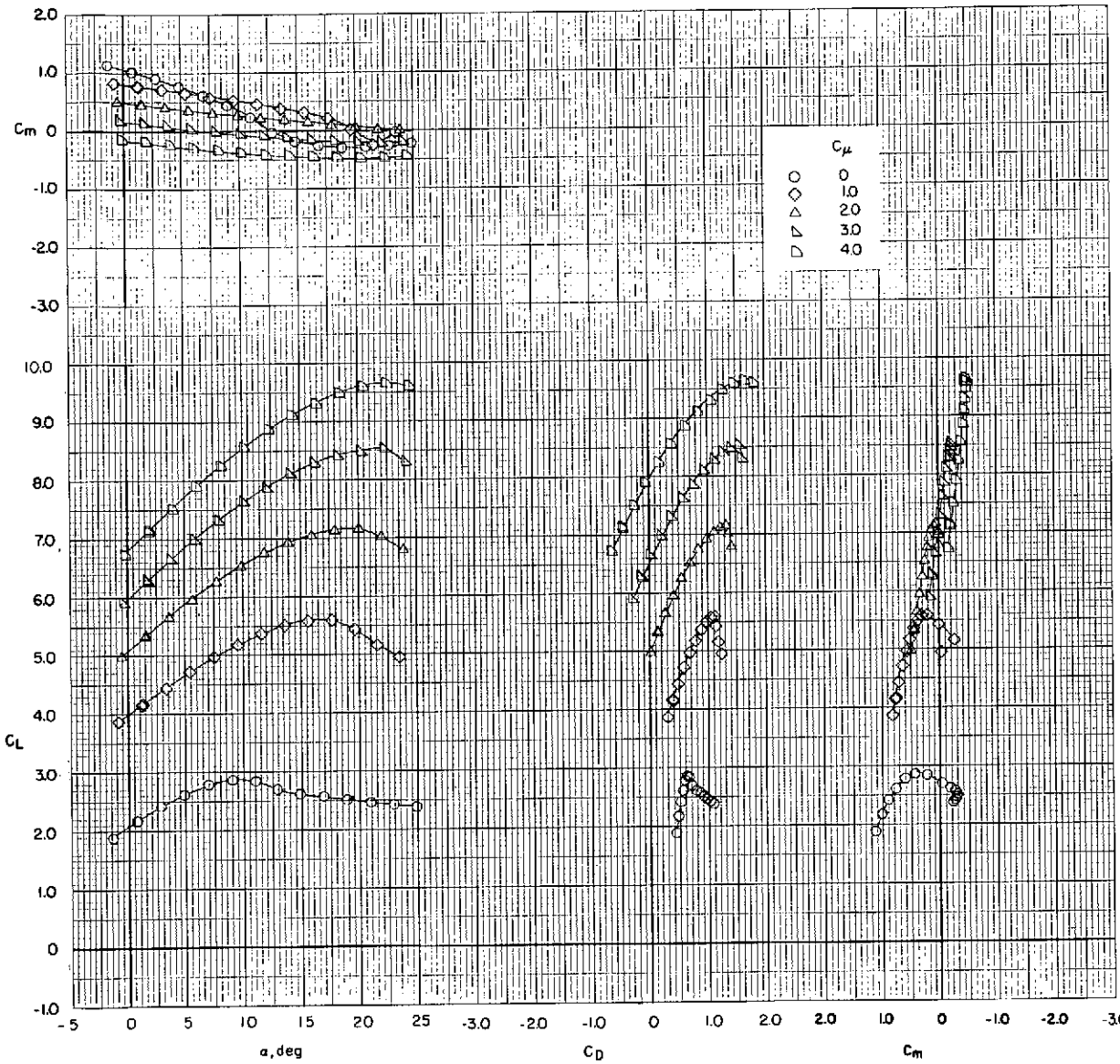

(c) $i_t = 0^o$; $\delta_e = -25^o$; $\delta_{sh} = -40^o$.

Figure 16.- Concluded.

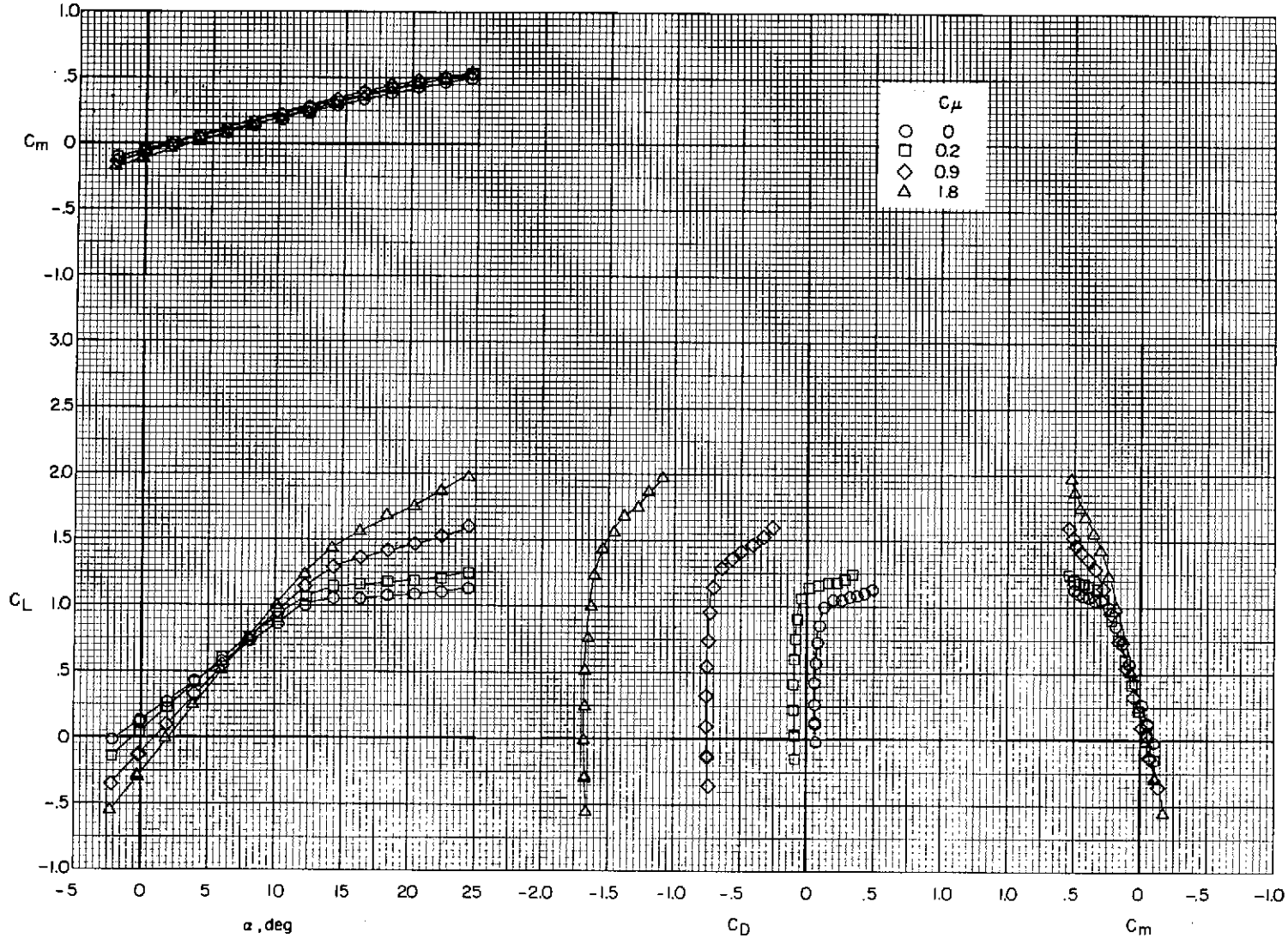

(a) Tail off.

Figure 17.- Effect of thrust coefficient on longitudinal aerodynamic characteristics. Modified bypass ratio 6.2; $\delta_f = 0^o$ (cruise); δ_{sw} = off.

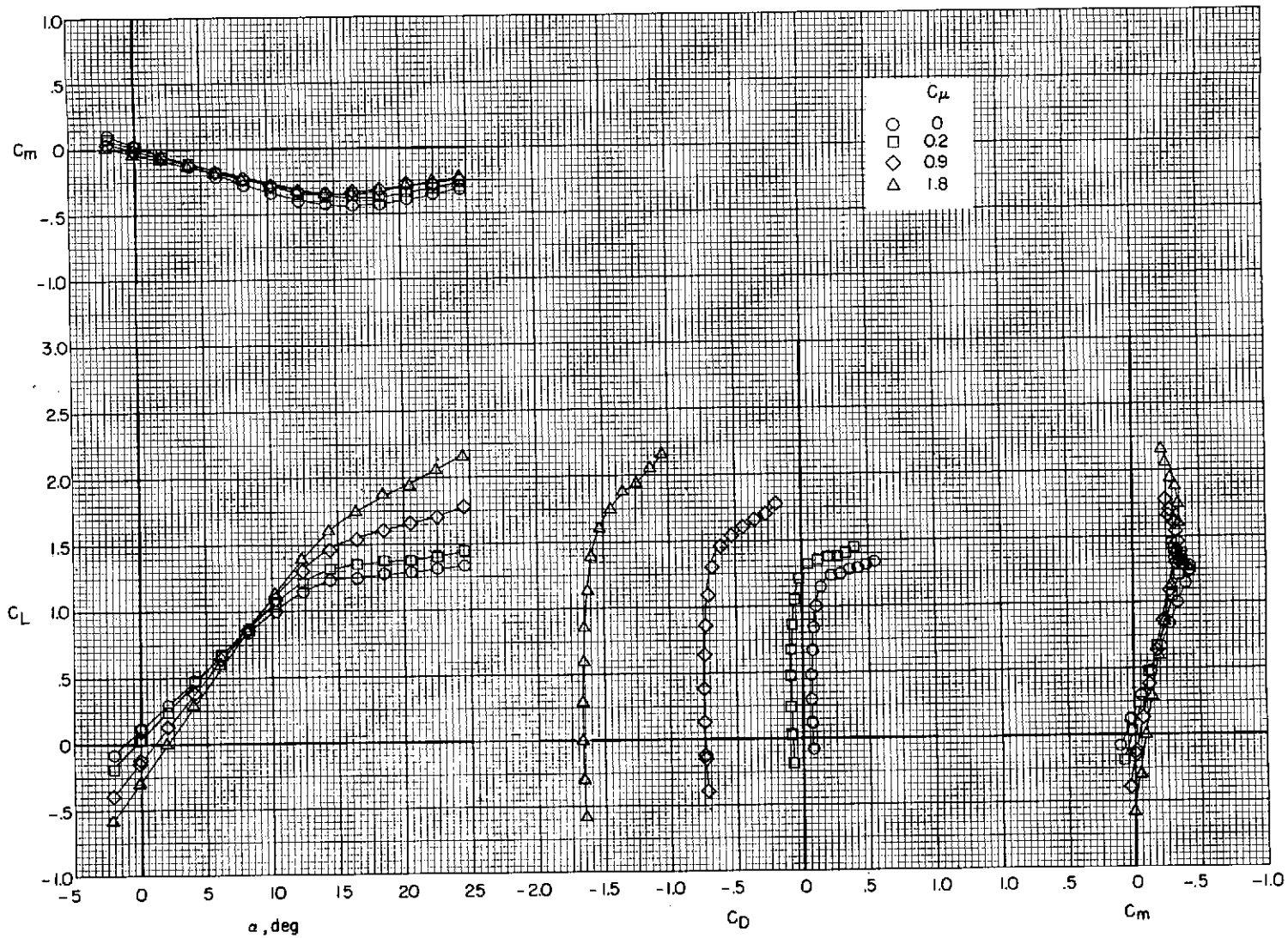

(b) $i_t = 0^o$; $\delta_e = 0^o$; δ_{sh} = off.

Figure 17.- Continued.

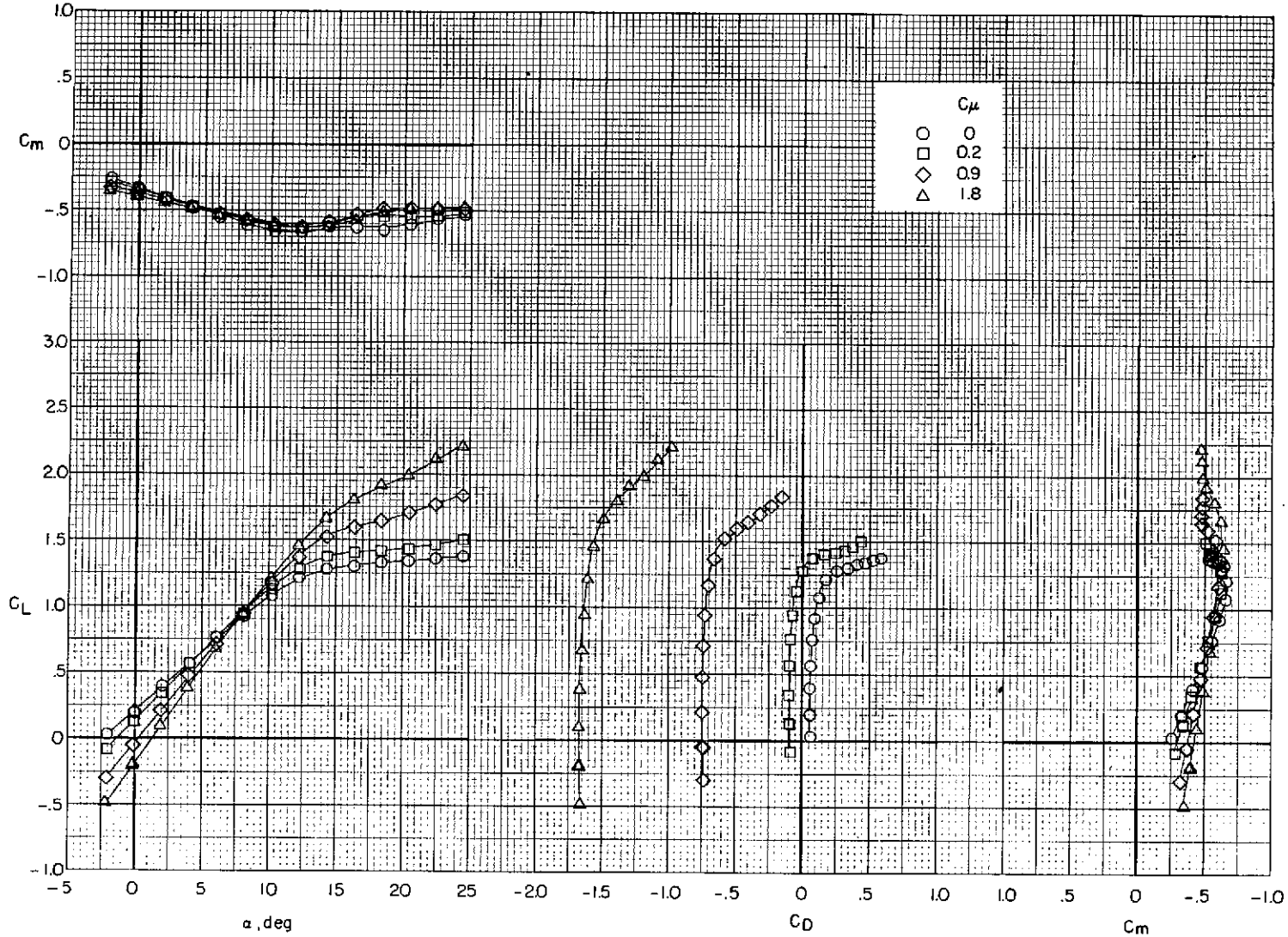

(c) $i_t = 5^o$; $\delta_e = 0^o$; δ_{sh} = off.

Figure 17.- Concluded.

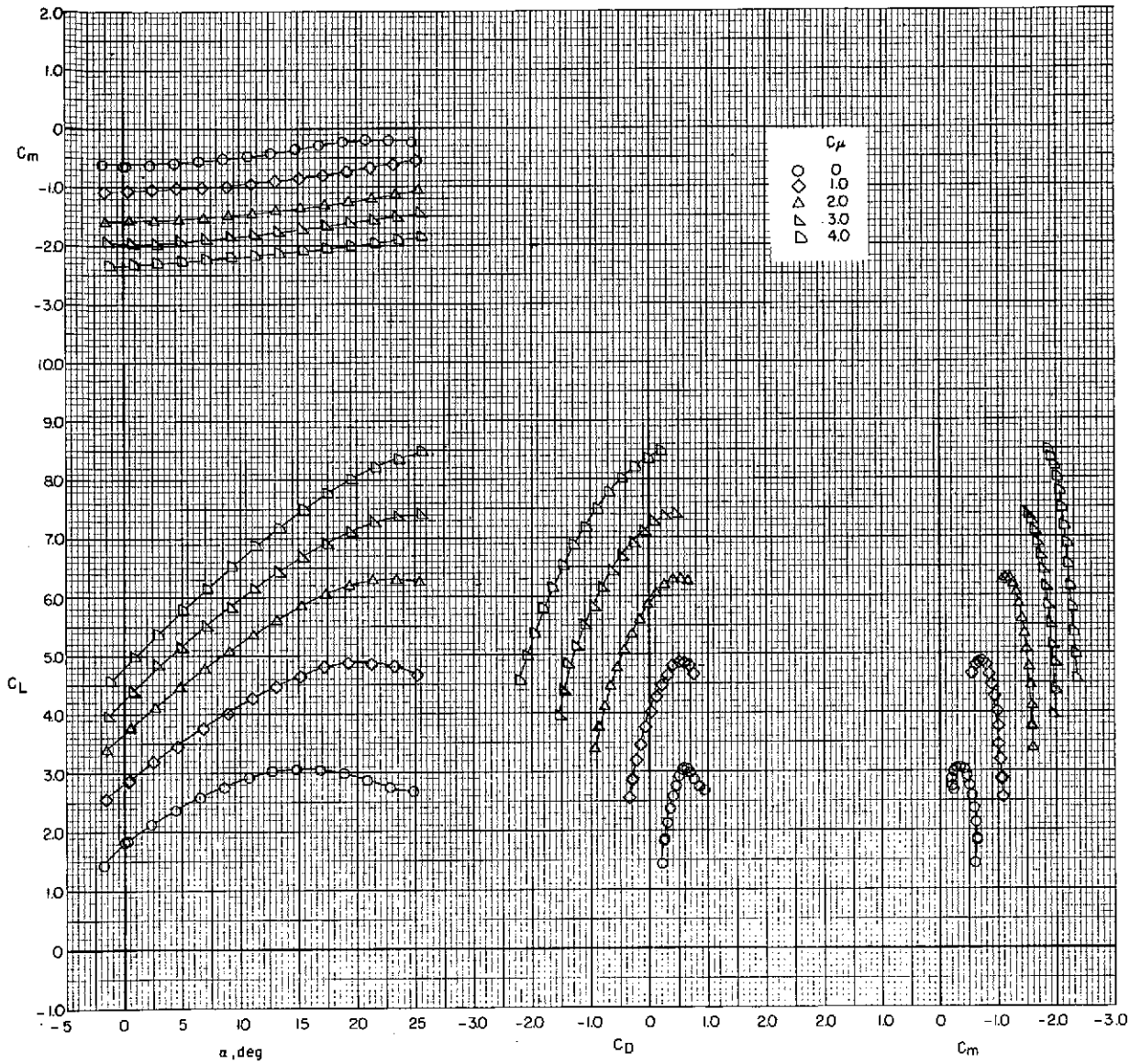

(a) Tail off.

Figure 18.- Effect of thrust coefficient on longitudinal aerodynamic characteristics. Modified bypass ratio 6.2; $\delta_f = 0^o/20^o/40^o$ (take-off); $\delta_{sw} = 50^o$.

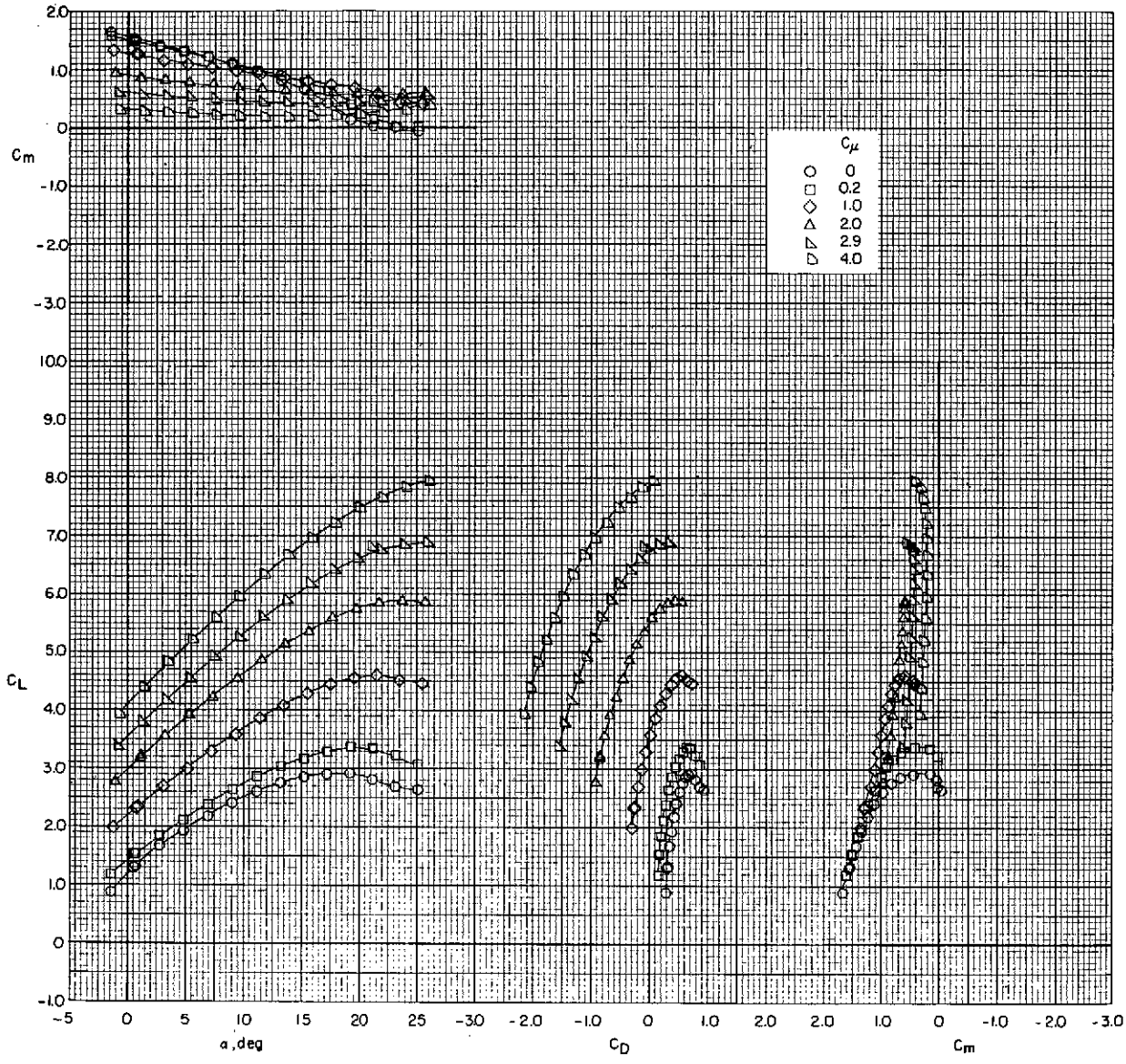

(b) $i_t = -5^o$; $\delta_e = -25^o$; $\delta_{sh} = -40^o$.

Figure 18.- Continued.

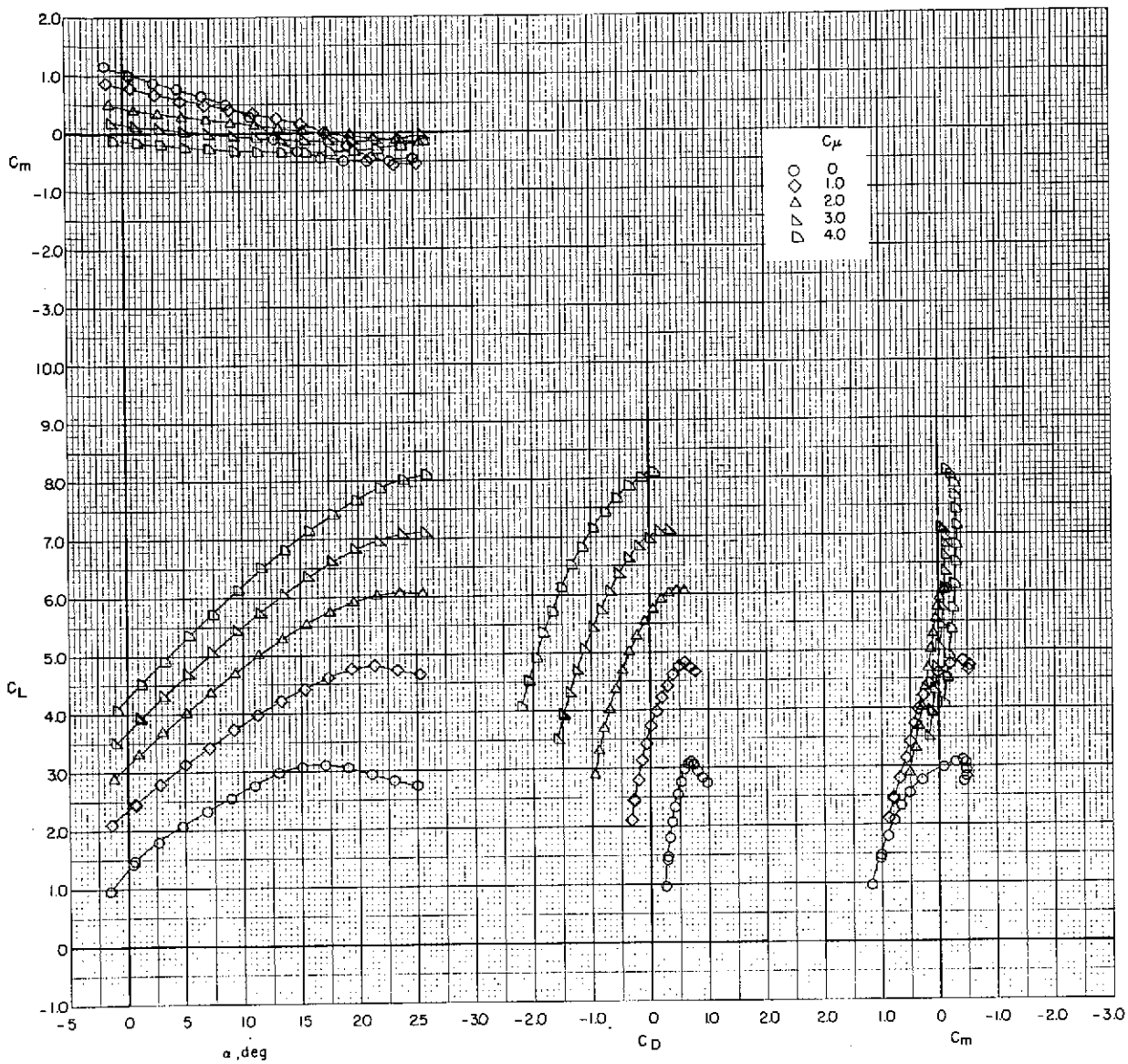

(c) $i_t = 0^o$; $\delta_e = -25^o$; $\delta_{sh} = -40^o$.

Figure 18.- Continued.

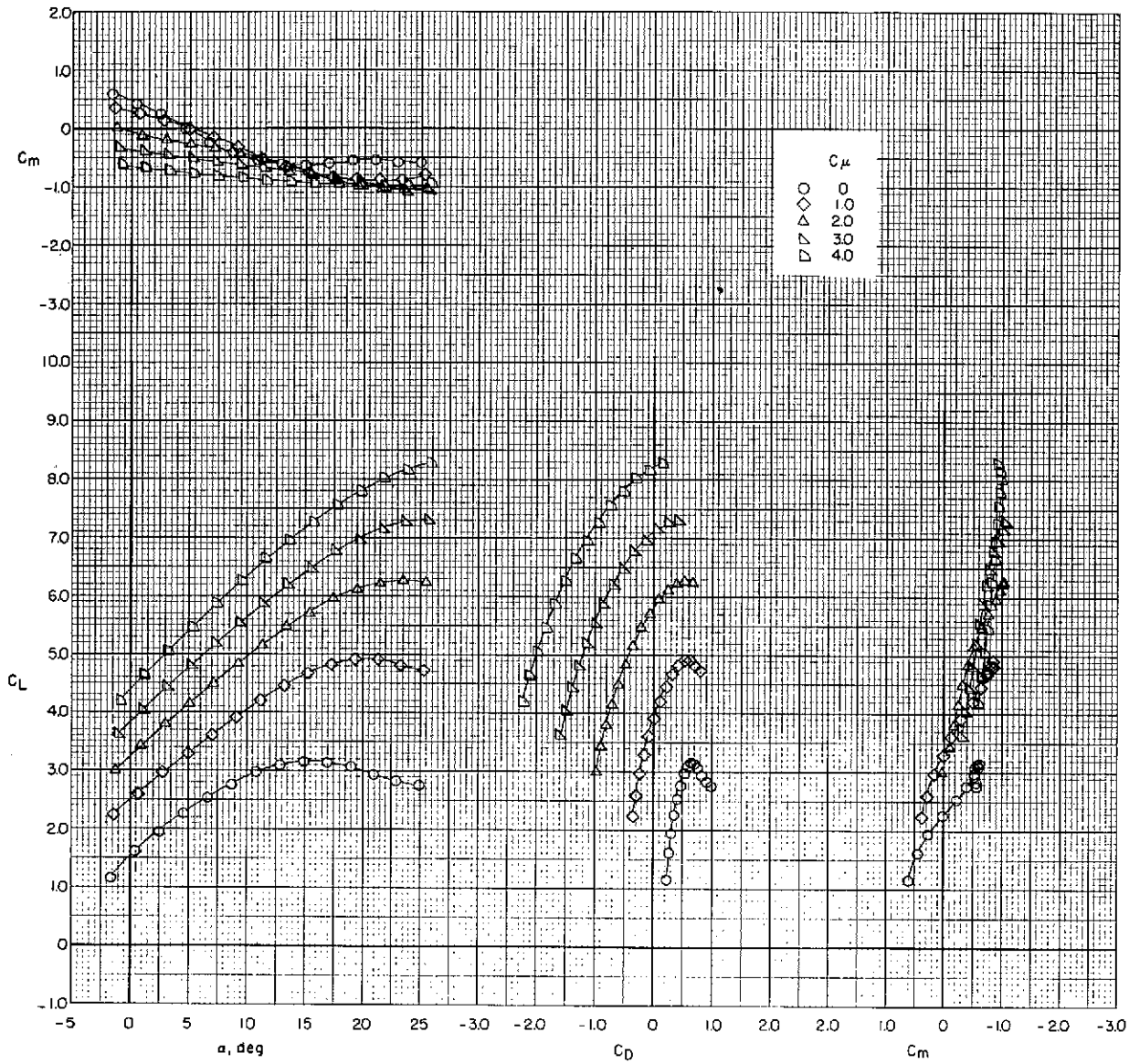

(d) $i_t = 5^o$; $\delta_e = -25^o$; $\delta_{sh} = -40^o$.

Figure 18.- Concluded.

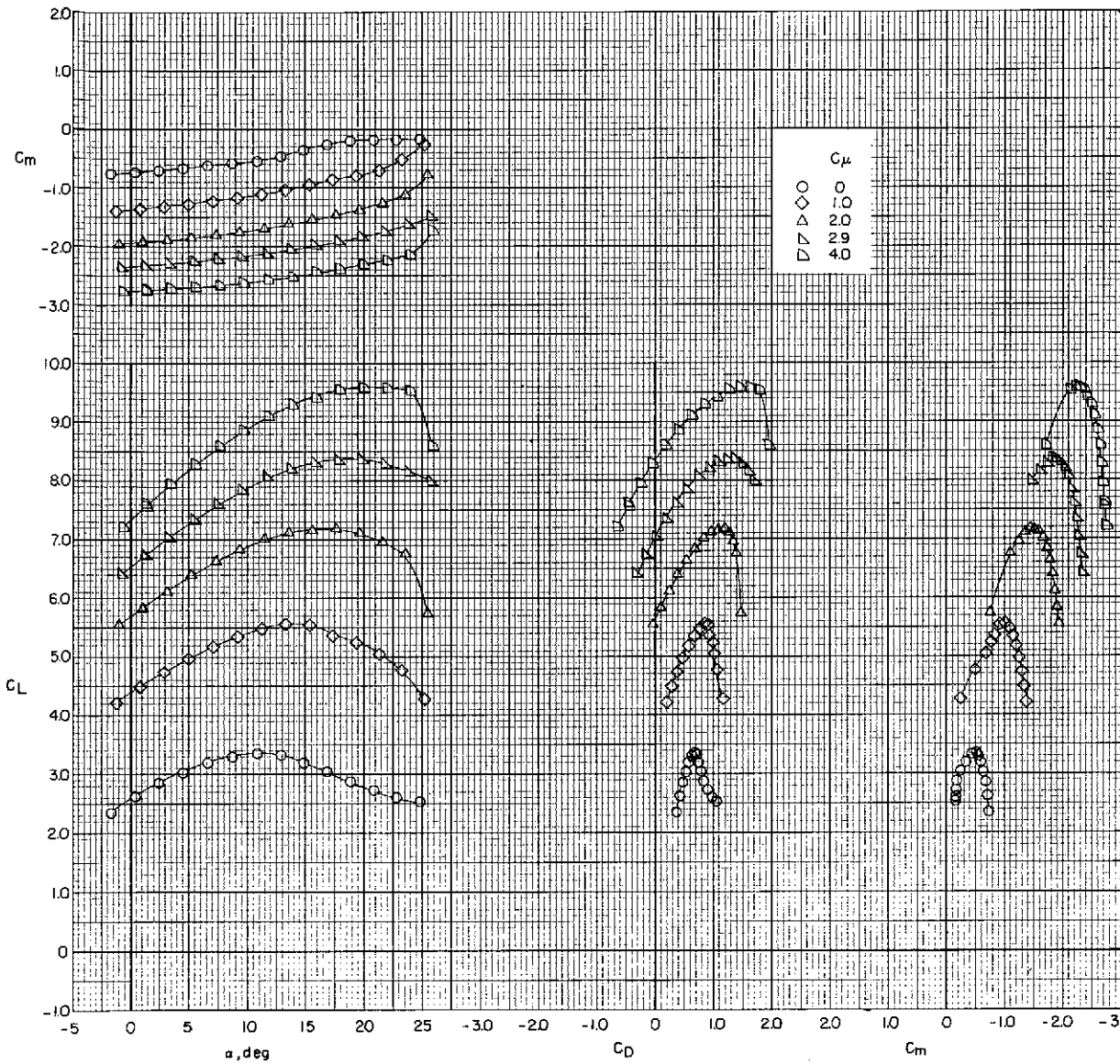

(a) Tail off.

Figure 19.- Effect of thrust coefficient on longitudinal aerodynamic characteristics. Modified bypass ratio 6.2; $\delta_f = 15^o/35^o/55^o$ (landing); $\delta_{sw} = 50^o$.

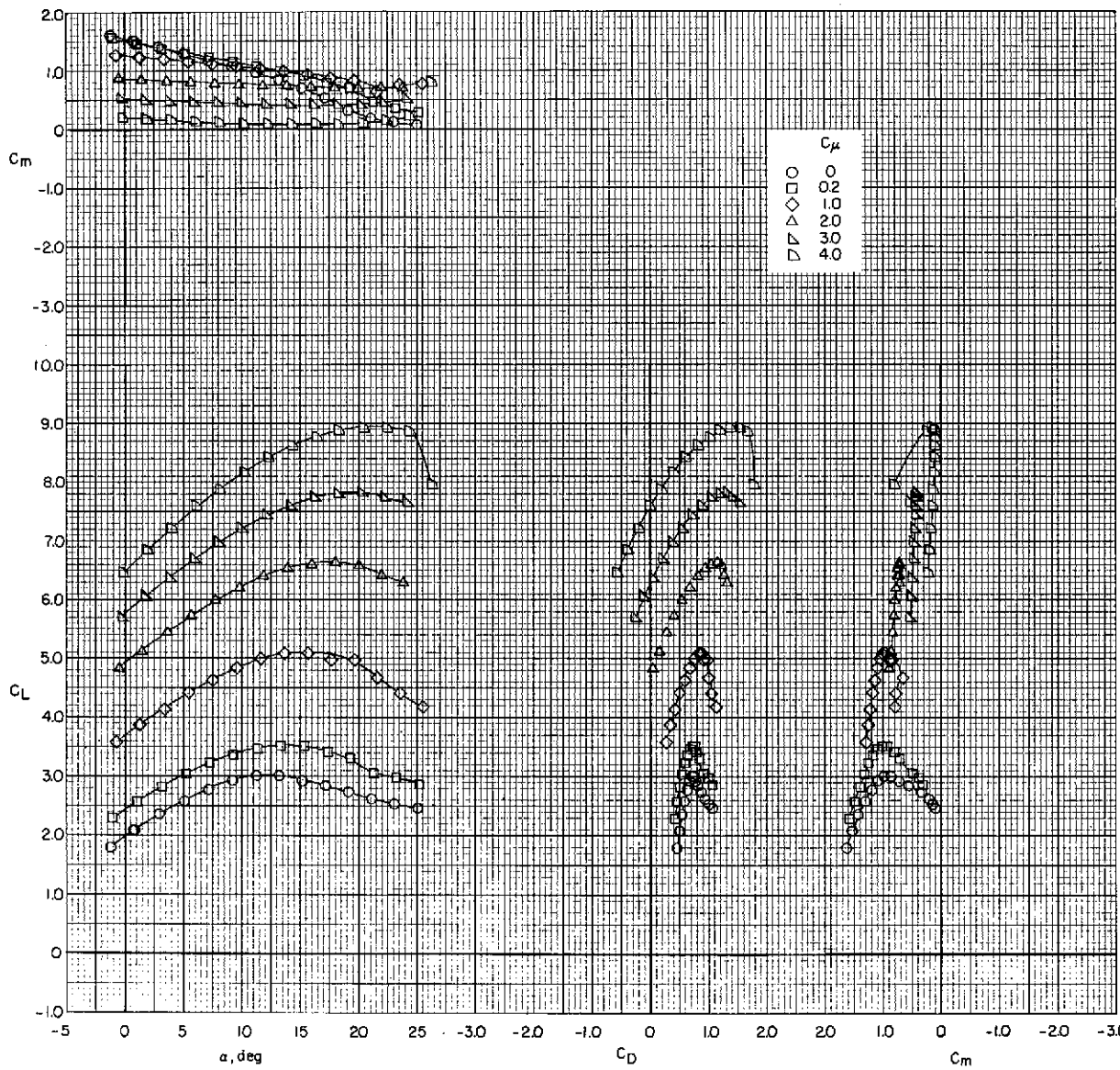

(b) $i_t = -5^o$; $\delta_e = -25^o$; $\delta_{sh} = -40^o$.

Figure 19.- Continued.

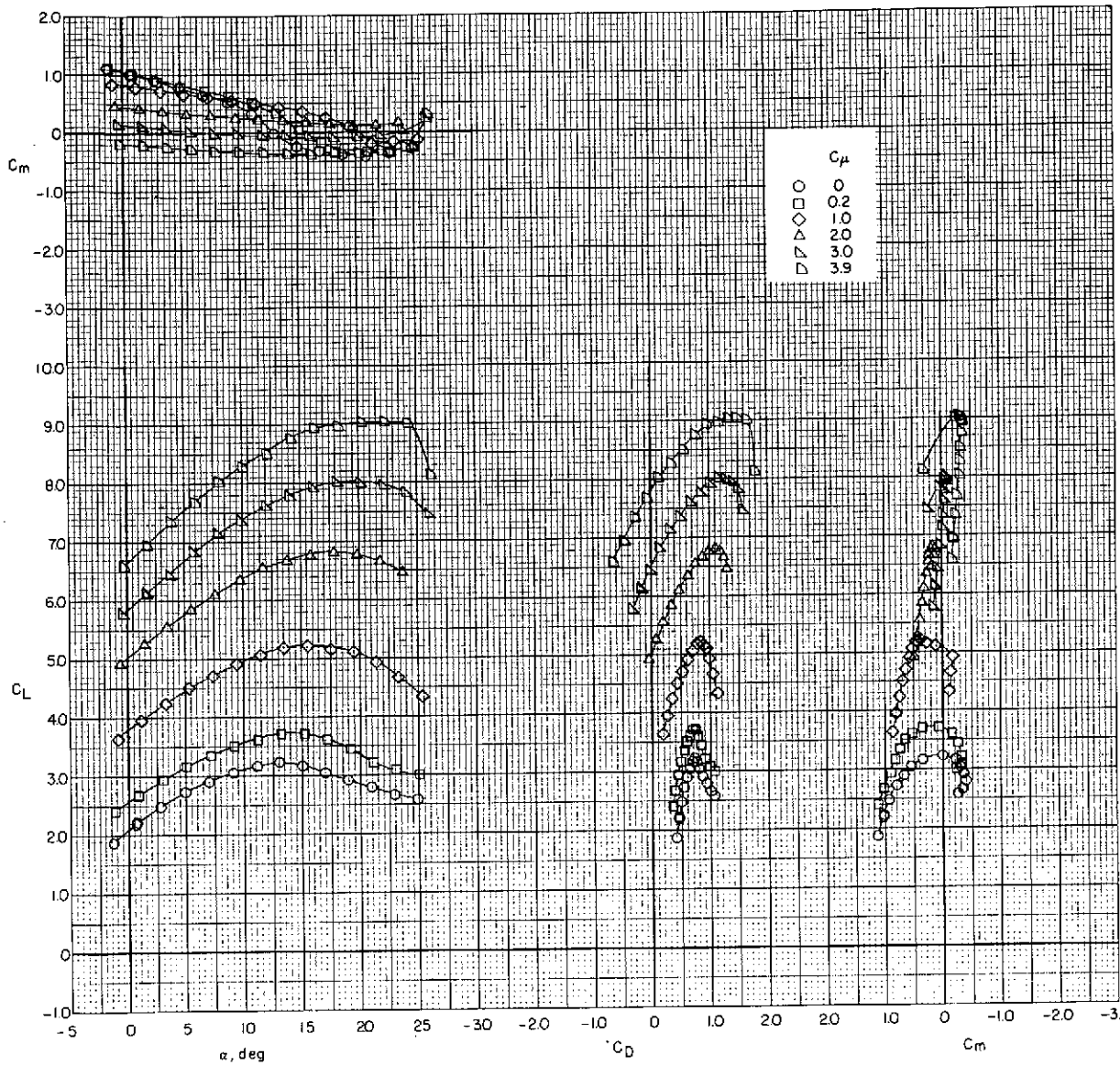

(c) $i_t = 0^o$; $\delta_e = -25^o$; $\delta_{sh} = -40^o$.

Figure 19.- Continued.

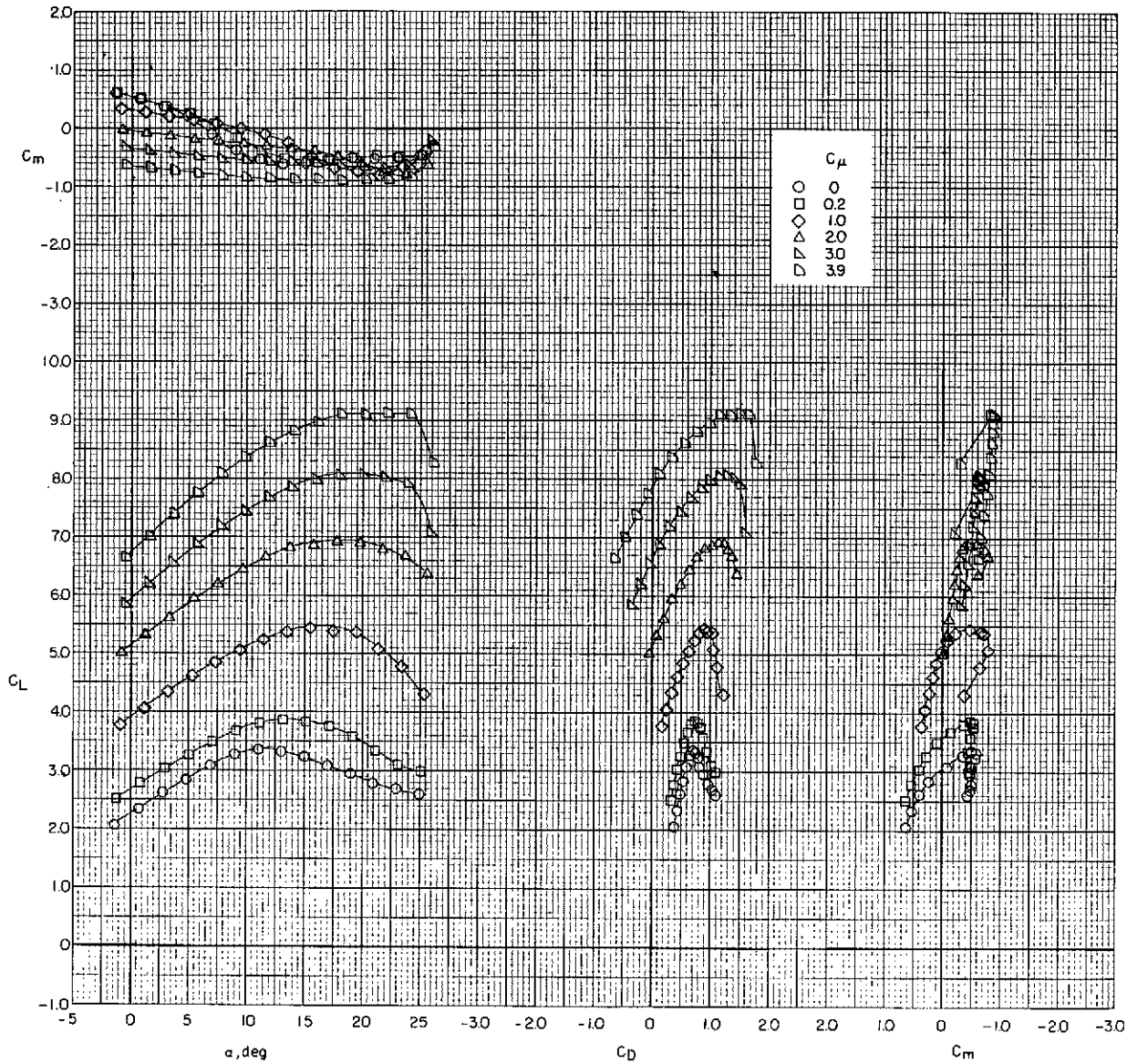

(d) $i_t = 5^o$; $\delta_e = -25^o$; $\delta_{sh} = -40^o$.

Figure 19.- Concluded.

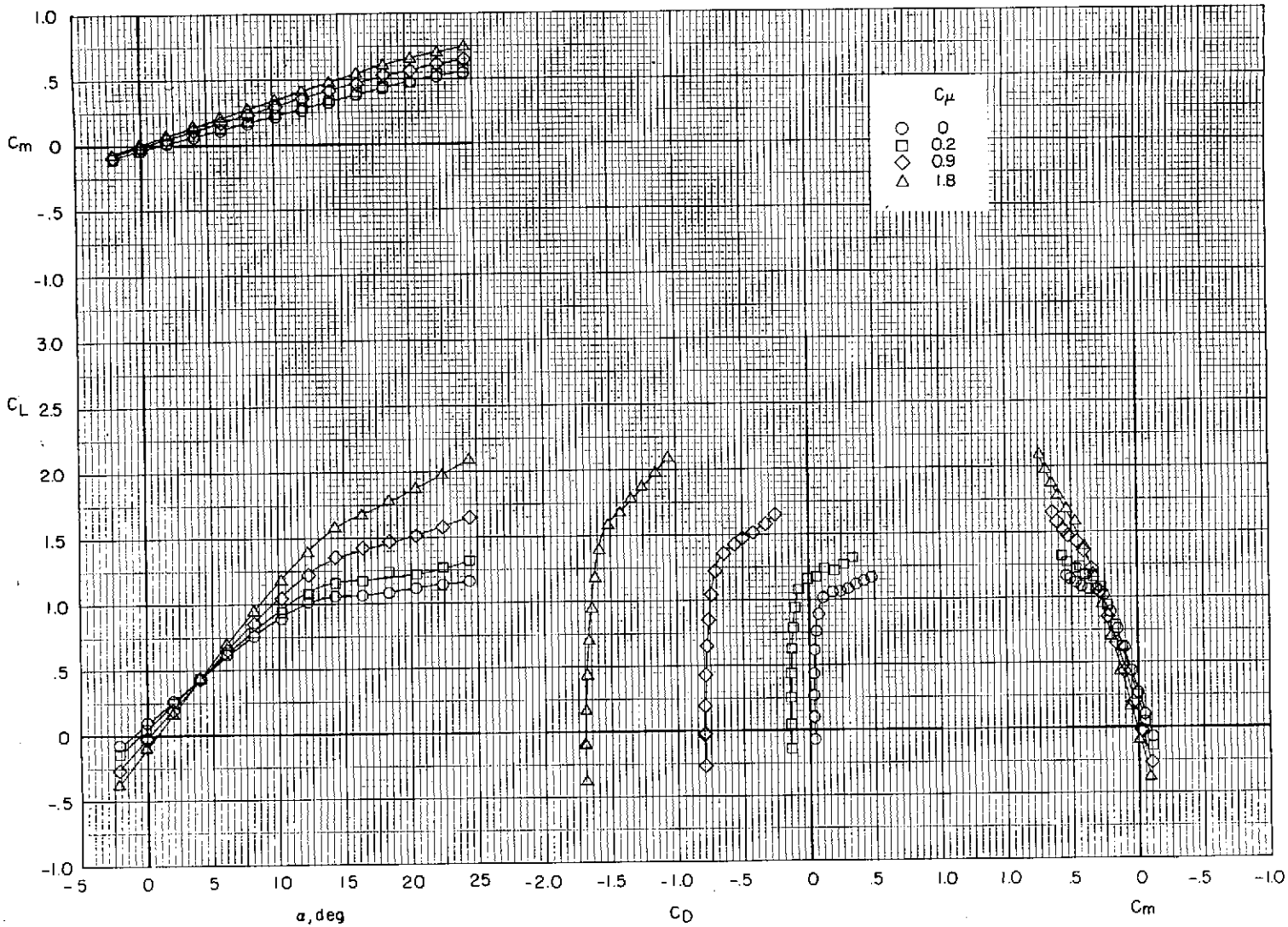

(a) Tail off.

Figure 20.- Effect of thrust coefficient on longitudinal aerodynamic characteristics. Bypass ratio 10.0; $\delta_f = 0^o$ (cruise); δ_{sw} = off.

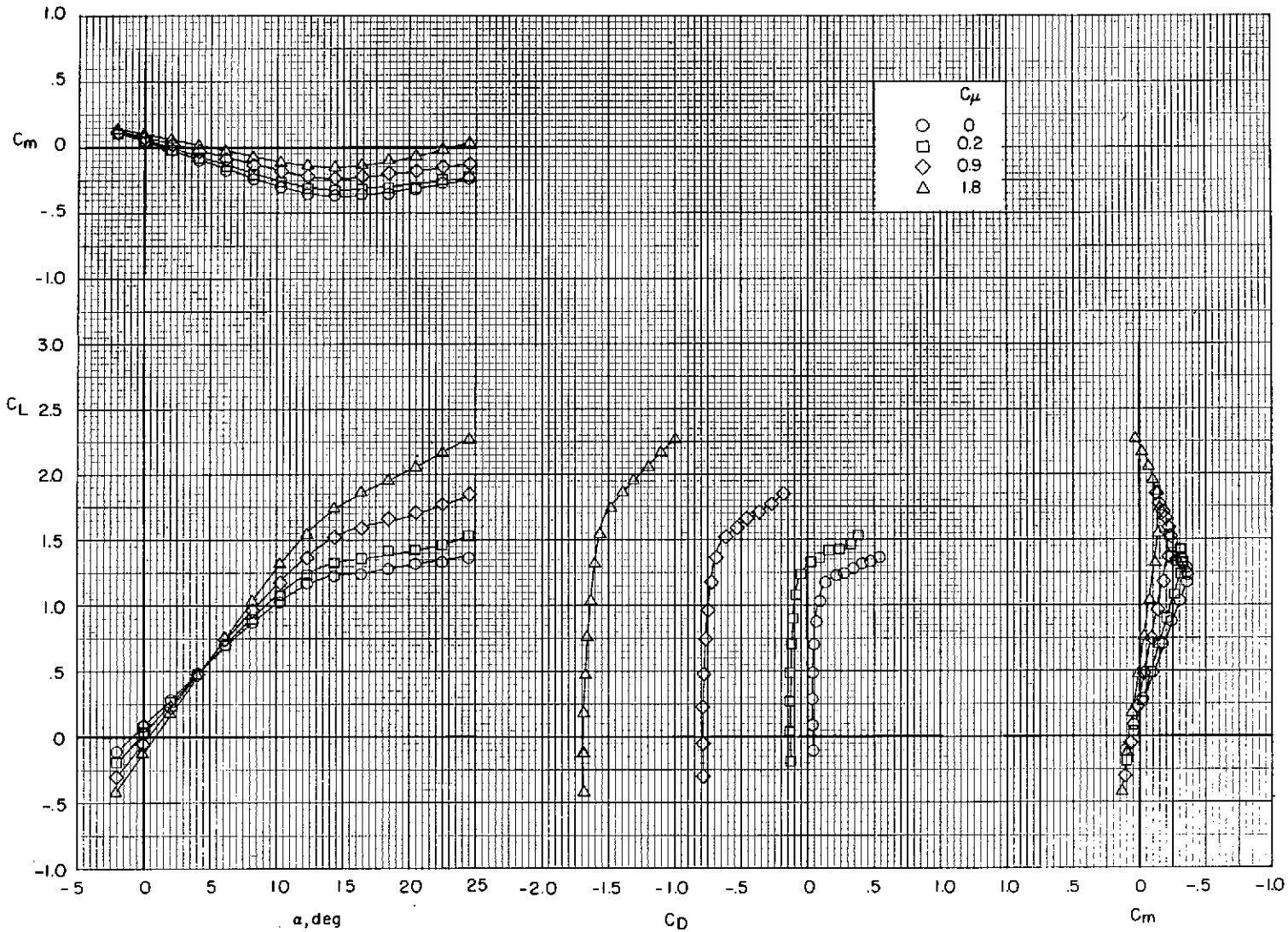

(b) $i_t = 0^o$; $\delta_e = 0^o$; δ_{sh} = off.

Figure 20.- Continued.

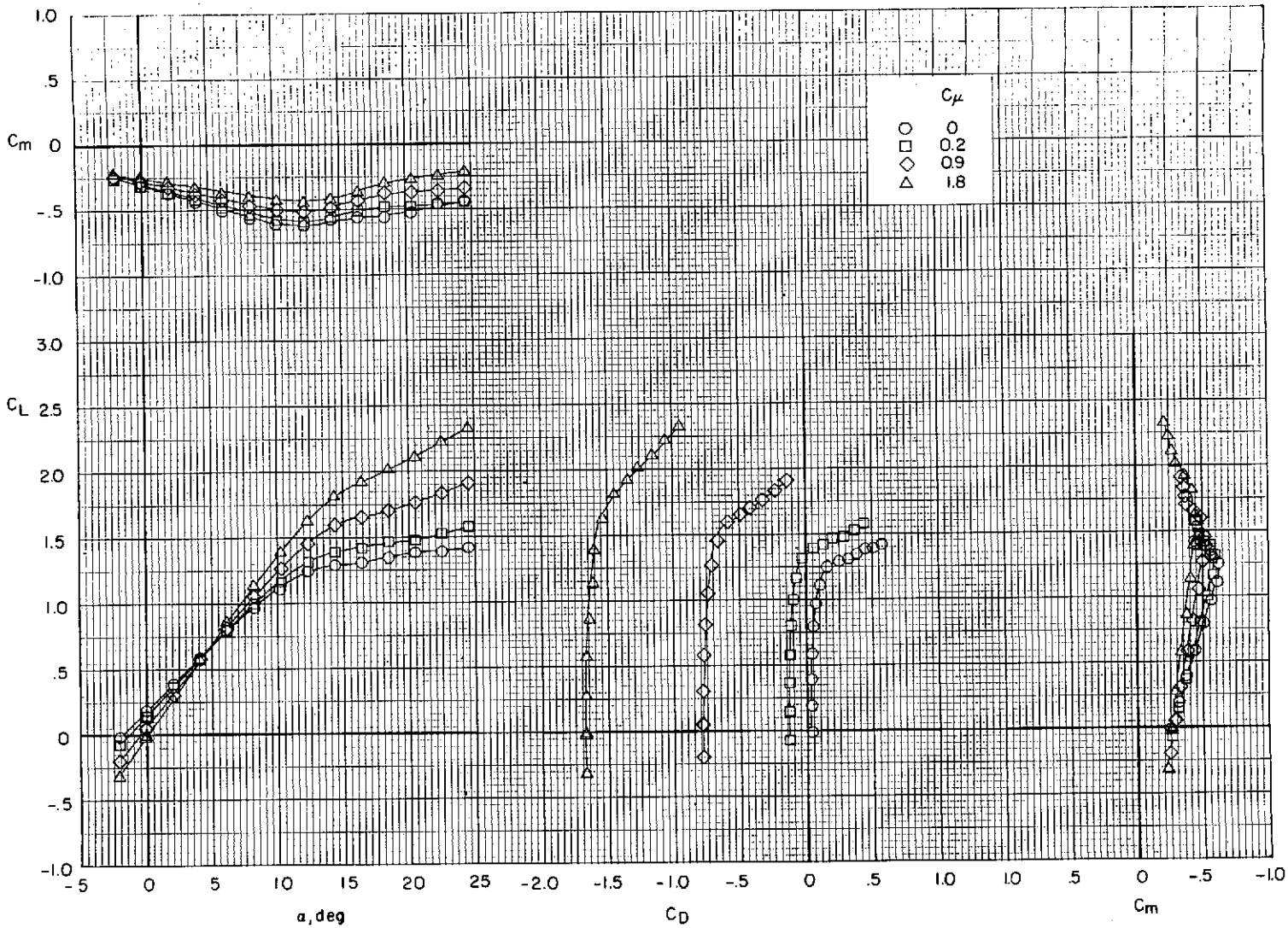

(c) $i_t = 5^o$; $\delta_e = 0^o$; δ_{sh} = off.

Figure 20.- Concluded.

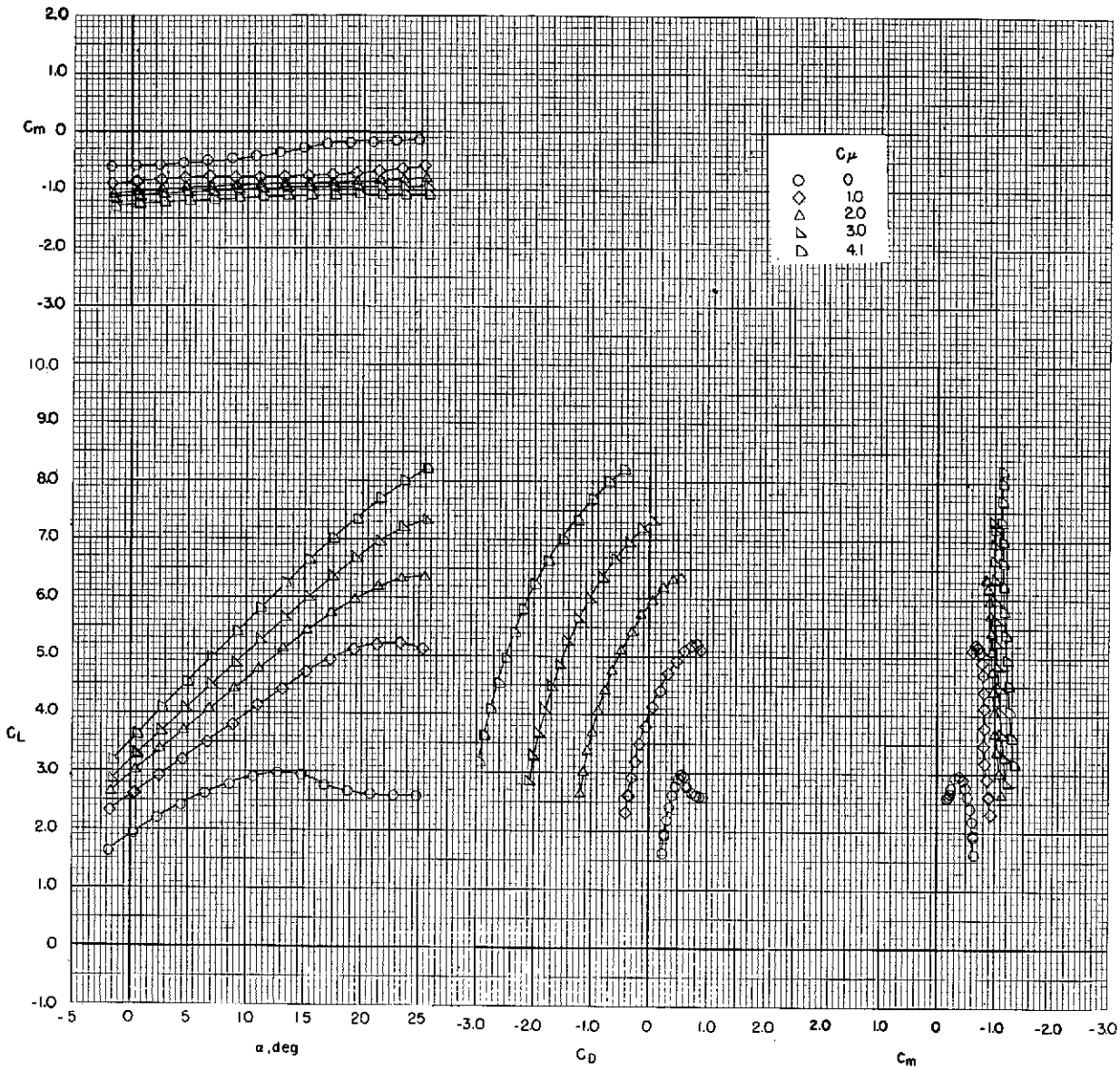

(a) Tail off.

Figure 21.- Effect of thrust coefficient on longitudinal aerodynamic characteristics. Bypass ratio 10.0; $\delta_f = 0^o/20^o/40^o$ (take-off); $\delta_{sw} = 50^o$.

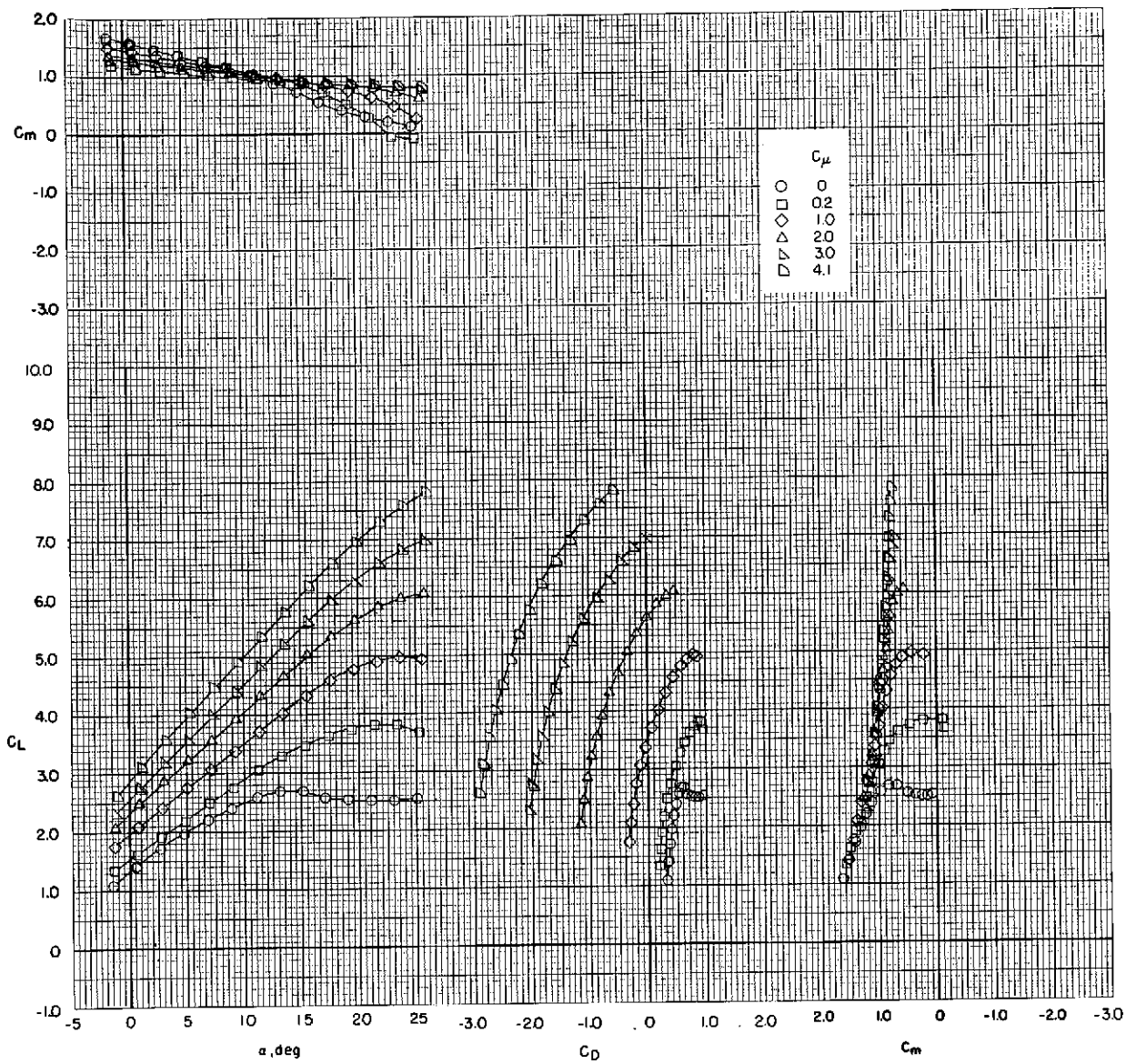

(b) $i_t = -5^o$; $\delta_e = -25^o$; $\delta_{sh} = -40^o$.

Figure 21.- Continued.

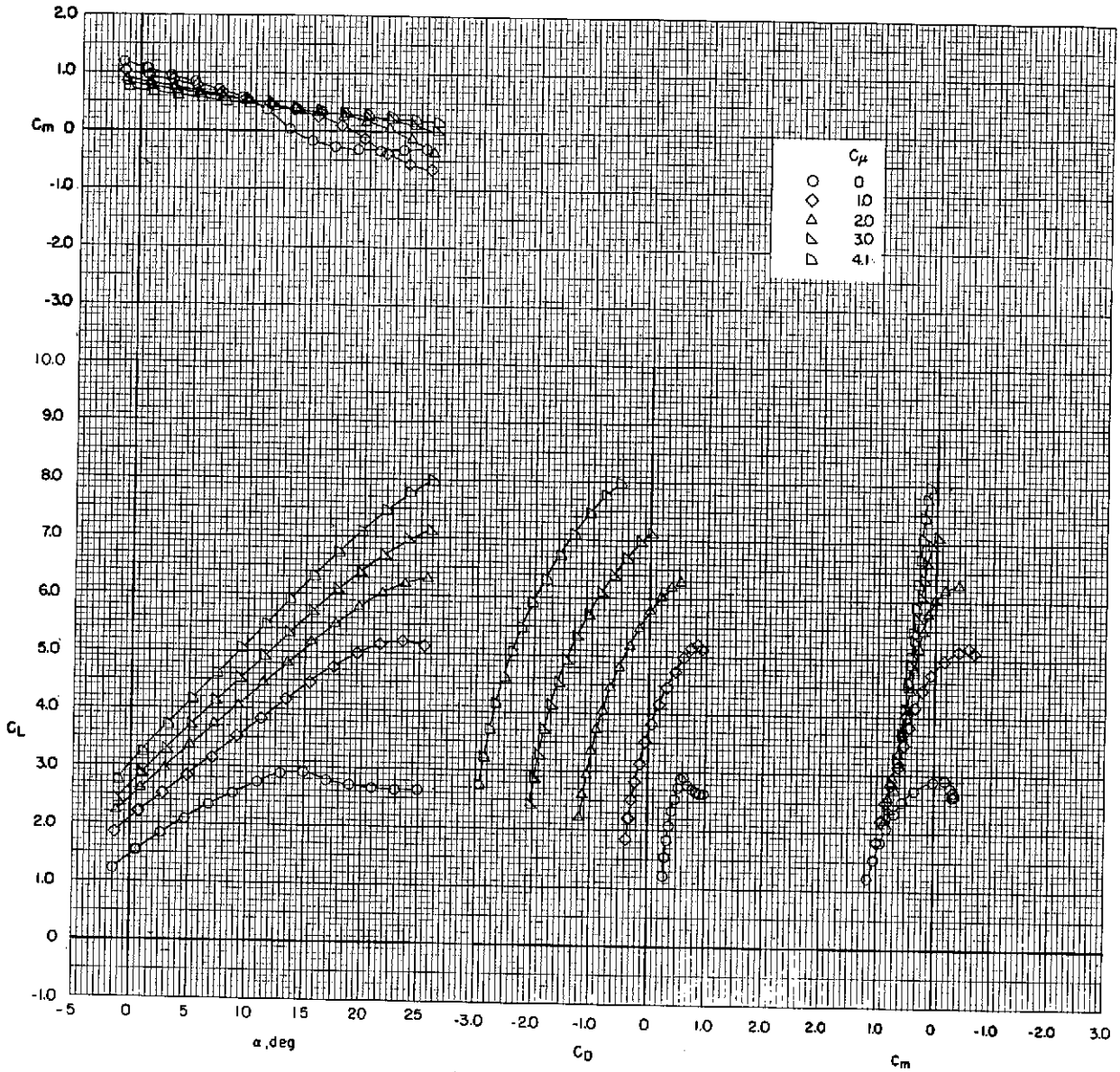

(c) $i_t = 0^o$; $\delta_e = -25^o$; $\delta_{sh} = -40^o$.

Figure 21.- Concluded.

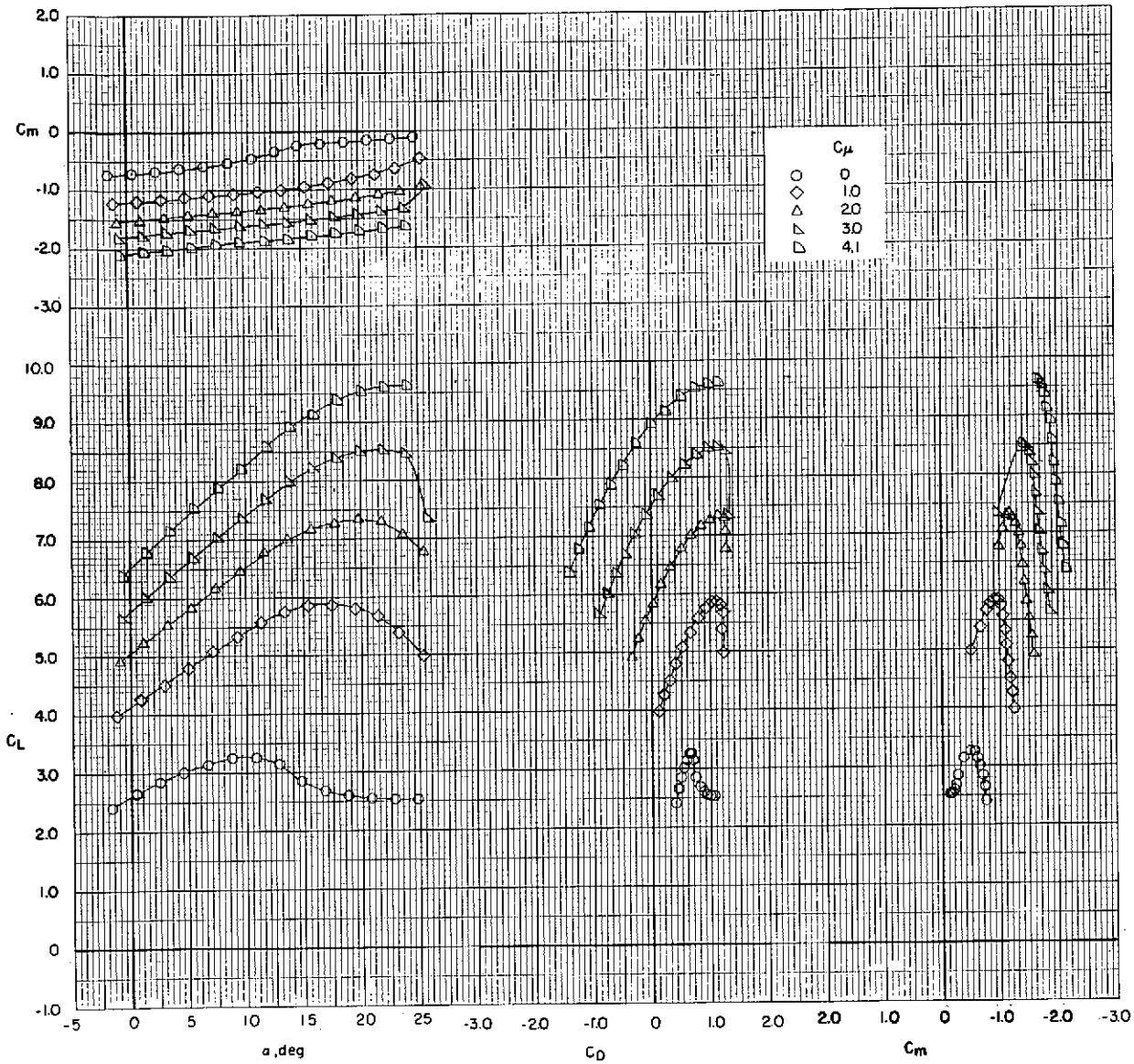

(a) Tail off.

Figure 22.- Effect of thrust coefficient on longitudinal aerodynamic characteristics. Bypass ratio 10.0; $\delta_f = 15^o/35^o/55^o$ (landing); $\delta_{sw} = 50^o$.

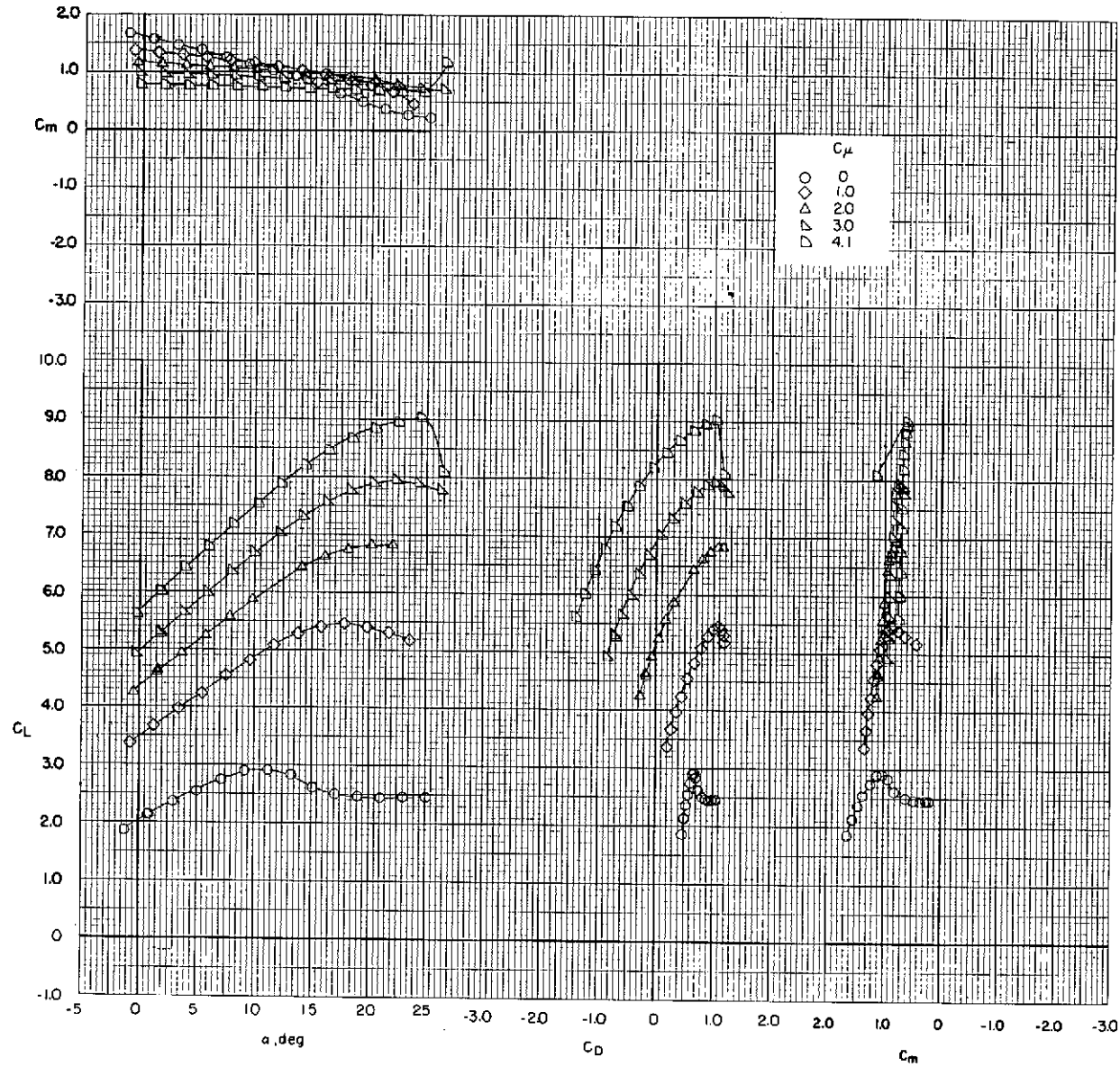

(b) $i_t = -5^o$; $\delta_e = -25^o$; $\delta_{sh} = -40^o$.

Figure 22.- Continued.

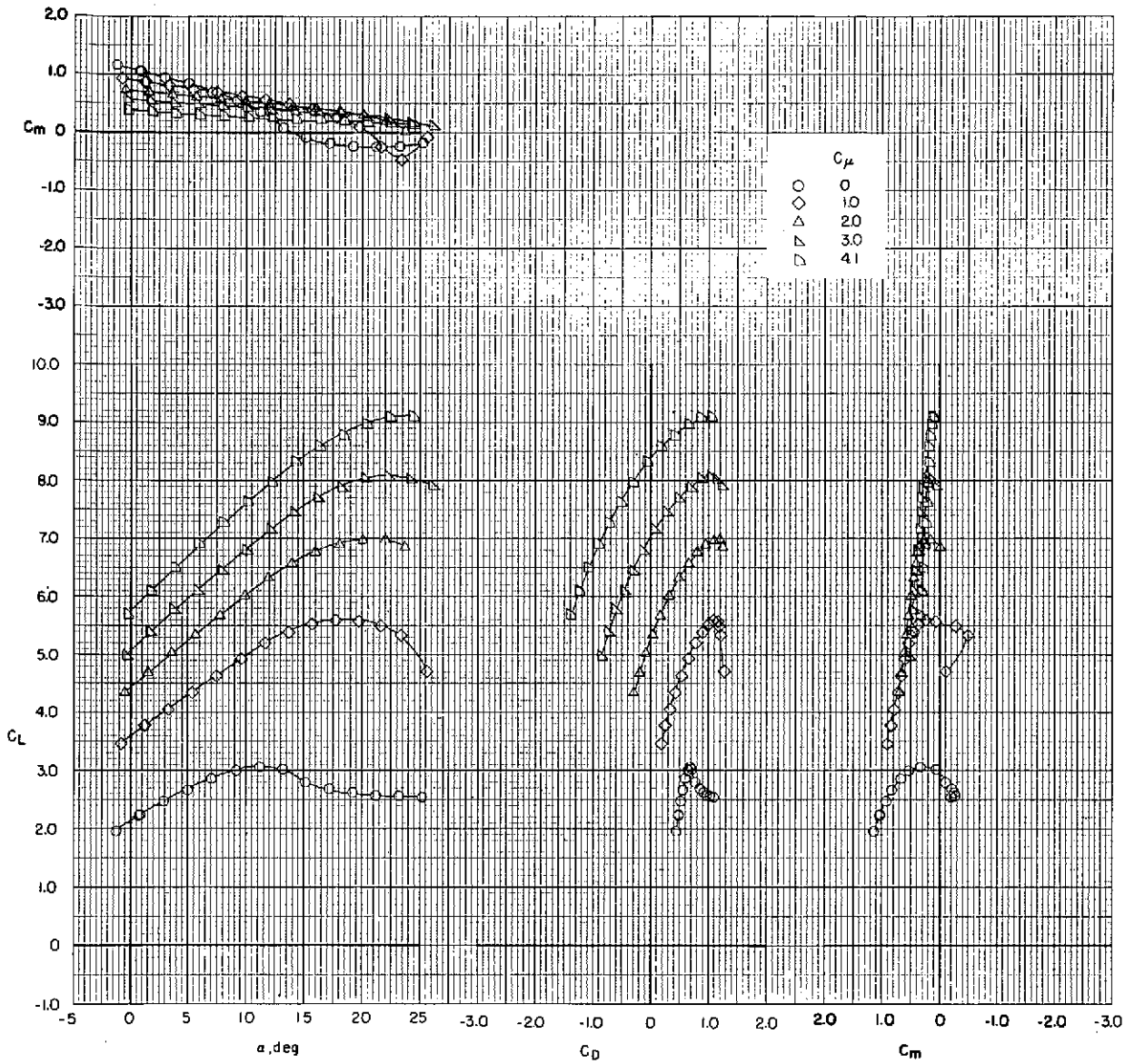

(c) $i_t = 0^o$; $\delta_e = -25^o$; $\delta_{sh} = -40^o$.

Figure 22.- Concluded.

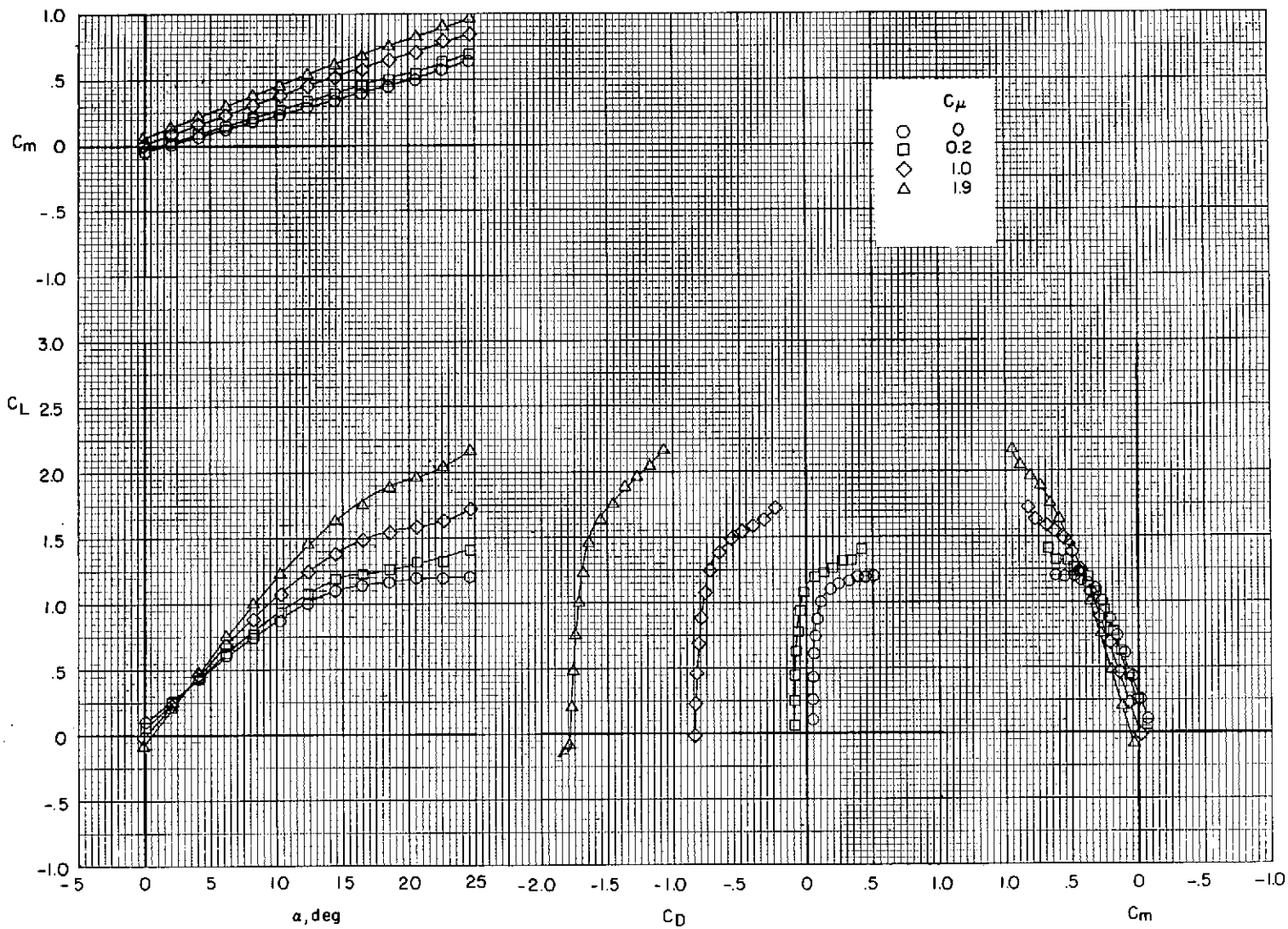

(a) Tail off.

Figure 23.- Effect of thrust coefficient on longitudinal aerodynamic characteristics. Bypass ratio 3.2; $\delta_f = 0^o$ (cruise); δ_{sw} = off.

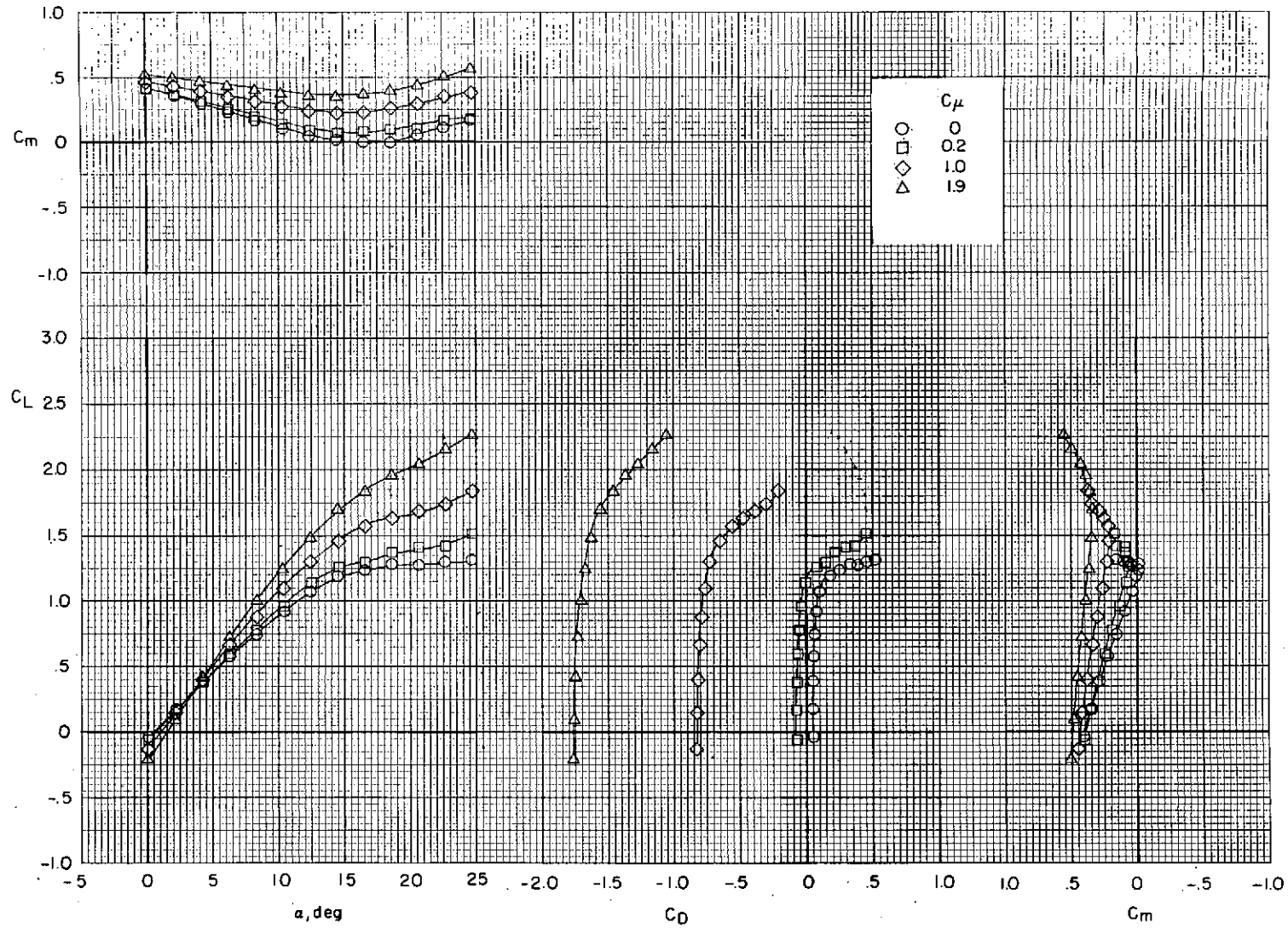

(b) $i_t = -5^o$; $\delta_e = 0^o$; δ_{sh} = off.

Figure 23.- Continued.

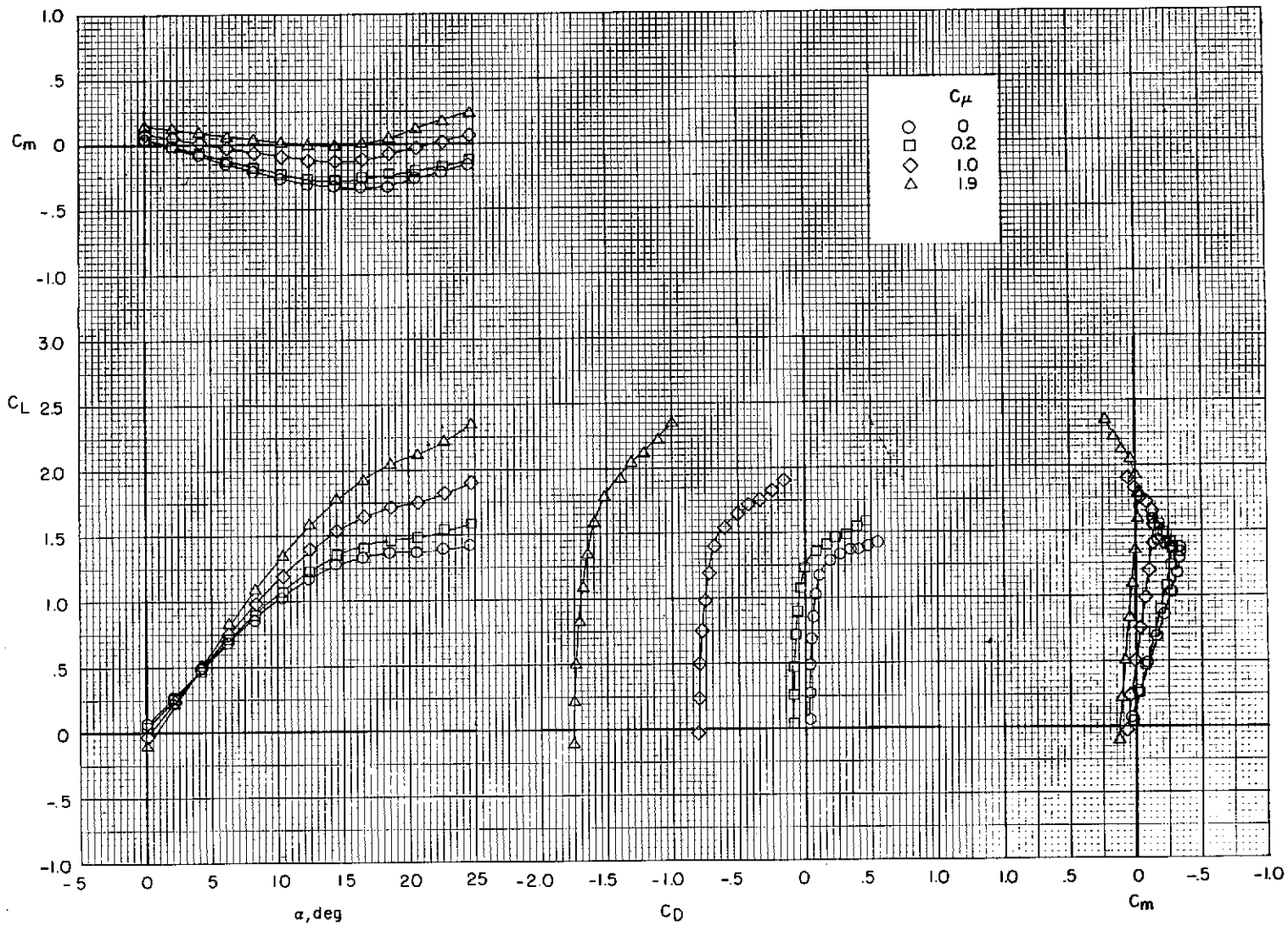

(c) $i_t = 0^o$; $\delta_e = 0^o$; δ_{sh} = off.

Figure 23.- Continued.

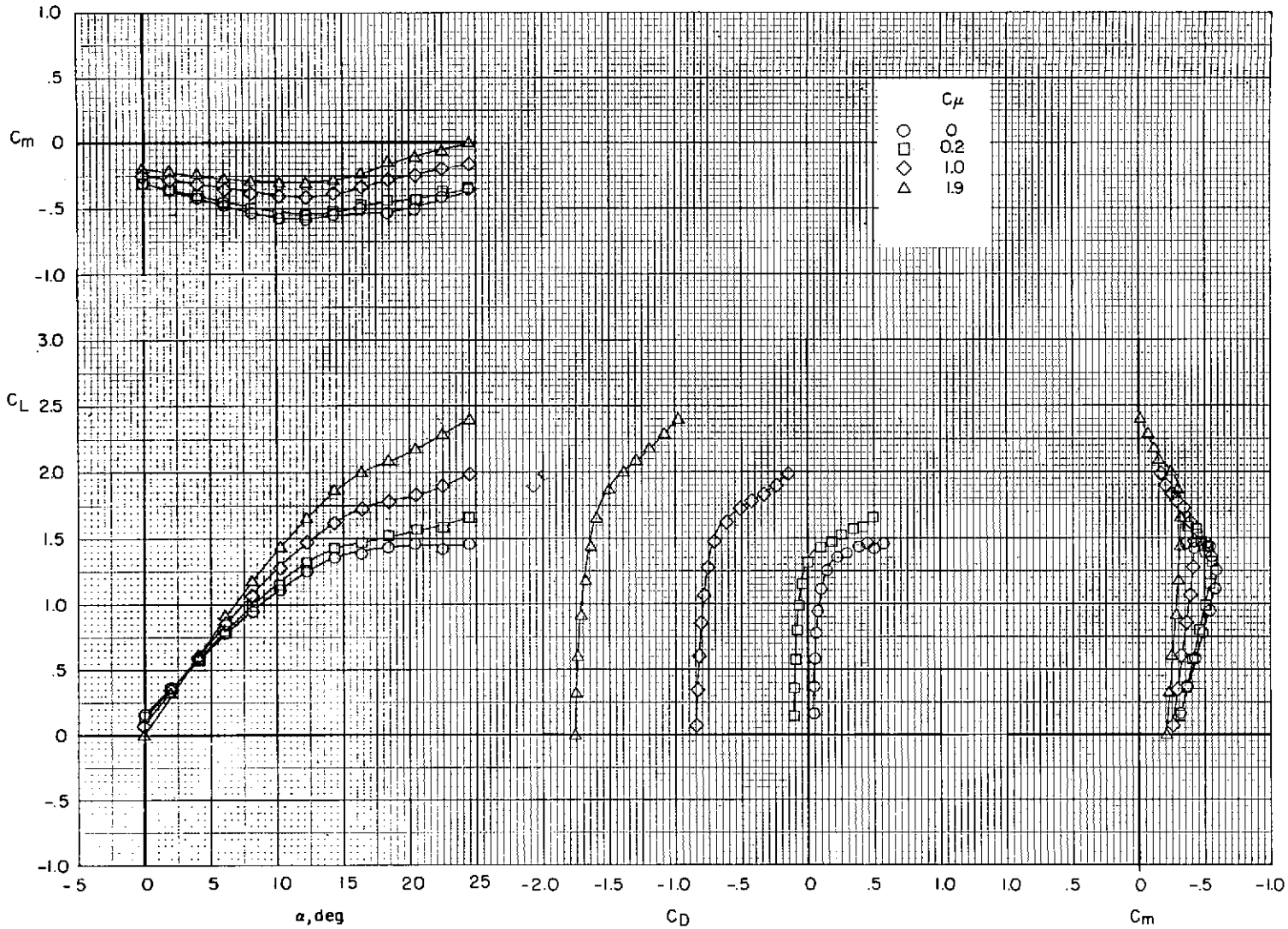

(d) $i_t = 5^o$; $\delta_e = 0^o$, δ_{sh} = off.

Figure 23.- Concluded.

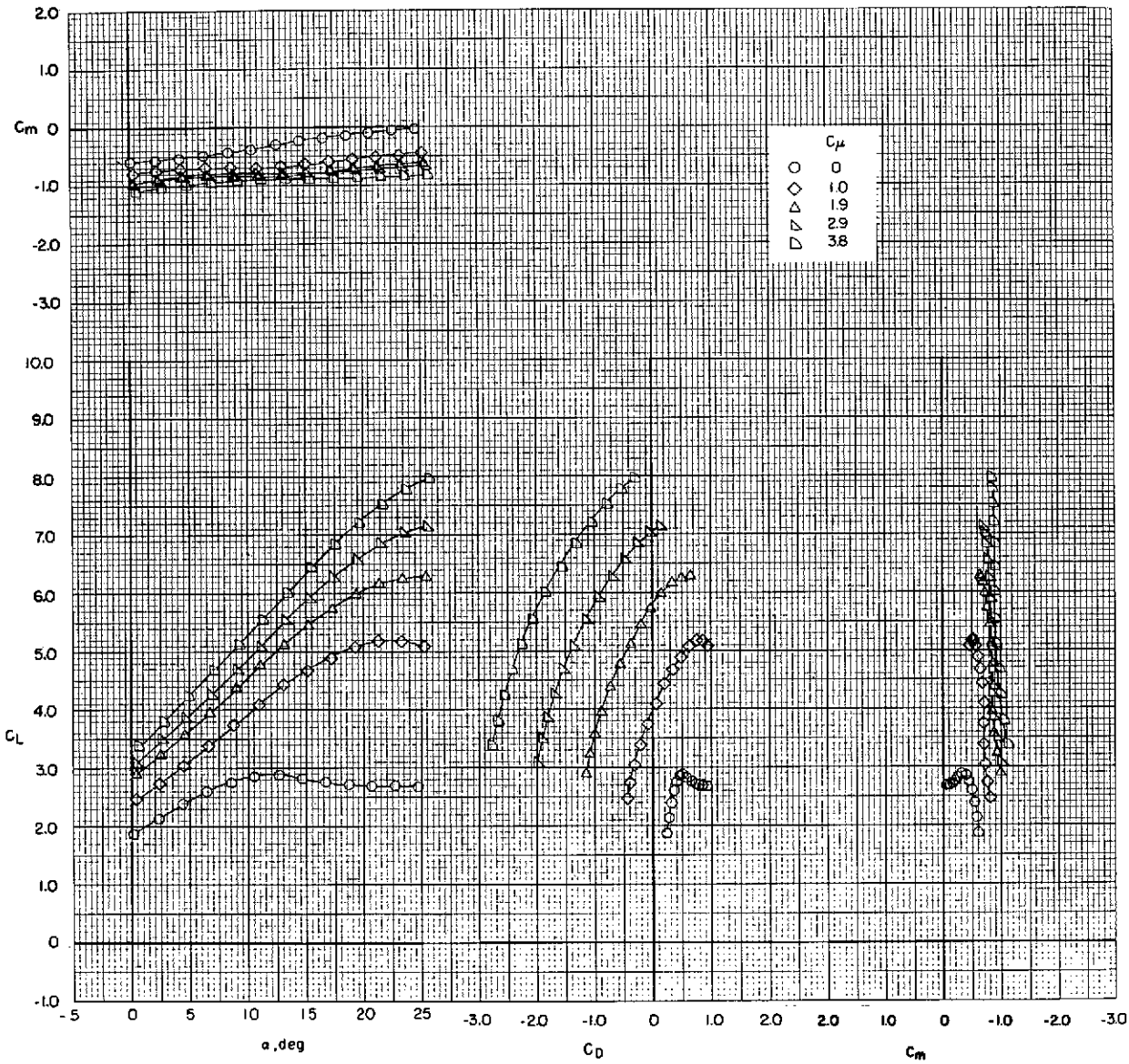

(a) Tail off.

Figure 24.- Effect of thrust coefficient on longitudinal aerodynamic characteristics. Bypass ratio 3.2; $\delta_f = 0^o/20^o/40^o$ (take-off); $\delta_{sw} = 50^o$.

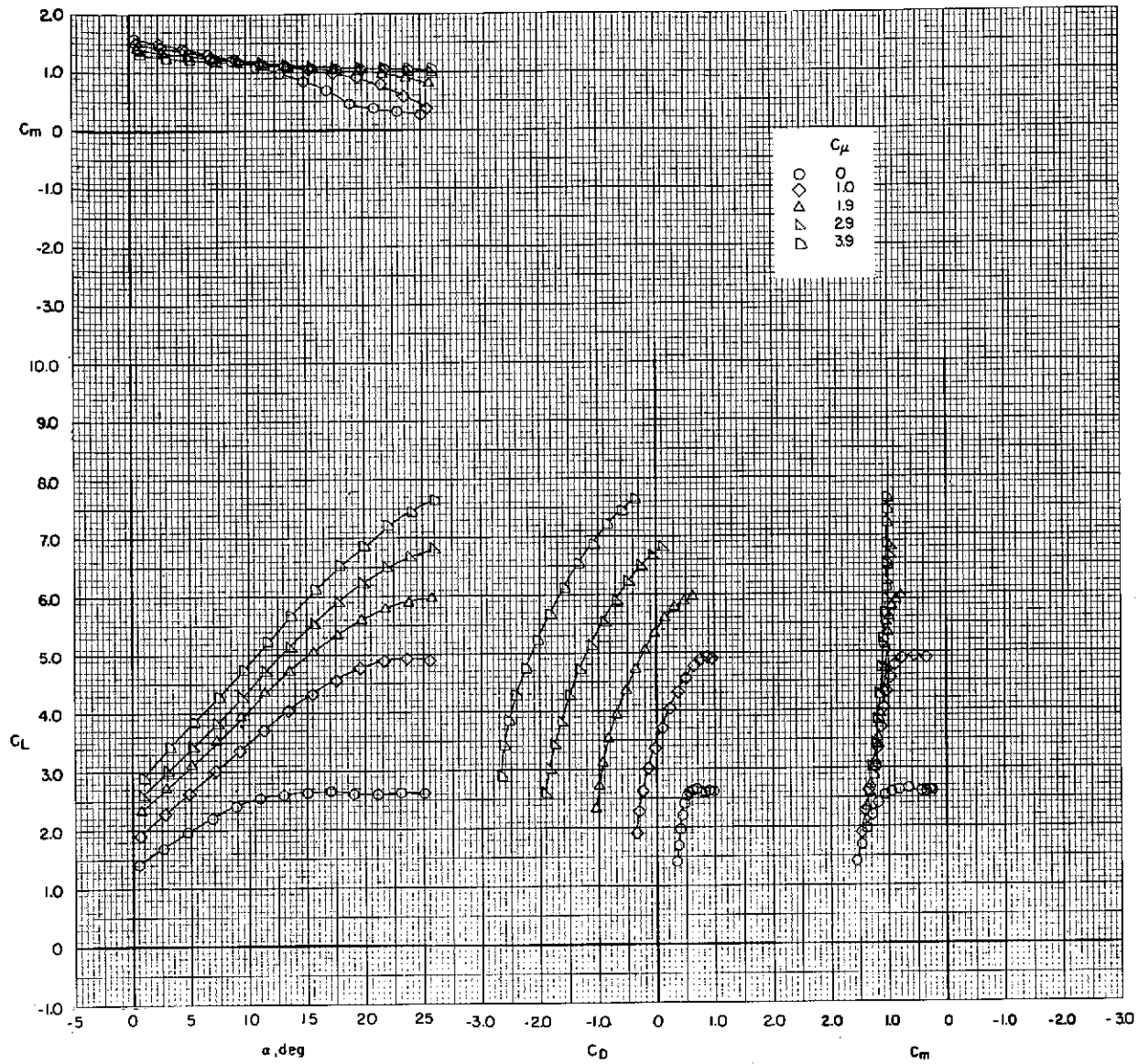

(b) $i_t = -5^o$; $\delta_e = -25^o$; $\delta_{sh} = -40^o$.

Figure 24.- Continued.

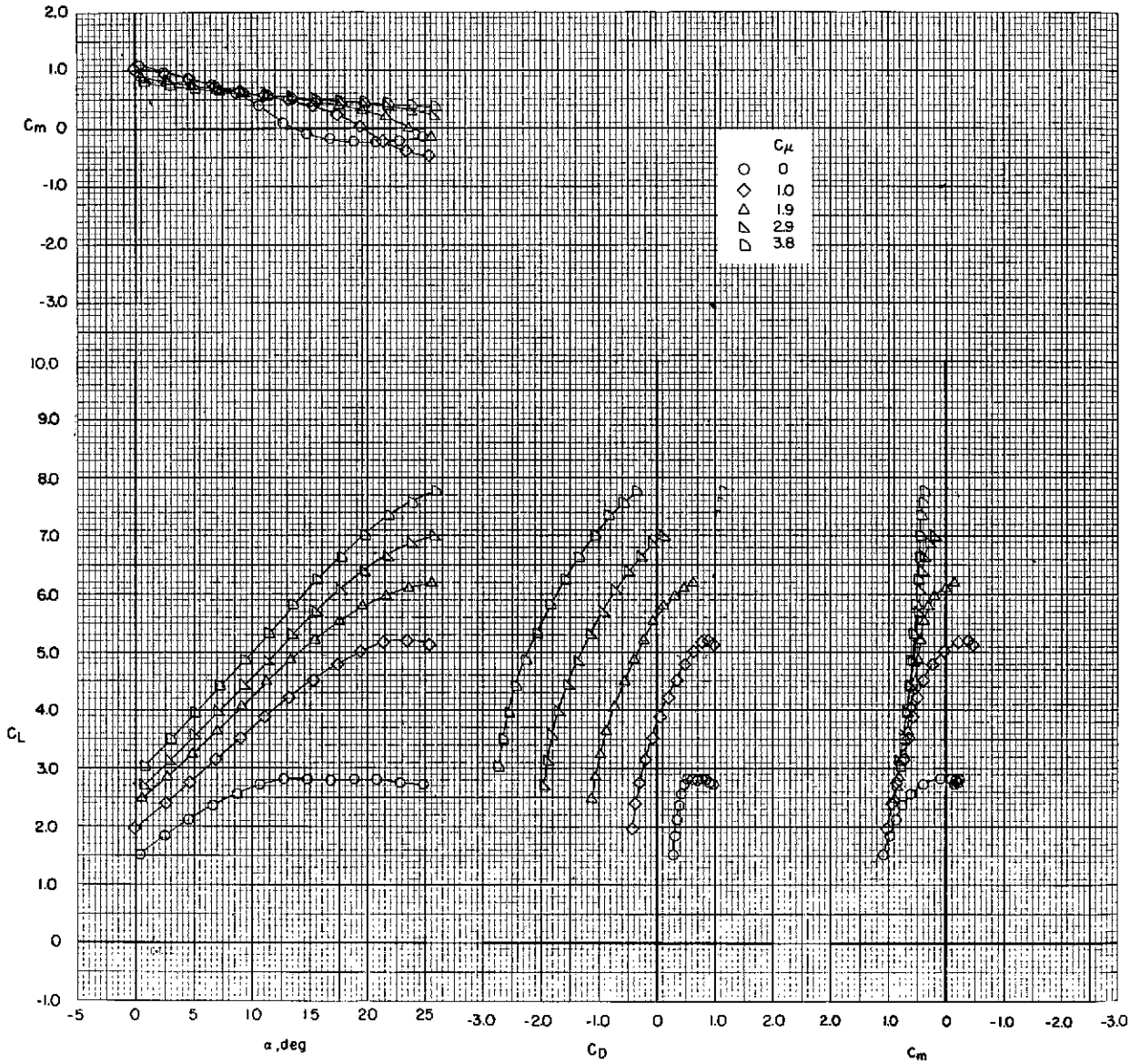

(c) $i_t = 0^o$; $\delta_e = -25^o$; $\delta_{sh} = -40^o$.

Figure 24.- Continued.

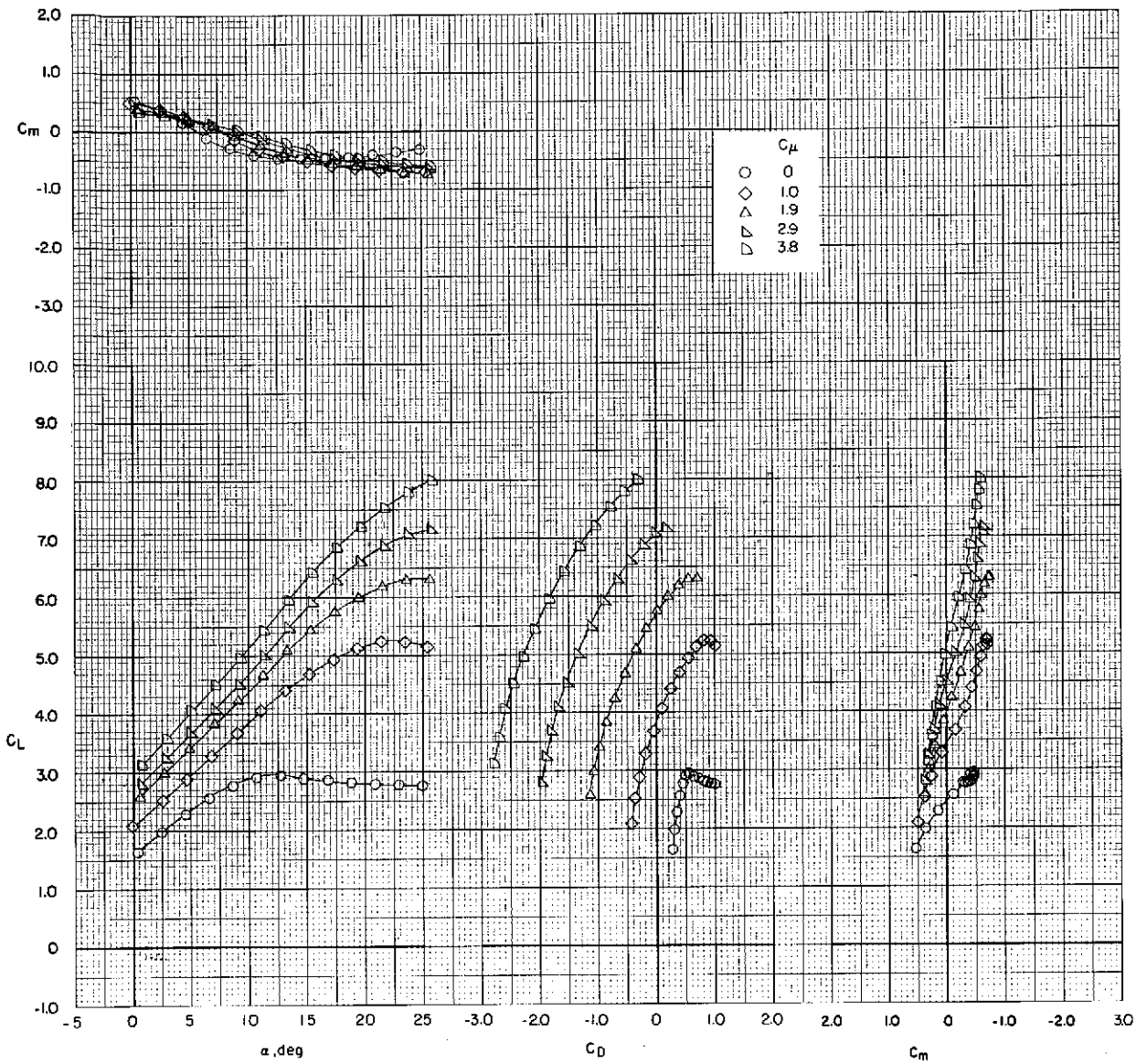

(d) $i_t = 5^o$; $\delta_e = -25^o$; $\delta_{sh} = -40^o$.

Figure 24.- Concluded.

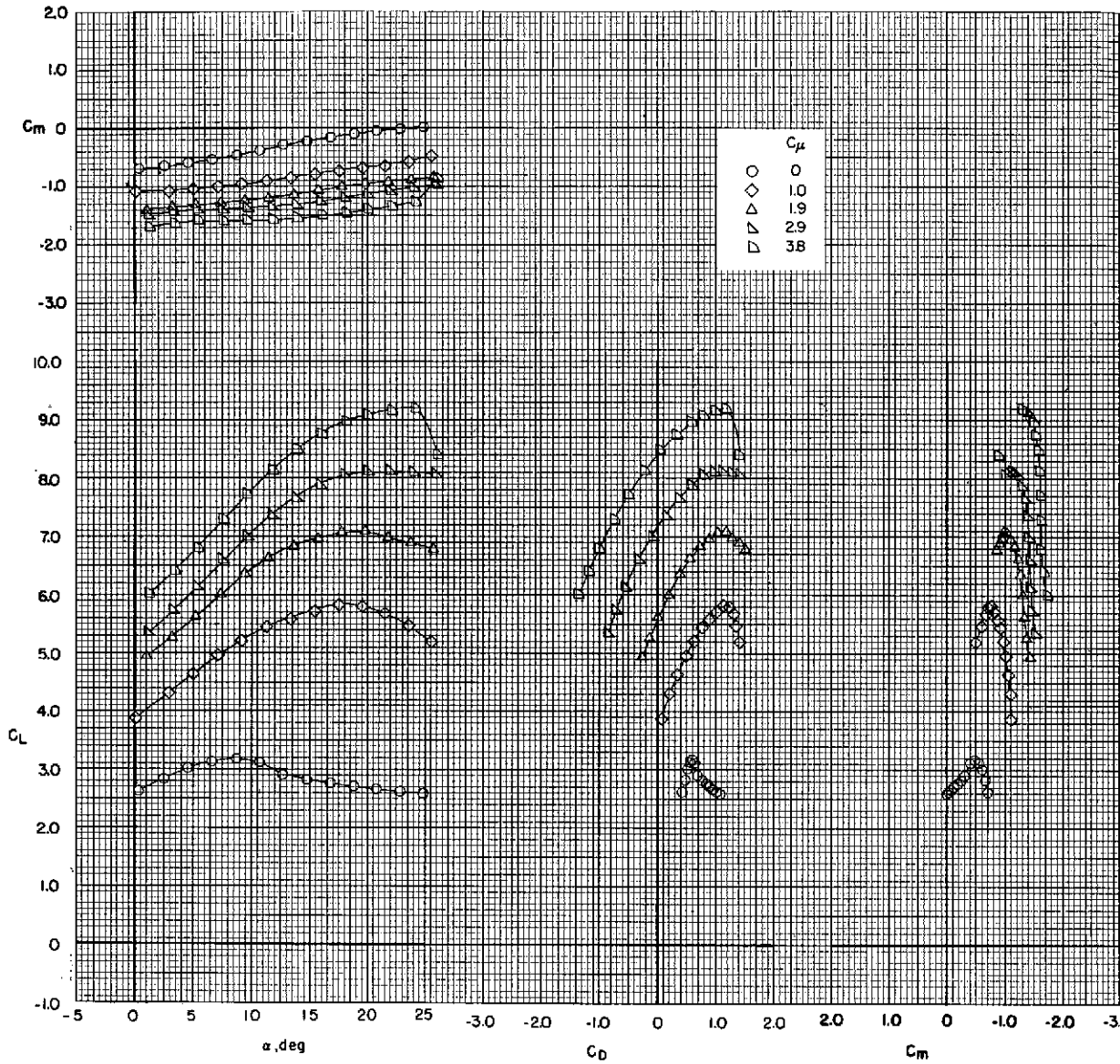

(a) Tail off.

Figure 25.- Effect of thrust coefficient on longitudinal aerodynamic characteristics. Bypass ratio 3.2; $\delta_f = 15^o/35^o/55^o$ (landing); $\delta_{sw} = 50^o$.

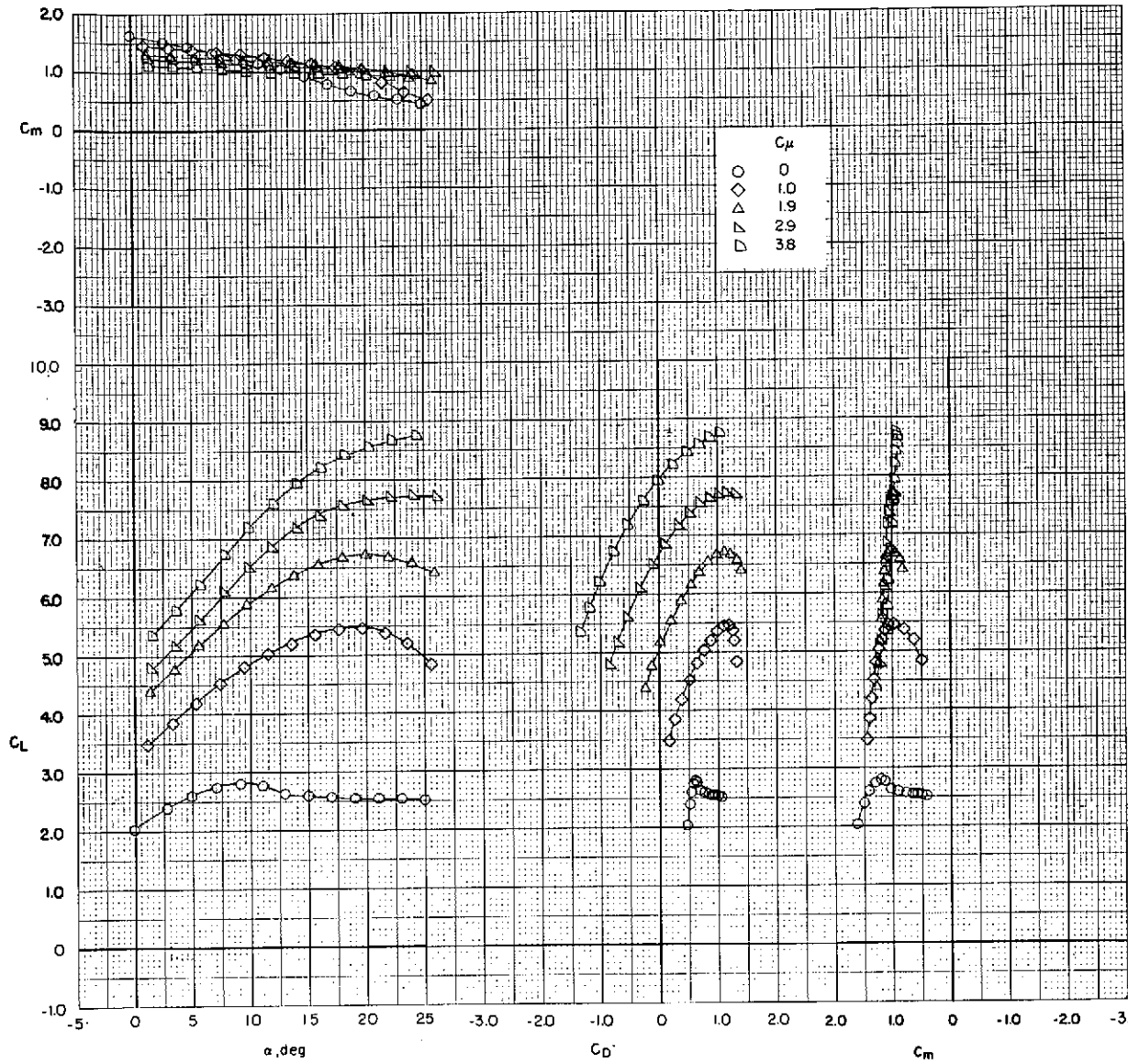

(b) $i_t = -5^o$; $\delta_e = -25^o$; $\delta_{sh} = -40^o$.

Figure 25.- Continued.

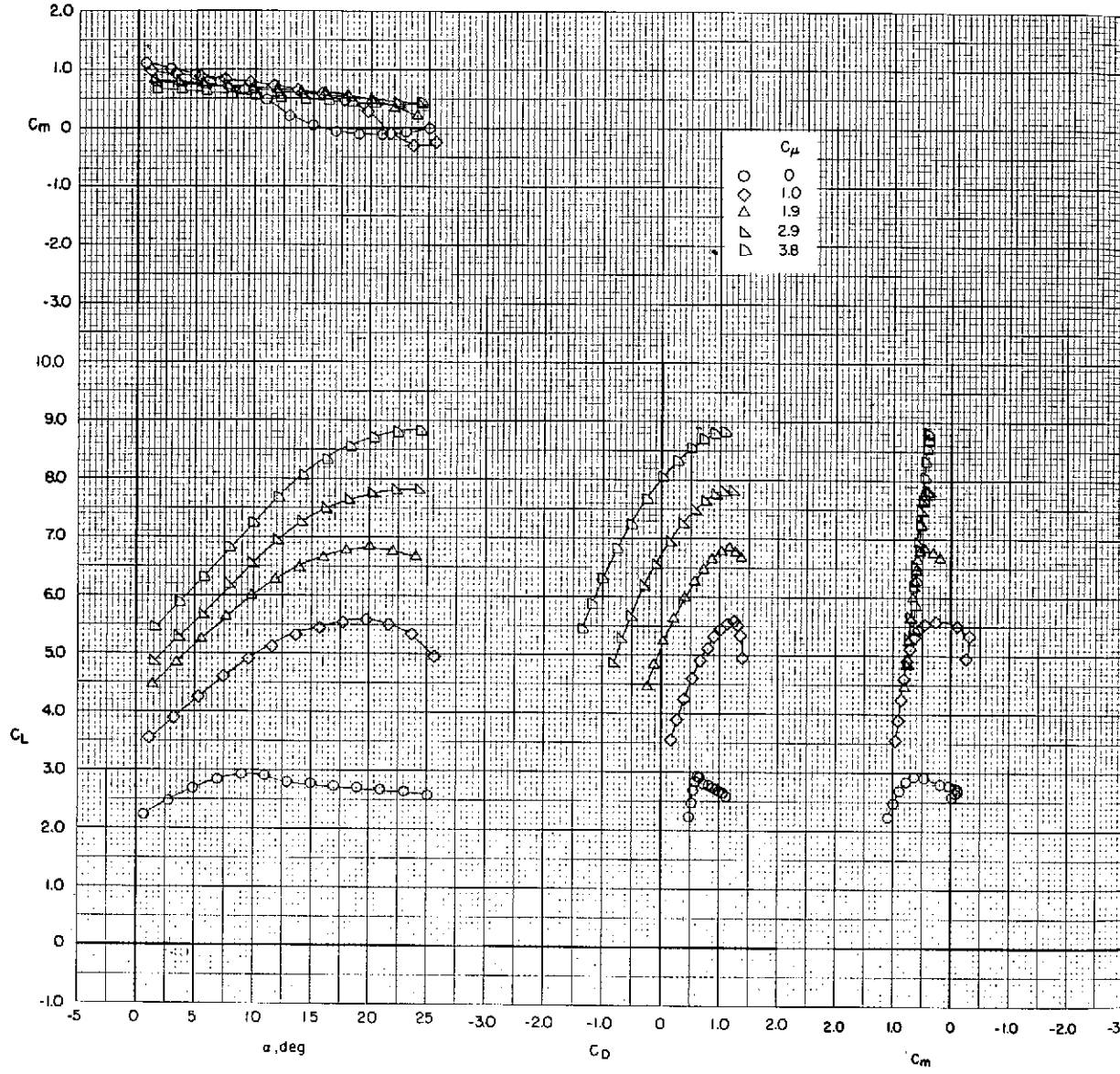

(c) $i_t = 0^o$; $\delta_e = -25^o$; $\delta_{sh} = -40^o$.

Figure 25.- Continued.

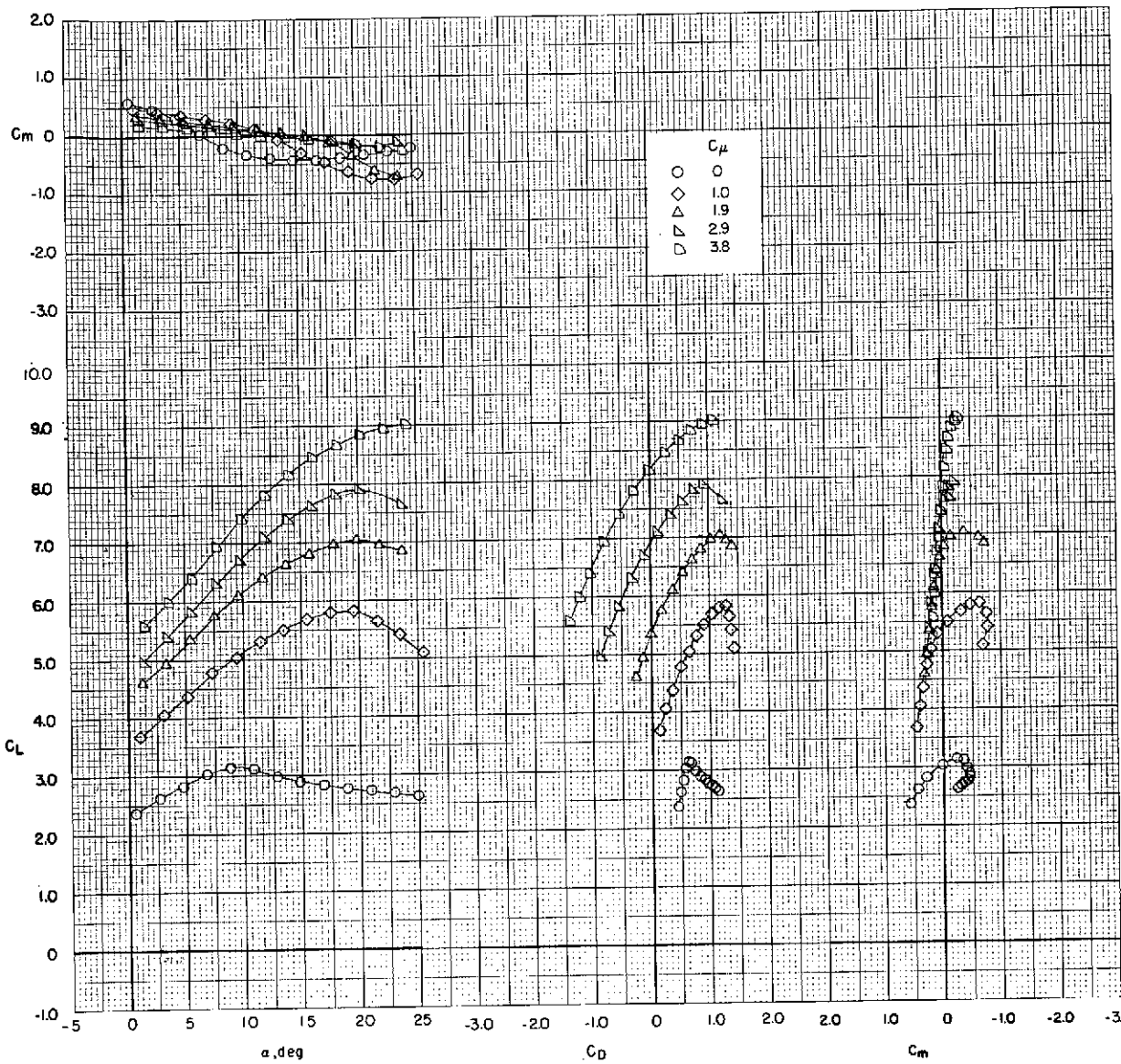

(d) $i_t = 5^o$; $\delta_e = -25^o$; $\delta_{sh} = -40^o$.

Figure 25.- Concluded.

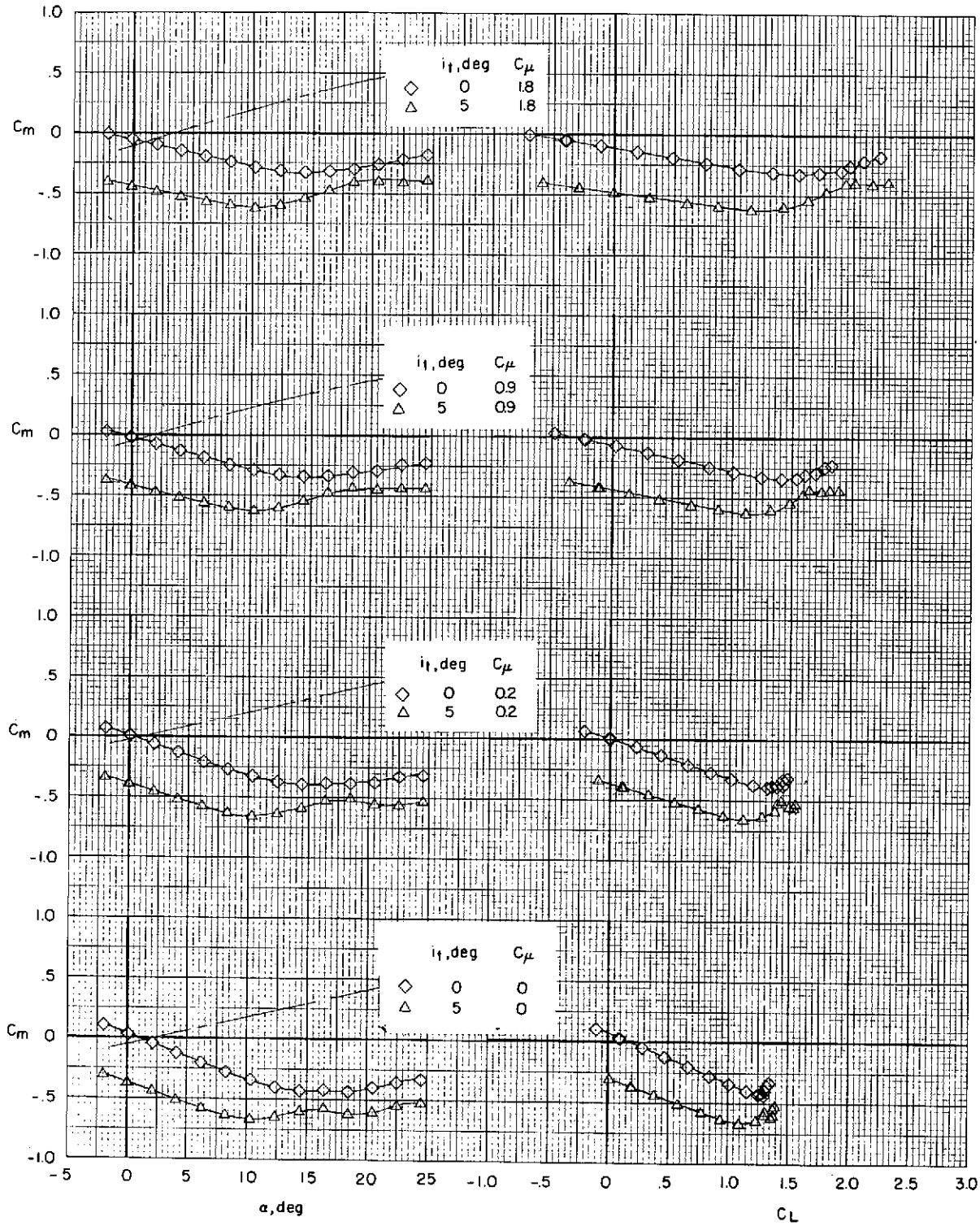

(a) $\delta_f = 0^o$ (cruise); δ_{sw} = off; $\delta_e = 0^o$; δ_{sh} = off.

Figure 26.- Effect of thrust coefficient and tail incidence on pitching-moment characteristics. Daisy nozzle.

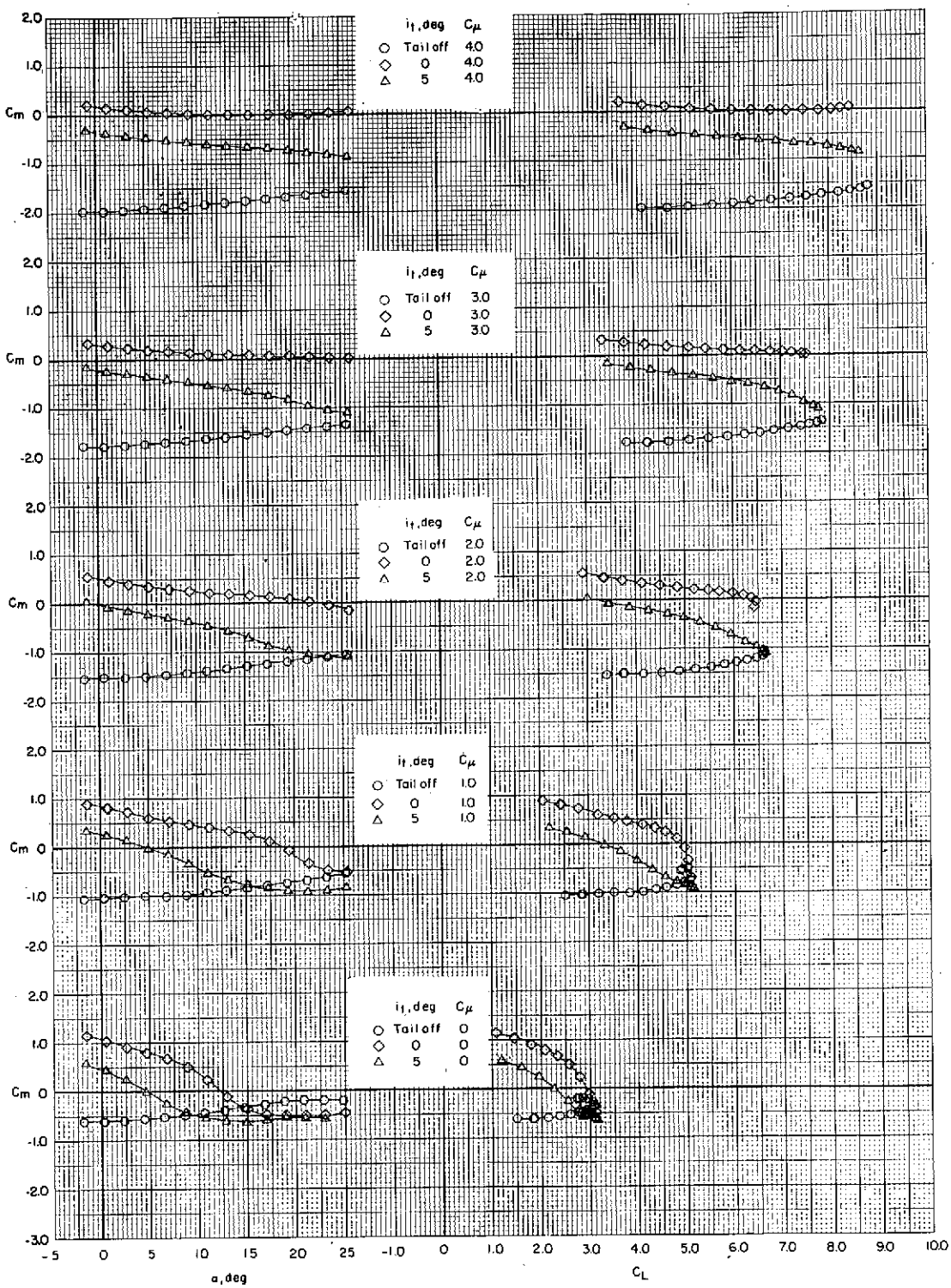

(b) $\delta_f = 0^o/20^o/40^o$ (take-off); $\delta_{sw} = 50^o$; $\delta_e = -25^o$; $\delta_{sh} = -40^o$.

Figure 26.- Continued.

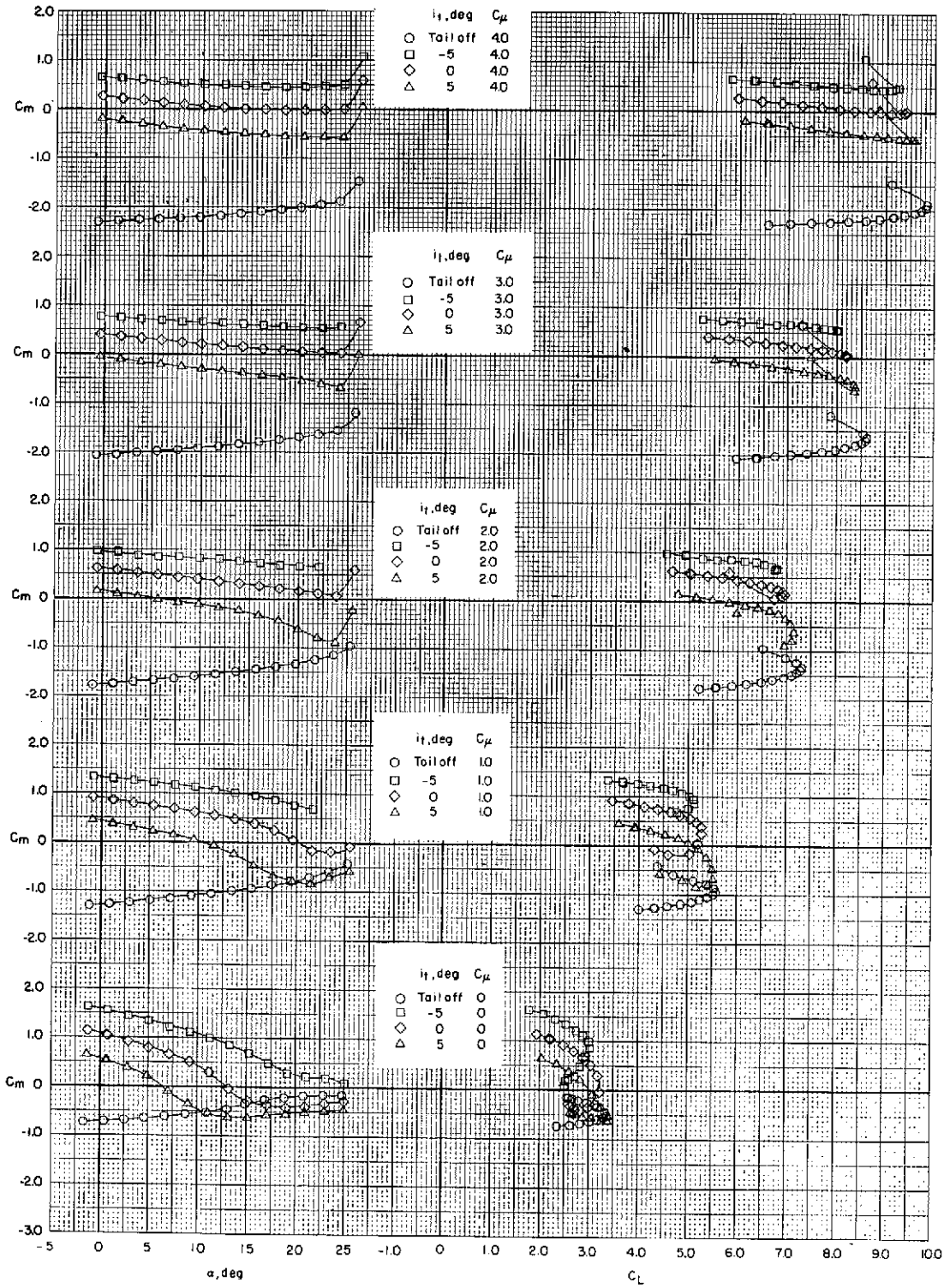

(c) $\delta_f = 15^o/35^o/55^o$ (landing); $\delta_{sw} = 50^o$; $\delta_e = -25^o$; $\delta_{sh} = -40^o$.

Figure 26.- Concluded.

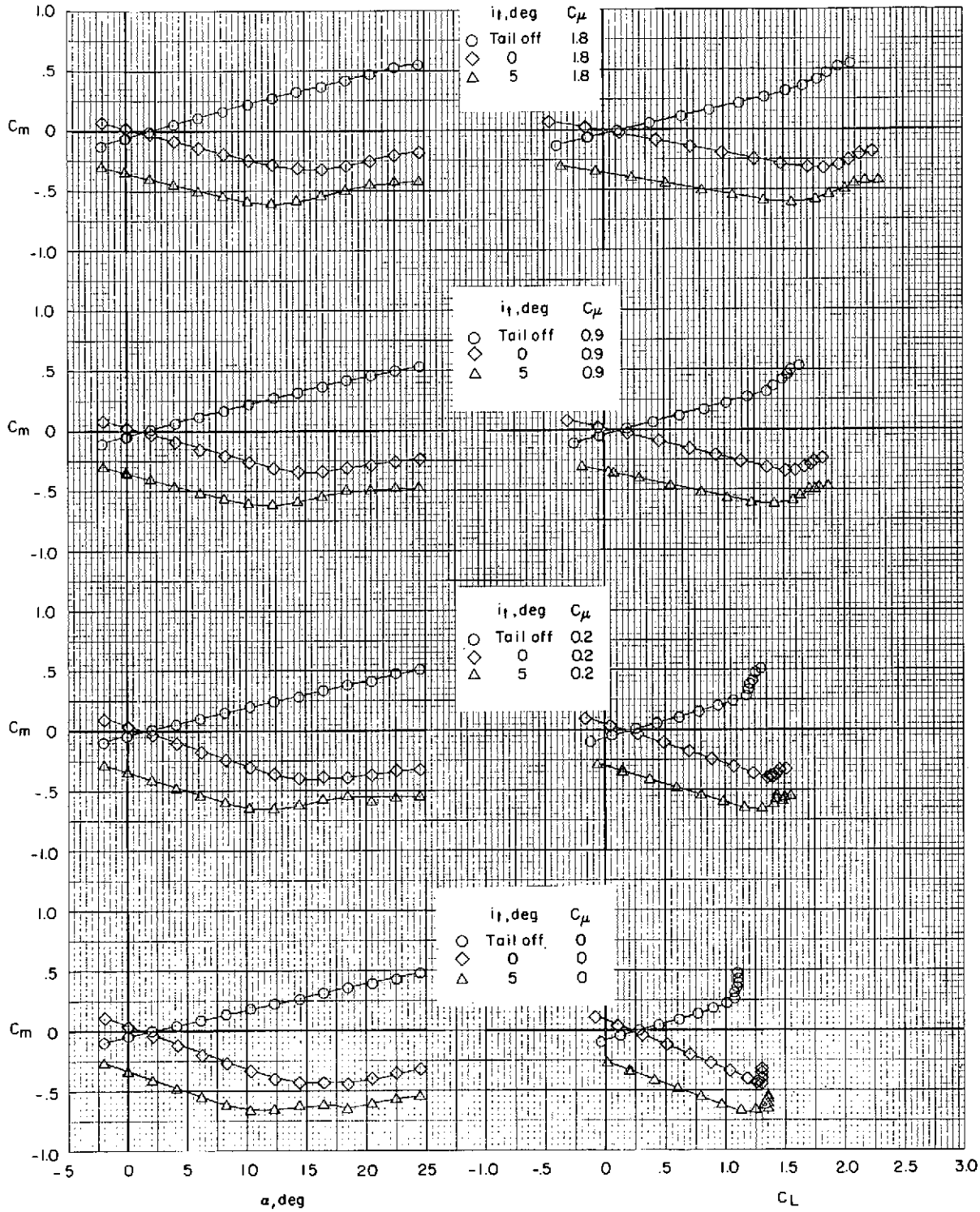

(a) $\delta_f = 0^o$ (cruise); δ_{sw} = off; $\delta_e = 0^o$; δ_{sh} = off.

Figure 27.- Effect of thrust coefficient and tail incidence on pitching-moment characteristics. Bypass ratio 6.2.

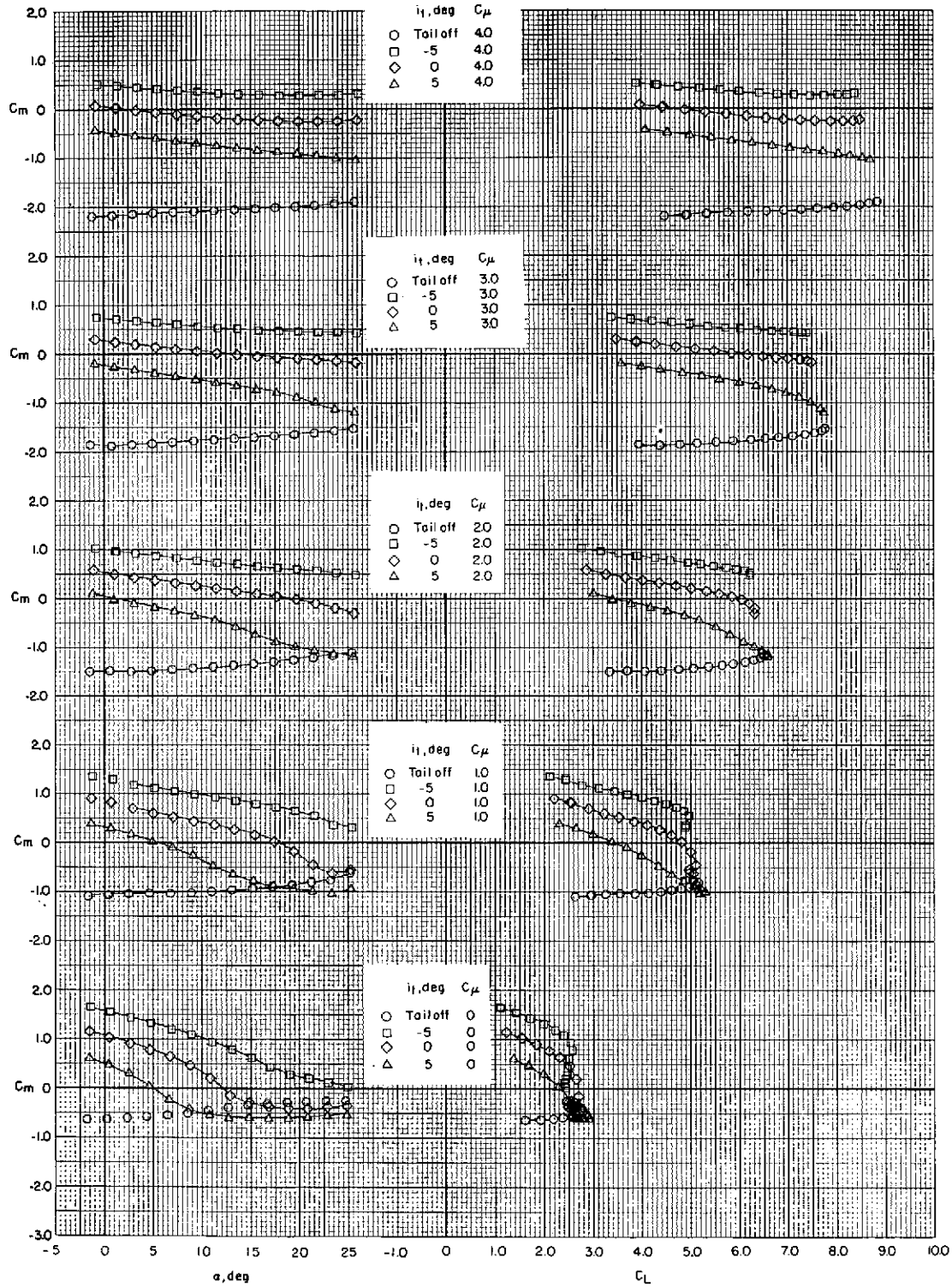

(b) $\delta_f = 0^o/20^o/40^o$ (take-off); $\delta_{sw} = 50^o$; $\delta_e = -25^o$; $\delta_{sh} = -40^o$.

Figure 27.- Continued.

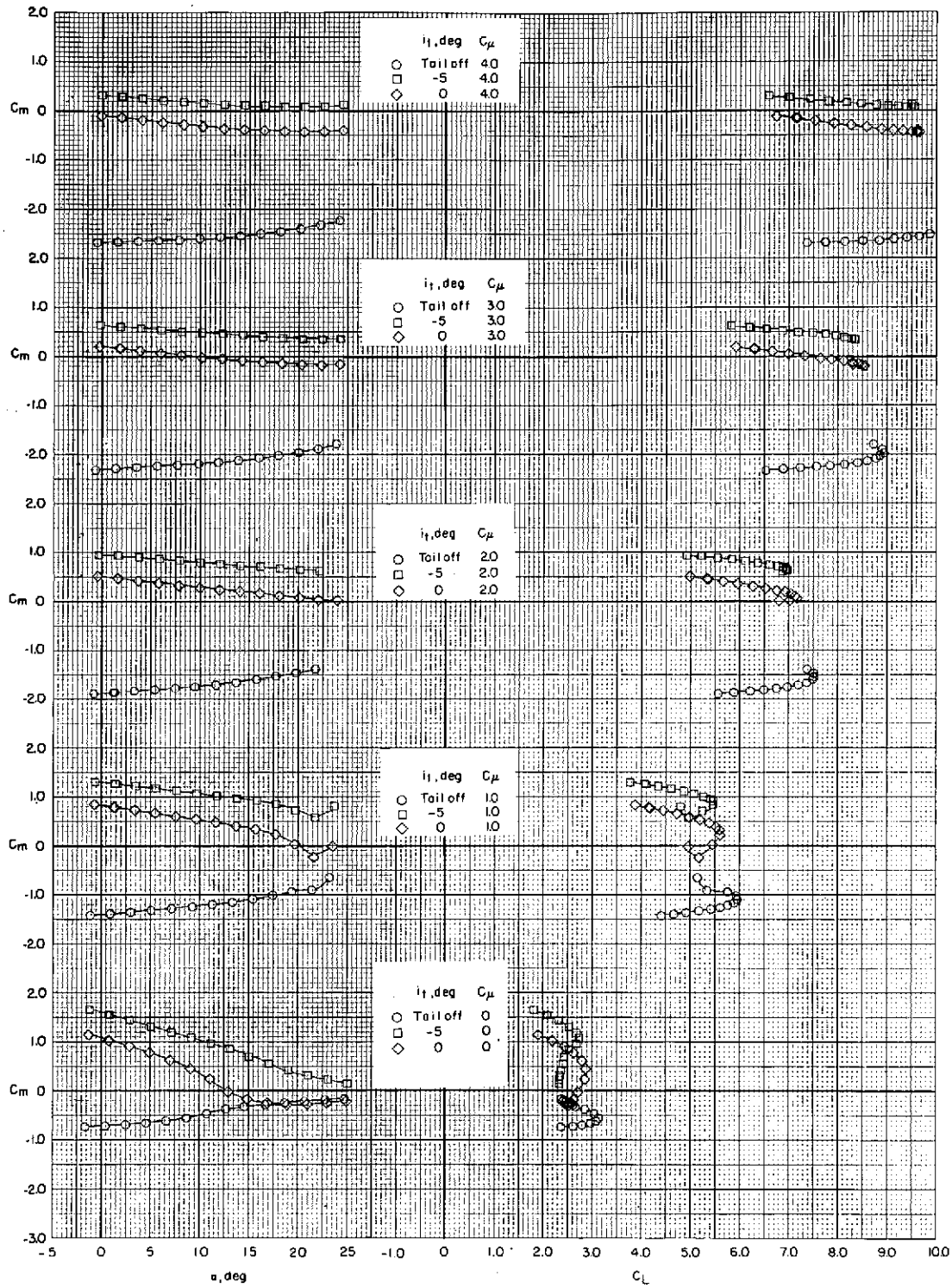

(c) $\delta_f = 15^o/35^o/55^o$ (landing); $\delta_{sw} = 50^o$; $\delta_e = -25^o$; $\delta_{sh} = -40^o$.

Figure 27.- Concluded.

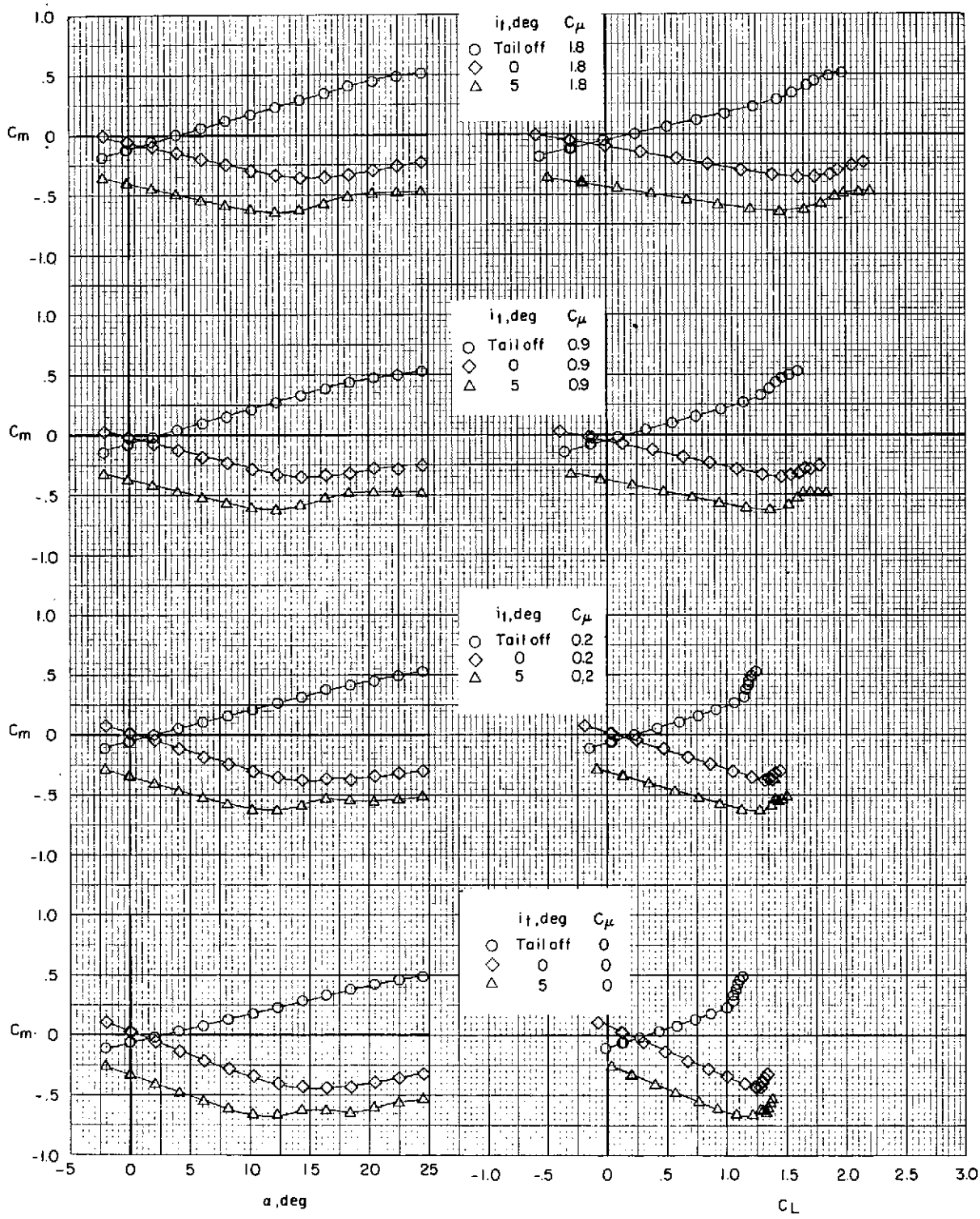

(a) $\delta_f = 0^o$ (cruise); δ_{sw} = off; $\delta_e = 0^o$; δ_{sh} = off.

Figure 28.- Effect of thrust coefficient and tail incidence on pitching-moment characteristics. Modified bypass ratio 6.2.

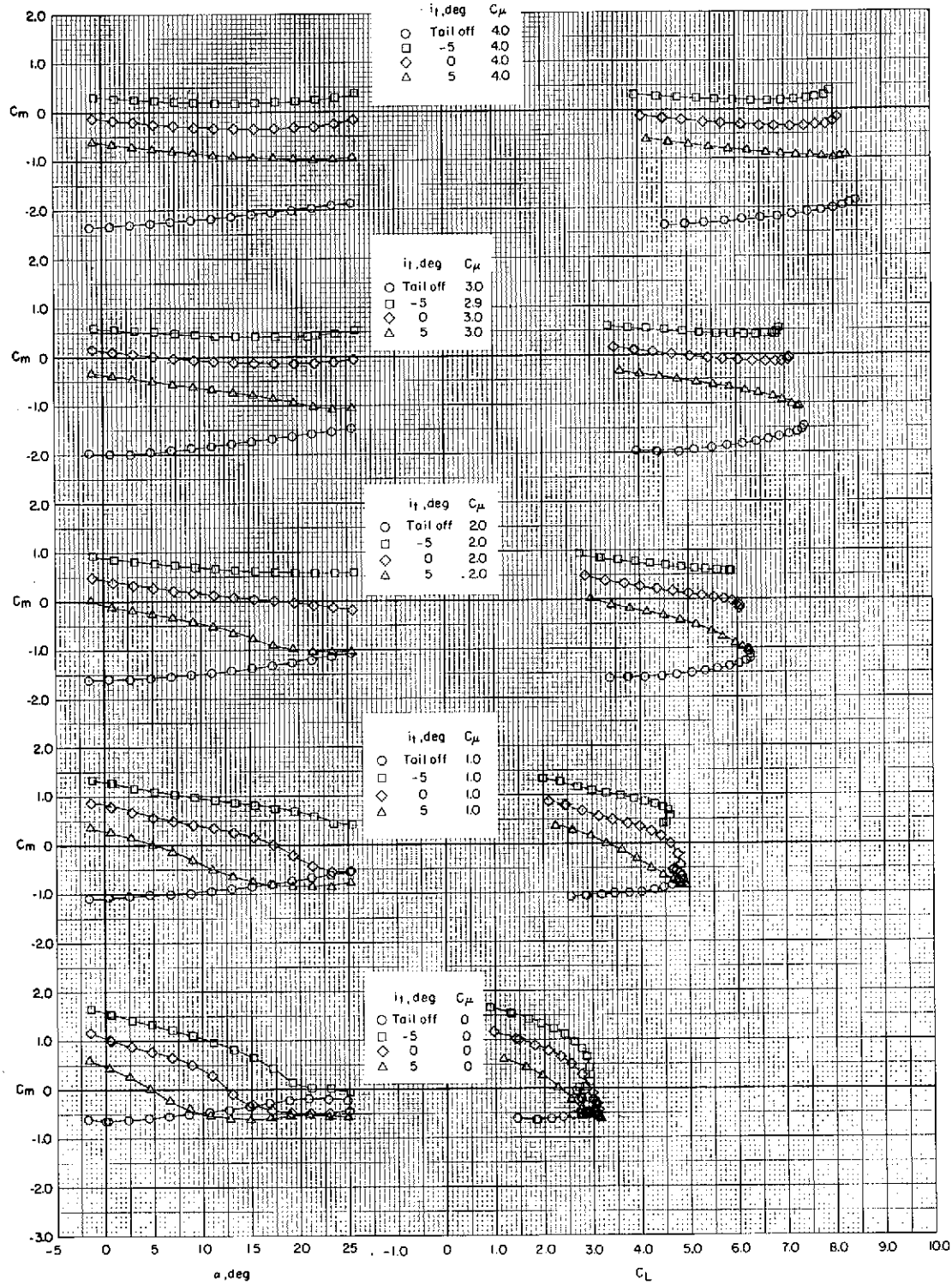

(b) $\delta_f = 0^o/20^o/40^o$ (take-off); $\delta_{sw} = 50^o$; $\delta_e = -25^o$; $\delta_{sh} = -40^o$.

Figure 28.- Continued.

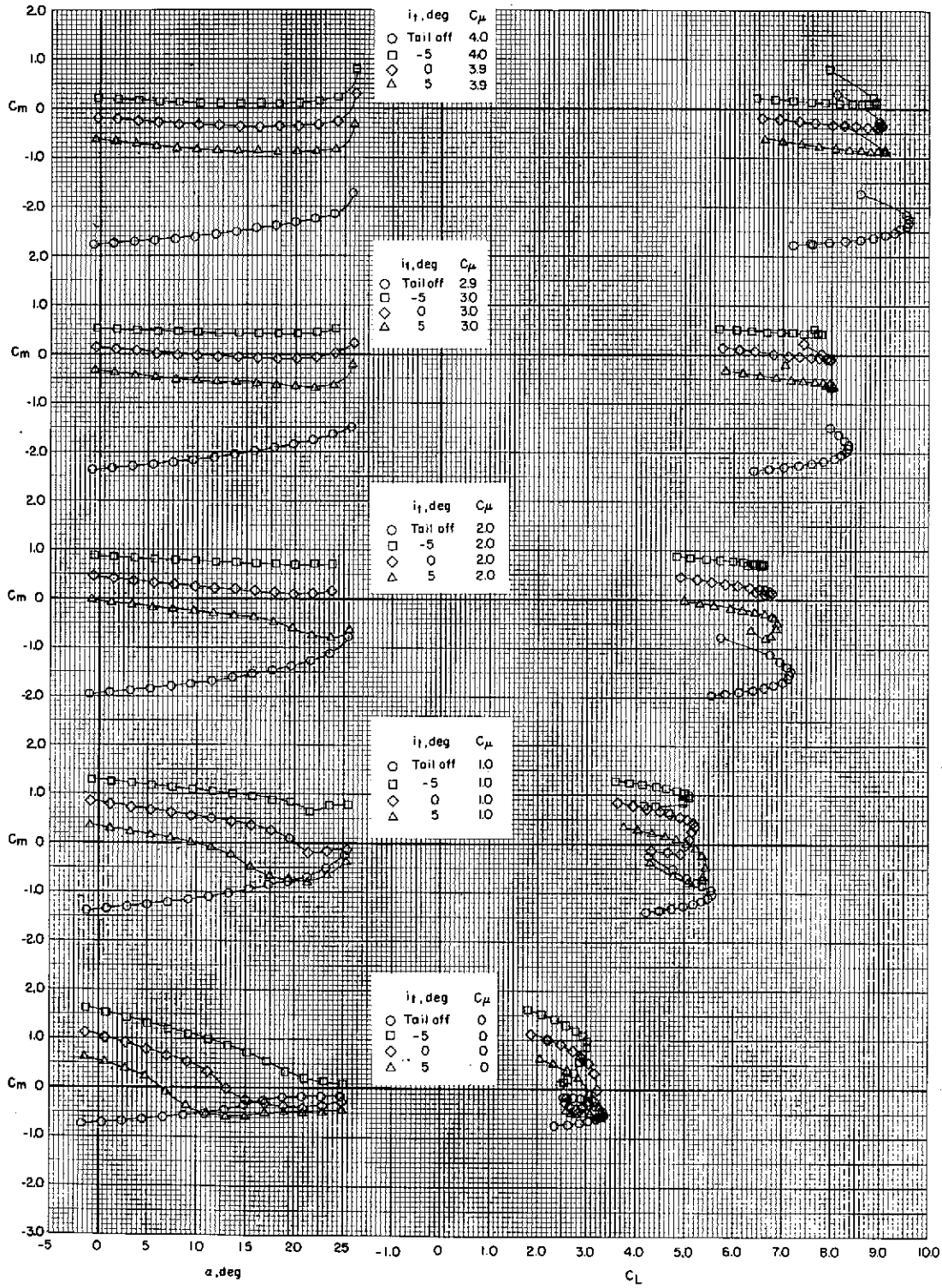

(c) $\delta_f = 15^o/35^o/55^o$ (landing); $\delta_{sw} = 50^o$; $\delta_e = -25^o$; $\delta_{sh} = -40^o$.

Figure 28.- Concluded.

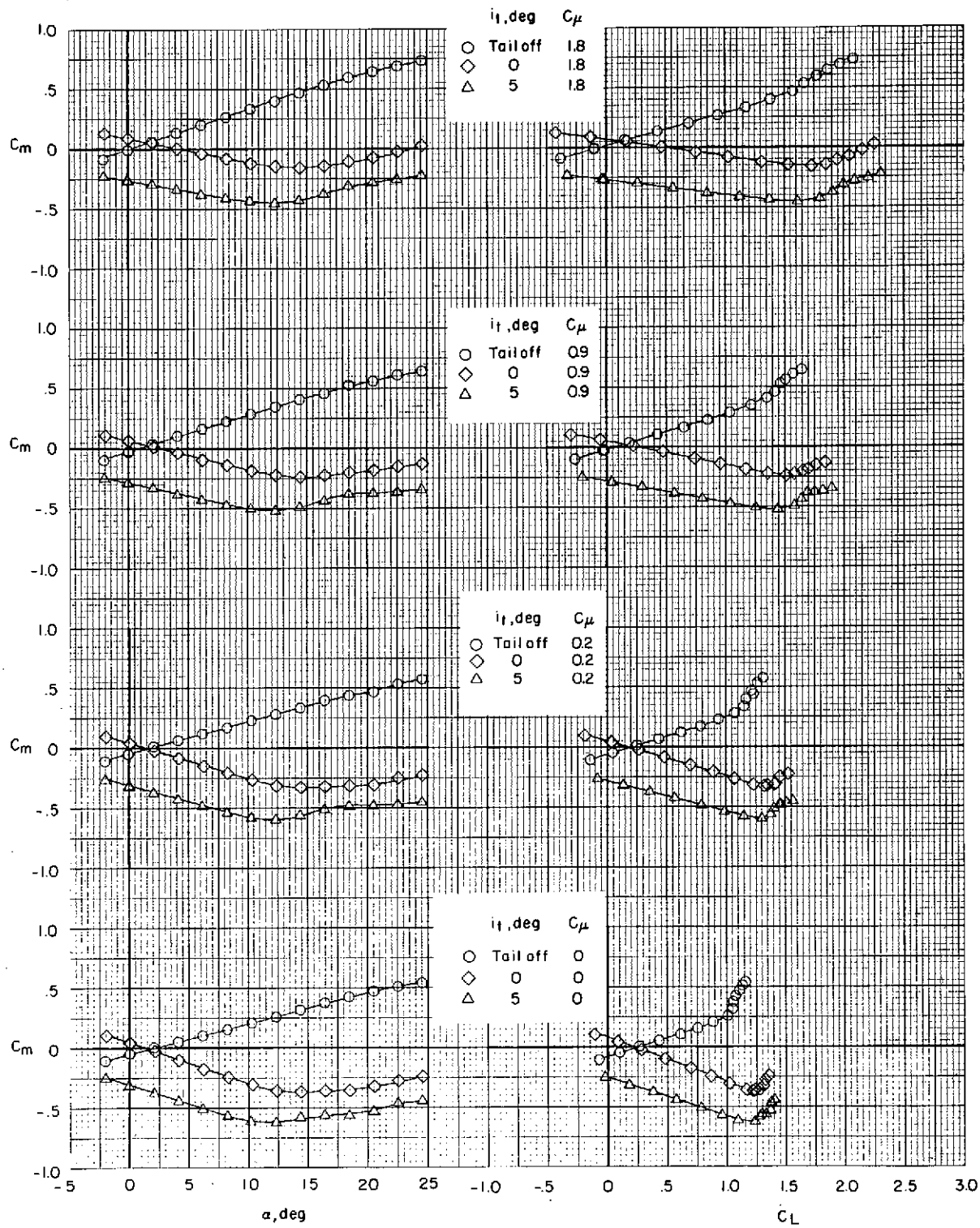

(a) $\delta_f = 0^o$ (cruise); δ_{sw} = off; $\delta_e = 0^o$; δ_{sh} = off.

Figure 29.- Effect of thrust coefficient and tail incidence on pitching-moment characteristics. Bypass ratio 10.0.

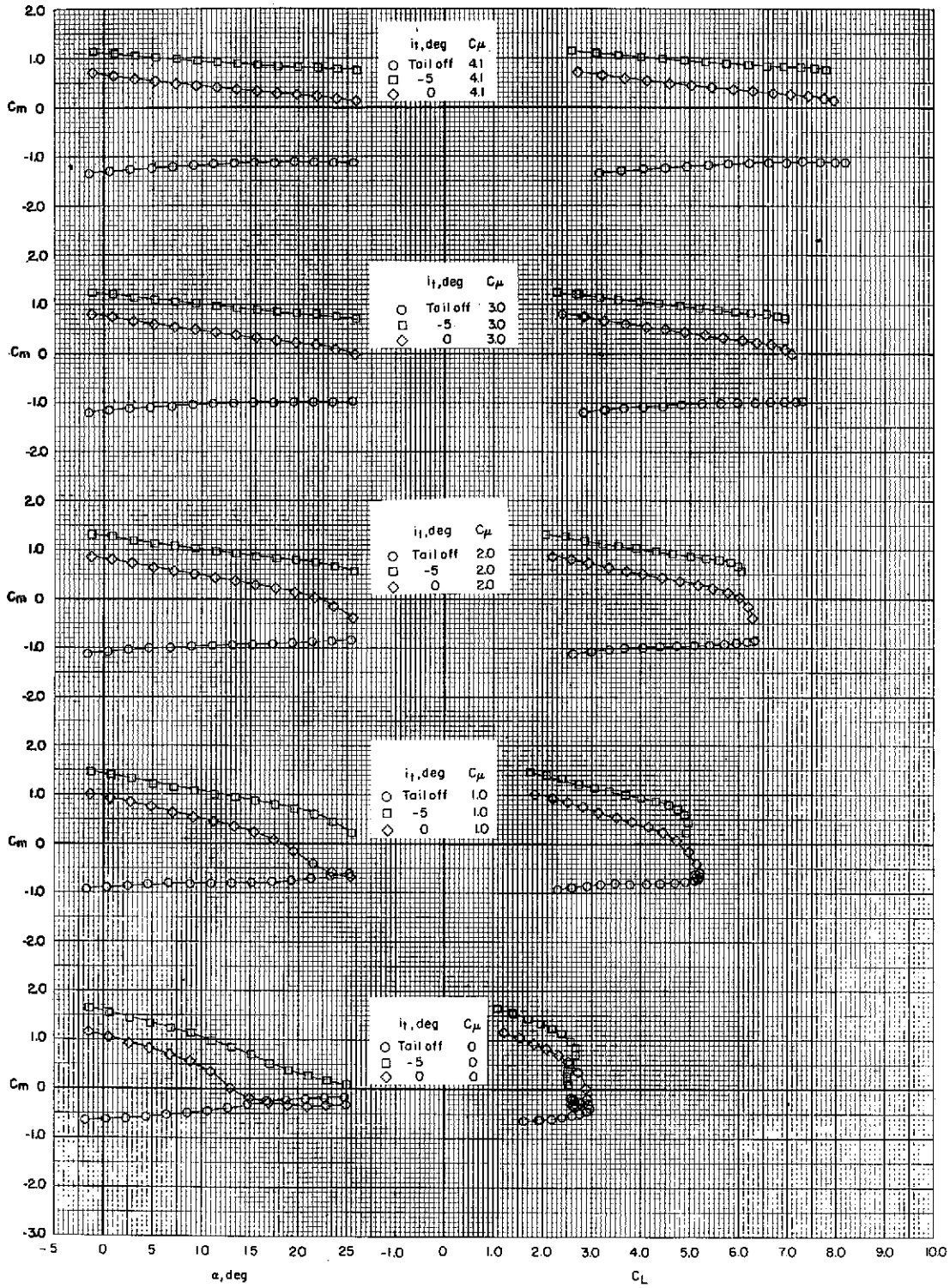

(b) $\delta_f = 0^o/20^o/40^o$ (take-off); $\delta_{sw} = 50^o$; $\delta_e = -25^o$; $\delta_{sh} = -40^o$.

Figure 29.- Continued.

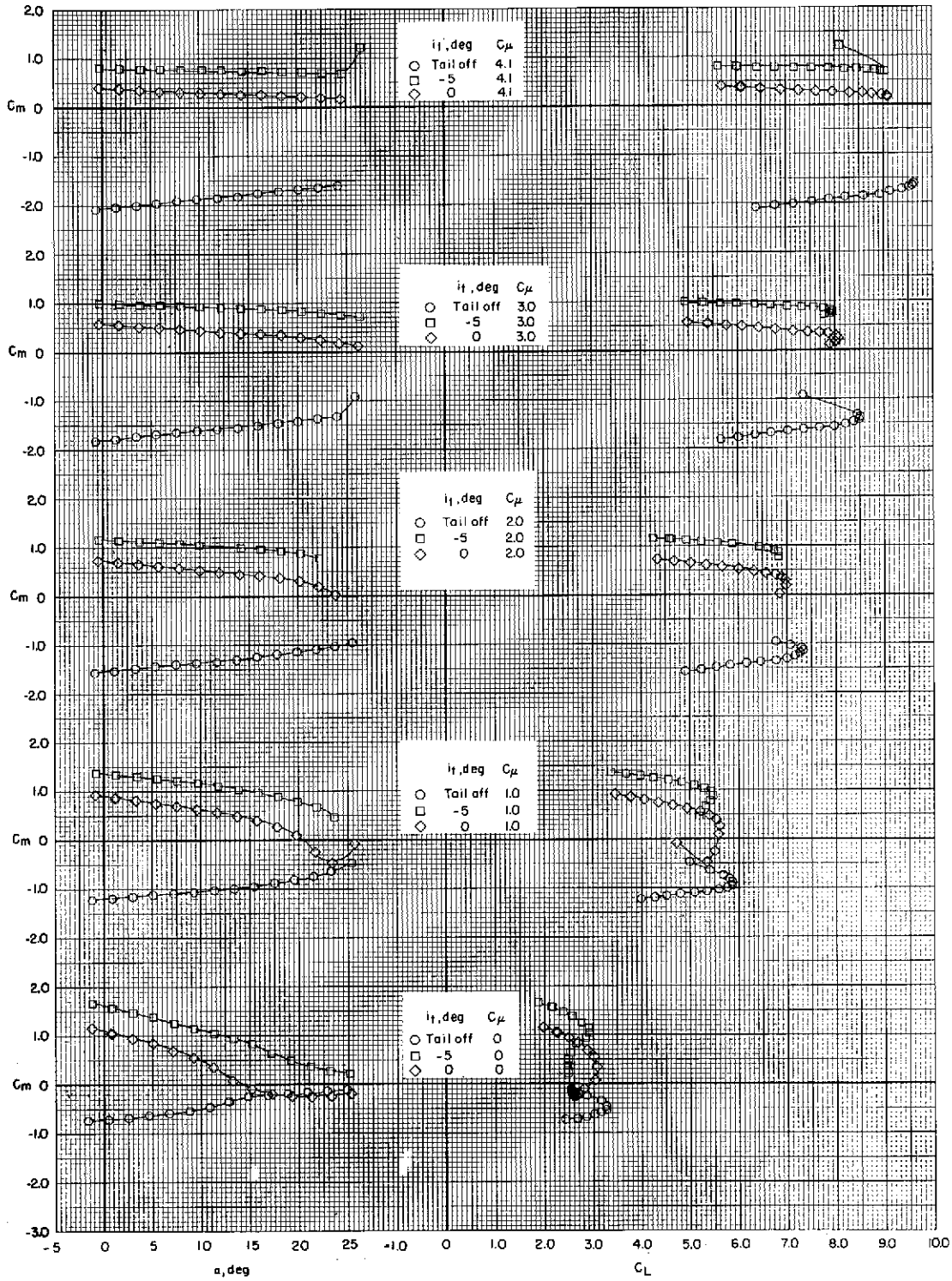

(c) $\delta_f = 15^o/35^o/55^o$ (landing); $\delta_{sw} = 50^o$; $\delta_e = -25^o$; $\delta_{sh} = -40^o$.

Figure 29.- Concluded.

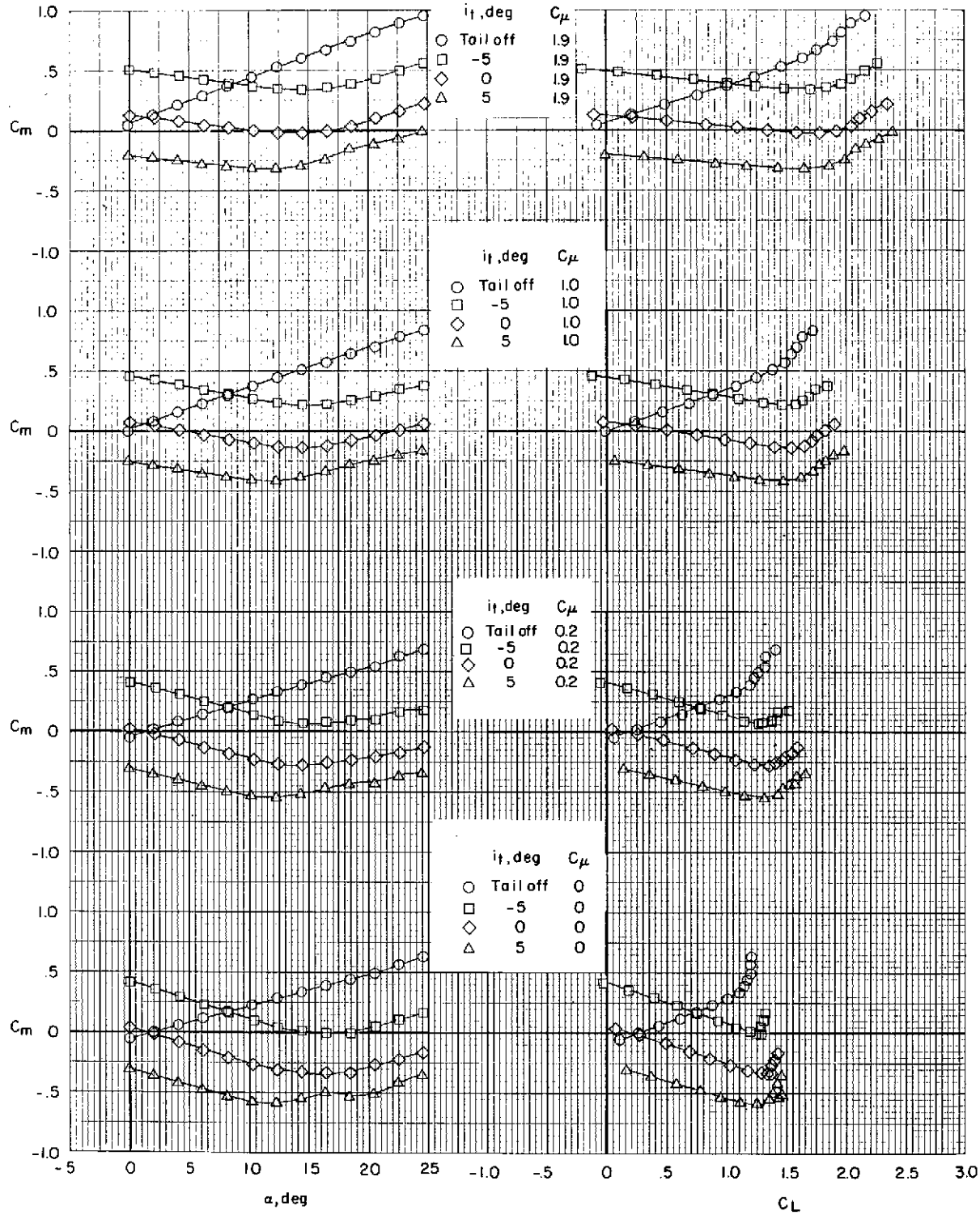

(a) $\delta_f = 0^o$ (cruise); δ_{sw} = off; $\delta_e = 0^o$; δ_{sh} = off.

Figure 30.- Effect of thrust coefficient and tail incidence on pitching-moment characteristics. Bypass ratio 3.2.

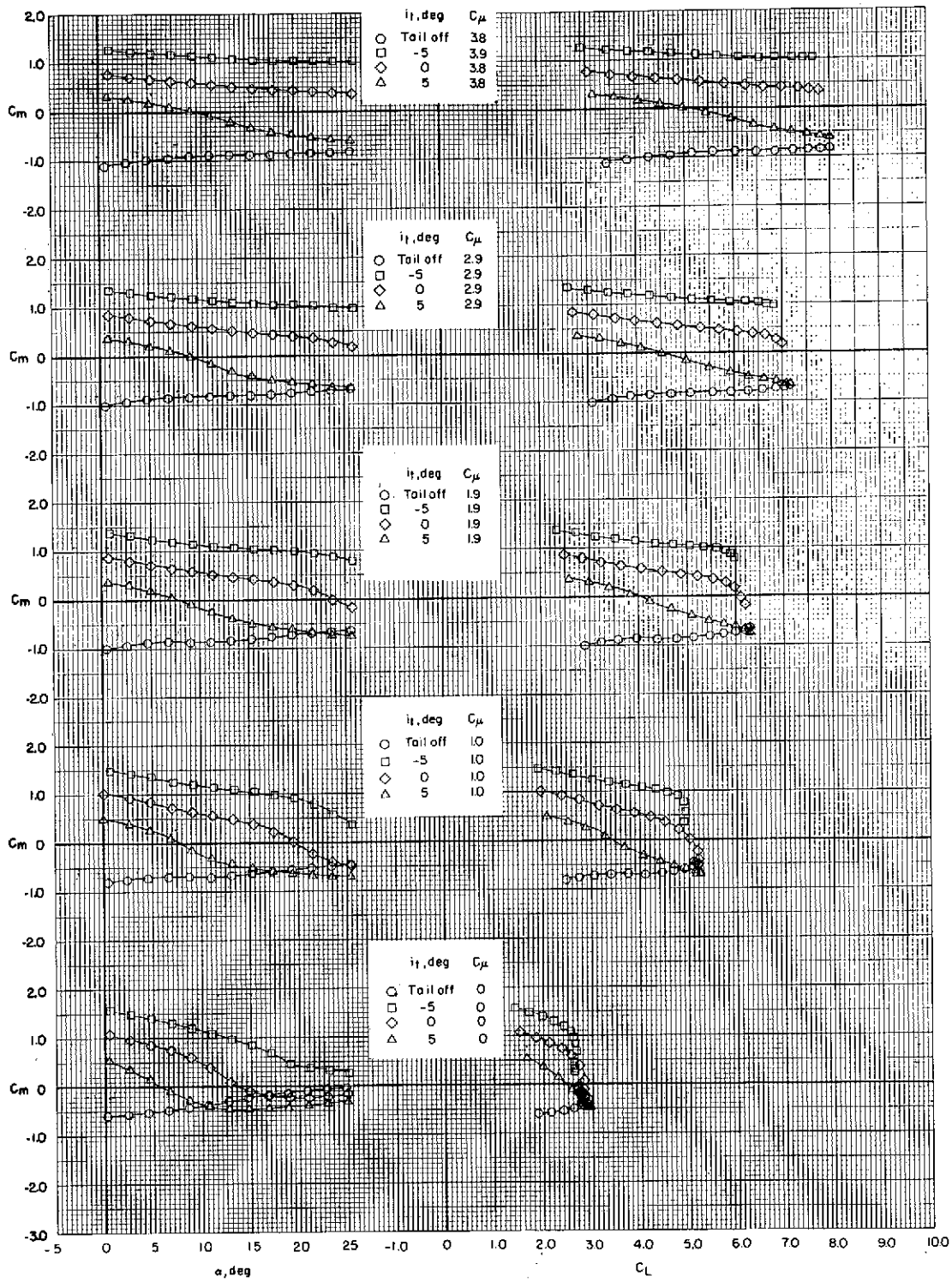

(b) $\delta_f = 0^o/20^o/40^o$ (take-off); $\delta_{sw} = 50^o$; $\delta_e = -25^o$; $\delta_{sh} = -40^o$.

Figure 30.- Continued.

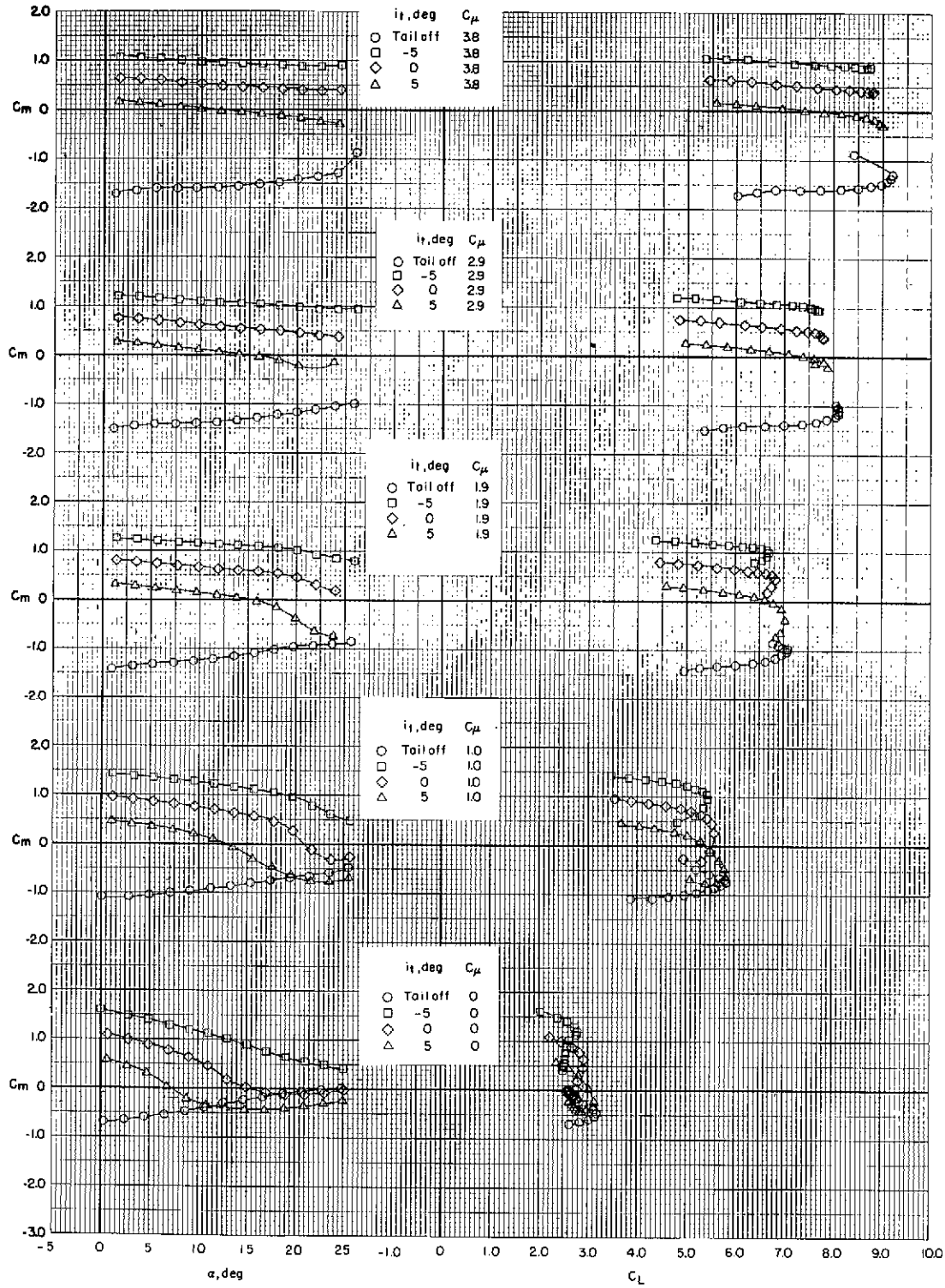

(c) $\delta_f = 15^o/35^o/55^o$ (landing); $\delta_{sw} = 50^o$; $\delta_e = -25^o$; $\delta_{sh} = -40^o$.

Figure 30.- Concluded.

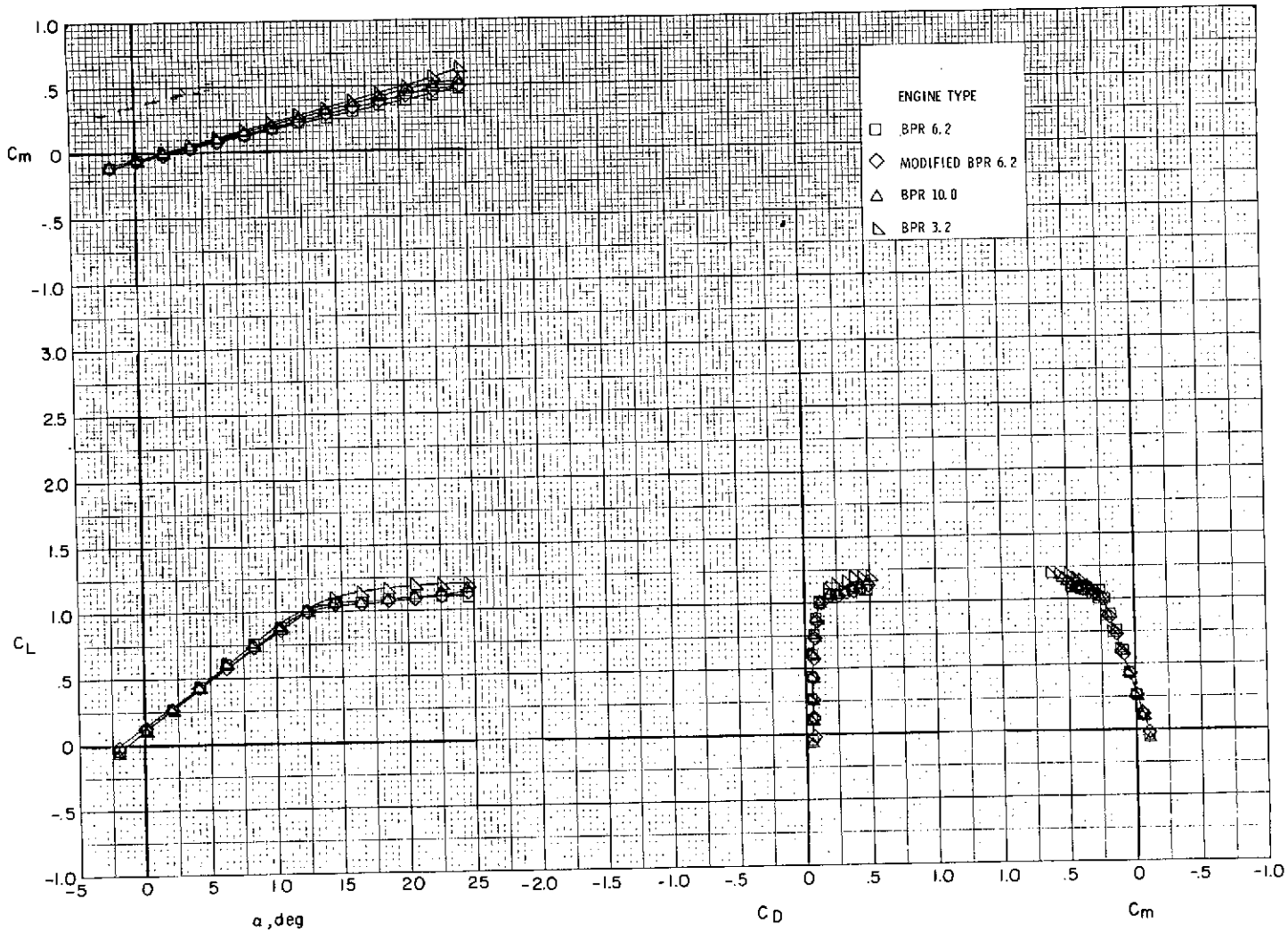

(a) $C_\mu = 0$.

Figure 31.- Effect of engine type on longitudinal aerodynamic characteristics. $\delta_f = 0^o$ (cruise); δ_{sw} = off; tail off.

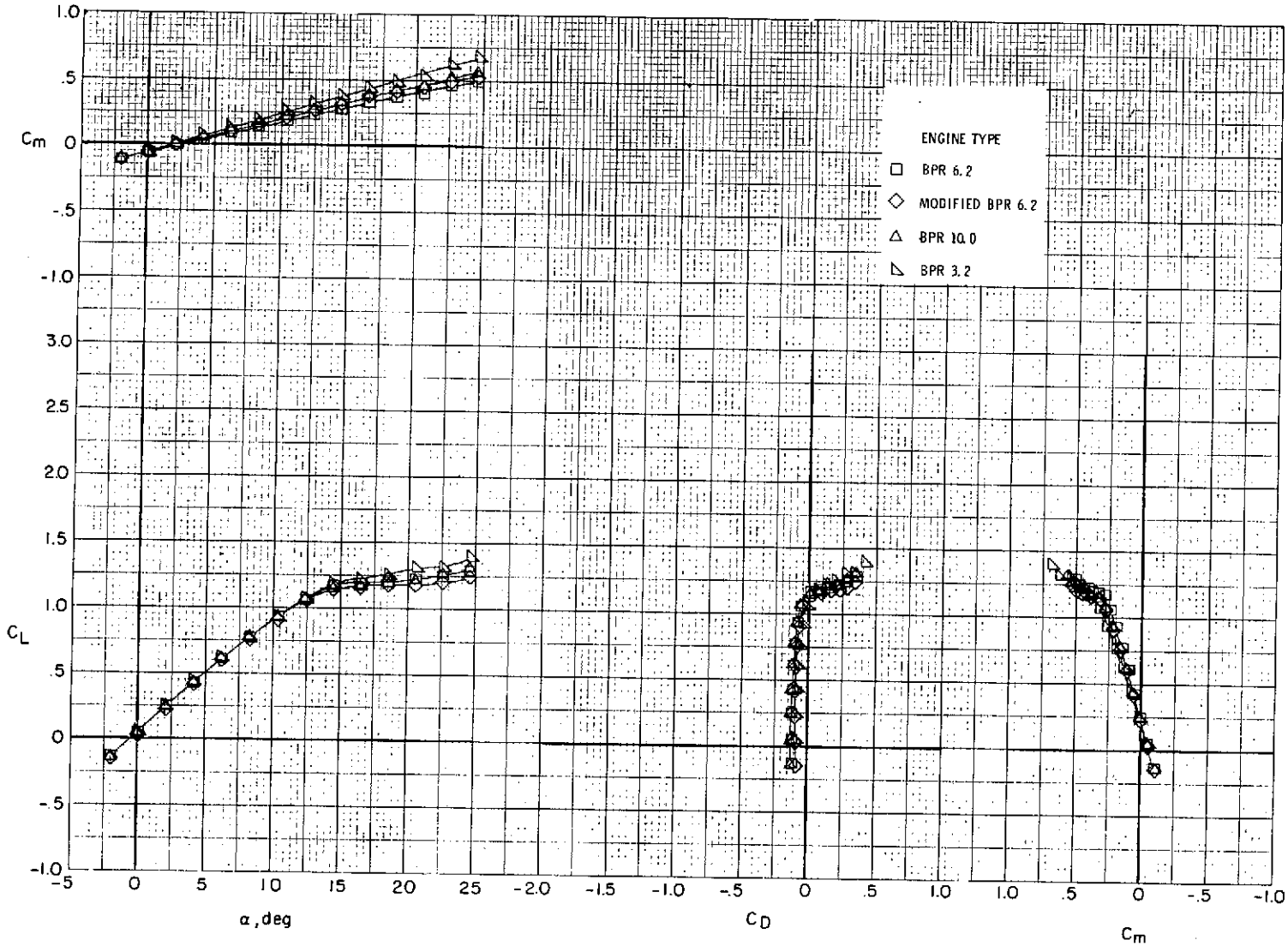

(b) C_μ = 0.2.

Figure 31.- Continued.

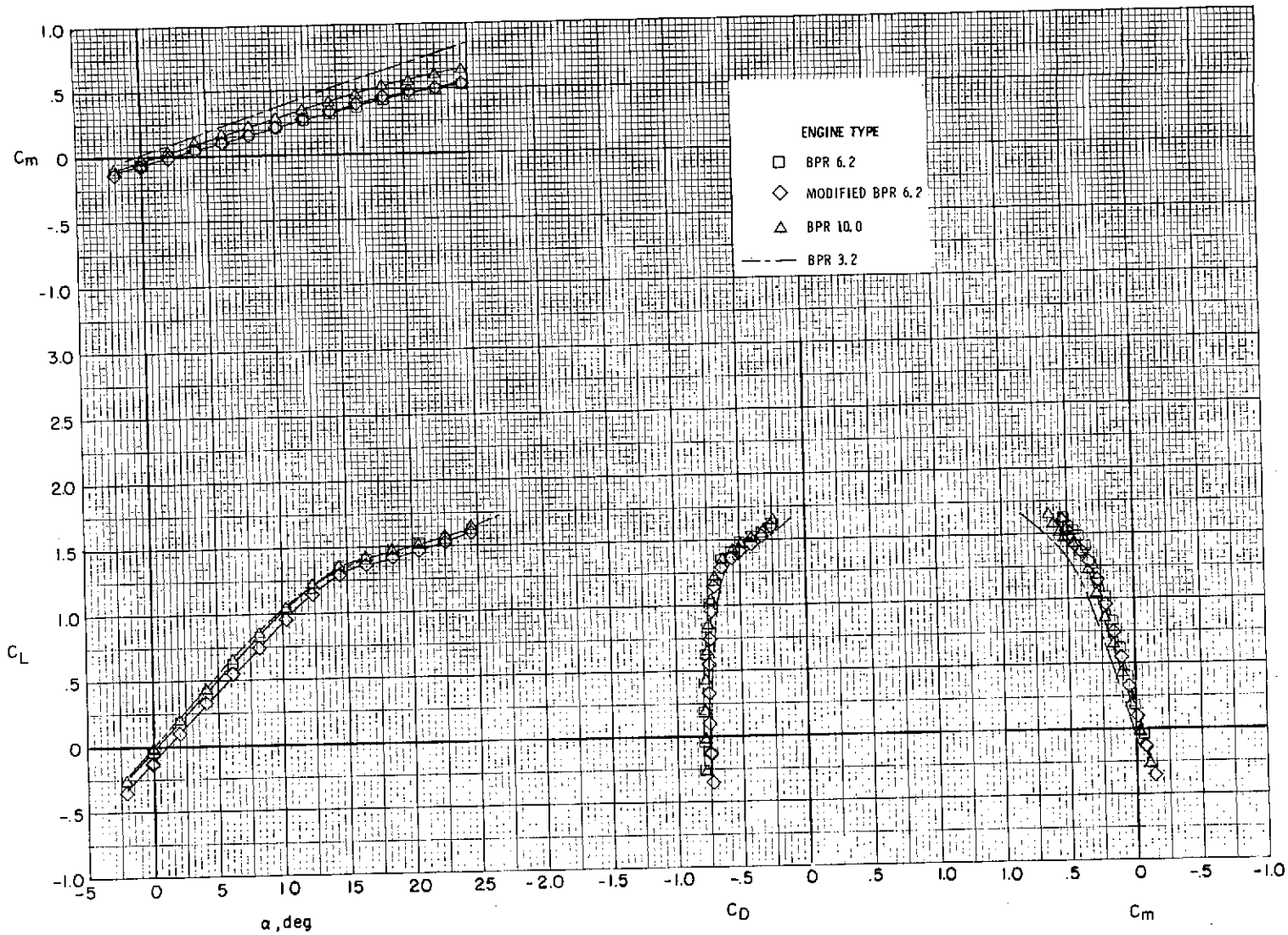

(c) $C_\mu = 0.9$.

Figure 31.- Continued.

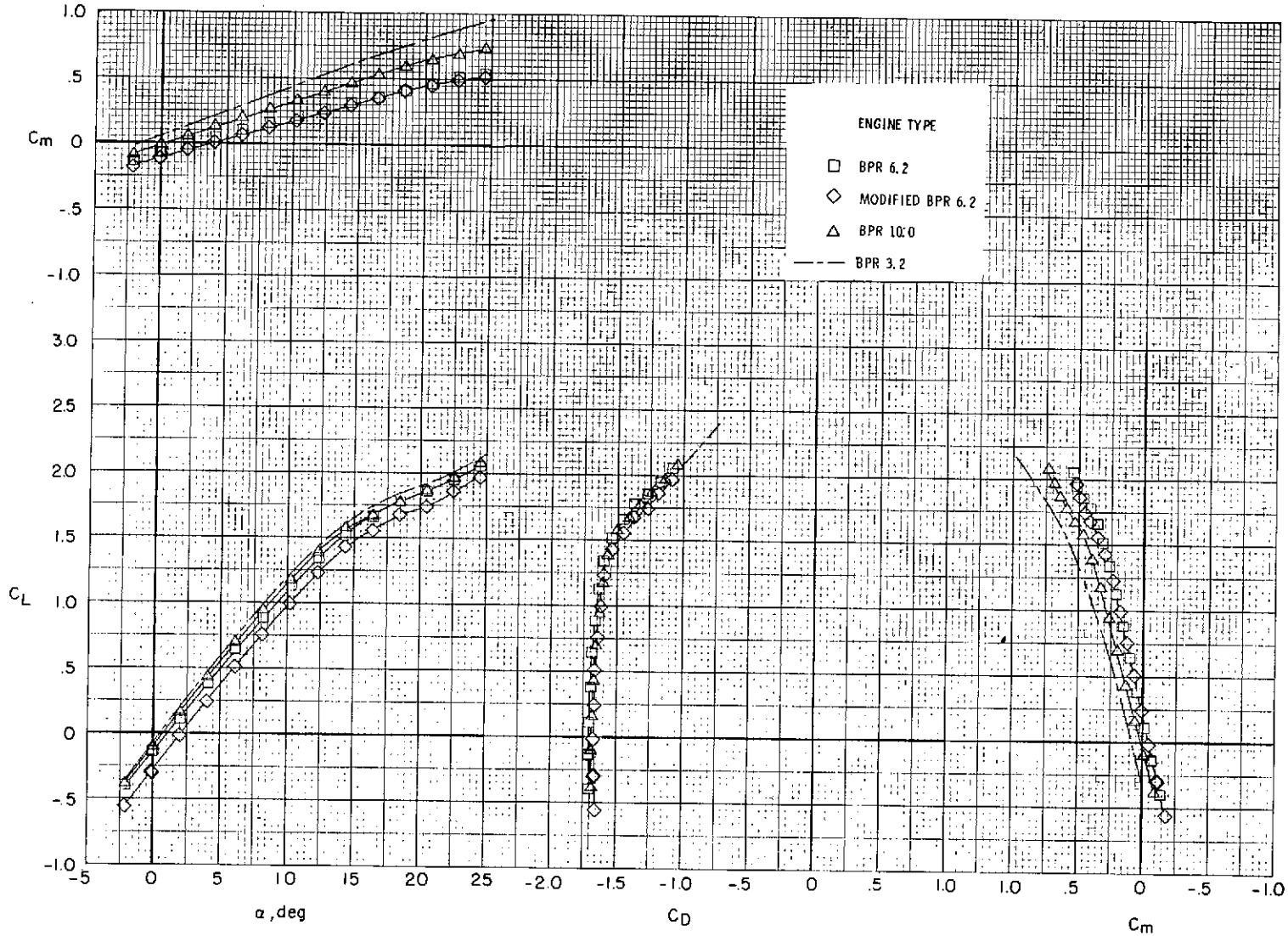

(d) $C_\mu = 1.8$.

Figure 31.- Concluded.

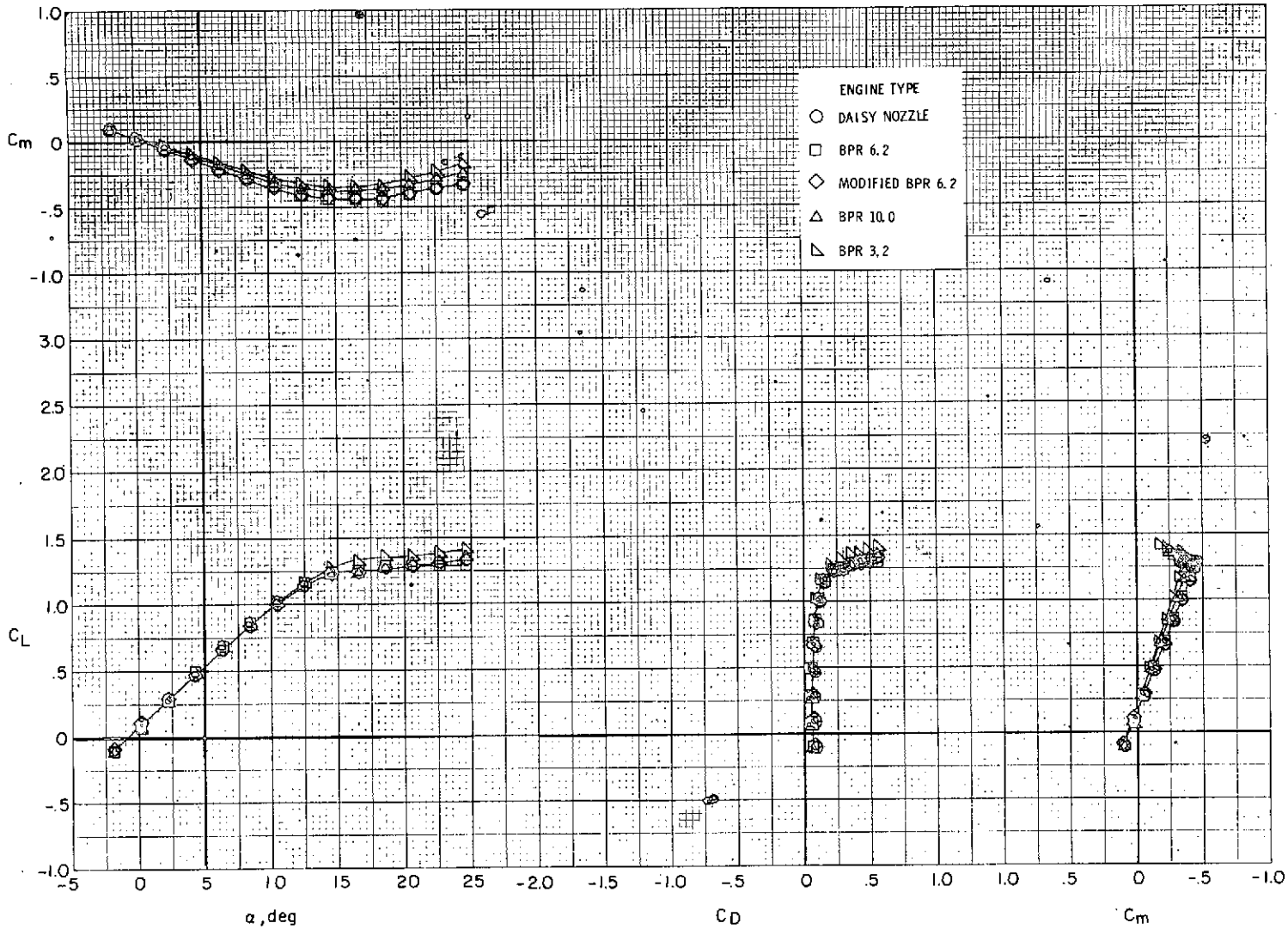

(a) $C_\mu = 0$.

Figure 32.- Effect of engine type on longitudinal aerodynamic characteristics. $\delta_f = 0^o$ (cruise); δ_{sw} = off; $i_t = 0^o$; $\delta_e = 0^o$; δ_{sh} = off.

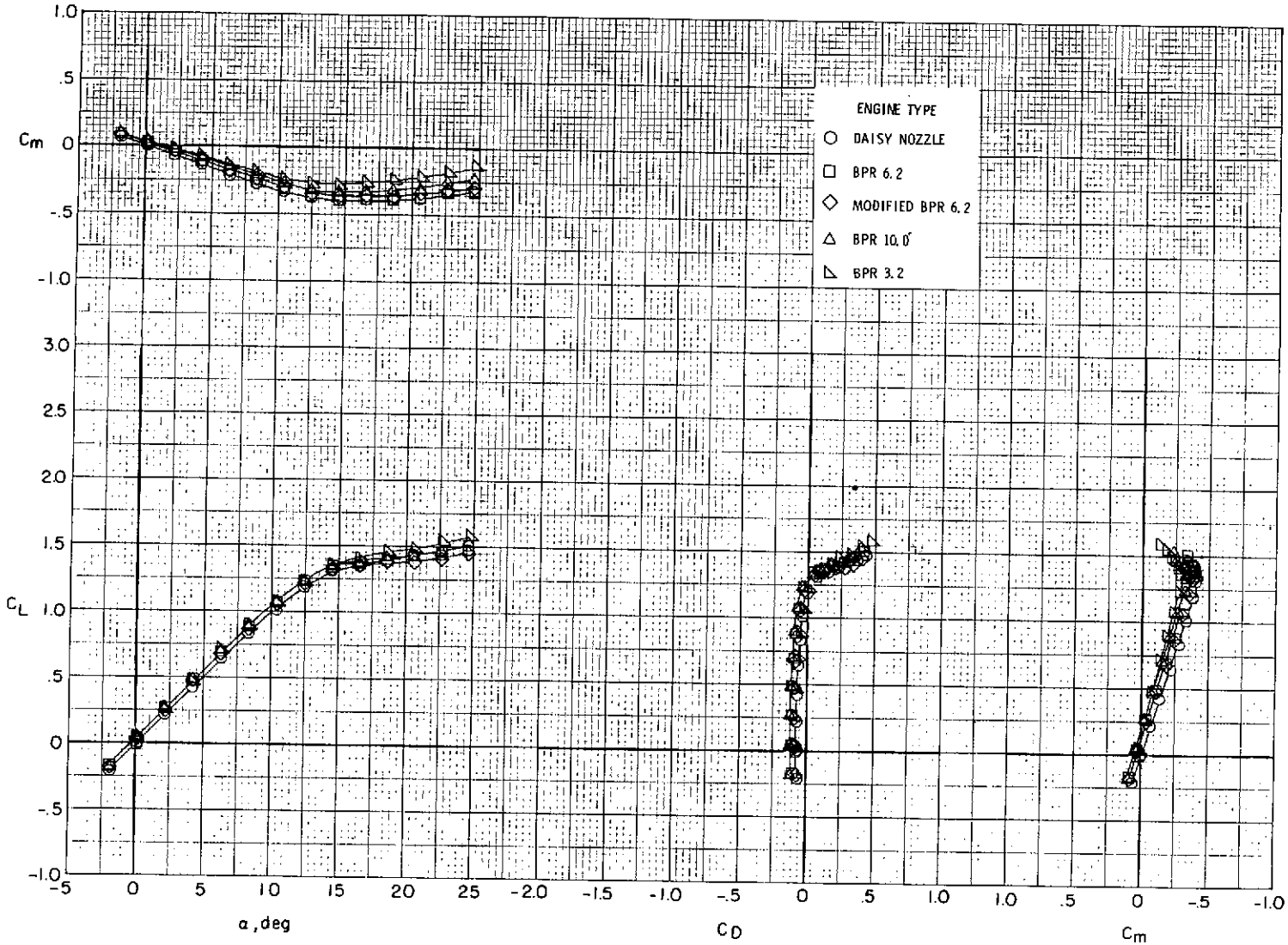

(b) $C_\mu = 0.2$.

Figure 32.- Continued.

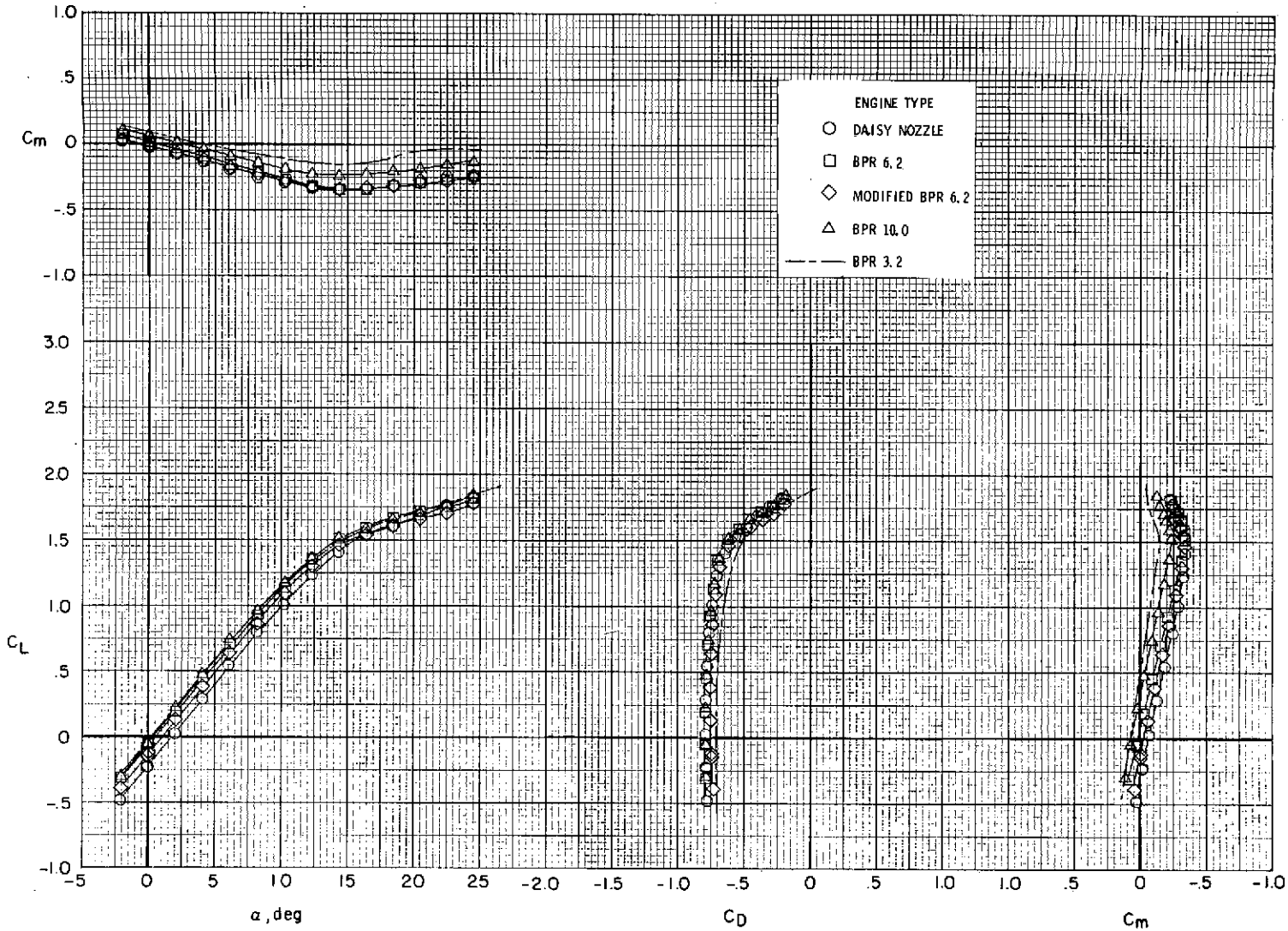

(c) $C_\mu = 0.9$.

Figure 32.- Continued.

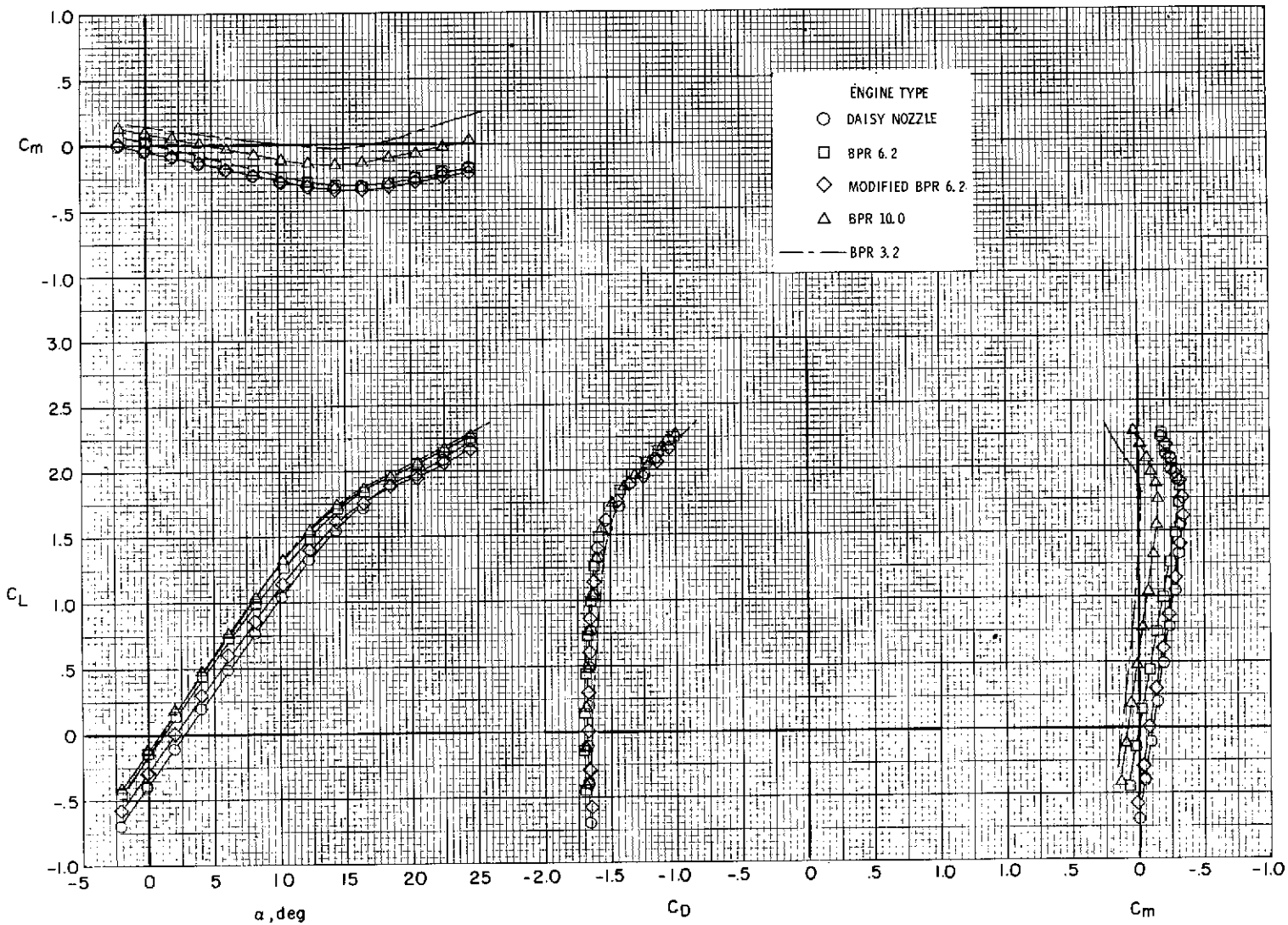

(d) C_μ = 1.8.

Figure 32.- Concluded.

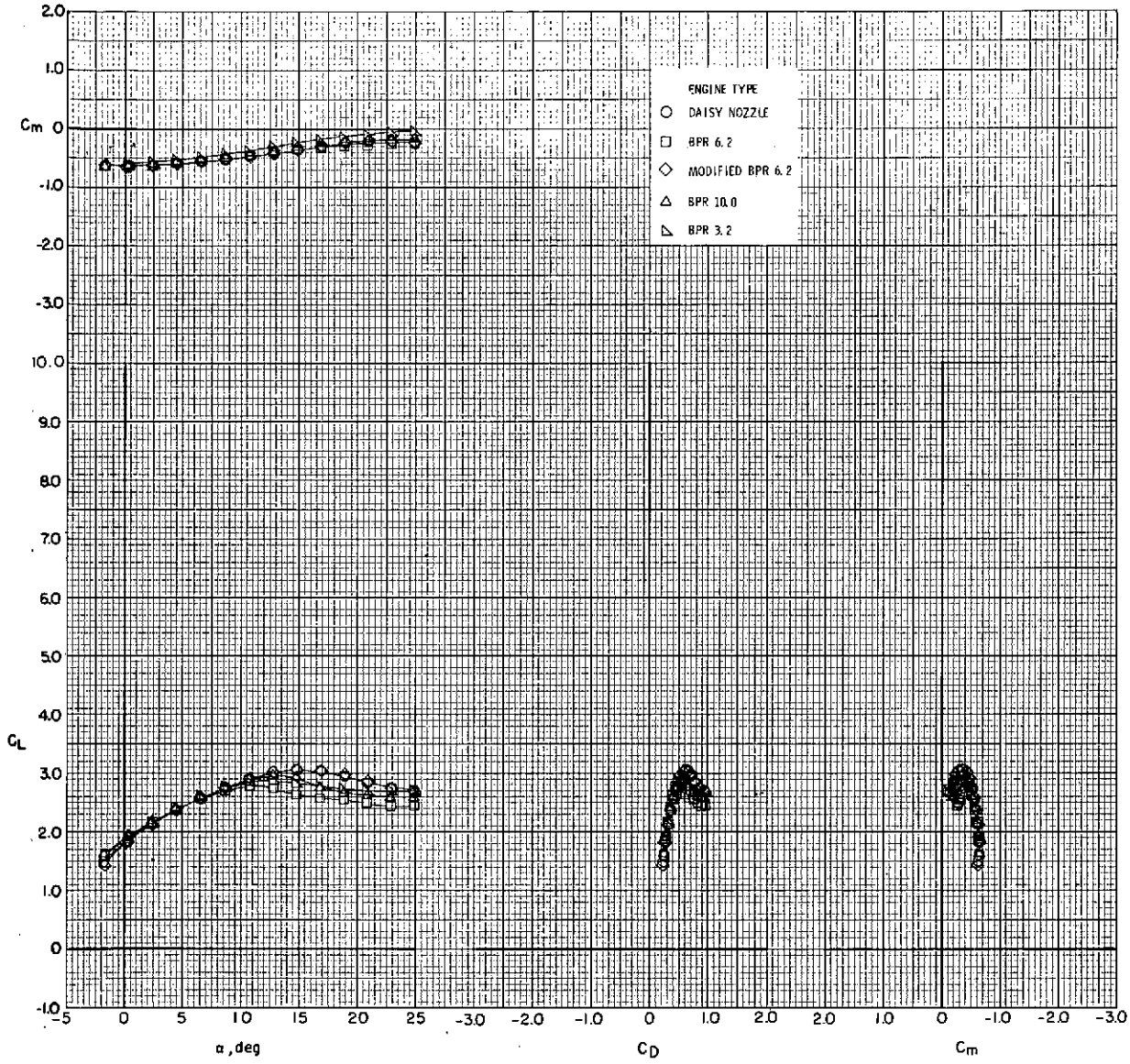

(a) $C_\mu = 0$.

Figure 33.- Effect of engine type on longitudinal aerodynamic characteristics. $\delta_f = 0^o/20^o/40^o$ (take-off); $\delta_{sw} = 50^o$; tail off.

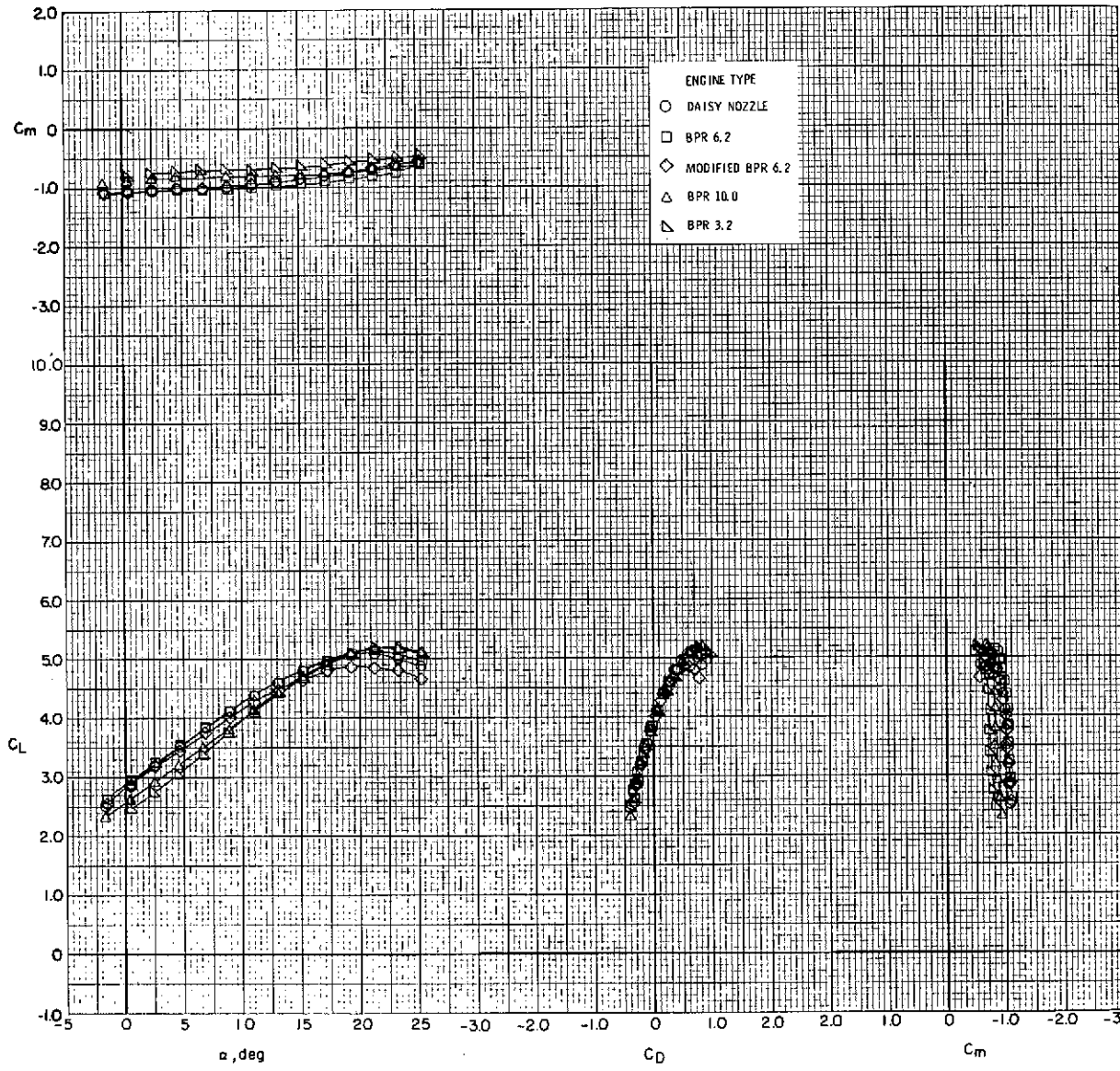

(b) $C_\mu = 1.0$.

Figure 33.- Continued.

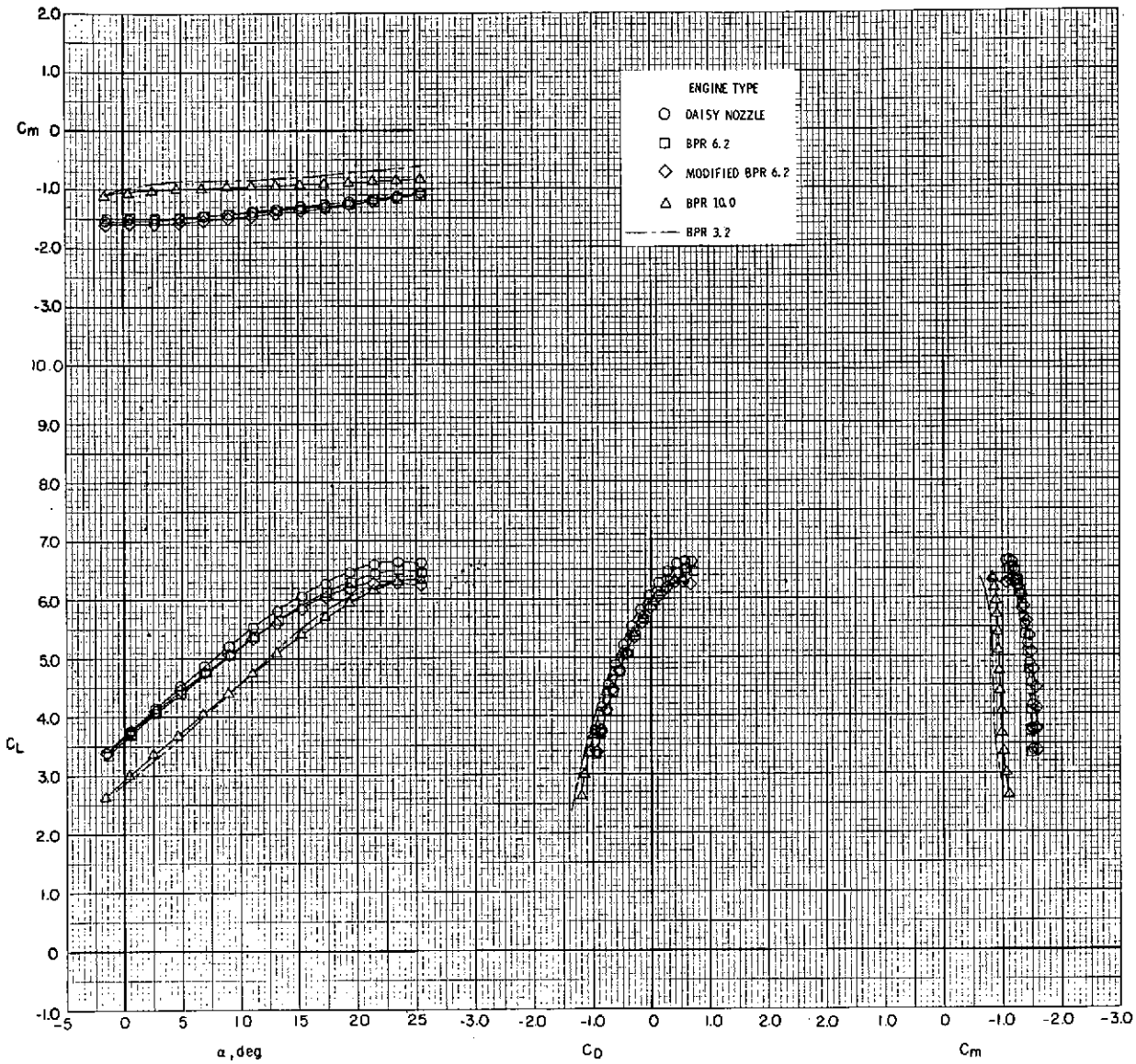

(c) $C_\mu = 2.0$.

Figure 33.- Continued.

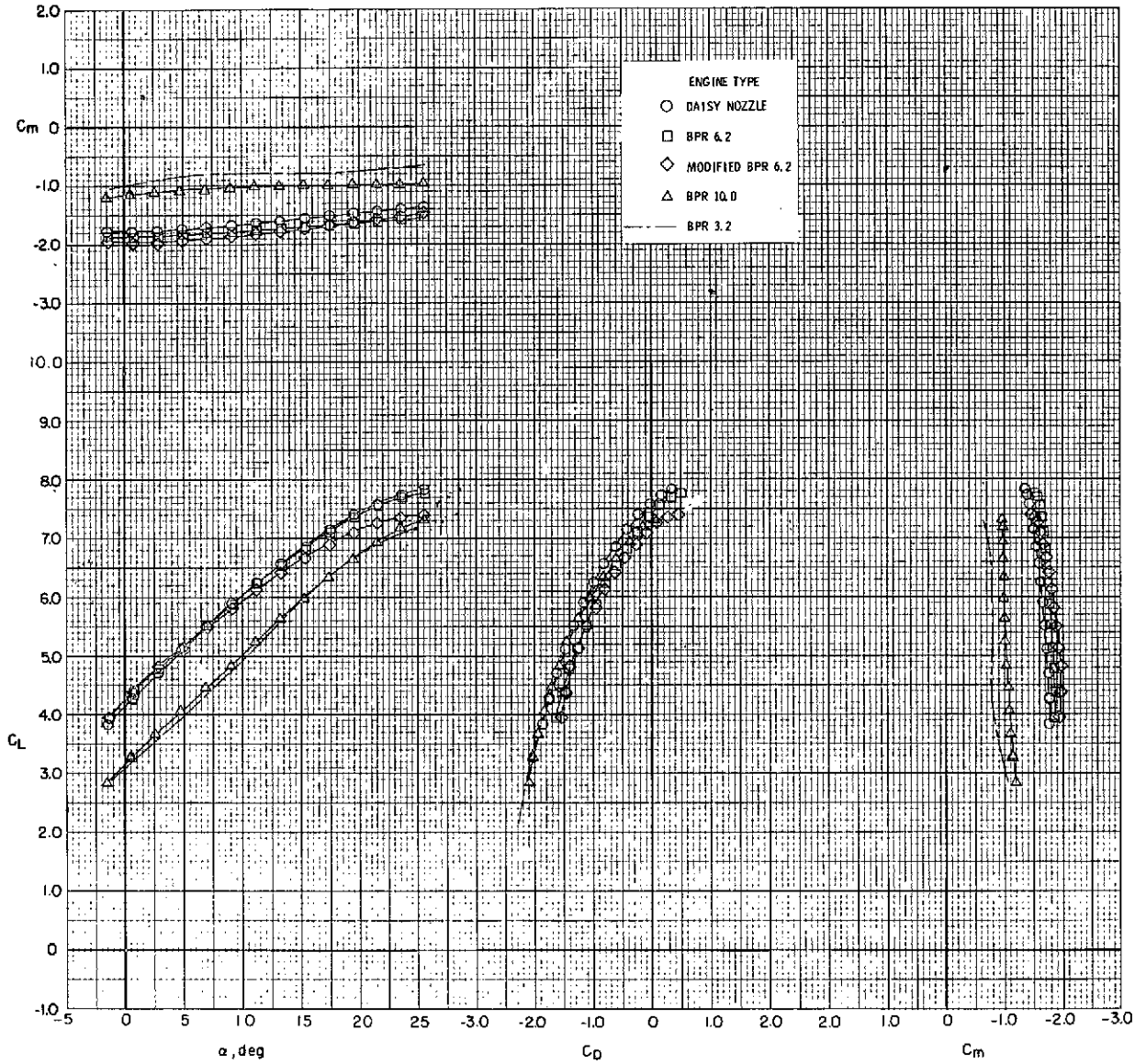

(d) $C_\mu = 3.0$.

Figure 33.- Continued.

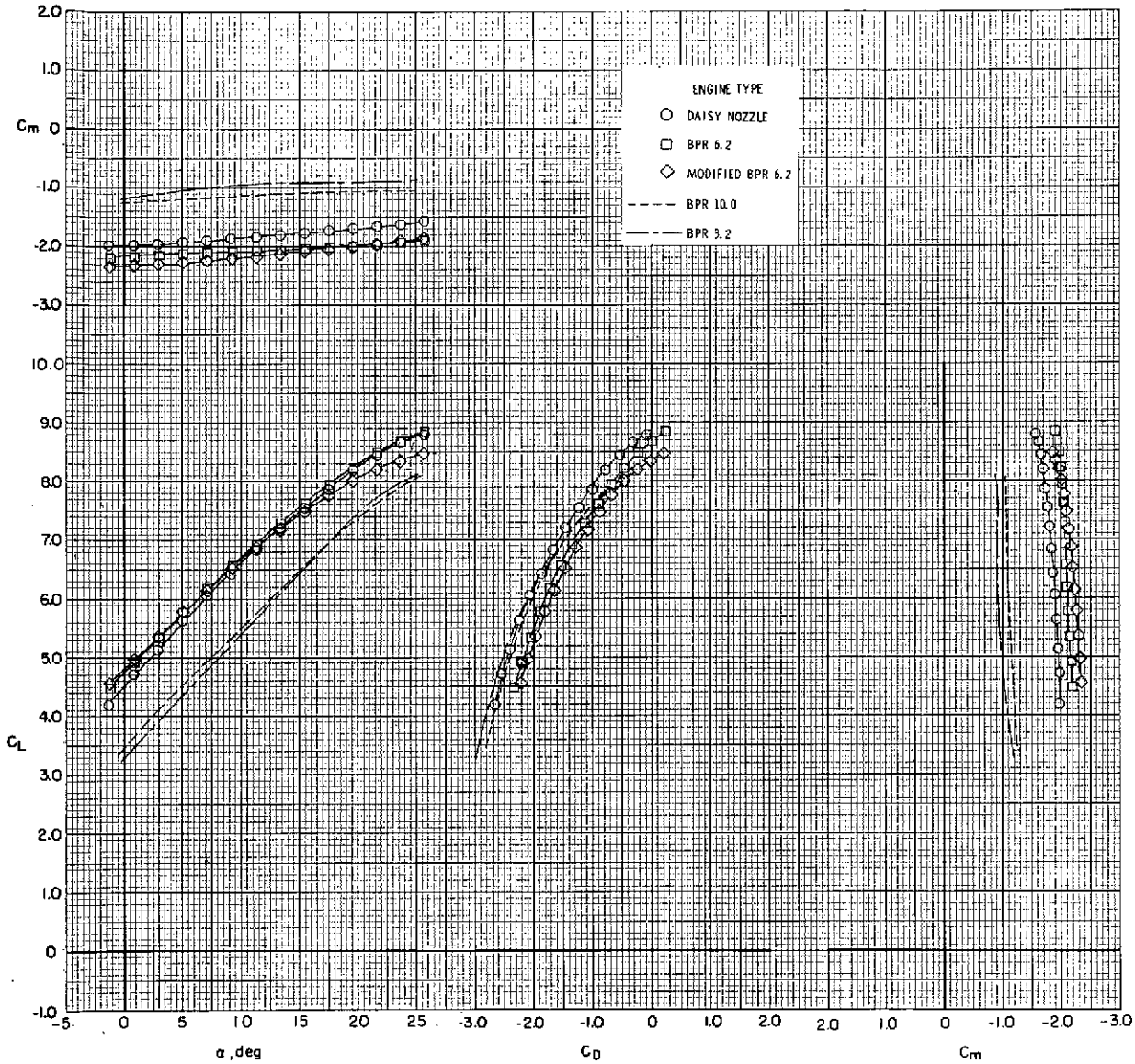

(e) C_μ = 4.0.

Figure 33.- Concluded.

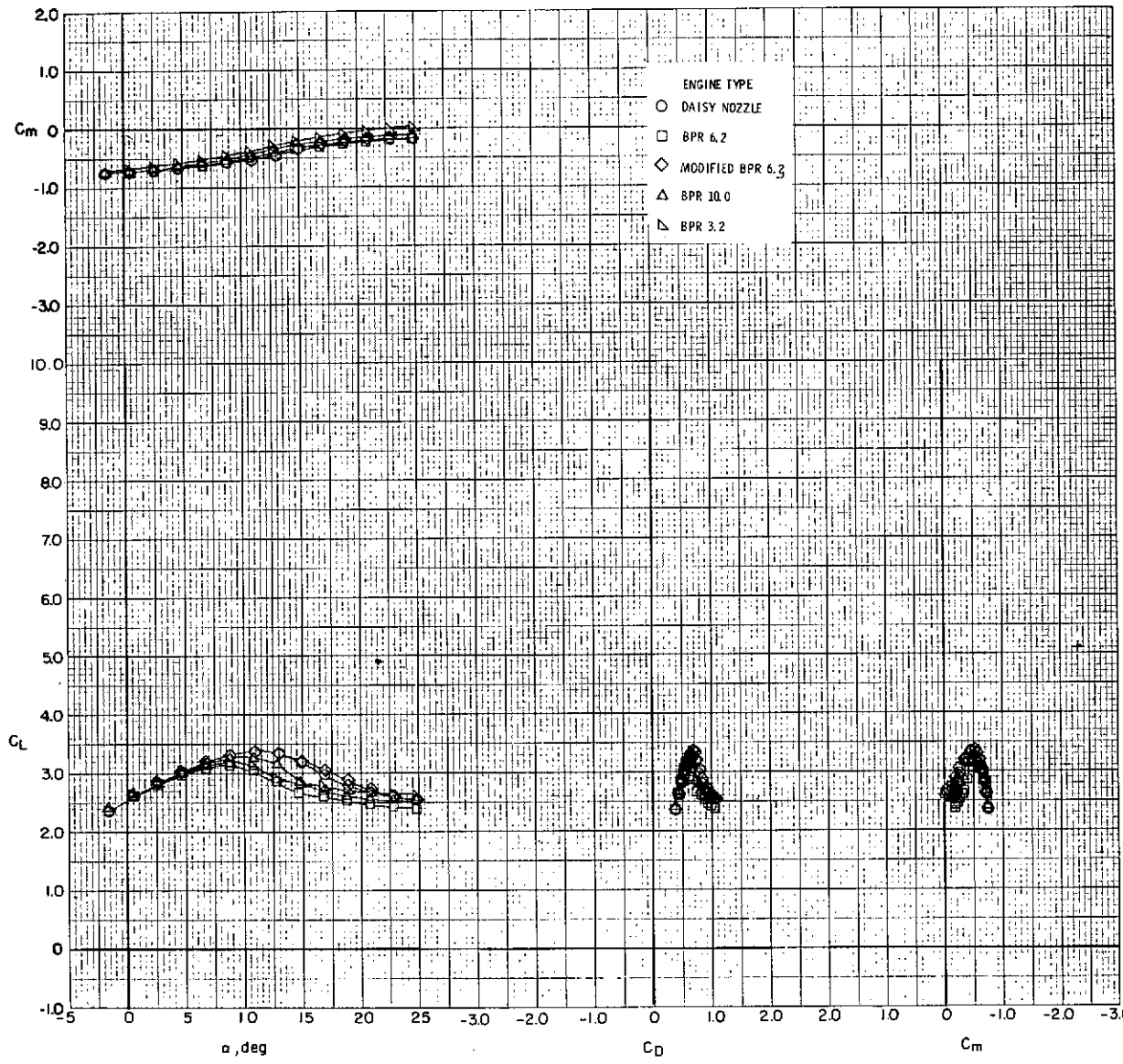

(a) $C_\mu = 0$.

Figure 34.- Effect of engine type on longitudinal aerodynamic characteristics. $\delta_f = 15^o/35^o/55^o$ (landing); $\delta_{sw} = 50^o$; tail off.

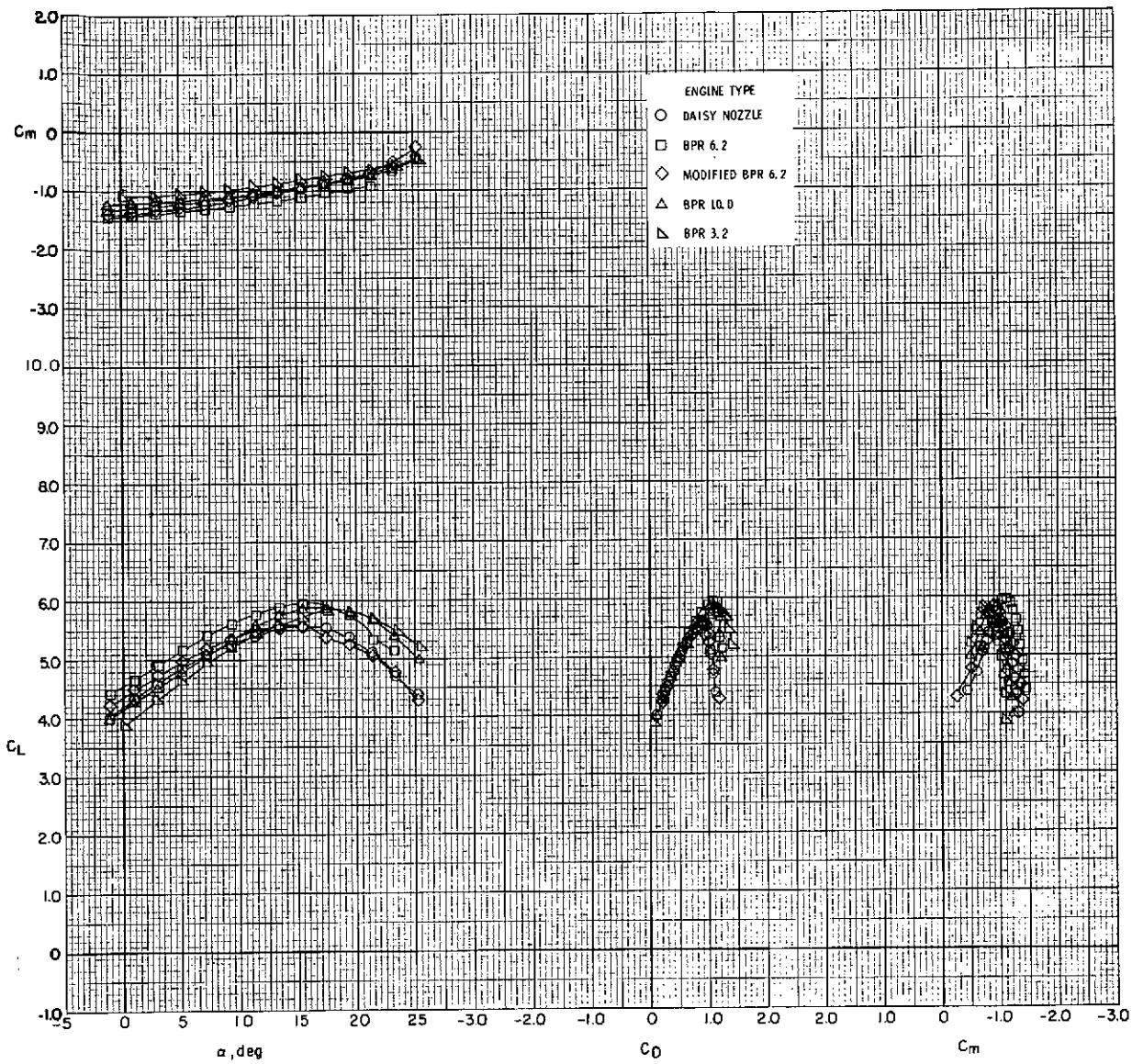

(b) $C_\mu = 1.0$.

Figure 34.- Continued.

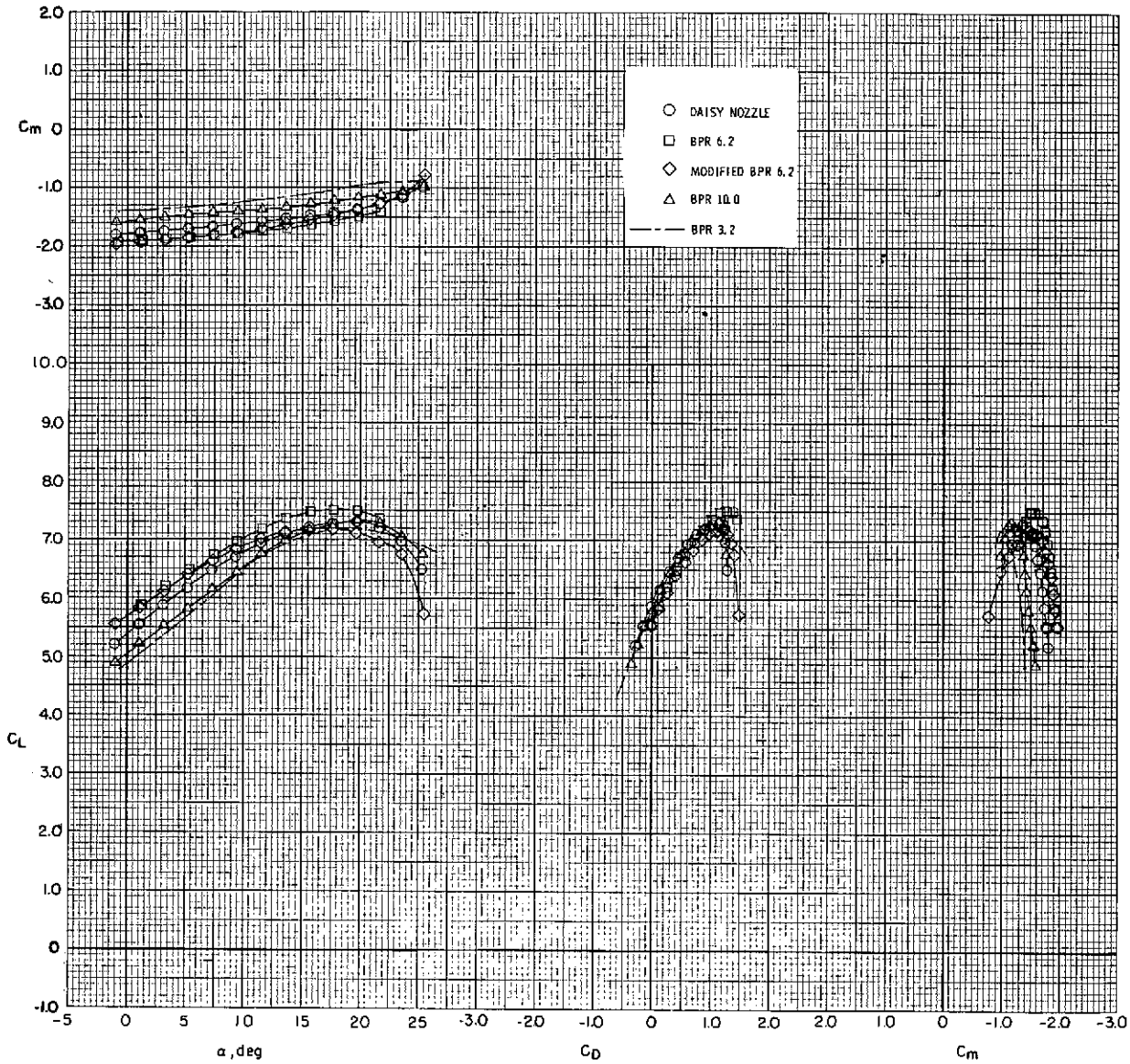

(c) C_μ = 2.0.

Figure 34.- Continued.

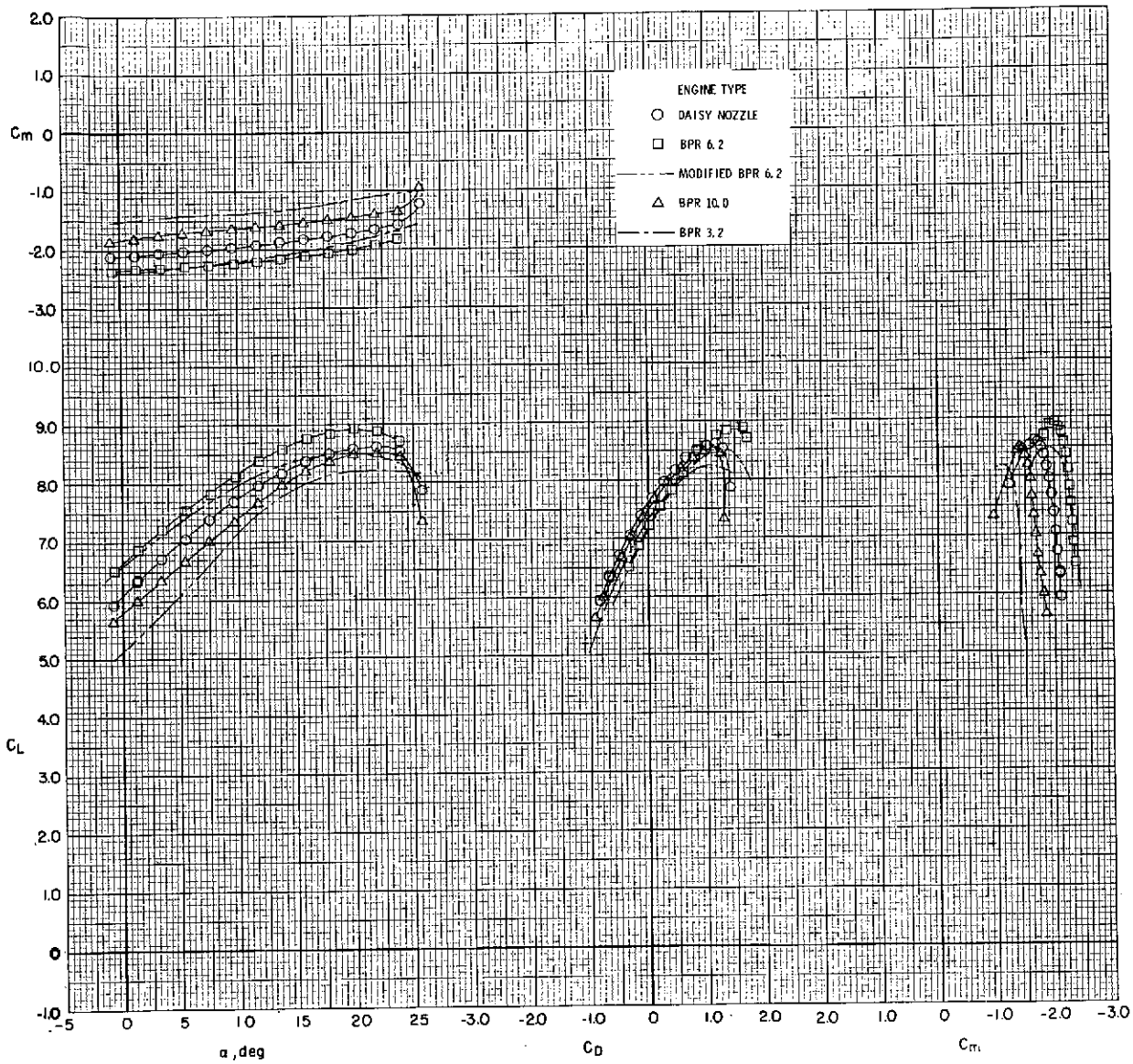

(d) C_μ = 3.0.

Figure 34.- Continued.

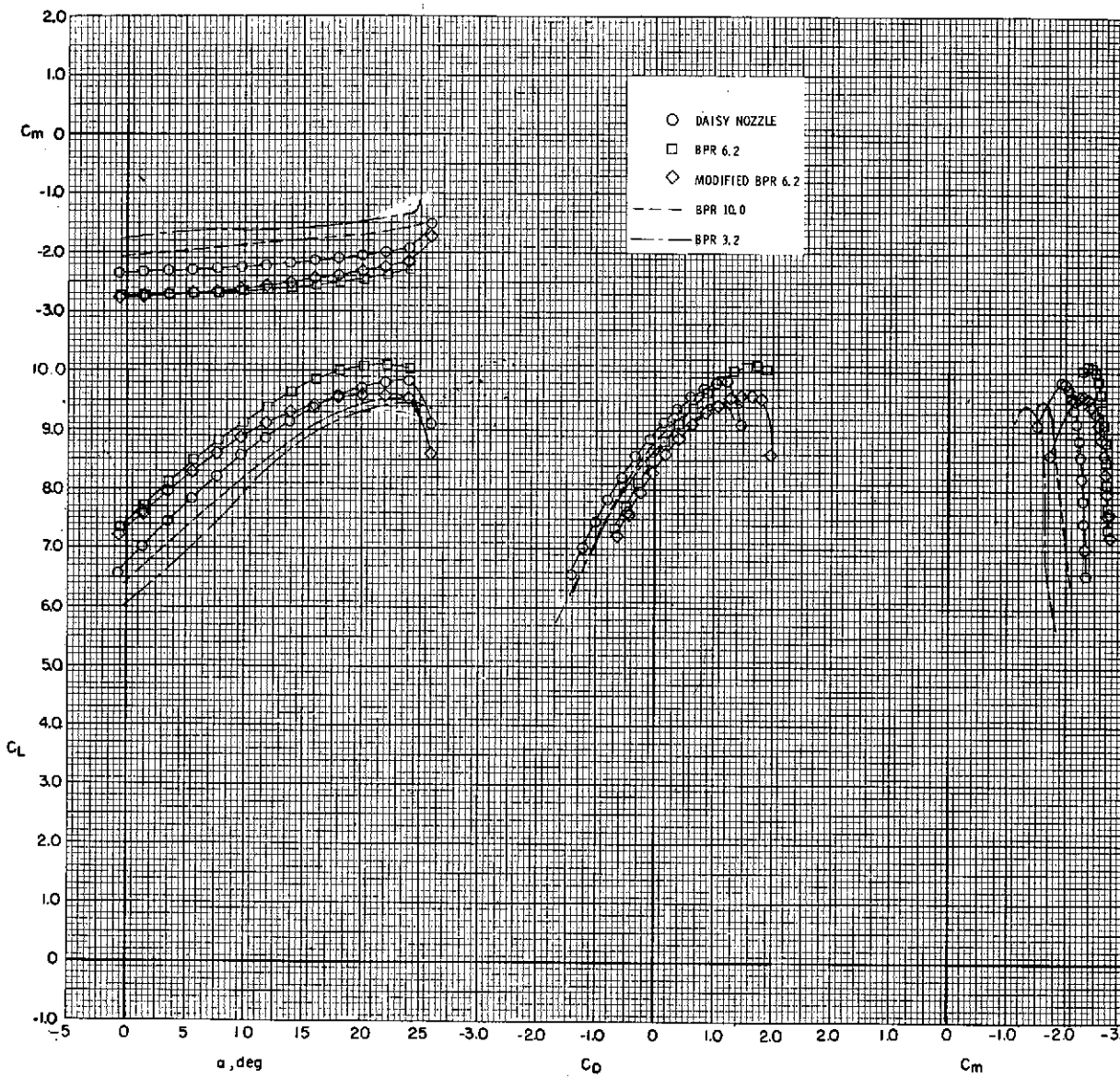

(e) $C_\mu = 4.0$.

Figure 34.- Concluded.

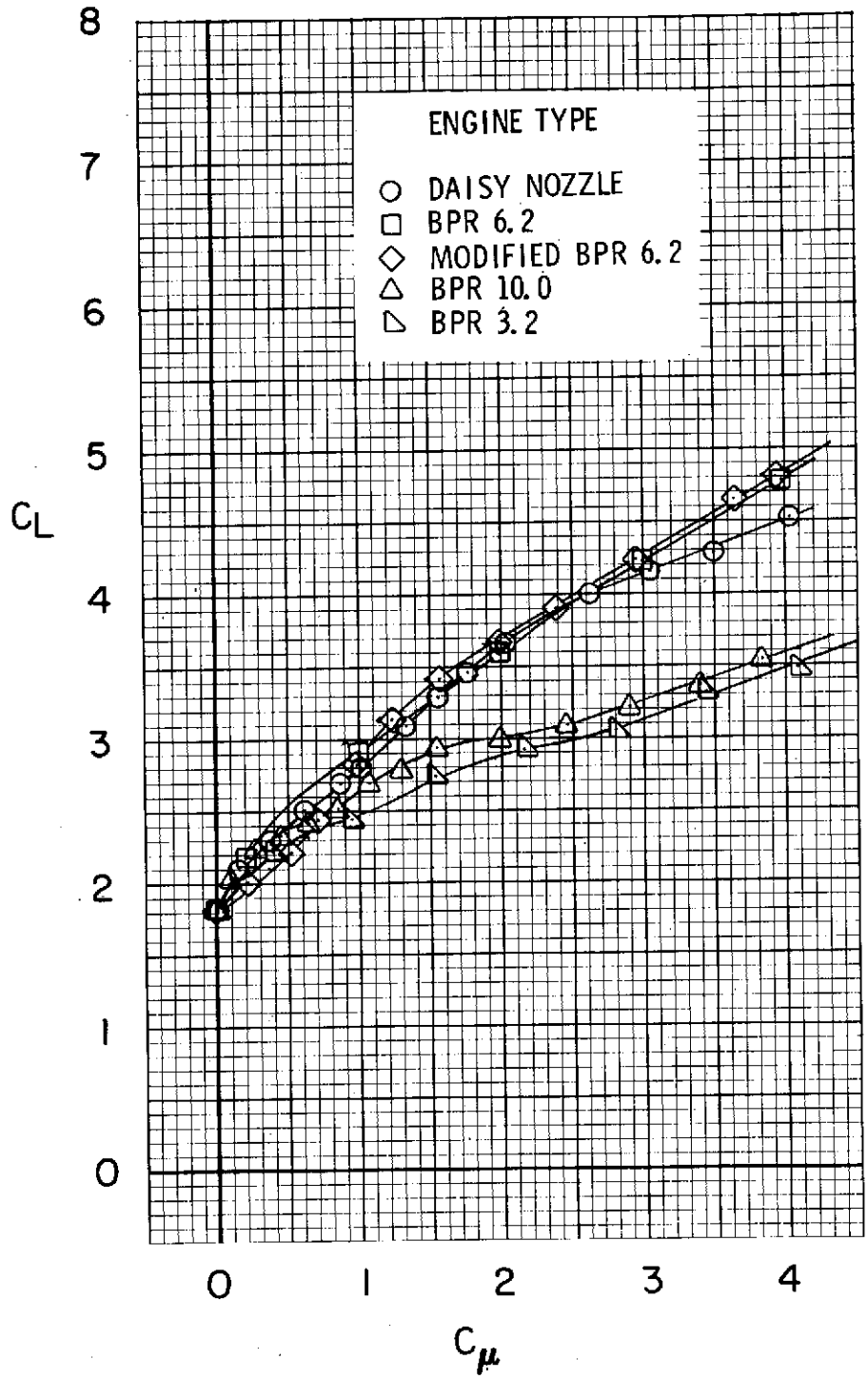

(a) $\delta_f = 0^o/20^o/40^o$ (take-off).

Figure 35.- Effect of engine type on variation of lift coefficient with thrust coefficient. $\alpha = 0^o$; $\delta_{sw} = 50^o$; tail off.

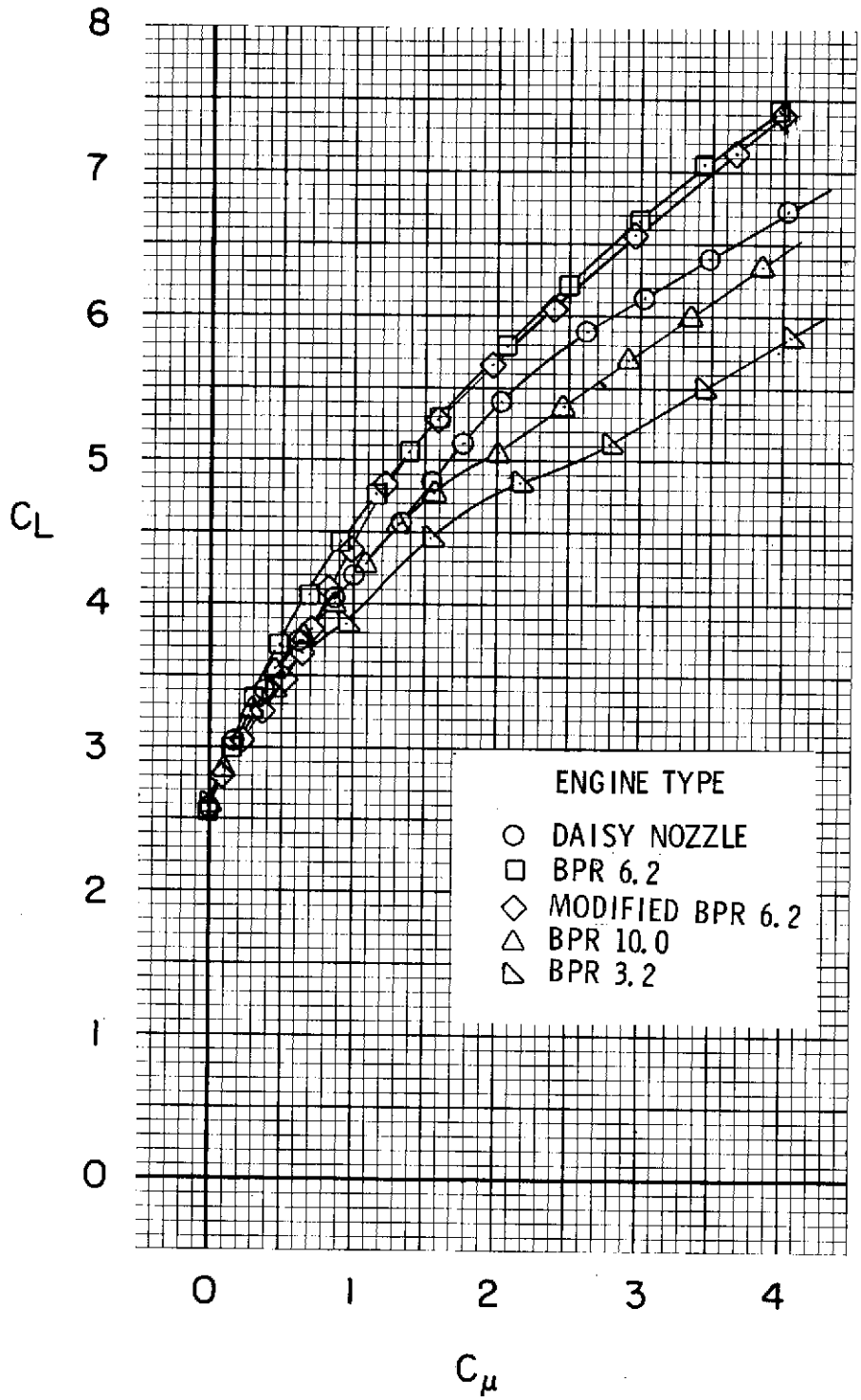

(b) $\delta_f = 15^o/35^o/55^o$ (landing).

Figure 35.- Concluded.

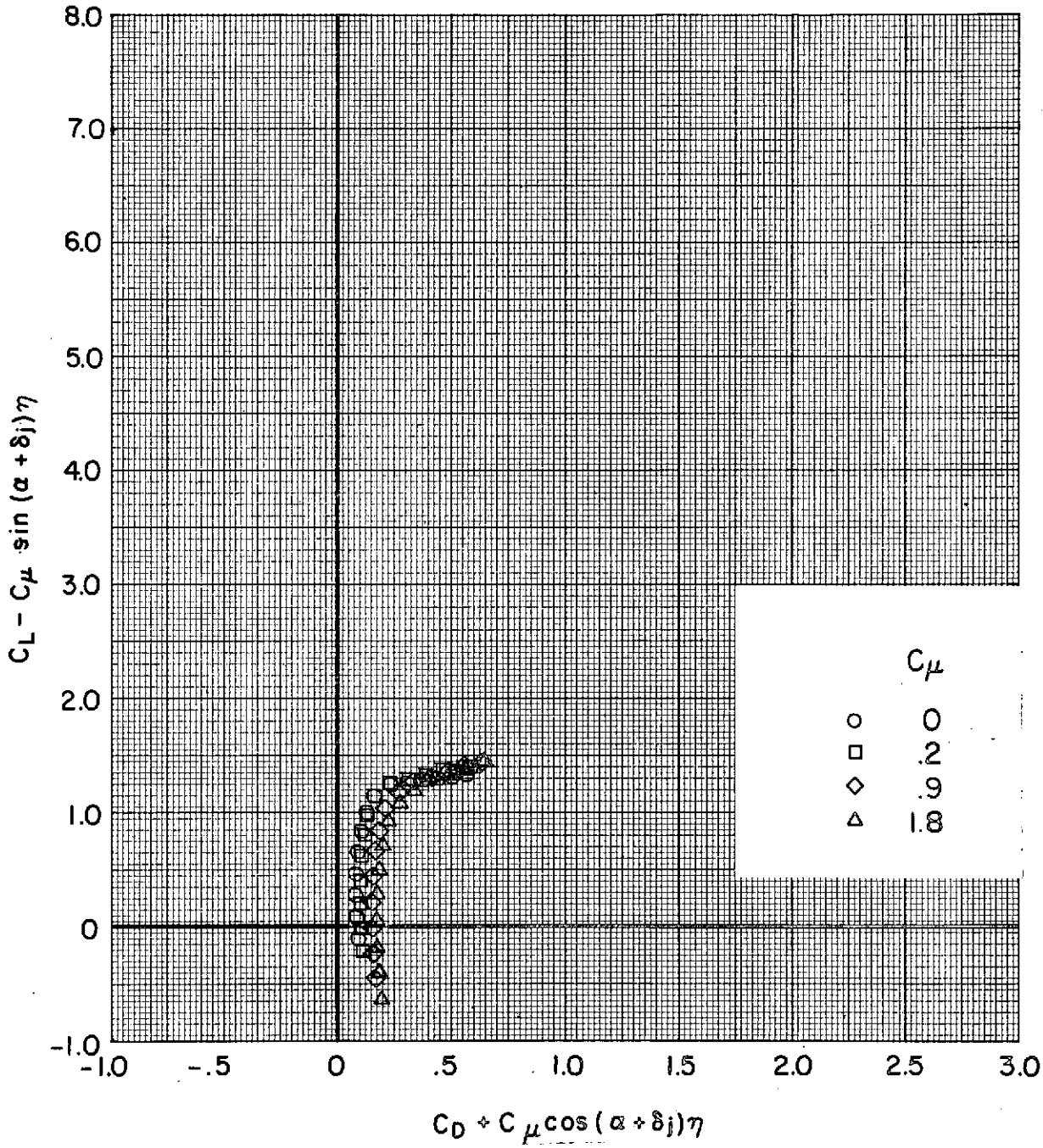

(a) $\delta_f = 0^o$ (cruise); δ_{sw} = off; $i_t = 0^o$; $\delta_e = 0^o$; δ_{sh} = off.

Figure 36.- Effect of thrust coefficient on thrust-removed lift coefficient and drag coefficient. Daisy nozzle.

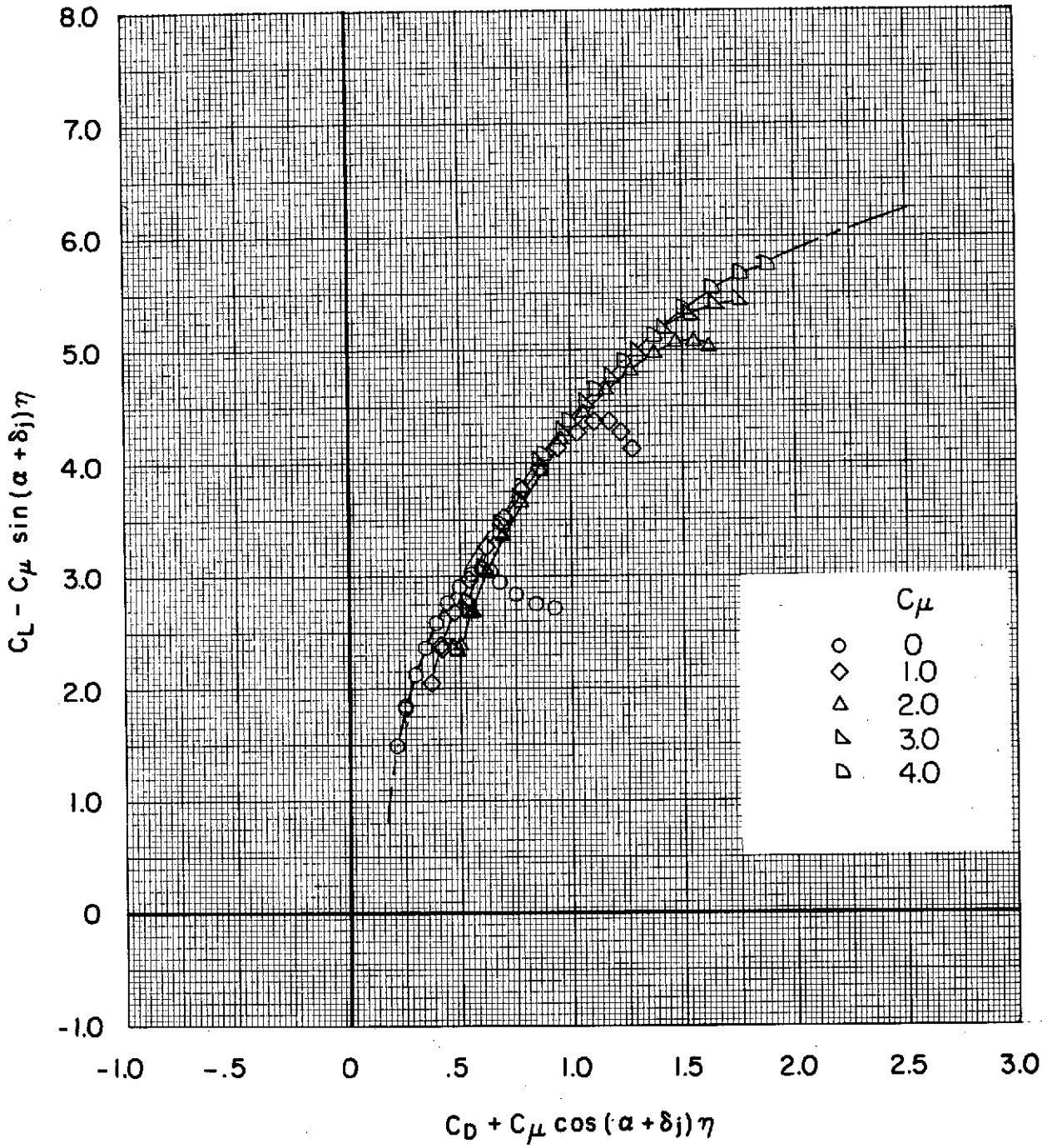

(b) $\delta_f = 0^o/20^o/40^o$ (take-off); $\delta_{sw} = 50^o$; tail off.

Figure 36.- Continued.

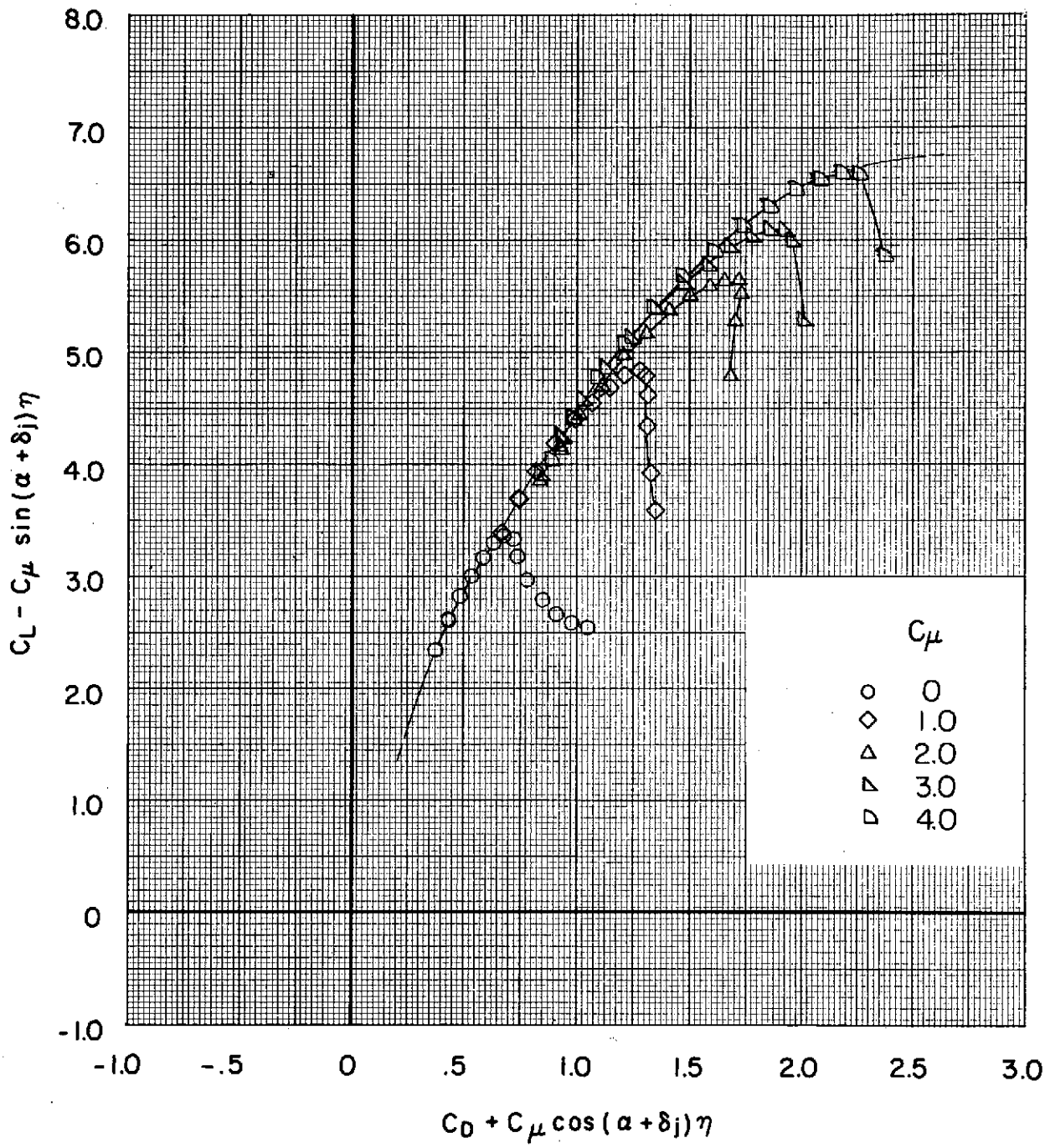

(c) $\delta_f = 15^o/35^o/55^o$ (landing); $\delta_{sw} = 50^o$; tail off.

Figure 36.- Concluded.

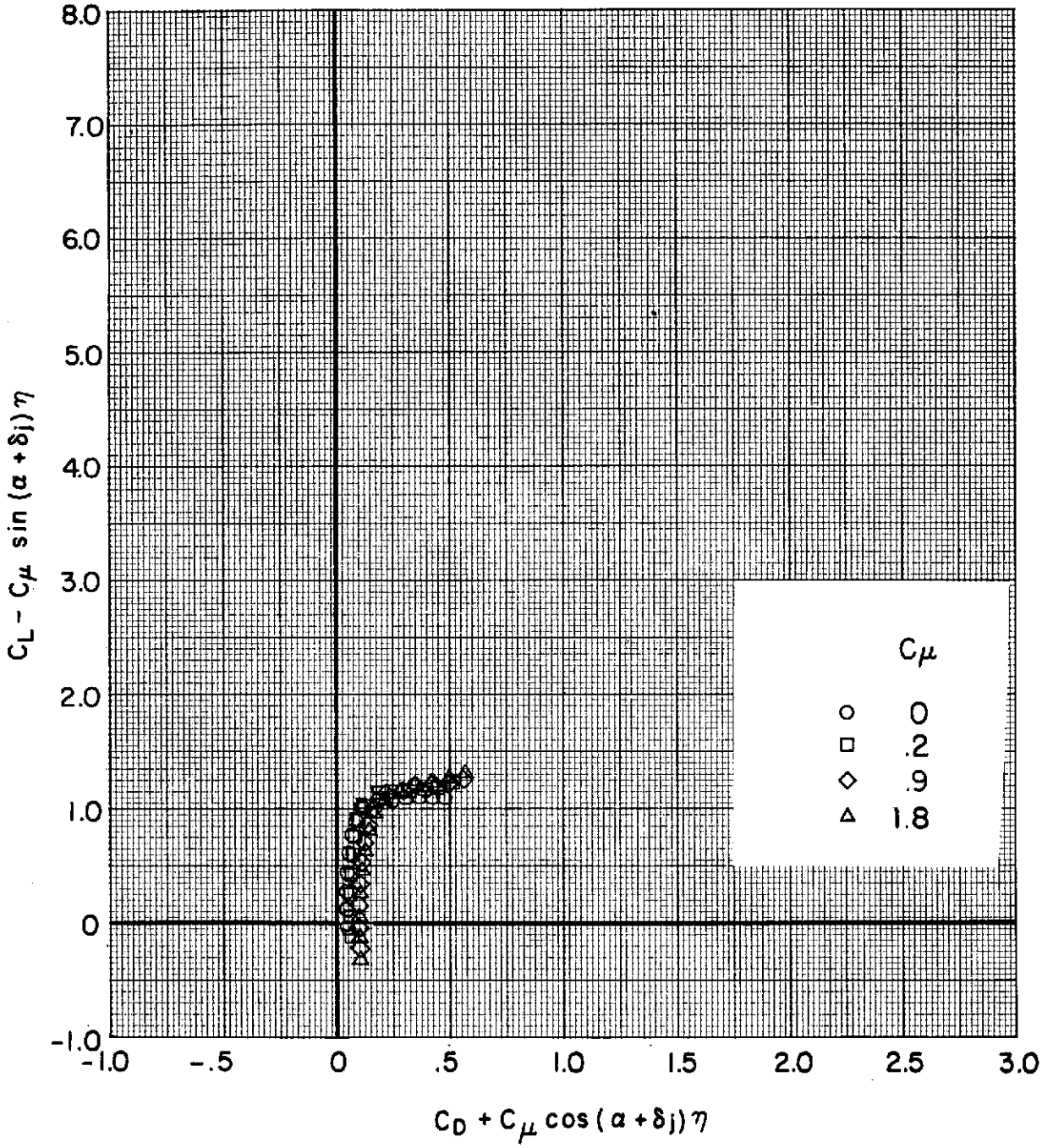

(a) $\delta_f = 0^o$ (cruise); δ_{sw} = off; tail off.

Figure 37.- Effect of thrust coefficient on thrust-removed lift coefficient and drag coefficient. Bypass ratio 6.2.

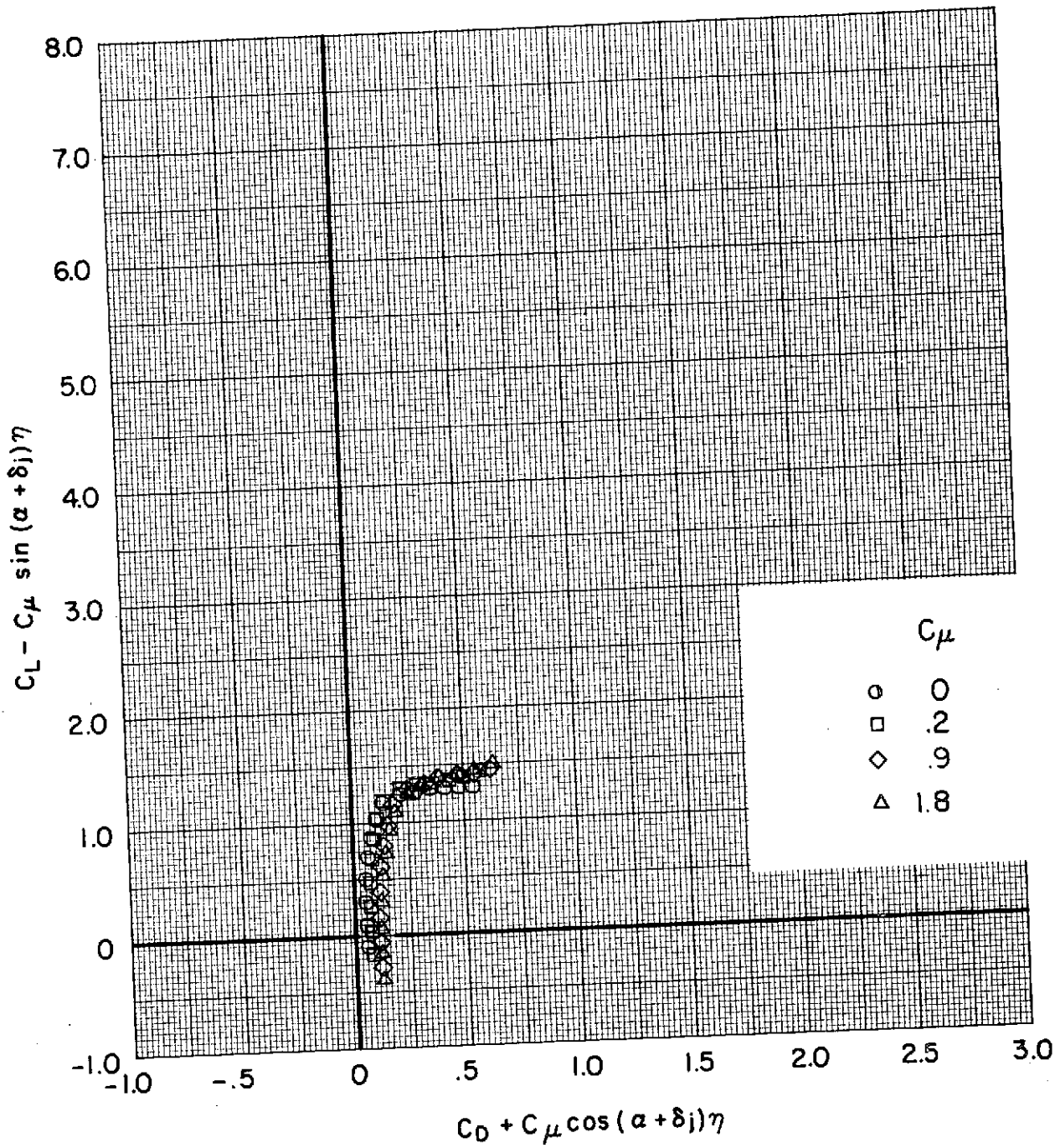

(b) $\delta_f = 0^o$ (cruise); δ_{sw} = off; $i_t = 0^o$, $\delta_e = 0^o$, δ_{sh} = off.

Figure 37.- Continued.

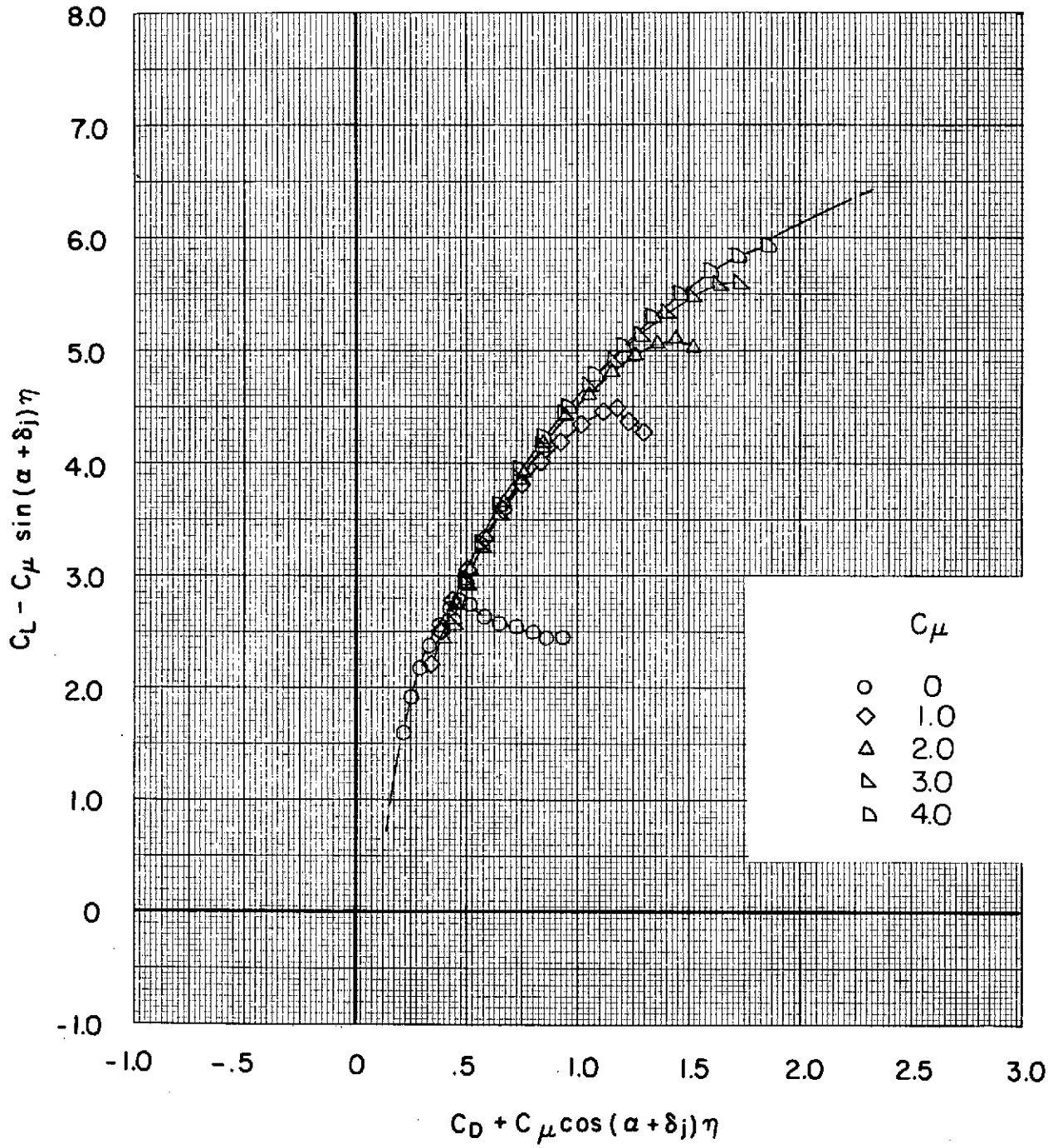

(c) $\delta_f = 0^o/20^o/40^o$ (take-off); $\delta_{sw} = 50^o$; tail off.

Figure 37.- Continued.

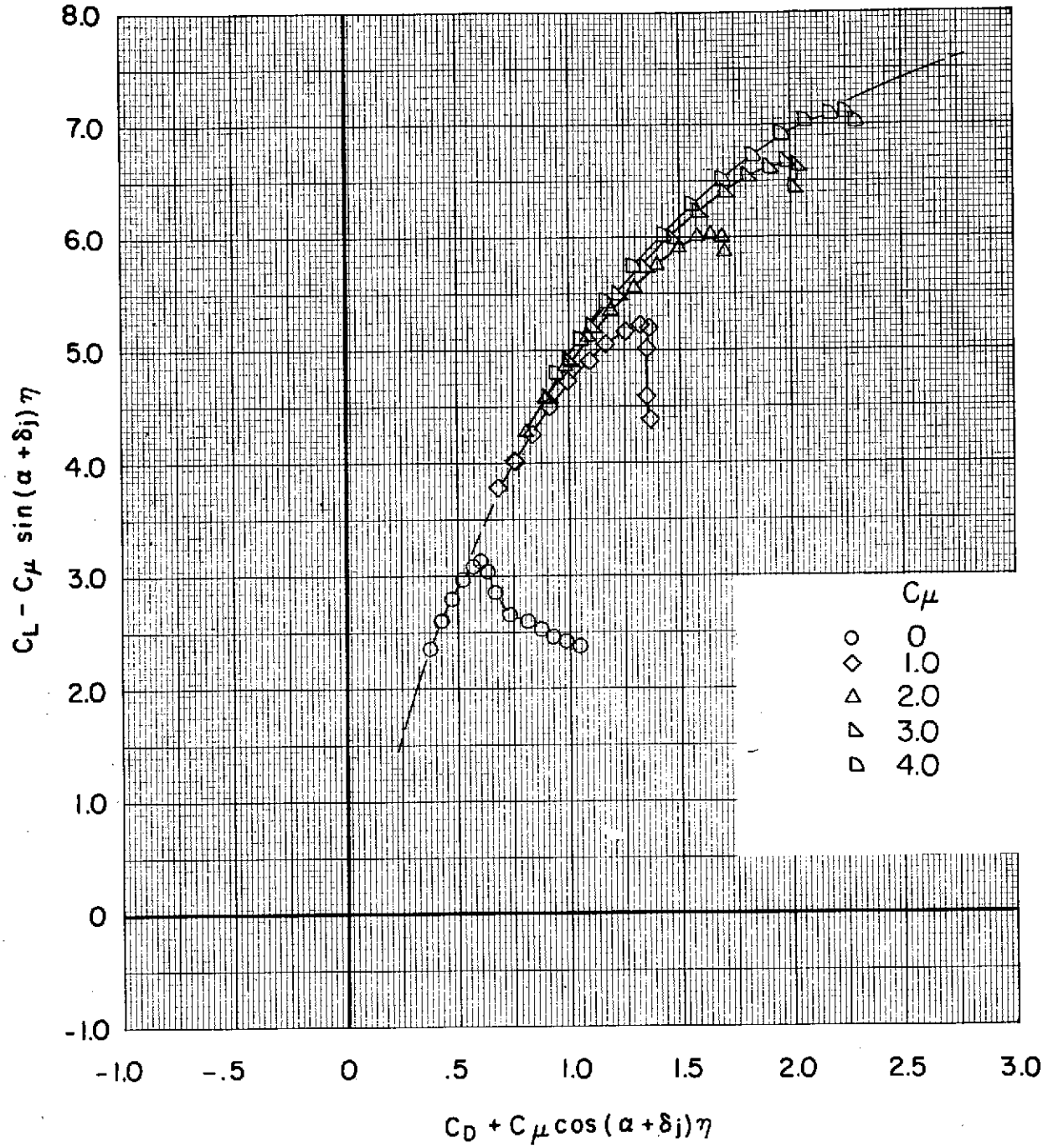

(d) $\delta_f = 15^o/35^o/55^o$ (landing); $\delta_{sw} = 50^o$; tail off.

Figure 37.- Concluded.

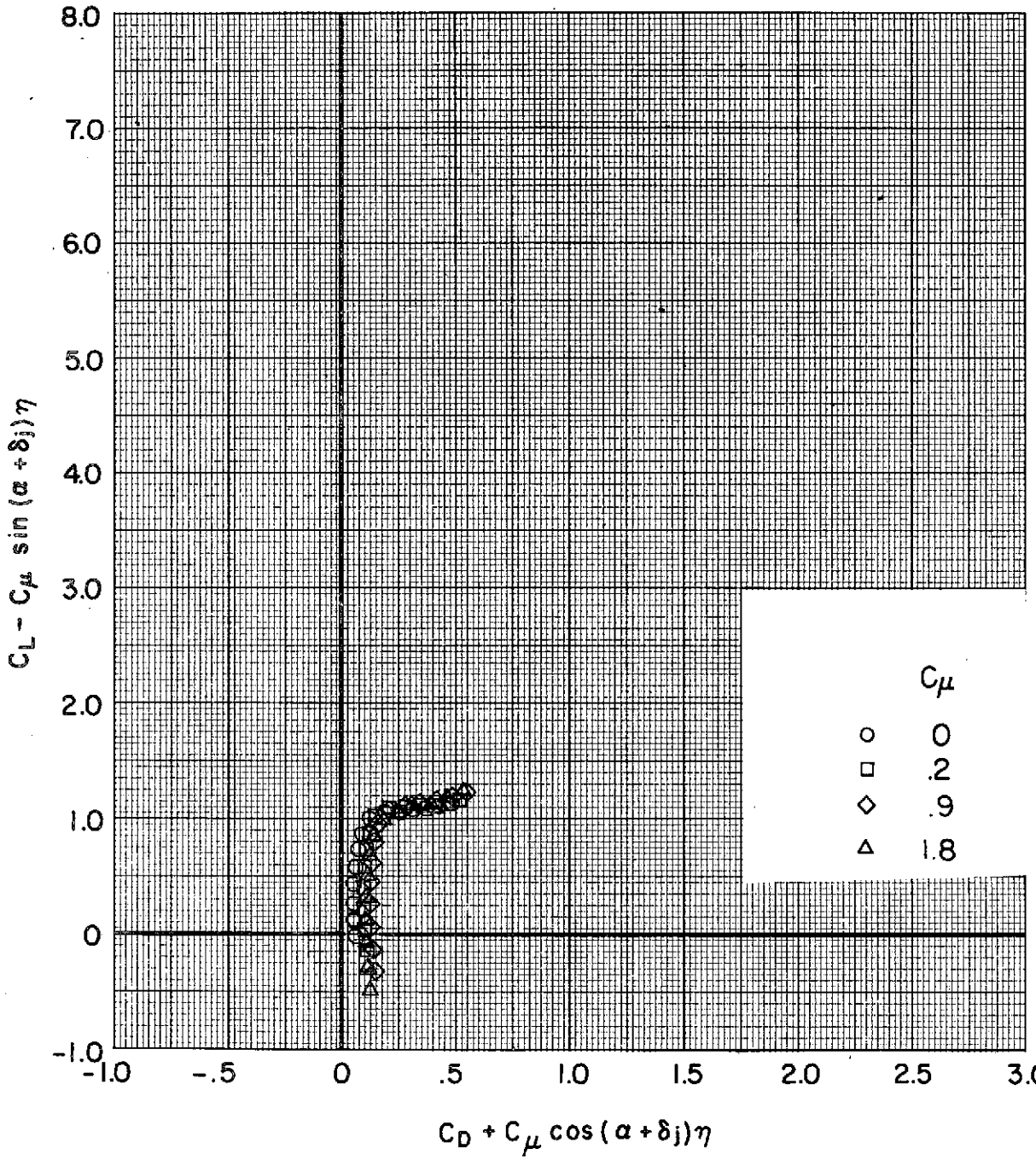

(a) $\delta_f = 0^o$ (cruise); δ_{sw} = off; tail off.

Figure 38.- Effect of thrust coefficient on thrust-removed lift coefficient and drag coefficient. Modified bypass ratio 6.2.

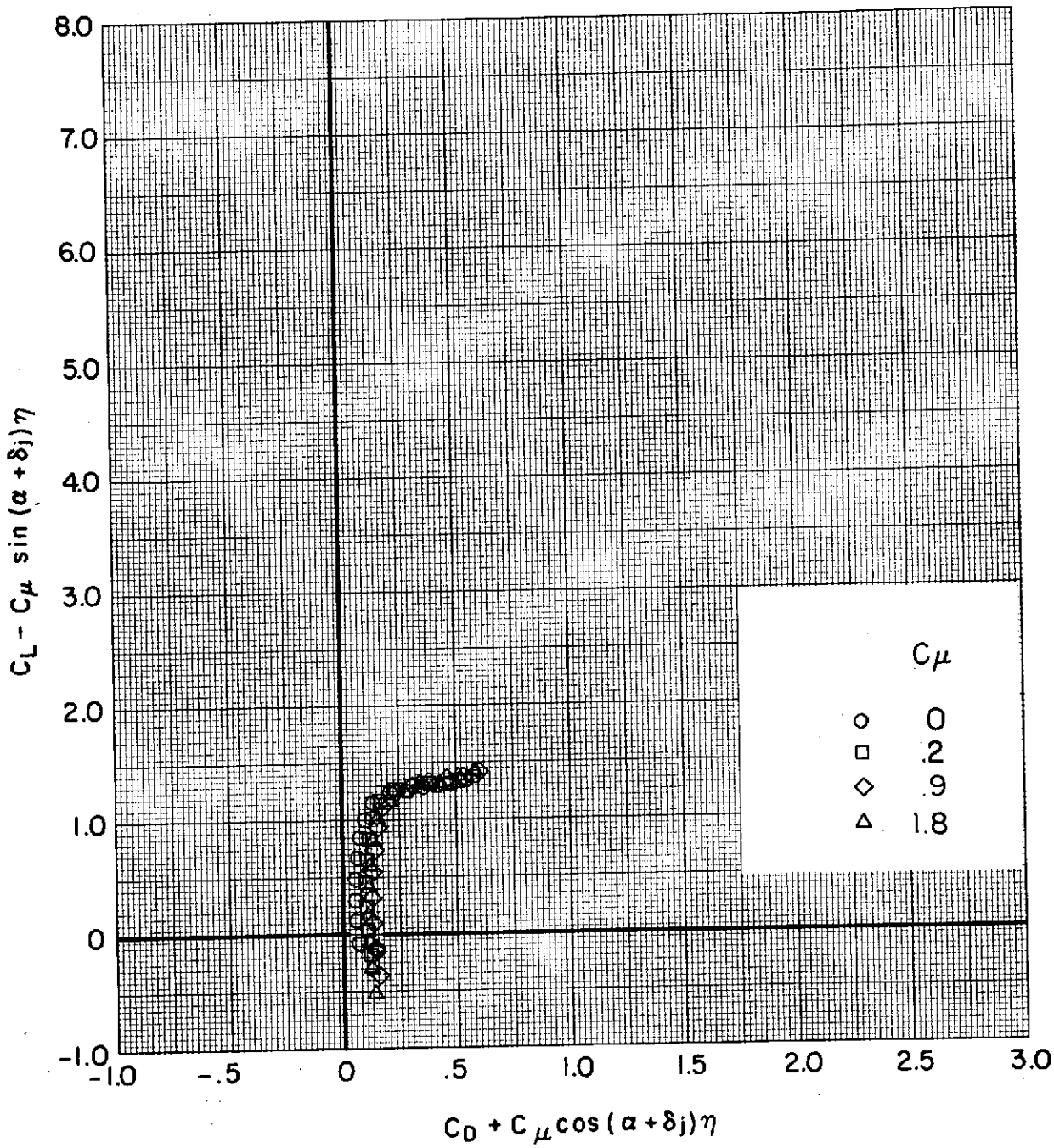

(b) $\delta_f = 0^o$ (cruise); δ_{sw} = off; $i_t = 0^o$; $\delta_e = 0^o$; δ_{sh} = off.

Figure 38.- Continued.

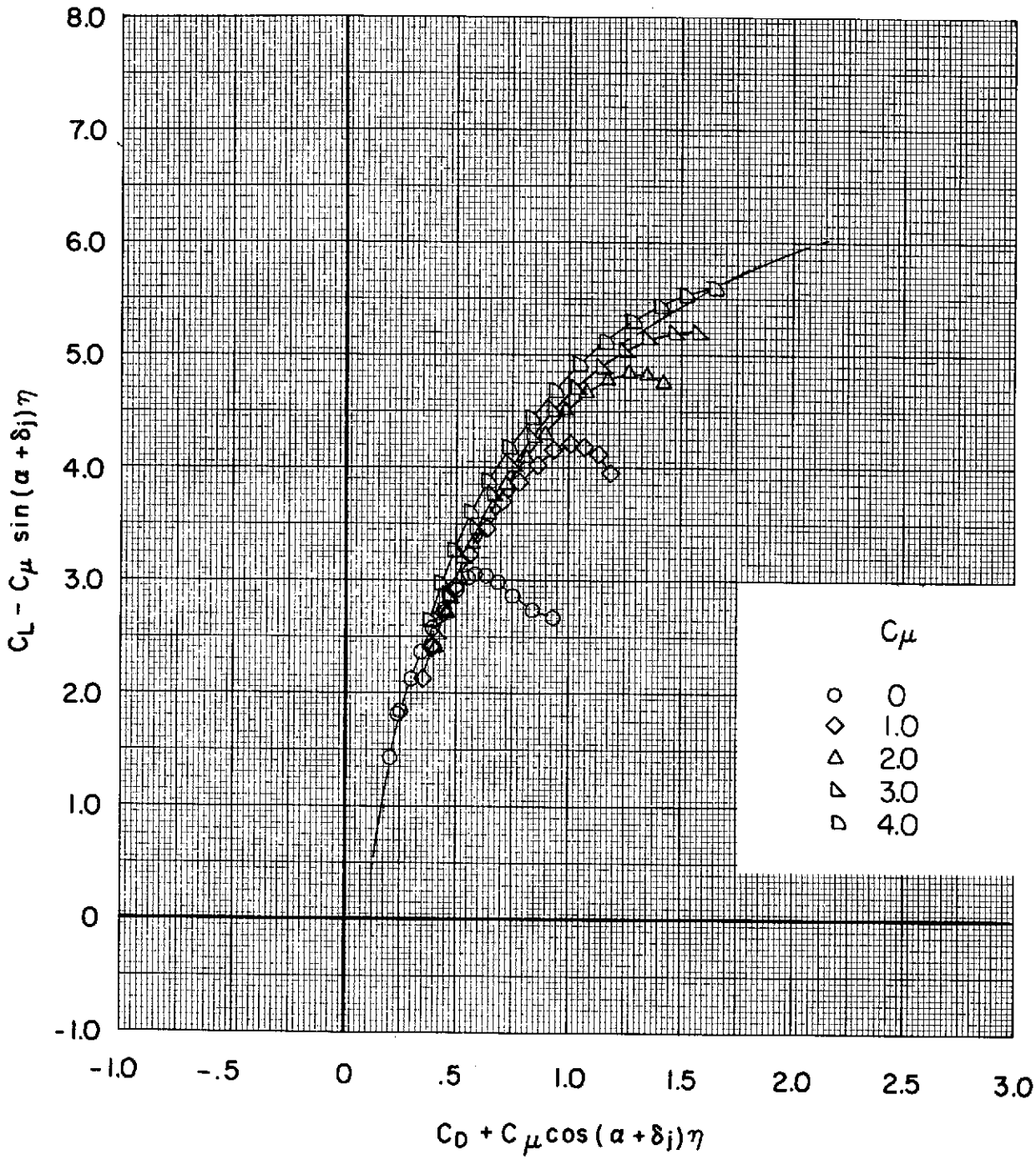

(c) $\delta_f = 0^o/20^o/40^o$ (take-off); $\delta_{sw} = 50^o$; tail off.

Figure 38.- Continued.

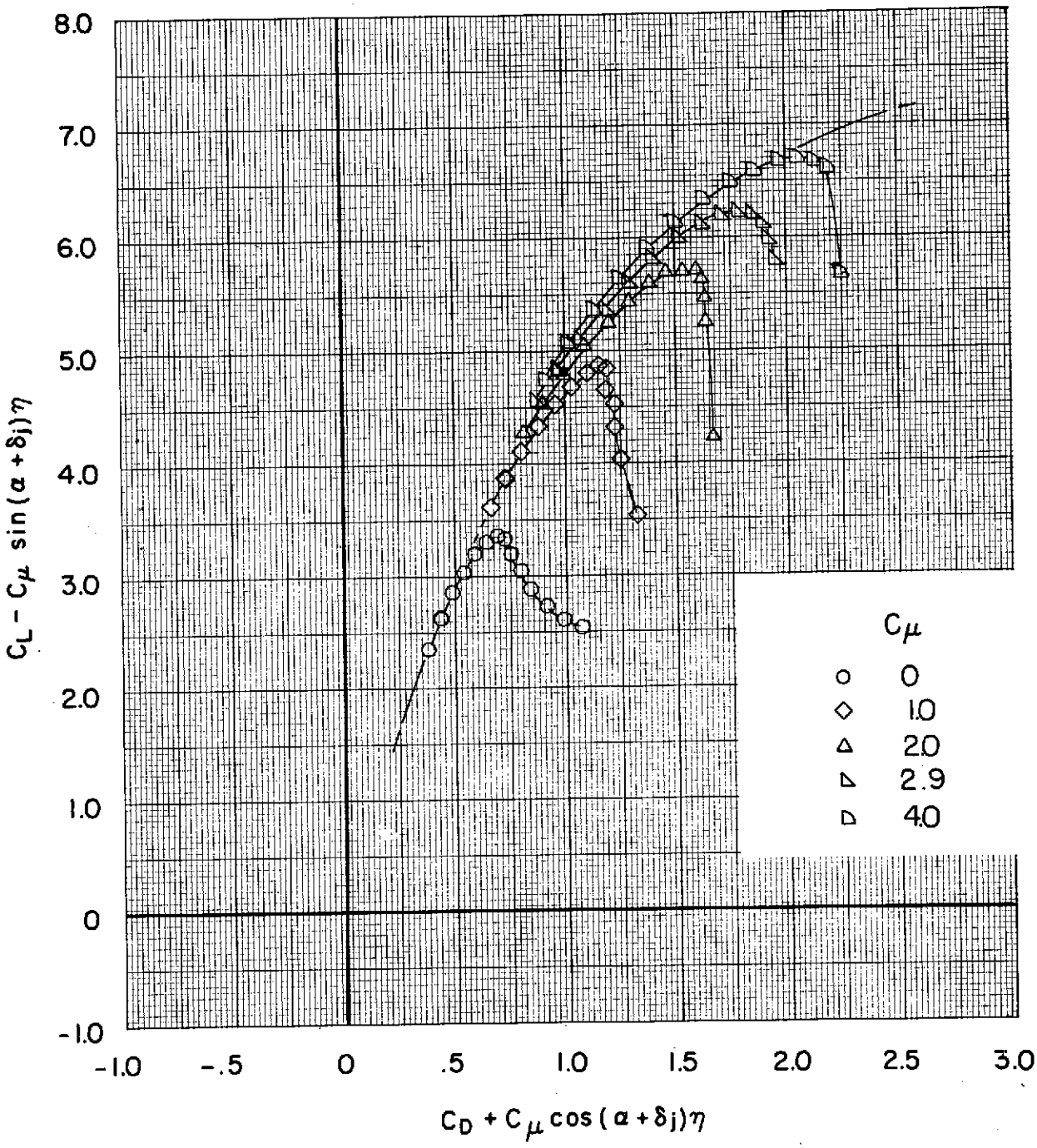

(d) $\delta_f = 15^o/35^o/55^o$ (landing); $\delta_{sw} = 50^o$; tail off.

Figure 38.- Concluded.

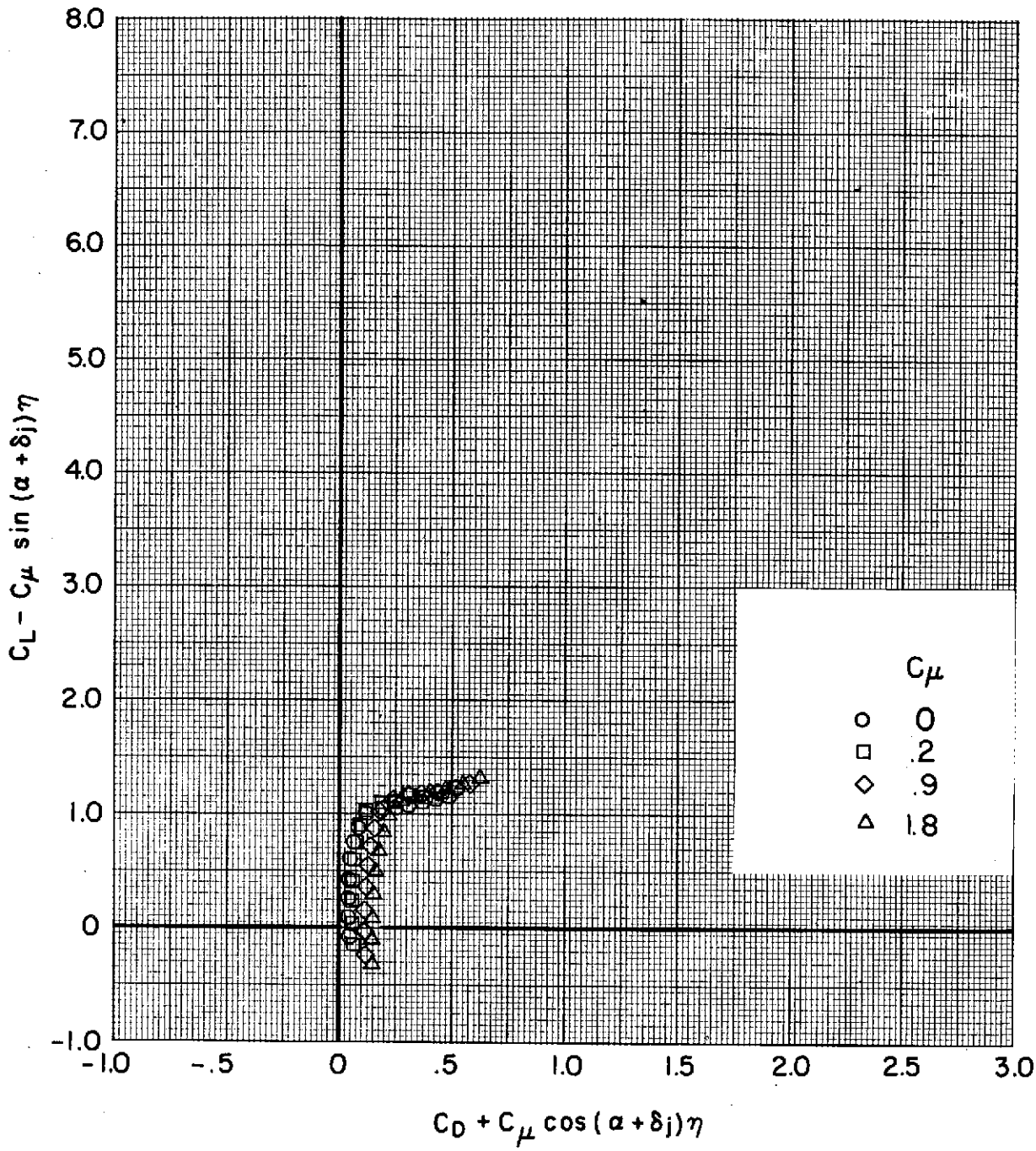

(a) $\delta_f = 0^o$ (cruise); δ_{sw} = off; tail off.

Figure 39.- Effect of thrust coefficient on thrust-removed lift coefficient and drag coefficient. Bypass ratio 10.0.

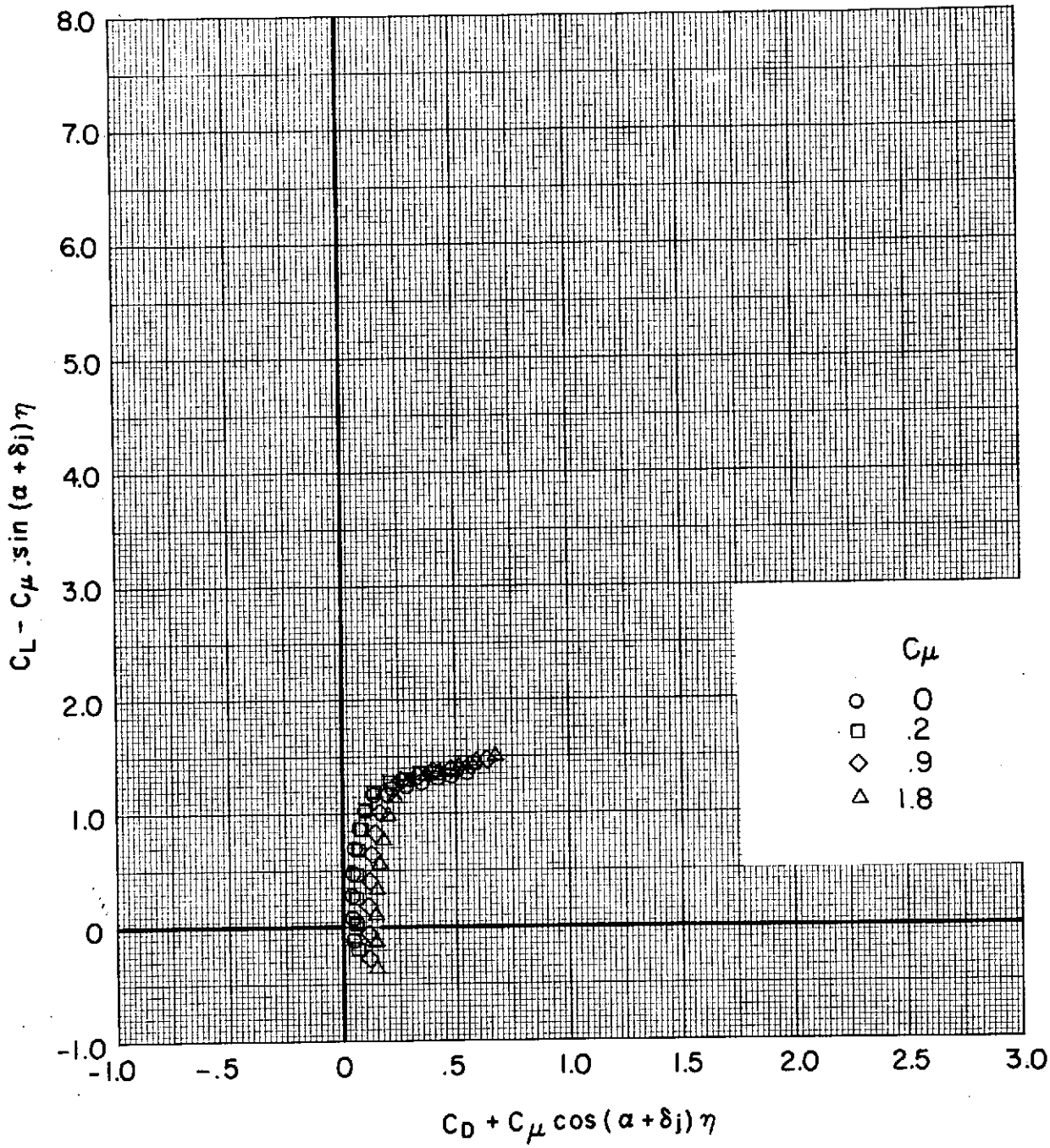

(b) $\delta_f = 0^o$ (cruise); δ_{sw} = off; $i_t = 0^o$; $\delta_e = 0^o$; δ_{sh} = off.

Figure 39.- Continued.

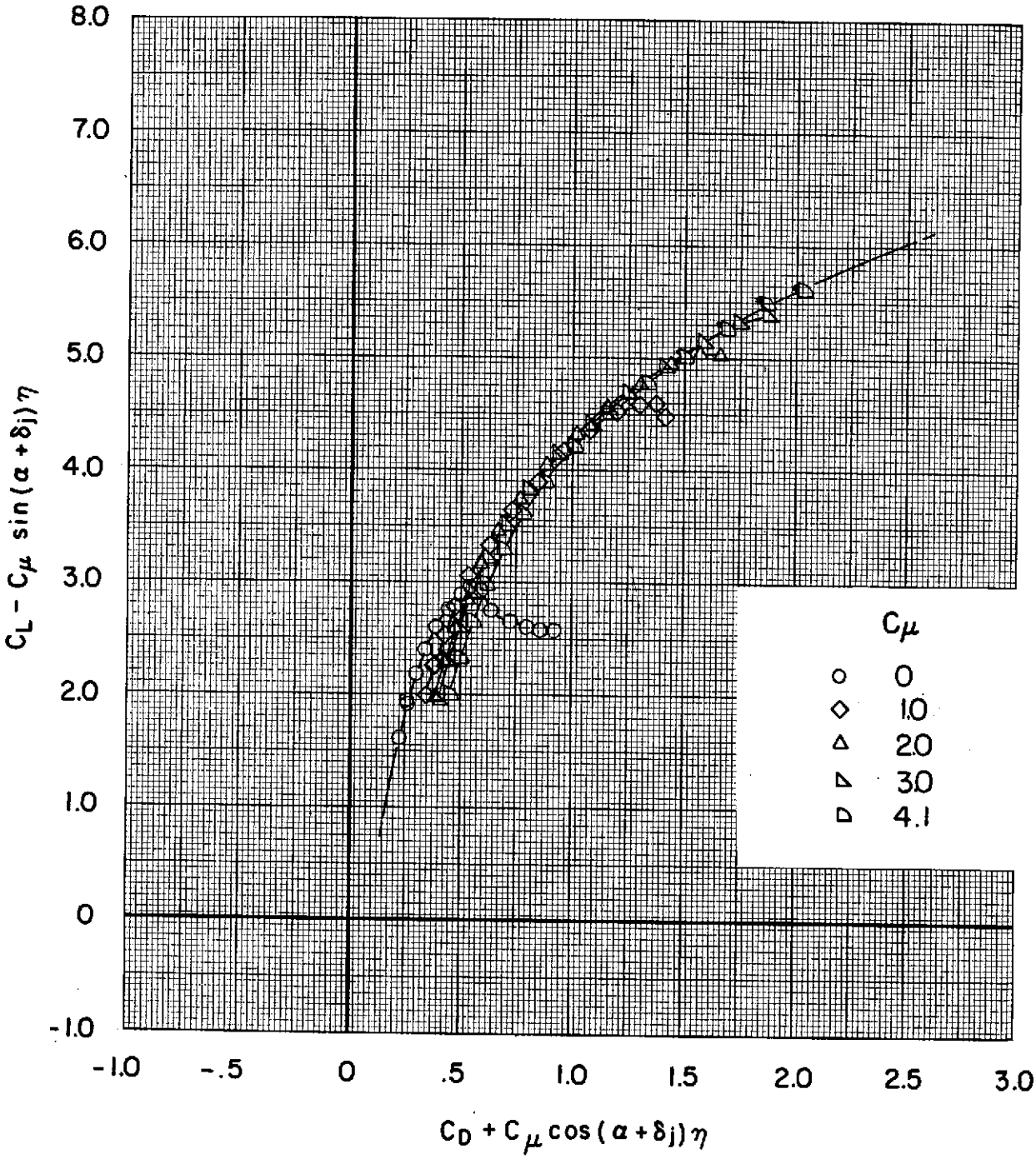

(c) $\delta_f = 0^o/20^o/40^o$ (take-off); $\delta_{sw} = 50^o$; tail off.

Figure 39.- Continued.

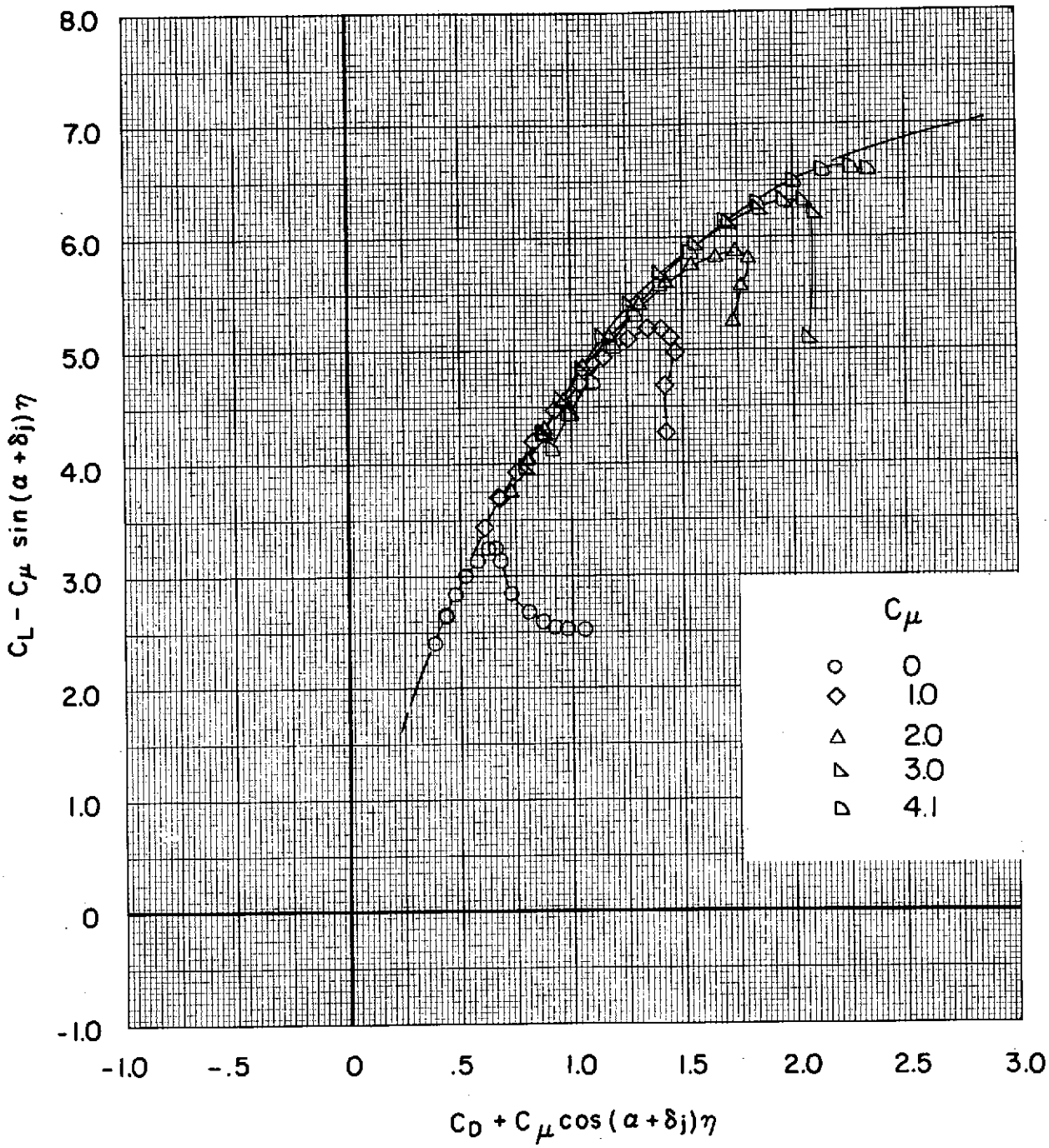

(d) $\delta_f = 15^o/35^o/55^o$ (landing); $\delta_{sw} = 50^o$; tail off.

Figure 39.- Concluded.

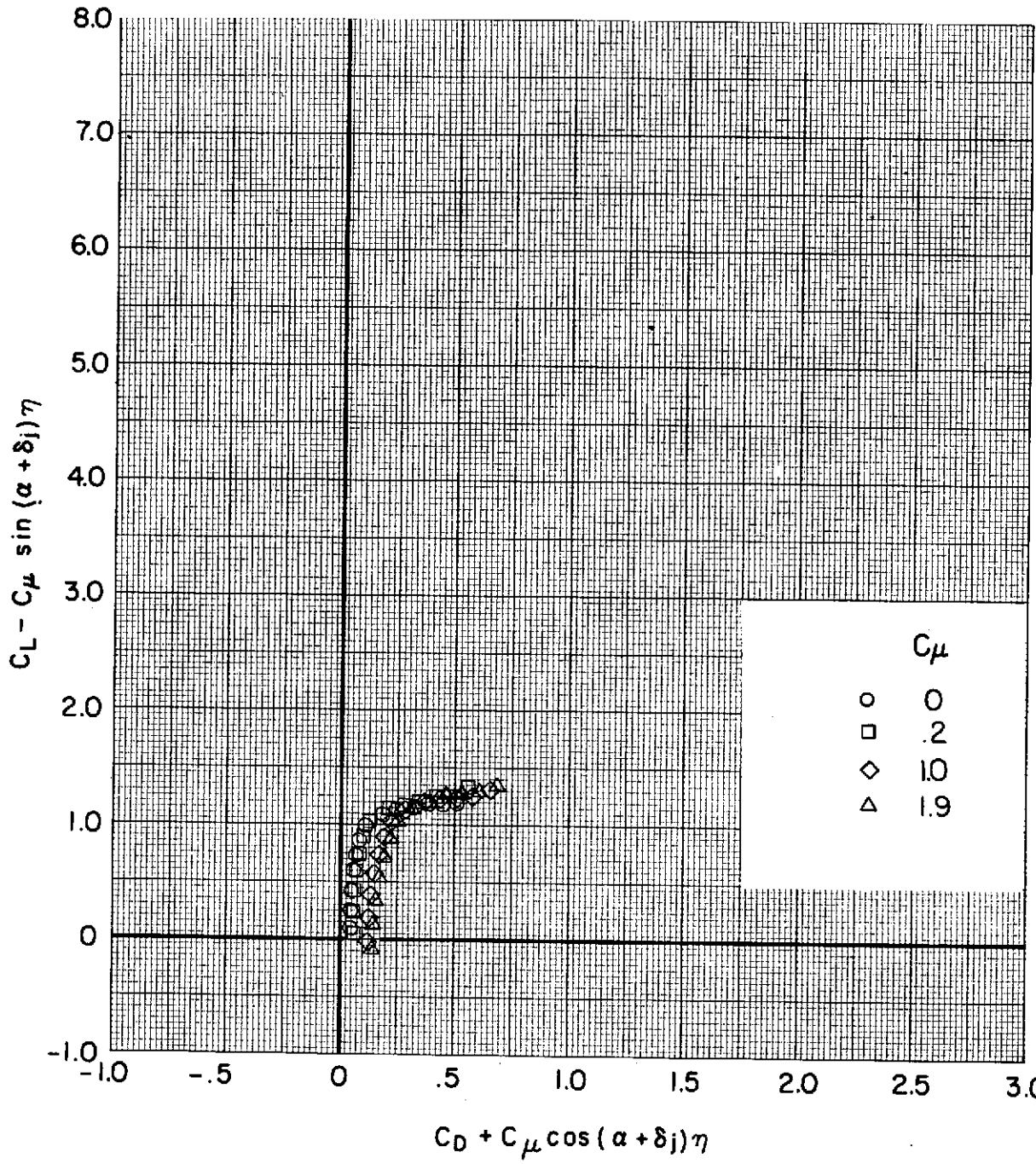

(a) $\delta_f = 0^o$ (cruise); δ_{sw} = off; tail off.

Figure 40.- Effect of thrust coefficient on thrust-removed lift coefficient and drag coefficient. Bypass ratio 3.2.

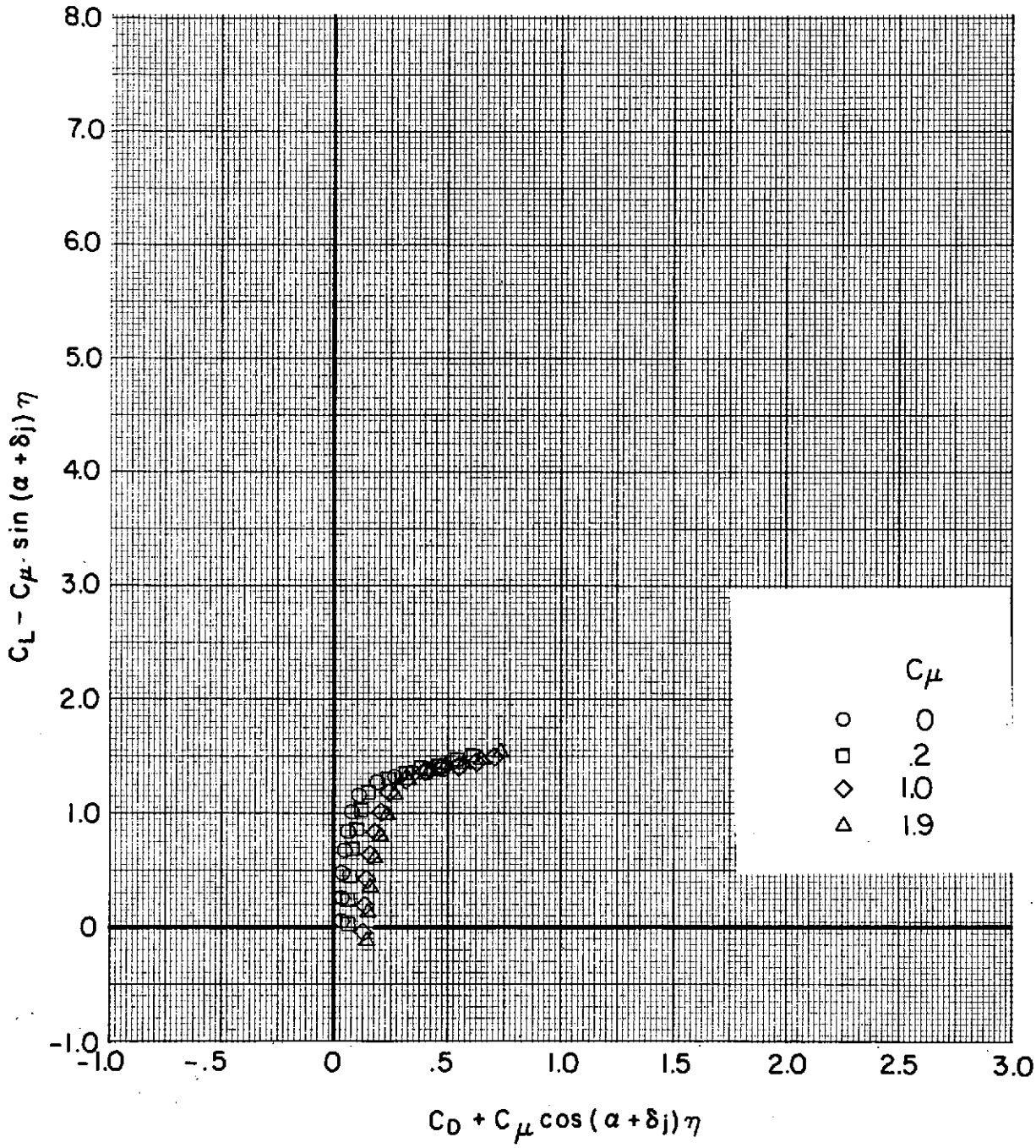

(b) $\delta_f = 0^o$ (cruise); δ_{sw} = off; $i_t = 0^o$; $\delta_e = 0^o$; δ_{sh} = off.

Figure 40.- Continued.

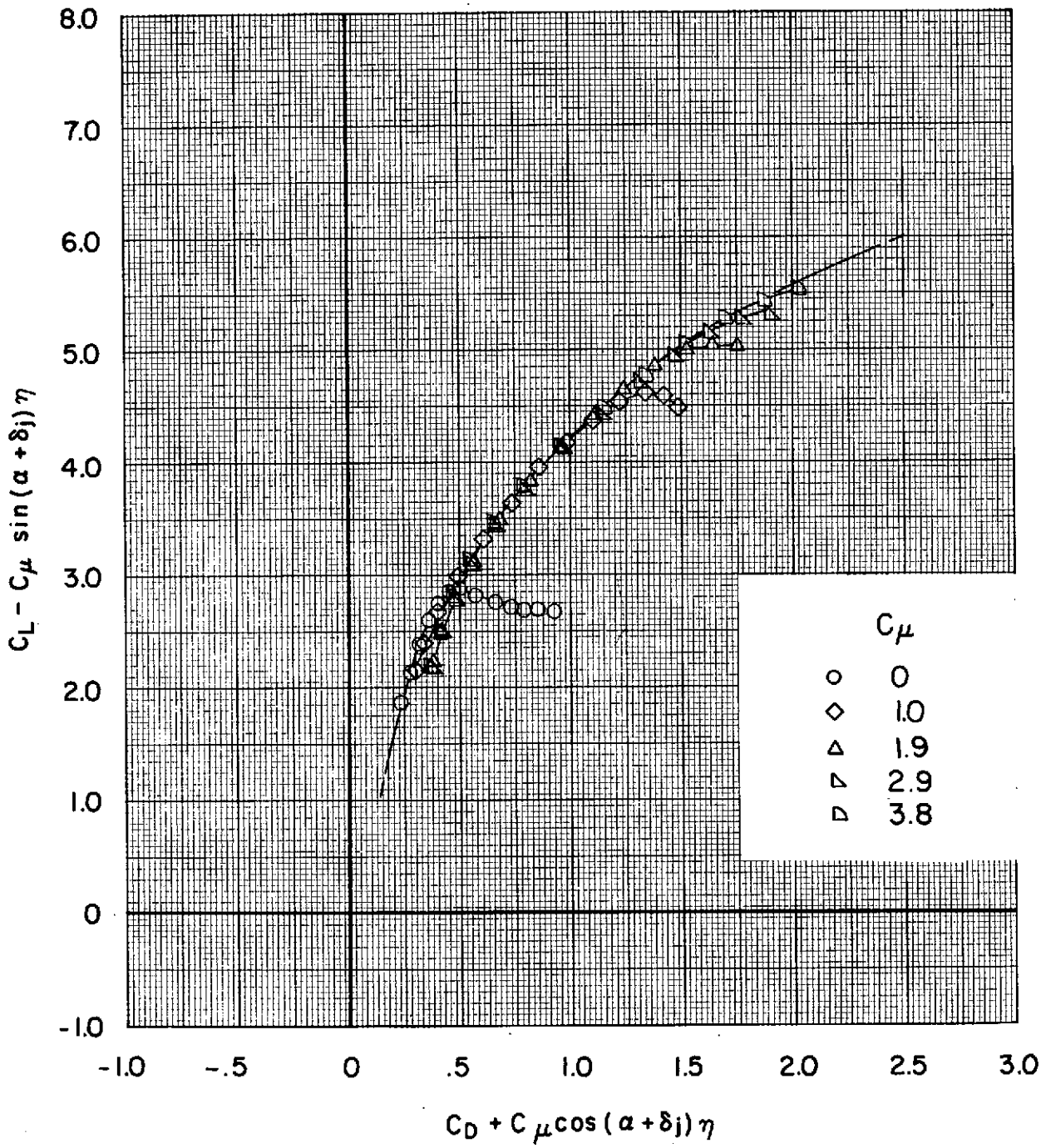

(c) $\delta_f = 0^o/20^o/40^o$ (take-off); $\delta_{sw} = 50^o$; tail off.

Figure 40.- Continued.

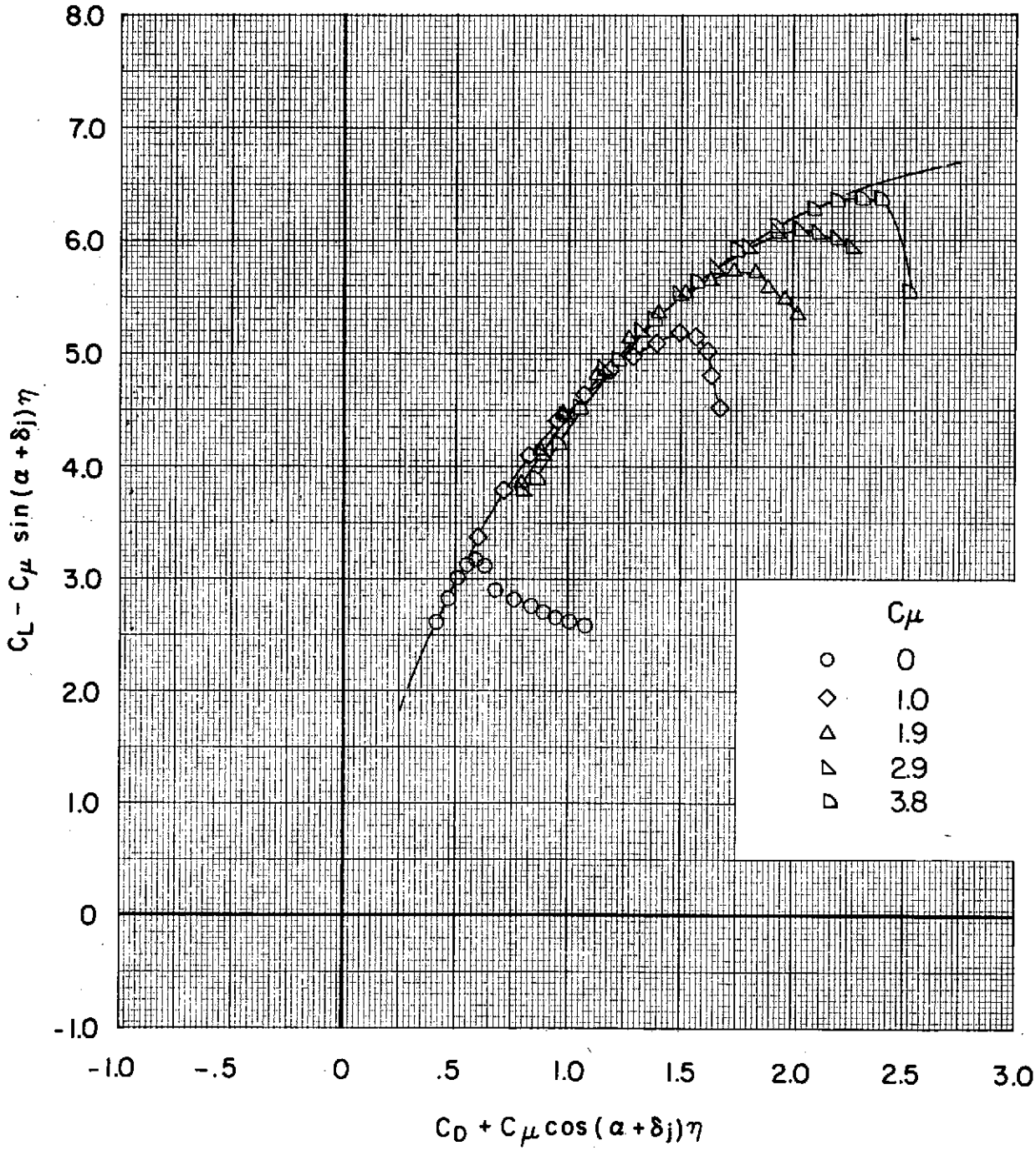

(d) $\delta_f = 15^o/35^o/55^o$ (landing); $\delta_{sw} = 50^o$; tail off.

Figure 40.- Concluded.

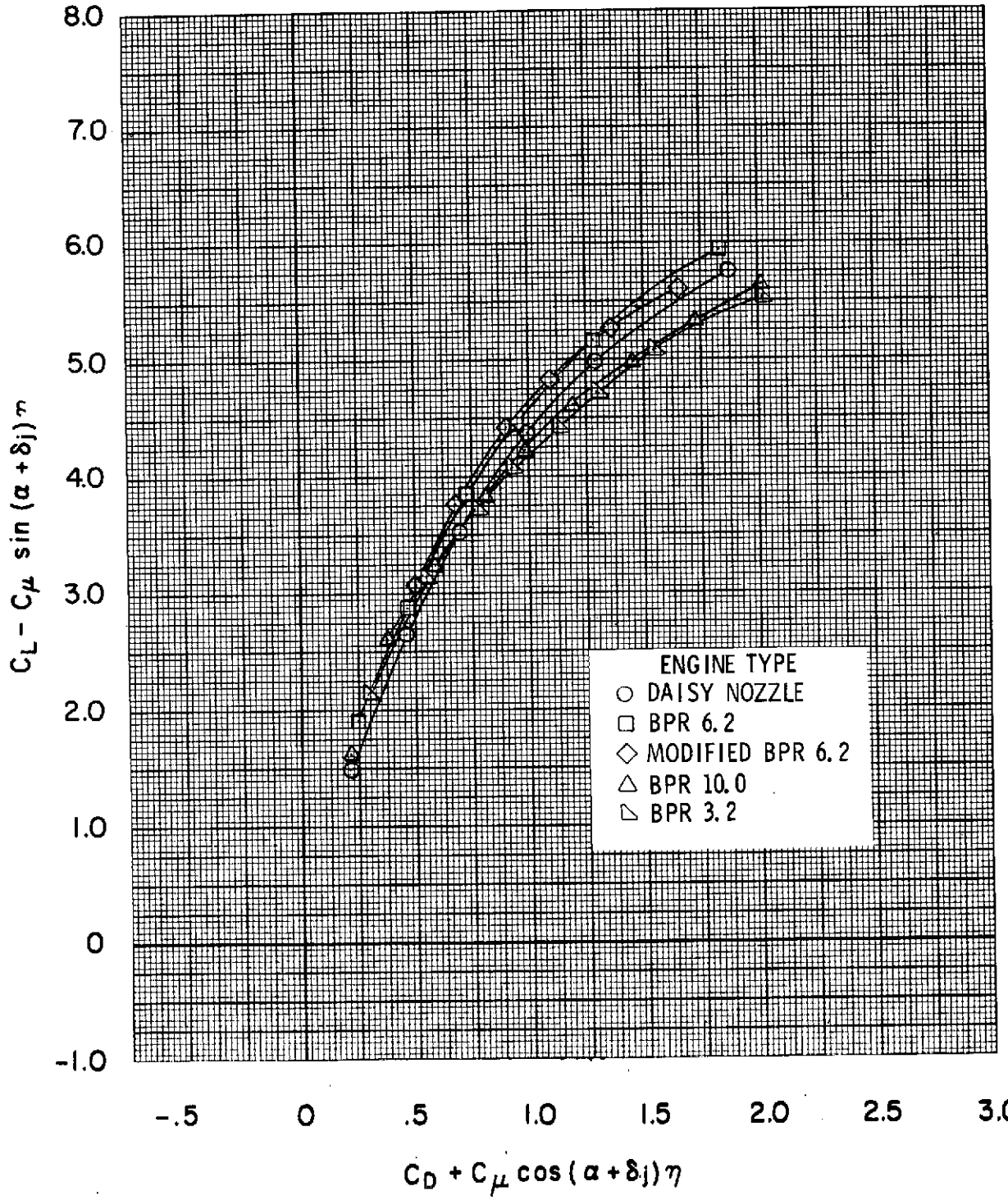

(a) $\delta_f = 0^\circ/20^\circ/40^\circ$ (take-off); $\delta_{sw} = 50^\circ$; tail off.

Figure 41.- Effect of engine type on thrust-removed lift coefficient and drag coefficient. $C_\mu = 0$ to 4.0.

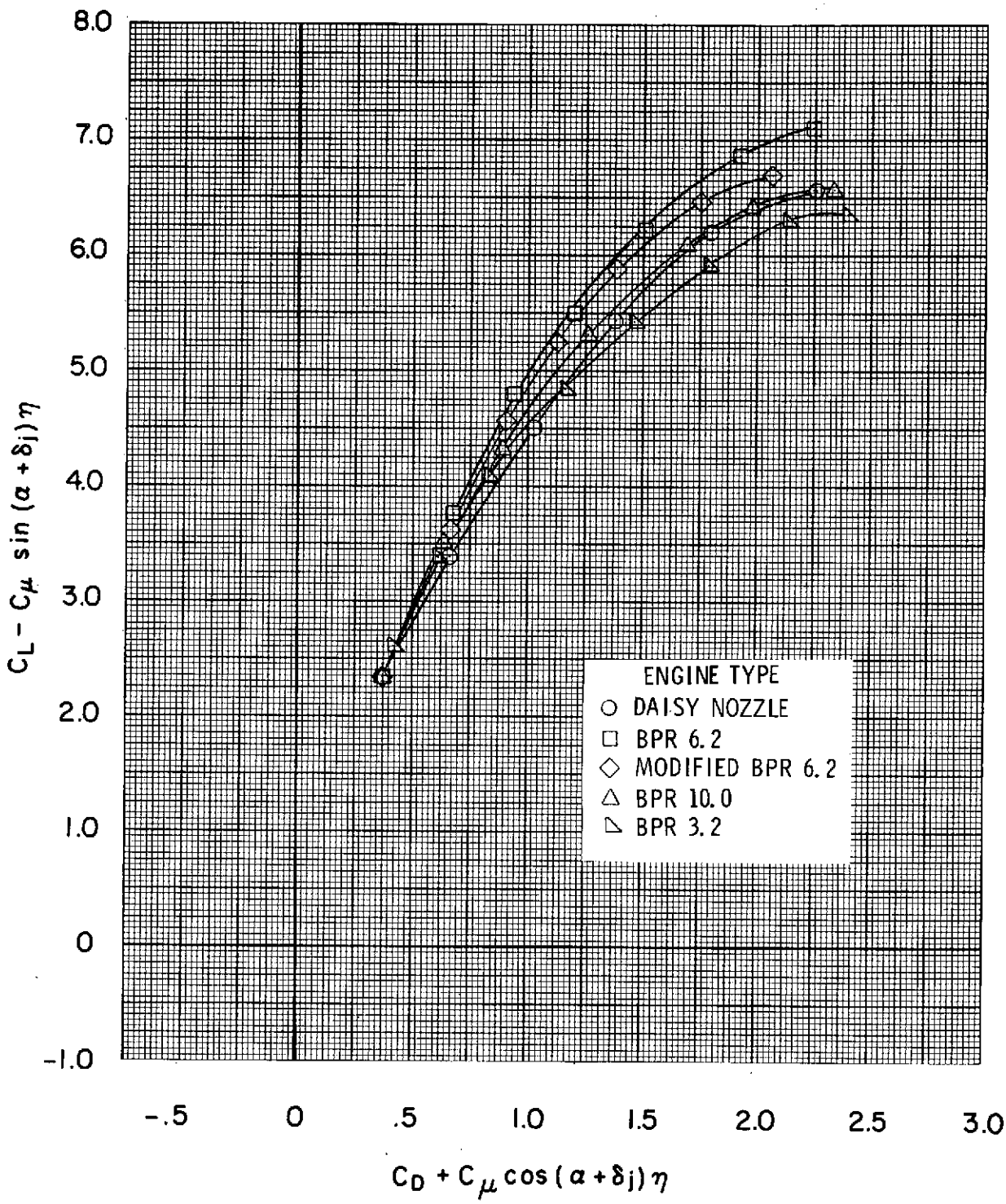

(b) $\delta_f = 15^o/35^o/55^o$ (landing); $\delta_{sw} = 50^o$; tail off.

Figure 41.- Concluded.

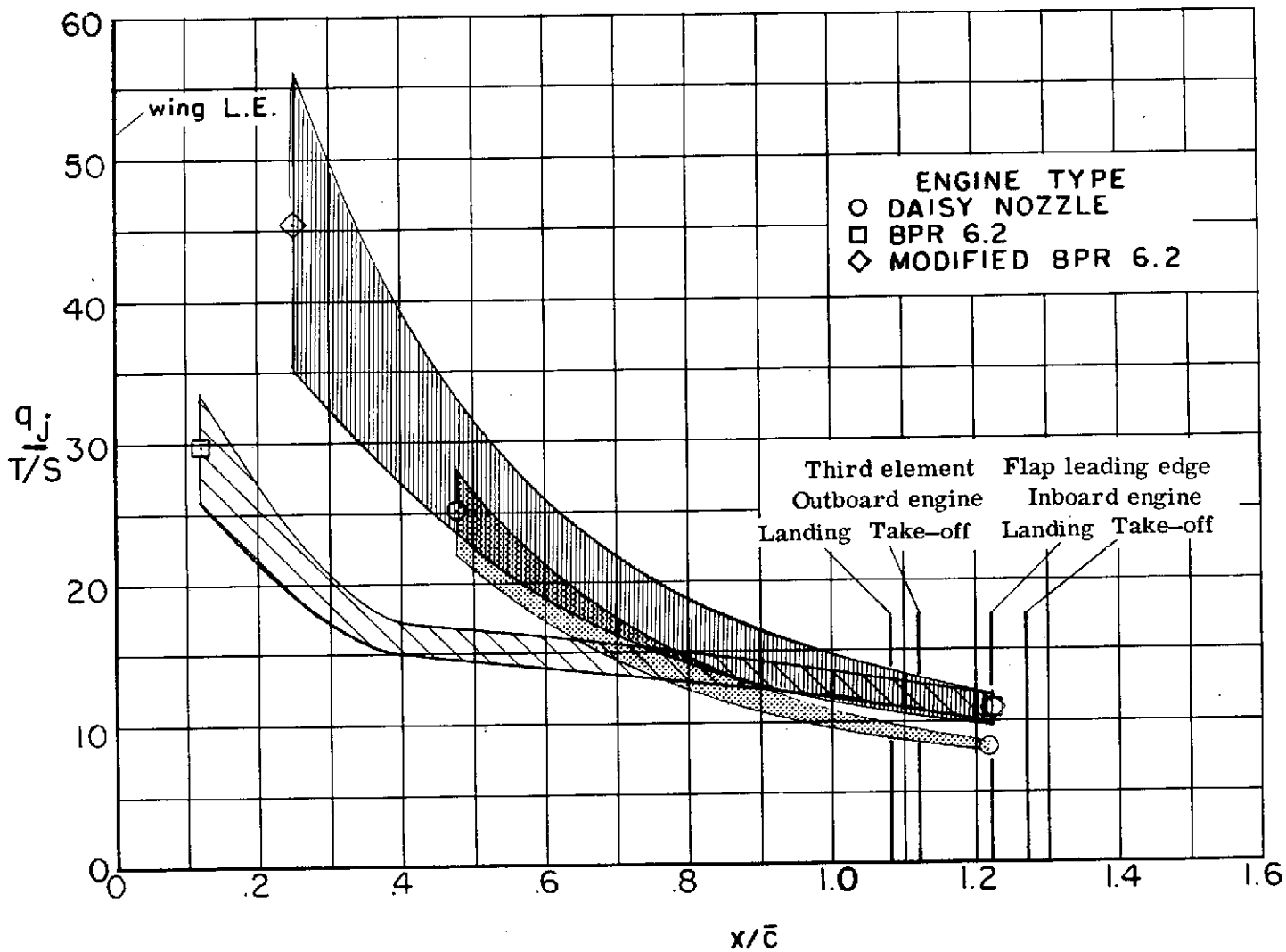

(a) Daisy nozzle; bypass ratio 6.2; modified bypass ratio 6.2.

Figure 42.- Isolated engine effective dynamic pressure decay.

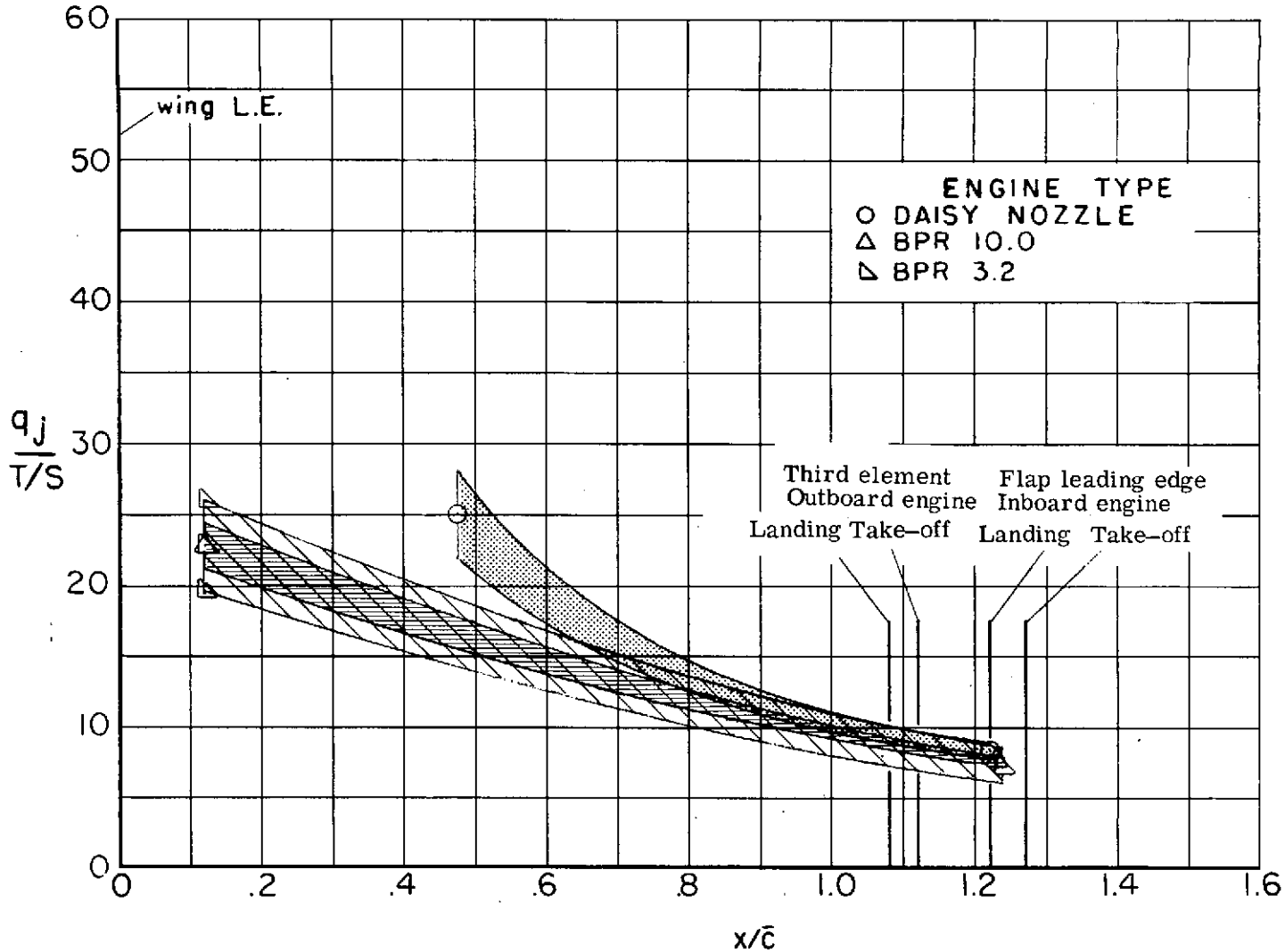

(b) Daisy nozzle; bypass ratios 10.0 and 3.2.

Figure 42.- Concluded.